



HAL
open science

Molecular Photocatalysis for Small Molecule Activation

Eva Pugliese

► **To cite this version:**

Eva Pugliese. Molecular Photocatalysis for Small Molecule Activation. Catalysis. Université Paris-Saclay, 2023. English. NNT: 2023UPASF054 . tel-04249723

HAL Id: tel-04249723

<https://theses.hal.science/tel-04249723>

Submitted on 19 Oct 2023

HAL is a multi-disciplinary open access archive for the deposit and dissemination of scientific research documents, whether they are published or not. The documents may come from teaching and research institutions in France or abroad, or from public or private research centers.

L'archive ouverte pluridisciplinaire **HAL**, est destinée au dépôt et à la diffusion de documents scientifiques de niveau recherche, publiés ou non, émanant des établissements d'enseignement et de recherche français ou étrangers, des laboratoires publics ou privés.

Molecular Photocatalysis for Small Molecule Activation

*Photocatalyse moléculaire pour l'activation de petites
molécules*

Thèse de doctorat de l'université Paris-Saclay

École doctorale n° 571, Sciences chimiques : molécules, matériaux,
instrumentation et biosystèmes (2MIB)
Spécialité de doctorat: Chimie
Graduate School : Chimie, Référent : Faculté de sciences d'Orsay

Thèse préparée à l'**Institut de chimie moléculaire et des matériaux
d'Orsay (Université Paris-Saclay, CNRS)**, sous la direction de **Ally
AUKAULOO**, professeur, la co-direction de **Zakaria HALIME**, chargé de
recherche CNRS

Thèse soutenue à Paris-Saclay, le 21 septembre 2023, par

Eva PUGLIESE

Composition du jury

Membres du jury avec voix délibérative

Frédéric AVENIER

Professeur, Université Paris-Saclay

Corinna HESS

Professeure, Technical University Munich (TUM)

Fabrice ODOBEL

Directeur de Recherche, Nantes Université

Marine DESAGE-EL MURR

Professeure, Université de Strasbourg

Président

Rapporteuse & Examinatrice

Rapporteur & Examineur

Examinatrice

Titre: Photocatalyse Moléculaire pour l'Activation de Petites Molécules

Mots clés: Photocatalyse - Réduction du CO₂ - Activation de O₂ - Complexes de Fer - Photocathode

Résumé: La nature nous enseigne beaucoup, notamment en ce qui concerne l'exploitation de l'énergie solaire pour la transformer en une forme d'énergie directement utilisable, comme les sucres. Dans une époque marquée par la crise énergétique et la nécessité d'abandonner les combustibles fossiles, les scientifiques se tournent vers ce système hautement optimisé qu'est la photosynthèse, pour transmettre ses enseignements à des systèmes artificiels, capables d'utiliser la lumière du soleil pour faire des réactions chimiques.

Dans cette thèse, nous avons cherché à étudier des systèmes moléculaires spécifiquement adaptés à différentes réactions photocatalytiques. Dans la première partie de la thèse, nous étudions la réduction photocatalytique du CO₂ par un système moléculaire homogène. Ici, nous avons mis en œuvre un catalyseur de porphyrine de fer avec des modifications sur la deuxième sphère de coordination qui facilitent la fixation du CO₂ et l'activité

catalytique. Cette étude implique aussi la compréhension ultérieure du mécanisme de réaction.

Nous nous sommes ensuite intéressés à l'intégration de ce même catalyseur moléculaire sur une surface pour constituer une photocathode pour la réduction du CO₂. Cette approche, malgré ses potentialités pour une stabilité et une recyclabilité accrues, nécessite encore des optimisations substantielles en termes d'assemblage de matériaux pour confirmer son activité catalytique.

Dans la dernière partie de ce manuscrit, nous avons étudié un autre type de réactivité, cette fois-ci l'activation de l'O₂ pour des réactions de transfert d'atomes d'oxygène. Cette photocatalyse homogène implique un complexe de fer non hémique capable de réagir avec le dioxygène réduit pour générer des intermédiaires très oxydants, qui ont été caractérisés par spectroscopie UV-vis et RPE.

Title: Molecular Photocatalysis for Small Molecules Activation

Keywords: Photocatalysis - CO₂ reduction - O₂ activation - Fe complexes - Photocathode

Abstract: Nature teaches us great lessons, one in particular is the harvesting of solar energy to transform it into a readily available form of energy, such as sugars. In an epoch marked by the energy crisis and the need to abandon fossil fuels, scientists are looking back to this highly engineered machine trying to capture some of these teachings and translate them into artificial systems, capable of using sunlight to perform chemical reactions.

In this thesis we aimed to study molecular systems specifically tailored for different photocatalytic reactions. In the first part of the thesis we are concerned with the photocatalytic CO₂ reduction by a homogeneous molecular system. Here, we implemented an iron porphyrin catalyst with modifications on the second coordination sphere that facilitate CO₂ binding and therefore enhance

the catalytic activity. This study also involves investigation of the reaction mechanism.

We then turned our interest towards integrating the same molecular catalyst into a surface to build a photocathode for CO₂ reduction. This approach, despite its potentialities of an increased stability and recyclability still needs substantial optimizations in terms of materials assembly to prove the overall catalytic activity.

In the last part of this manuscript, we investigated a different kind of reactivity, this time involving O₂ activation for oxygen atom transfer reactions. This homogeneous photocatalysis involves a non-heme iron complex that reacts with reduced dioxygen to generate highly oxidizing intermediates, which were characterized by UV-vis and EPR spectroscopies.

Acknowledgements

First and foremost, I would like to express my gratitude to my two supervisors Prof. Ally Aukauloo and Dr. Zakaria Halime for giving me the opportunity of carrying out my PhD thesis in the Artificial Photosynthesis group of ECI in ICMMO and for their guidance throughout the years. Thank you Zak for the time invested in discussing the projects and the results, thank you for giving me the rudiments of porphyrin synthesis with its never-ending columns. Thank you Ally for your trust and the scientific discussions.

I would also like to deeply thank Dr. Winfried Leibl and Dr. Annamaria Quaranta for the possibility of carrying out my experimental work also in the I2BC laboratory at CEA Saclay and for their incredible help in these years, you have always been available for my doubts, scientific and not.

I feel truly honored for the jury members to have agreed to evaluate my PhD work and I would like to acknowledge them: Prof. Corinna Hess, Dr. Fabrice Odobel, Prof. Marine Desage-El Murr and Prof. Frédéric Avenier.

I am grateful to all of the team members of the two laboratories that I had the pleasure to encounter along the way: Dr. Gotico, Dr. Sircoglou, Dr. Trapali, Dr. Amanullah, Dr. Khadhraoui, Dr. Kumar, Dr. Bousfiha, M.Sc. Zhang, M.Sc. Smith, M.Sc. Rashid, M.Sc. Lin, M.Sc. Viet-Dung, M. Sc. El Moqaouil, B.S. Nguyen for the friendly and collaborative environment.

I want to thank all the ECI members for welcoming me in these years, and all the friendly and helpful ICMMO staff that I was lucky to interact with: Jean-Pierre and Amandine for the NMR, Tanya and Helene for the MS, Diana for the XPS, Régis for my unsuccessful XRD (but still tried to get something), Christian for the EPR. Also, a special thanks to Pr. Banse for the collaboration on the OAT project and providing us with the catalyst compound and to Dr. Boussac for the EPR performed in CEA Saclay.

This three-year journey would have never been the same without all the amazing friendships that grew in parallel to the PhD roller-coaster, and to these people I owe a special thank you. Thank you Adelaida for being our lab expert and one of the most passionate chemists I know, not letting aside the beautiful person and friend that you are, thank you Amanda (Mamanda) for being the LCI mom and always such a smart and caring person, grazie Nicolò per essere stato il primo membro LCI con cui ho interagito (telefonicamente) e per avermi insegnato a massaggiare le arance per lo spritz, il termine "tora" e per il buonumore che porti sempre con te, thank you Adrien for the interesting music you put in the lab and pour m'avoir enseigné plein de choses en français, surtout que l'électrode est FEMENIN! Merci J-No and gracias Christian for putting up with us millenials (or even GenZ) and for bringing your wisdom and fun jokes to the Petit Club apéros. Thank you Juan for all the beers and trips together, thank you Laura for your energy and the amazing falafels, thank you Haroon, Rongning, Sandeep, Alexis, Duong and Thai for the moments of fun in the lab (which is not only unsuccessful experiments...). Merci Sandra pour les pauses café et les leçons de français, merci Zineb pour ton sourire et merci Asmae pour ta gentillesse.

A big thank you also to all the LCI students and post-docs past and present, even if we may have interacted more or less along the years, the whole friendly and fun environment was really special: thank you Kévin, Alberto, Thimothé, Flora, Daiann, Elvin, Asma, Axel, Adama, Arthur, Riya, Sophie, Morane (honorary LCI member), Grégory, Abdoul, Thomas, Aristide, Idris, Solène, Maria, Madeleine... I will surely not forget all the nice people and moments in the LCI.

Few more words also go to all my friends from home and from abroad that have been always there for me. Thank you to all of the SERP buddies and for the trips around the world together. Thank you to all

the wonderful friends always waiting for me back in Italy and resisting through the years. A special thank you to the Parisian gang that put up with all my stories and complaints about PhD life and brought so many crazy and fun moments.

Thank you Isma for all of your love and support, to remind me everyday to be strong and to believe in myself.

Lastly, I want to immensely thank my family for the support that they gave me in all of my decisions and for their unconditional love.

Contents

1	INTRODUCTION	13
1.1	General context	13
1.2	Natural photosynthesis	16
1.3	Artificial photosynthesis	25
1.3.1	Mimicking antenna complexes	26
1.3.2	Mimicking reaction centers: charge separation	28
1.3.3	Coupling antennas and reaction centers	32
1.3.4	Coupling reaction centers and charge accumulation: towards catalysis	33
1.3.5	Heterogeneous systems and devices	36
1.4	CO ₂ conversion	39
1.4.1	Context	39
1.4.2	Iron porphyrins for catalytic CO ₂ reduction	41
1.4.3	Photocatalytic CO ₂ reduction	47
1.5	O ₂ activation	57
1.5.1	Context	57
1.5.2	Non-heme Fe complexes for O ₂ activation	60
1.5.3	Light-induced O ₂ activation	64
1.6	Goal of the thesis	68
2	CO₂ REDUCTION IN A HOMOGENEOUS SYSTEM	81
2.1	Introduction and objectives	81
2.2	Catalyst synthesis and characterizations	83
2.3	Developments and optimizations of the photocatalytic system	85
2.4	Capturing reaction intermediates and their spectral fingerprints	97
2.4.1	Chemical reductions	97
2.4.2	UV-vis spectroelectrochemistry	98
2.4.3	Photoaccumulation of reaction intermediates	101
2.5	Unravelling the mechanism	104
2.5.1	Limiting factors in the catalysis	104
2.5.2	<i>In situ</i> investigation of CO ₂ binding to UrFe	107
2.5.3	DFT and mechanism proposal	114
2.6	Conclusions	118
3	HETEROGENEOUS PHOTOCATALYSIS FOR CO₂ REDUCTION	121
3.1	Introduction and objectives	121
3.1.1	Cuprous oxide as semiconductor and photoabsorber	122
3.2	Catalyst synthesis and characterization	125

3.3	Catalyst immobilization	130
3.4	Photoelectrode preparation	134
3.5	Photoelectrochemical study	139
3.6	Conclusions and perspectives	147
4	PHOTOCATALYSIS FOR OXYGEN ATOM TRANSFER REACTIONS	151
4.1	Introduction and objectives	151
4.2	Understanding the photophysical events	153
4.3	Photocatalysis	159
4.4	Trapping reactive intermediates	166
4.5	Mechanism proposal	172
4.6	Conclusions	175
5	CONCLUSIONS AND PERSPECTIVES	179
6	ANNEX	187
6.1	Chapter 2: CO ₂ reduction in a homogeneous system	187
6.1.1	Synthesis and characterization	187
6.1.2	Electrochemical characterizations	193
6.1.3	Photocatalysis	196
6.1.4	UV-Vis spectroelectrochemistry	197
6.1.5	Photoaccumulation	198
6.1.6	Infrared spectroscopy	198
6.1.7	Computational study	199
6.2	Chapter 3: Heterogeneous photocatalysis for CO ₂ reduction	201
6.2.1	Catalyst synthesis and characterizations	201
6.2.2	Electrode assembly	203
6.2.3	Electrode characterizations	204
6.3	Chapter 4: Photocatalysis for oxygen atom transfer reactions	211
6.3.1	Materials and instrumentation	211
6.3.2	Photocatalysis	211
6.3.3	Electronic paramagnetic resonance spectra	214

Abbreviations

ACN	Acetonitrile
ALD	Atomic Layer Deposition
ATR	Attenuated Total Reflectance
AZO	Aluminum-doped Zinc Oxide
BIH	3-dimethyl-2-phenyl-2,3-dihydro-1Hbenzo[d]imidazole
bpy	Bipyridine
CA	Chronoamperometry
Cat	Catalyst
CB	Conduction band
CCS	Carbon capture and storage
CCU	Carbon capture and utilization
CE	Counter electrode
CODH	Carbon monoxide dehydrogenase
CV	Cyclic voltammetry
DCM	Dichloromethane
DFT	Density functional theory
DMF	Dimethylformamide
EDTA	Ethylenediaminetetraacetic acid
EPR	Electron paramagnetic resonance
ESI	Electrospray ionization
EtOH	Ethanol
FTO	Fluorine-doped Tin Oxide
HR-MS	High resolution Mass spectrometry
KIE	Kinetic isotope effect
LED	Light emitting diode
LFP	Laser flash photolysis
LSV	Linear sweep voltammogram
MALDI	Matrix-assisted laser desorption/ionization
MeOH	Methanol
MV ²⁺	Methyl viologen
NMR	Nuclear magnetic resonance
OAT	Oxygen atom transfer
PEC	Photoelectrochemical cell
PSI	Photosystem I
PSII	Photosystem II
RE	Reference electrode
SCE	Saturated calomel electrode

SEC	Spectroelectrochemistry
SED	Sacrificial electron donor
THF	Tetrahydrofuran
TLC	Thin layer chromatography
TOF	Turnover frequency
TON	Turnover number
TPP	Tetraphenyl porphyrin
VB	Valence band
WE	Working electrode
XPS	X-ray photoelectron spectroscopy
XRD	X-ray diffraction analysis
μ -GC	Micro- Gas chromatography

1 - INTRODUCTION

1.1 . General context

Every second, on the Earth soil, we receive between 170 and 180 J/m² of energy from the sunlight. Globally, that makes about 90 PW (Peta = 10¹⁵), a huge amount when compared to the global energy demand at the beginning of the 21st century, estimated to be 15 TW (Tera= 10¹²)[1]. Even after taking into account all the energy absorbed by all plants and organisms of the planet that use it for photosynthesis, which accounts for about 1% of it, we are left with an enormous potential energy source[1][2].

The idea of direct use of sunlight as energy source has been inspiring scientists' minds for more than one century. In 1839, physicist Edmond Becquerel defined the photovoltaic effect in one of his experiments, when he observed a voltage and current increase from shining light on a silver chloride electrode in a two-electrodes cell[3]. This discovery gave rise to further studies until the assembly of the very first solar cell in 1883 by Charles Fritts[4]. Italian chemist Giacomo Ciamician dedicated his research to the understanding of the chemical processes initiated by light in plants during photosynthesis, and to trying to reproduce organic chemistry initiated by light[5][6][7][8].

Today, collecting and transforming solar energy into a chemical potential or a chemical form is on the top of the agenda of scientists. However, when we look at the global energy mix of 2021, we find that 83% of energy consumption is from fossil fuels (oil, coal and gas), and solar energy accounts for 1.65%[9]. Even if we restrict our vision to only European Union, known to have raised more attention to the environment and sustainability, we find that the energy mix of 2021 is made up by 72% of fossil fuel sources and solar energy reaches 2.58%.

Back in the early 1910s, Ciamician argued that fossil fuels are fossil forms of solar energy. This energy has been stored in the form of chemical bonds by nature for eons. The open question he leaves is whether it is not possible to use *actual* solar energy[5].

Given the above considerations, one may wonder why we still take so little advantage of the solar radiations. The two main drawbacks for energy applications are: low energy density and intermittency. The latter is easily understandable, as we know from experience that the sun is not shining at all moments. This

limitation is the less problematic of the two, as it is possible to go around it by energy accumulation. The former is more complex to solve because when we represent the sunlight energy in terms of power density, we realise that the needs of an energy intensive industrial activity are much larger than the 170-180 W m⁻² incoming from the sun. Therefore, while it can be feasible to directly power a household from solar energy, for many other applications we would need to rethink of a grid where the energy flow can be concentrated instead of diluted, as the current system is constructed[1].

Nevertheless, in a context where the continuous emission of CO₂ in the atmosphere from the burning of fossil fuels is causing more and more tangible effects, the development of "decarbonized" technologies is getting very urgent. At the present moment, the direct harvesting of solar radiations and transformation into more ready-to-use forms of energy still represents multiple advantages and it is worth further investigation.

Compared to other sources of energy, solar is often defined as *renewable*. This term might be misleading, as pointed out by Missemmer[10]; it means that its amount is virtually infinite, given its continuous emission from the sun, predicted to last much longer than humankind existence on Earth. The main difference with fossil fuels lies in the fact that they may also be renewed, but their cycle of formation is infinitely slower than the rate at which men have been extracting and burning them. Also compared to other renewable energies, solar energy has much less related and widely debated problems, like in the case of nuclear energy and its waste.

The second and more important factor to keep in mind when talking about "decarbonization" is the net emissions of greenhouse gases when we utilize a source of energy. In this sense, solar energy represents a "free" and "infinite" energy that does not cause emission of harmful side products. The most diffused example of device for solar energy use is a solar panel, which is capable to convert the radiation energy into electrical energy. However, for some applications, electricity might not be the best fit, in this case solar energy should be converted into a form of chemical energy (fuel), which can be stored, the same ways of classic fossil fuels. For instance light can be used as a source of energy to initiate chemical reactions that otherwise would be demanding high energy input ; (heat, pressure, electricity). Another example application is the conversion of atmospheric CO₂ into fuels by means of light; this kind of process aims at carbon neutrality between re-utilization and re-emission of CO₂.

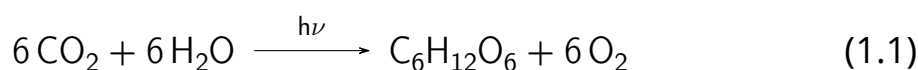
In order to develop new technologies that can take advantage of the energy

incoming from the sun, a deeper understanding of the multiple steps occurring in light-induced reactions is necessary. The next sections are an introduction on photochemical processes, starting from natural systems, and their translation into "man-made" systems.

1.2 . Natural photosynthesis

The most classic example of light induced reactions, is given indeed by natural photosynthesis: the process where photosynthetic organisms use sunlight to power all forms of life in our biosphere.

The basic principles of oxygenic photosynthesis are quite famous: from water and ambient carbon dioxide, with the input energy coming from light, photosynthetic organisms are able to produce sugars and dioxygen as side product (Eq. 1.1).



When looking in more detail into this biological process, a much greater level of complexity is found, and it is not fully deciphered yet.

The understanding of photosynthesis as we have it nowadays, came through the centuries from many different contributions of scientists. The very first observations that led to our modern vision, started in 1640s, when Van Helmont assessed that the weight increase in a plant growth derives from water and not from the soil, detaching from the classical view derived from Aristotle. This concept, even if incomplete due to the total ignorance of carbon dioxide in these times, came 100 years before Lavoisier enunciated the law of conservation of matter[11]. Another crucial step in the comprehension of natural photosynthesis was in 1779 when Jan Ingenhousz discovered that plants use sunlight to produce O_2 (based on previous experiments of Priestley) and that in the dark *respiration* occurs[12][11]. Few years later, with Senebier and De Saussure, the role of carbon dioxide was defined. However, it took another 60 years before the equation could be written in a way that the organic matter produced was ascribable to a carbohydrate, with the simplified formula " CH_2O ", thanks to the determination of the photosynthetic quotient by Boussingault in 1864[11]. The name "photosynthesis" came only at beginning of the 20th century[12].

A general definition of the term *photosynthesis* is given by Blankenship[13] as

"A process in which light energy is captured and stored by an organism, and the stored energy is used to drive cellular processes."

This broad definition also includes rhodopsin-based bacteria, which adopt light to access transport of ions through the membrane. To facilitate the description of the steps involved in photosynthesis, we will restrict to the description of "chlorophyll-based photosynthesis" which differentiates from the above

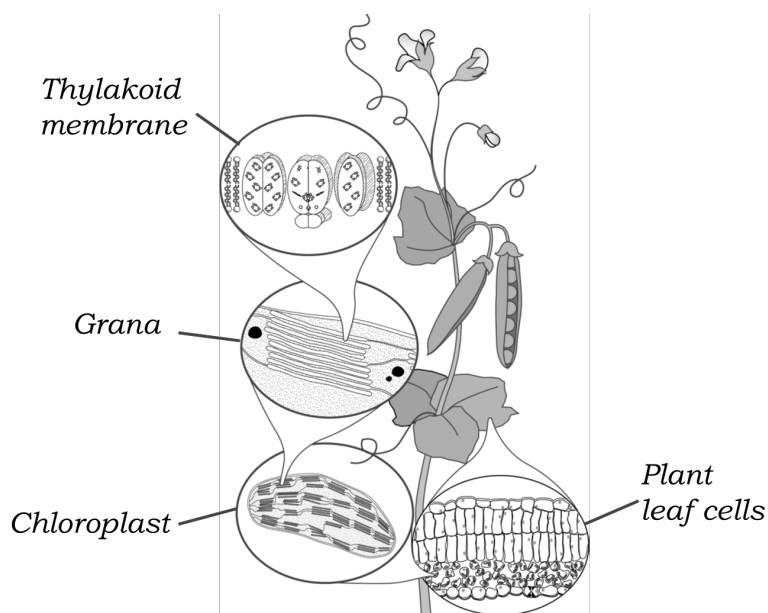


Figure 1.1: Scheme of the thylakoid membrane organization within the chloroplasts present in higher plants cells. Image adapted from [13]

mentioned for the occurrence of light-induced electron transfers.

For all of the organisms in this group, photosynthesis can be subdivided into four steps:

1. Light harvesting and energy transfer;
2. Primary electron transfer at the reaction center;
3. Stabilization of charge separation by secondary reactions;
4. Synthesis and transportation of stable products.

Generally, the first three steps are grouped under the name of light-dependent reactions, whereas the last is also called light-independent reactions (previously named "dark reactions", considered misleading).

In all photosynthetic organisms, photosynthesis is a membrane-based process, as the lipid bilayer membranes play an important role for energy storage. For eukaryote cells the photosynthetic process takes place in the chloroplasts (organelles responsible for the green colour we observe), more specifically around the membrane of thylakoid vesicles. Thylakoids are organised into stacked structures (grana); the light-dependent reactions take place on the membrane itself and in its inner fluid (lumen), whereas the outside fluid (stroma) is where the light-independent reactions occur (see Fig 1.1).

As a classic example, the units composing oxygenic photosynthesis of plants, algae and cyanobacteria will be briefly described; to then discuss in more detail

the main components[13].

As depicted in Fig. 1.2, in oxygenic photosynthesis two main units or *photosystems* (PS) come into play when irradiation occurs. The journey starts when light shines on photosystem 2 (PSII), here it is collected by antenna complexes and conveyed into the reaction center (RC); see later paragraphs for details. Once the energy of the photon reaches the "special pair" of the RC, P680 (two chlorophyll molecules very close together), primary charge separation occurs by an electron transfer process. Such electron transfer generates a reduced pheophytin and oxidized P680⁺, one of the most oxidizing species known in biological media. The latter restores its electron from the *Oxygen evolving complex* (OEC), which is capable of storing a high oxidation power, until extracting electrons from water to give molecular oxygen.

In the meantime, the reduced pheophytin transfers in two steps 2 electrons and 2 protons to the quinone pool, where the plastoquinone (PQ) is reduced until plastoquinol (PQH₂). For the charge separation to be effective, it is crucial that the electron transfer steps after the primary charge separation are extremely rapid, to out-compete charge recombination. The sequence of cascade electron transfers, also named electron transport chain, has the function of providing spacial separation across the membrane to the charge-separated states, preventing recombination.

With the help of the scheme, we can picture that the energy level of the originally excited electron will slowly decrease at every transfer step, passing through cytochrome b₆f, until it reaches photosystem 1 (PSI). Here the energy of the electron is pushed again higher in energy, thanks to the absorption of a second red photon in a similar fashion than for PSII. Antenna complexes funnel the energy until the RC and here a second photochemical reaction takes place. In this case the special pair is chlorophyll P700, and differently from the previous case, its excited state holds reductive potential. The primary charge separation gives raise to oxidized P700⁺, which is then recovers one electron from reduced plastocyanin (in the lumen), and another reduced chlorophyll (called A₀). After a series of electron transfers, eventually the electron reaches the soluble protein ferredoxin, that ultimately reduces NADP⁺.

Another concomitant key step is the production of ATP thanks to the electrochemical potential generated on the membrane from the pumping of protons across the membrane.

Eventually, the reduced ATP and NADPH will participate in the carbon fixation and reduction.

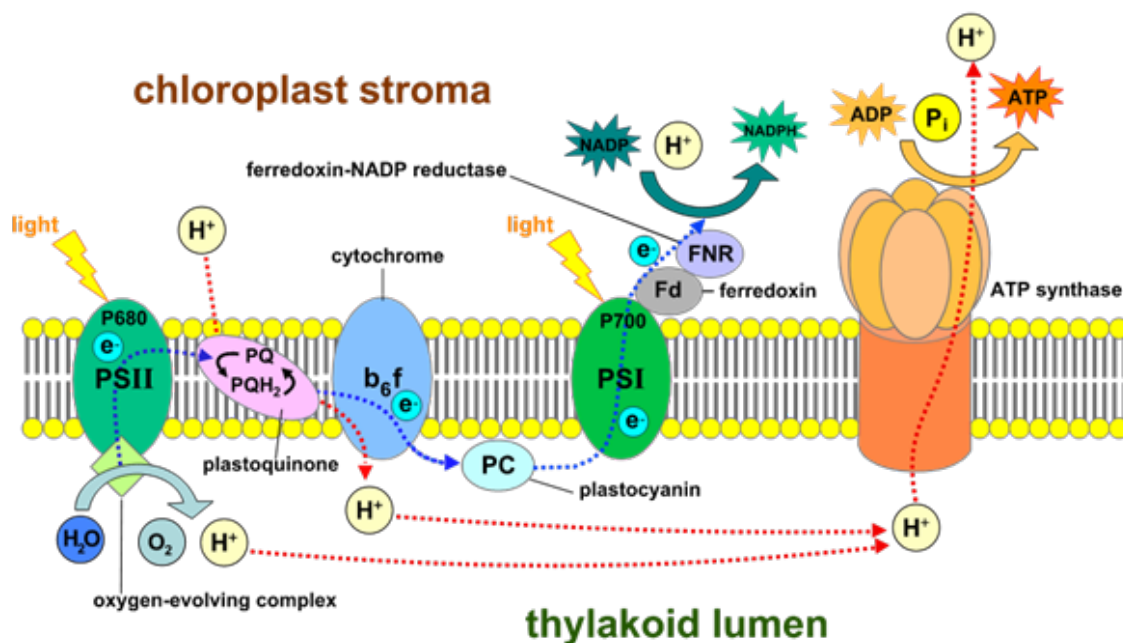


Figure 1.2: Z-scheme representation within the thylakoid membrane. Image credits: Wikipedia https://en.wikipedia.org/wiki/Light-dependent_reactions

With this general scheme in mind, let us now analyze in more depth the units mentioned above, especially in terms of light interaction and energy conversion.

Antenna complexes have very different structures across different organisms but are present in all "chlorophyll-based" photosynthetic systems. In general they can be described as pigment-protein units where the pigment molecules (chlorophyll, carotenoids or others) are associated to the protein to form a unique structure.

The role they play was initially hard to decipher. It was first discovered in an experiment of Emerson and Arnold in 1932 that for a single molecule of CO_2 to be reduced, thousands of chlorophylls are needed[14]. This was unexpected, as previously it was assumed that each pigment molecule in the leaf is able to perform photochemistry. It is possible to estimate the number of photons that can reach, on a sunny day, a given chlorophyll molecule to about 10 per second[15]. Taking into account the timescale of molecular processes, this value gives an extremely diluted energy flux (recall Section 1.1). This would mean that a long time would elapse before any pigment molecule could capture a photon, and even in the successful case of the first photochemical event taking place, the unstable intermediates generated would possibly degrade before a second photochemical event occurs. Therefore, in a way, antennas play the important role of collecting and "concentrating" the light energy to the reaction center, acting as an energy funnel.

How does that happen? Overall, the process involves energy transfers that can be described in terms of Förster energy transfers [16], and exciton couplings[17], as two extreme cases. The former involves non-radiative energy transfer on long distance ranges, too long to include any electron transfer contributions, whereas the latter comes into play with a series of pigments close together (less than 10 Å) forming an exciton.

It is important to highlight that the directionality of these transfers comes together with an energy gradient, meaning that outer antenna pigments will absorb higher energy photons that are transferred to the reaction center with gradual small energy losses under the form of heat. This does not necessarily mean for all individual energy transfers to be energetically downhill, in fact it is possible for uphill ones to take place, but the probability becomes exponentially smaller with energy gap increase, so that globally the energy is delivered from high-energy pigments to low-energy ones.

Another note should be taken on the existence of different possibilities of energy trapping once the energy is transferred to the reaction center. General models indicate these as "deep trap" when photochemical reactions quench irreversibly each excited state transferred to the RC, "shallow trap" when the excited state hops in and out the RC before being successfully quenched, and the third extreme case is when the trap is so shallow that even the photochemical event is not fully irreversible, so the excitation can escape back to the antenna[18]. These mechanisms are quite complex and still under study; currently PSI is considered to fall into the second model[19] and PSII into the third one[20], whereas the first simpler model applies to purple bacteria.

Antenna complexes can be grouped based on their location and interaction with the RC[15]. One main grouping divides peripheral and integral membrane antennas. As the names suggest, in the first case the antenna is sitting on the periphery of the membrane, even though associated with elements buried in the membrane. On the other hand, integral membrane antennas are deeply buried inside the membrane and cross the whole lipid bilayer. These second ones can be further subdivided into *core antenna complexes*, *fused antenna/reaction center complexes* and *auxiliary antenna complexes*. The first two subgroups are both associated to the RC, but in the second case it is not possible to biochemically separate the two units as they are bound to the same polypeptide. Auxiliary antennas are found in addition to one of the other two kinds and they play an important role in regulation processes of antennas.

A didactic example of antenna complex is LHCI (Light harvesting complex II),

an integral membrane accessory antenna found in plants and algae and associated with PSII. It is composed of three transmembrane helices coordinating chlorophyll *a* and chlorophyll *b* molecules. Two carotenoids molecules are arranged in an "X" fashion and help hold the complex together. This antenna is associated with one of the different regulation processes that organisms adopted to face changing environmental conditions. This particular process goes under the name of "state transition" and it occurs when the energy reaching the two photosystems is not well-balanced, meaning that one is in a state of energy excess and the other of energy deficiency. When PSII is receiving excess light, a kinase enzyme is activated by the excess in reduction of the quinone pool and it phosphorylates some complexes linked to LHCII. This change has as a consequence an extra negative charge on LHCII, which then "pushes" by electrostatic repulsion the movement of LHCII from PSII (located in the grana stacked region) to PSI (located outside the stacked region, where the electrostatic repulsion is lowered). Through this transfer of the antenna, more energy will be delivered to PSI. This process is reversed by a phosphatase enzyme which can remove the phosphate groups and make the antenna migrate back to its original location[21][15].

Reaction center complexes are also pigment-containing proteins, which cross the membrane entirely (integral membrane) and are precisely oriented with respect to the sidedness of the membrane[22]. All of them are responsible for charge separation across the membrane, in some cases they can also pump protons, coupling it with the electron transfer.

The components and number of pigment molecules can vary substantially between organisms. A common feature is the presence of a "special pair" of chlorophylls which gives up an electron upon excitation, generating its oxidized form.

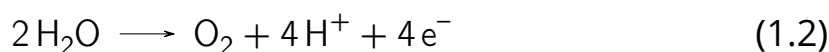
The most well-understood example of reaction center is the one of purple bacteria, which was also the first to be biochemically isolated in the late 1960s by Clayton[23]. This simpler system allowed a much deeper analysis of the whole photosynthetic apparatus, also thanks to high resolution imaging techniques. The notions learnt from it can be transferred to help decipher PSII and PSI of oxygenic photosynthesis[24].

Before giving more detailed description of PSII and PSI reaction centers, an interesting point to make is about the distribution of the different protein units across the membrane. It was already described how in higher plants the thylakoids are organized in stacked grana structures (or grana lamellae); these

are interconnected by some non-stacked thylakoid regions (stroma lamellae). Different experiments [25][26][27][28][29] showed how PSII, PSI, *Cyt_b6f* and ATP-synthase are distributed non-homogeneously across the membrane; with PSII found preferentially in the stacked region, PSI mainly in the stroma lamellae or non-stacked region, *Cyt_b6f* equally in both regions, and ATP-synthase exclusively in the non-stacked regions. This finding brings as a consequence that a diffusion process over a long-distance needs to take place in order to connect the different units along the non-cyclic electron flow. Studies suggest that this process is done mainly by the plastocyanin diffusing in the lumen to reach PSI[30]; however the reason of this very specific distribution is not yet understood, possibly being linked to the regulatory processes of antennas cited above.

Photosystem II has been extensively studied, as it is the only known biological system able to oxidize water molecules to dioxygen. Recent electron microscopy images showed that PSII is present in the form of a dimer, with two PSII-LHCII units bound together, although each entity operates independently[31][32][33][34]. Each PSII entity is composed of more than 25 polypeptides, with D1 and D2 proteins constituting the core of the reaction center, and many others with still unknown function. The core complex is made up of six chlorophyll *a*, two pheophytin *a* and two β -carotene molecules. The main difference of PSII with purple bacterial RC is the oxidizing side: oxidized P680⁺ is such a strong oxidizing agent (estimated +1.2 V)[24], that the D1 protein is rapidly damaged during photosynthetic activity. Specific recovery mechanisms can then take place, where PSII is disassembled, the D1 protein is synthesized and then it is all reassembled back[35].

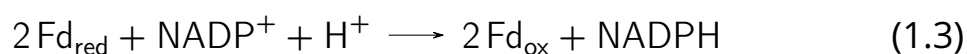
The half-reaction of water oxidation (Eq. 1.2) requires +0.82 V at pH 7, and somewhat higher potential in the acidic environment where water oxidation takes place.



The oxidizing potential of P680⁺ is transferred to the Mn₄Ca cluster of the OEC (through a tyrosine residue Y_Z as intermediate), which is ultimately allowing conversion of H₂O to O₂. Quite obviously there is a mismatch between the four electrons being abstracted from H₂O and the generation of one oxidizing equivalent at the time for each incoming photon. Questions on how the Mn₄Ca cluster of OEC operates have been subject of debate over the years: two extreme possible mechanisms are either storage of oxidizing equivalents on four different centers that then cooperate together, or one single center is capable of accu-

mulating four oxidizing equivalents until when water is converted in a concerted way. The second option has been supported since the experiments in the 1960s of Pierre Joliot and then separately Bessel Kok, where they could measure oxygen produced in a single flash, modeling the *S state mechanism* [36][37][38][39]. Very recent developments of femtosecond crystallography [40][41][42][43] allowed some more clear insights on the complex's structure being modified upon sequential flashes. Still different theories exist on the reaction mechanism at a molecular level; not too long ago it was evidenced the crucial role that the Ca^{2+} and Cl^- ions play. Common outlines of the mechanism are now starting to emerge, two example mechanisms were for instance described by Cox *et al.* [44]

Photosystem I is described as a fused antenna/reaction center complex. In fact, compared to PSII or purple bacterial RC, it has a much greater pigment component, with around 100 chlorophylls and between 12 and 16 β -carotene molecules. In eukariotic organisms it is found in its monomeric forms, whereas in cyanobacteria it is found in a trimeric form. In the core of the RC we find the special pair P700, together with four other chlorophylls and two phylloquinones. After few transfers, the electron coming from the excited P700* reaches a set of three Fe-S clusters, which act as early electron acceptors. Interestingly, it has been evidenced that one of this electron transfer steps is energetically uphill (from F_A to F_B) of about 60 mV, which is in agreement with electron transfer theory, as long as the two units are in close proximity [45]. At this point of the journey, the electron leaves PSI to reduce the water-soluble protein ferredoxin (Fd), with a reduction potential of -430 mV vs. NHE. Together with ferredoxin-NADP reductase (FNR), it is able to reduce NADP^+ to NADPH, following the overall reaction in eq. 1.3.



Where FNR acts as catalyst, converting the one electron incoming from Fd for each photon, to two electrons transferred to NADP^+ . This electron storage effect occurs thanks to the flavin adenine dinucleotide (FAD) cofactor, of which the redox active terminal is shown in Fig. 1.3 The concept of electron storage will be seen again in this chapter, specifically in Section 1.4.2.

At this point of the journey, the main elements of the light-induced reaction have been described, but carbon fixation still needs to be achieved. The metabolic conversion of CO_2 into sugars is known as Calvin-Benson cycle, or more rarely as reductive pentose phosphate (RPP) cycle and it takes place in the stroma [46][47][48]. The set of experiments that allowed understanding of this

Overall, the stoichiometry of triose phosphate production that is "left" for sucrose or starch synthesis is close to one triose phosphate for each evolved O_2 molecule, with the need of three CO_2 molecules in order to replenish RuBP in the cycle. The efficiency of the cycle in ideal conditions is estimated to be 27%, including all the previous light-induced steps.

1.3 . Artificial photosynthesis

Artificial photosynthesis can have a quite wide definition, corresponding to any chemical system that carries out functions similar to natural photosynthesis (sunlight conversion to other forms of energy). Here, the definition will be restricted to a narrower group: photochemical systems that harvest light with molecular materials and convert it to an electrochemical potential which can then in turn generate a fuel (storage as chemical energy)[49][12].

In current literature, numerous works talk about artificial photosynthesis in terms of electrocatalytic systems[50][51][52]. This terminology is taking for granted that the source of electrical energy would ideally be harvested in a "sustainable" way by a photovoltaic module, so that in the electrochemical cell only the last step of conversion of electrochemical potential into chemical bond takes place.

In this section, the term "artificial photosynthesis" will be used more literally, dealing with photo-initiated and photocatalytic systems.

As part of this growing field of study, photocatalytic activation of small molecules has seen a tremendous increase in terms of number of publications[53][54]. Few examples which will not be further discussed as they cover a wider scope are quantum dots(QD), metal organic frameworks (MOF), covalent organic frameworks (COF), polyoxo metallates (POM) and other more complex supramolecular structures[55]. Here, we will focus our attention onto the more direct mimicking of the natural system: molecular systems.

With a clearer view of the components of natural photosynthesis in mind, it is possible to follow the strategies that chemists have followed in the development of artificial photosynthesis systems[49].

Breaking down the elements just analyzed, an ideal artificial photosynthetic system should be composed of:

1. A light harvesting antenna
2. A reaction center to allow charge separation

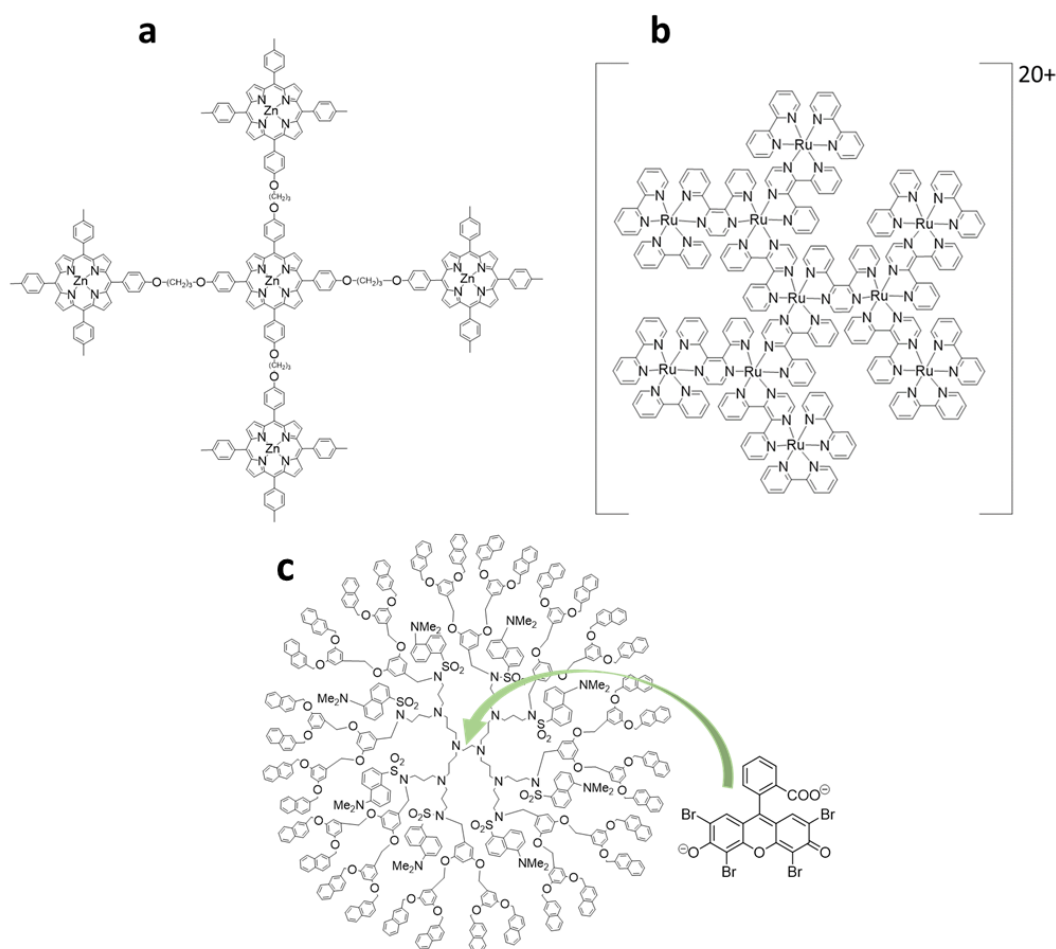


Figure 1.5: **a.** Porphyrin-based synthetic antenna complex. **b.** Synthetic antenna complex based on ruthenium metal complexes. **c.** Host-guest antenna complex.

3. One catalyst on each side of the reaction (oxidation and reduction)
4. A membrane to separate the two reaction sides and the products

Until now, efforts have been made to improve the individual elements, by mimicking simple photosynthetic functions with simplified synthetic models. However, global assemblies into a self-sustained system are nearly nonexistent, exception given for the *artificial leaf* assembly in Nocera's laboratory reported in 2012[56].

1.3.1 . Mimicking antenna complexes

The mimicking of light harvesting antennas has followed different approaches, many of them following the scheme of dendrimers assembly. A dendrimer is composed of a core with branching units in different directions, similar to the branches of a tree. Within the dendrimer family, different subgroups exist. To

give a few examples, they can be based on metal complexes, on porphyrins or on host-guest systems[49]. Examples are shown in Fig. 1.5. The interesting aspects of using this approach is the possibility to control the molecular architecture during the synthetic steps, and to insert photoactive units in different parts of the structure, even inserted without covalent bonds in the cavities.

The use of porphyrins to construct antennas comes quite obvious from the mimicking of natural systems. An early example of a porphyrin-based artificial antenna is in Fig 1.5, **a**[57]. Energy transfer is expected to occur from singlets state of the excited peripheral Zn porphyrins to the core one. However, in this case the energy transfer could not be observed directly, probably due to the low rigidity of the linkers, which can favor faster non-radiative deactivation pathways. Later studies tuned the rigidity of the linker and could achieve energy transfer of adjacent porphyrins with a rate of 180 ps[58].

Another interesting study on porphyrin dendrimers[59] highlighted the relationship between the dendrimer morphology and the quantum yield of energy transfer. Spherical morphology gives a very efficient antenna, where the energy rapidly migrates through the whole array until reaching the trap. Breaking this symmetry has a significant effect on the transfer quantum yield, together with the observation that less rigid structure are greatly influenced by temperature (more rotations increase deactivation competition and therefore lower energy transfer quantum yield).

In parallel, investigation on antenna systems based on non-heme metal complexes have also been reported since the early stages of this field of study. Common features of this kind of antennas are having mainly Ru and Os metal centers linked by bis(pyridyl)pirazine type bridging ligands[49]. Antenna complex **b** of Fig. 1.5 was reported in 1995 to be able to have fast energy transfers on the femtosecond scale, quenching possible luminescence[60].

A last example of antenna complex belongs to the family of host-guest systems (Fig. 1.5, **c**)[61]. Here, peripheral naphthalene and dimethoxybenzene units transfer energy to the fluorescent dansyl unit with an efficiency of 90% when excited. A molecule of eosin can be inserted in the cavity thanks to specific interactions. In these conditions, the dansyl fluorescence is no longer observed, and instead the eosin fluorescence is detected, with an overall efficiency of energy transfer from the branches over 80%. In this example the mechanism is

attributed solely to a Förster type¹ of transfer, given the strong overlap of spectra of donor and acceptor.

Antennas are considered appealing also for other applications not related to artificial photosynthesis, since they act as an energy lens, they can be used for signal amplification in sensors, for photodynamic cancer therapy and up-conversion processes[62][63].

1.3.2 . Mimicking reaction centers: charge separation

The ability of transforming energy from a photon to an electrochemical potential through a charge-separated state is key in the photosynthetic process. To reproduce this effect, two main approaches are envisaged: inter and intramolecular electron transfer, which translates into a bimolecular process or a dyad respectively.

The first studies done around the mid-70s, dealt with the simpler approach of monitoring electron transfer processes of bimolecular systems in solution [12]. The main drawback in this case was found to be the limitation of electron transfer rate by the diffusion of the species in solution. In the natural system, the primary charge separation occurs with the quenching of an excited singlet state of the chlorophylls or bacteriochlorophylls. These singlet states of the excited chromophores are in general too short lived to be quenched in a diffusion-limited regime, as it is the case for studies in solution. Under these conditions, the electron transfer will occur from the longer-lived triplet state of the chromophore, which however after undergoing inter-system crossing (ISC) has already lost part of its initial energy, lowering the overall efficiency of the reaction[12].

To overcome these issues, many studies have turned to dyads and more complex systems, which will be discussed later. A dyad, as the name suggests, is composed of two units, namely an electron donor and an electron acceptor, linked by a covalent bond, with a controlled distance and specific electronic interactions. A simple scheme depicting the steps of charge separation is given in Fig. 1.6, and it also applies to the case of the bimolecular system mentioned above, with the difference that the two units are not covalently bonded. After light excitation (step 1), the electron transfer from the singlet excited state of the chromophore (or triplet state in the case of bimolecular; step 2) is in competition with all other possible deactivation pathways (step 3). The elec-

¹Förster resonance energy transfer (FRET) is a phenomenon occurring when the excited state of a chromophore transfers its energy to a second acceptor chromophore. Certain conditions need to be satisfied to observe FRET, such as overlap between emission energy of the donor and absorption of the acceptor, distance between the two, and their dipole orientation [16].

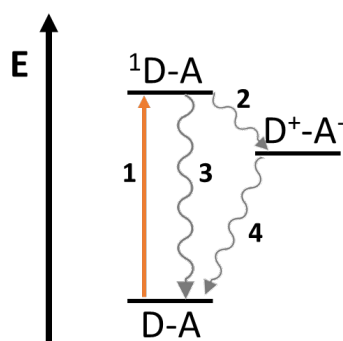


Figure 1.6: Energy diagram scheme for a generic dyad.

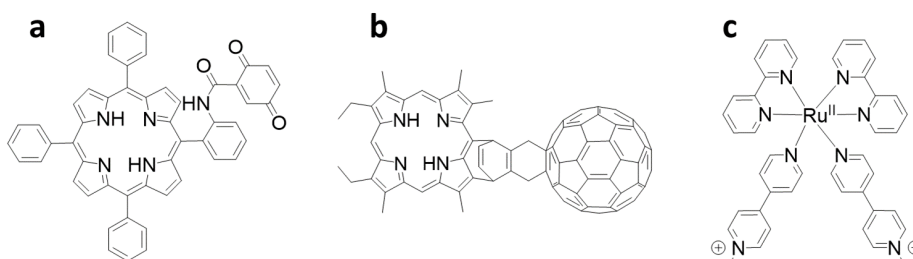


Figure 1.7: **a.** Porphyrin-quinone dyad, **b.** porphyrin-fullerene dyad, **c.** ruthenium complex with pyridinium acceptor unit acting as dyad.

tron transfer will generate an oxidized donor and a reduced acceptor, which in the case of a dyad will rapidly recombine back to the ground state (step 4). In the case of an oxidative quenching, the donor species corresponds to the chromophore, whereas in reductive quenching the chromophore is the acceptor. Few examples of this type of assembly are given below.

The most directly related systems to PSII are based on porphyrin-quinone dyads. One of the first compounds reported is shown in Fig. 1.7, **a**[64]. The porphyrin unit mimics the function of the chlorophyll or bacteriochlorophyll, with quite similar oxidation potentials, allowing it to act as excited state electron donor. On the other hand, the quinone acts as electron acceptor, analogously to the quinone pool in the natural system. Both porphyrins and quinones are widely used in the field of artificial photosynthesis, more than just for the resemblance to the molecules found in nature, but also thanks to the easy synthesis and tunability of optical and redox properties through structural modifications. Overall, this and other similar systems show a very efficient light-induced electron transfer, with QY up to 0.99 at a rate constant close to 10^{10} s^{-1} [64][65]. However such charge-separated states of porphyrin-quinone dyads (P^+-Q^-) suffer from an extremely short lifetime. In extreme cases the rate of charge recombination to the ground state (step 4 fig. 1.6) may be greater than the rate of its forma-

tion. Nevertheless, many lessons could be learnt from the study of these dyads. Investigations on the influence of the distance between donor and acceptor and of the thermodynamic driving force (tuned by adjusting substituents) on the rate of electron transfer were interpreted in terms of Marcus theory[66].

Different kinds of acceptors have been studied in combination with porphyrin dyads. One interesting example is the use of fullerene, reported for the first time in 1994 and shown in Fig. 1.7, **b**[67]. Both faster light-induced electron transfer and longer lifetime were observed, leading to numerous more studies on analogous dyads. Also in this case, the theory developed by Marcus could rationalise the observed electron transfer rates, even though most examples lay within the normal region². The better performances of porphyrin-fullerene dyads compared to porphyrin-quinone dyads were attributed to the smaller solvent reorganization energy for the reduced fullerene, enabling a long-lived charge-separated state with a high formation rate.

Parallel to the study on porphyrins, also metal complexes have been used as photosensitizers for generation of charge-separated states. One of the most studied metal complexes (seen earlier in a modified form for artificial antennas) is based on Ruthenium (II) coordinated to three bipyridine ligands ($[\text{Ru}(\text{bpy})_3]^{2+}$). From the characteristic metal-to-ligand-charge-transfer (MLCT) band in the visible region, the chromophore can undergo oxidation in presence of an acceptor or reduction in presence of a donor. In Fig. 1.7, **c**, shows the pioneer work of the group of Meyer[68] where the ruthenium complex acts as chromophore and donor and the linked pyridinium as an acceptor. A charge-separated state could also be observed with this type of system .

Looking back at the natural model, we can observe charge separation occurs efficiently with a long lifetime thanks to the cascade of reactions that rapidly lead to separation over a long distance. This concept has inspired the construction of multi-components models, starting with triads (three components) to then continue with tetrads, pentads, *etc.*

Examples of triads are shown in Fig. 1.8. In the case of molecule **a**[69][70], we can see the resemblance with the previously described porphyrin-quinone dyad (Fig. 1.7). In fact, its principle of operation is very similar: the porphyrin once irradiated can transfer one electron from its singlet excited state to the

²Marcus theory describes the rate of electron transfer. When describing the relationship between energy stabilization of the products (reaction free Gibbs energy ΔG^0) and the rate of the transfer, two extreme cases are described. In the normal region the reaction rate increases with increased stabilization of the final products, until reaching a maximum where further product stabilization gradually decreases the reaction rate - the inverted region [66].

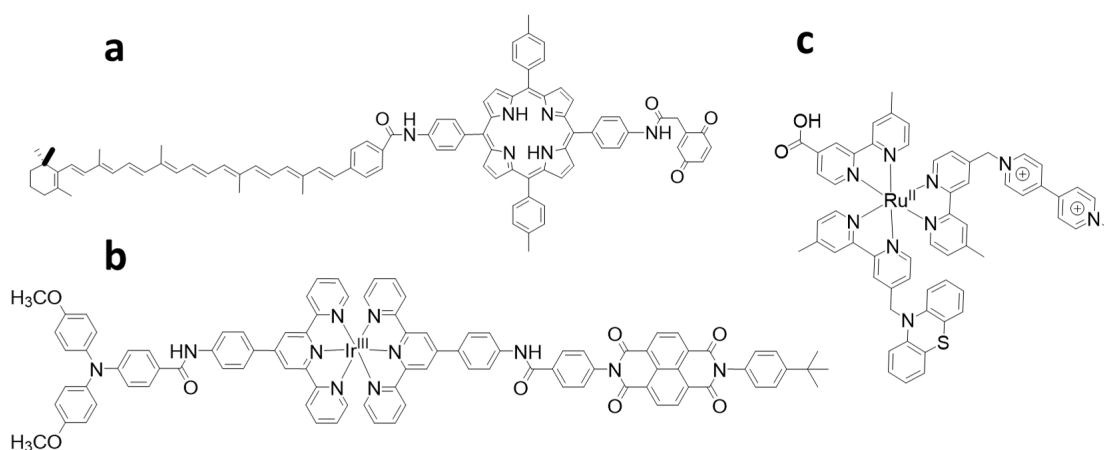


Figure 1.8: **a.** Triad based on a porphyrin chromophore, a quinone acceptor and a carotene donor; **b.** triad based on an iridium complex chromophore, an amine donor and a naphthalene acceptor; **c.** triad based on a ruthenium complex central chromophore, a methyl viologen acceptor and a phenothiazine donor.

quinone unit. However here, the attached carotenoid moiety acts as secondary electron donor, bringing the porphyrin back to its ground state and creating a charge-separation with a longer distance. In this reported work, the first charge separation, generating the $C-P^+-Q^-$ state, occurs with a QY near unity, once again suffering from a very fast rate of charge recombination. Competing with this, the electron transfer from the carotenoid to the porphyrin generates the C^+-P-Q^- state with a QY of 0.13. Even if the yield is much lower, this latter state shows a lifetime of 420 ns, an important increase compared to the few ps of the dyad.

Other examples of triads shown here involve metal complexes as chromophores, as it was already shown in the case of dyads. Triad **b** in Fig. 1.8[71] is composed of an Ir^{III} bis-terpyridine chromophore linked to a triphenylamine electron donor and a naphthalene-bisimide acceptor. In this case either the chromophore or the donor can be excited and in both cases this will lead to a 100% yield of formation of the D^+-Ir-A species in about 20 ps. The secondary electron transfer occurs with a yield of 10%, that enables the generation of the D^+-Ir-A^- species with a remarkable lifetime of 120 μ s.

In 2000 the group of Meyer attached to the commonly used $[Ru(bpy)_3]^{2+}$ chromophore a methyl viologen (MV) acceptor moiety and a phenothiazine donor on the periphery of the bipyridine ligands (molecule **c** in Fig. 1.8)[72]. Once the ruthenium complex is excited in the MLCT, the primary charge transfer was observed towards the acceptor side (MV), followed by a rapid secondary electron transfer from the donor to the oxidized Ru^{III}. In this case the rate of

back electron transfer is on the range of 10^6 s^{-1} . Even though this lifetime is not long compared to the previous examples, this study shows how a fine tuning of the substituents enables a control on the rate of electron transfer.

Following the same logic, more complex systems have been assembled enabling even greater stabilization of the charge-separated state where the intramolecular back electron transfer competes with bimolecular processes[73], but of course this comes together with an increased complexity of possible competing reactions which may affect the overall yield.

1.3.3 . Coupling antennas and reaction centers

While building more complex supramolecular structures, some research groups directed their interest to the coupling of the two entities: antennas and reaction centers. Such an assembly would have the advantage of maximizing the light absorption, which is focused and directed towards the moiety where primary charge separation takes place[49].

In 2001, the group of Miyasaka[74] reported a "windmill" porphyrin assembly (Fig. 1.9, **a**), where two core zinc porphyrins (ZnP_C) are covalently bound to two extra peripheric zinc porphyrins each (ZnP_P). Ultimately, the two connected ZnP_C are also bound to an acceptor unit, which varies between a free-base porphyrin or a naphthalenetetracarboxylic diimide. It was shown that light excitation from the peripheral porphyrins is quickly transferred to the core ones, which can then transfer one electron to the acceptor and eventually recover the electron from the peripheral ZnP_P , giving place to the $\text{ZnP}_P^+ - \text{ZnP}_C - \text{A}^-$ state. However in this system, charge recombination after the first charge separation is much faster than secondary charge transfer. In addition, they reported that using the free-base porphyrin as acceptor enables an increase in the efficiency of the production of the final charge-separated state, as it slows down back electron transfer from the reduced acceptor to the oxidized ZnP_C . This was modeled using Marcus theory which shows that the porphyrin acceptor has smaller reorganization energy (λ) and similar reduction potentials to the core ZnP_C (ΔG^0 close to 0).

Another example reported in 2006 by Kodis et al. [75] makes use once again of the fullerene unit as a very efficient electron acceptor (Fig. 1.9, **b**). In this case, the rigid hexaphenylbenzene central unit holds together five derived anthracene antenna chromophores (BPEA) and a donor-acceptor module consisting on a porphyrin-fullerene. The chosen anthracene absorbs in a similar region to the carotenoids found in photosynthesis. Upon excitation, the peripheral antennas give rise to energy transfer mainly Förster type with a yield of unity to the por-

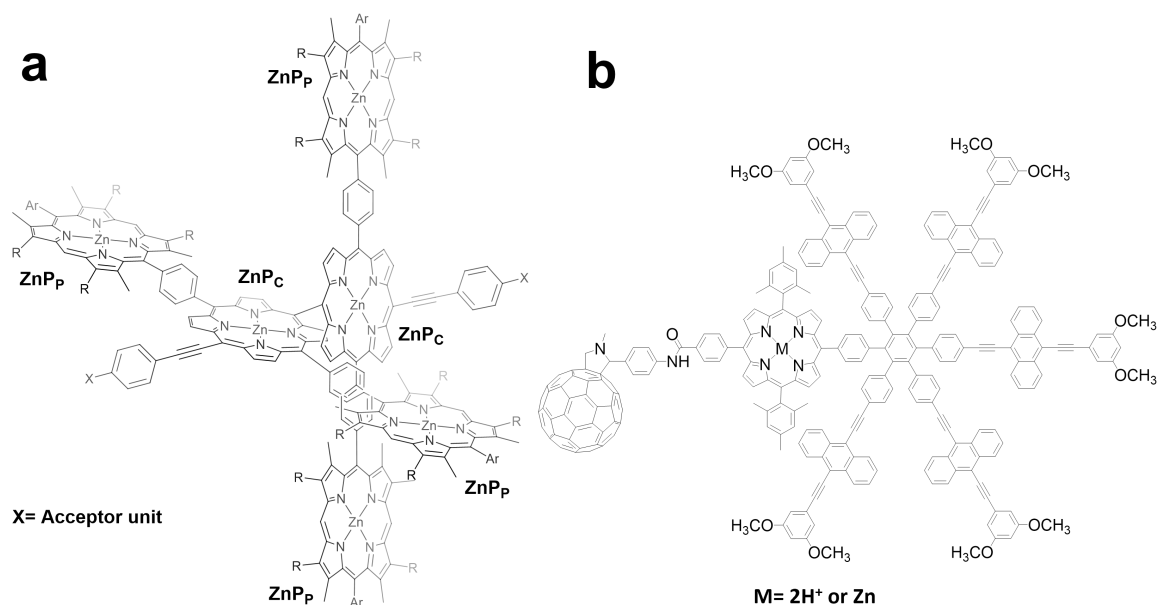


Figure 1.9: **a.** Windmill structure coupling antenna and reaction centers functions. **b.** Anthracene antennas coupled to a porphyrin-fullerene reaction center mimick.

phyrin. Two different porphyrins were investigated in this work: free-base and zinc porphyrin. For both, charge separation from the porphyrin to the fullerene occurs rapidly, forming a species with a lifetime of few ns and with a high global QY. The structure containing the zinc porphyrin achieved an impressive QY of 0.96 based on the light absorbed by the antennas.

Finally, a quite different approach was developed by the group of Meyer, which reported the study on the photophysical properties of a polystyrene with appended $[\text{Ru}(\text{bpy})_3]^{2+}$ complexes[76] [77] [78]. On few of these repeating units, the complex was linked to a donor and acceptor modules, as shown in Fig. 1.8. Following the processes occurring after irradiation, the charge-separated state was detected, with about 30% of energy contribution from the antenna ruthenium complexes. The curious finding here is that in addition to the previously described charge-separated state with a lifetime of 160 ns, a small fraction (0.5%) is a much longer lived species (20 ms) that corresponds to the charge separation on two different ruthenium units. This translates to a polymer capable of preserving for much longer time redox power coming from the light excitation.

1.3.4 . Coupling reaction centers and charge accumulation: towards catalysis

Possibly the biggest challenge in artificial photosynthesis design is to couple the aforementioned light-induced charge separation with the effective sub-

strate conversion, for instance water to dioxygen[12] [49] [79] [80] . Charge-separated states are indeed formed by one photon-one electron transfer at the time, whereas the final reaction always consists of multi-electron transfers.

Nature teaches us the need of a charge-accumulating unit, that we can eventually call *catalyst* in artificial systems. One of the most studied components of photosynthesis is the Oxygen Evolving Complex (OEC), present in oxygenic photosynthetic organisms and capable of oxidizing water to molecular oxygen (described in Section 1.2). Thanks to the Mn_4Ca cluster, it is capable to store the oxidizing equivalents on the metal centers to then concertedly give place to the four-electron four-proton oxidation of water[81].

The design of catalysts which can withstand the addition or withdrawal of multiple electrons without impacting their molecular structure is one of the key elements in the current research for the development of molecular catalysts for artificial photosynthesis. At the same time, their reduced or oxidized forms should also be reactive enough to be able to inject or withdraw electrons from the substrate for its ultimate conversion to the desired products. Balance between these factors is crucial for an efficient catalysis and this concept will be further elaborated in Section 1.4.2.

To combine the reaction center with the charge accumulating catalyst, two different approaches are found in the literature, as it was the case for combining light absorption and charge separation units: inter or intramolecular transfers (dyads, triads, *etc.*). Previously, it was highlighted how dyads present the advantage of rapid electron transfer, that mimicks more faithfully what occurs in natural photosynthesis. However, when we shift our interest towards the catalytic conversion of a substrate, we understand that the reaction rates will be in any case limited by substrate diffusion in the medium. For this reason, working with bimolecular systems does not impose any extra restriction and the two approaches can be studied in parallel.

The pioneering work of Calvin's group reported in 1986[82] follows the accumulation of charge on a Mn porphyrin (Fig. 1.10, **a**) inspired by the Mn center in the Mn_4Ca cluster of PSII, using bimolecular processes. In all the previous examples shown here, porphyrins were used as the light-absorbing unit that undergoes electron or energy transfer from its long-lived excited state. In this case, the presence of manganese in the porphyrin, changes completely its photophysical properties, manifesting an excited state too short-lived to access an electron transfer. In this work, $[Ru(bpy)_3]^{2+}$ complex is used as chromophore (or reaction center unit) and it is coupled with an electron acceptor, $[CoCl(NH_3)_5]^{2+}$.

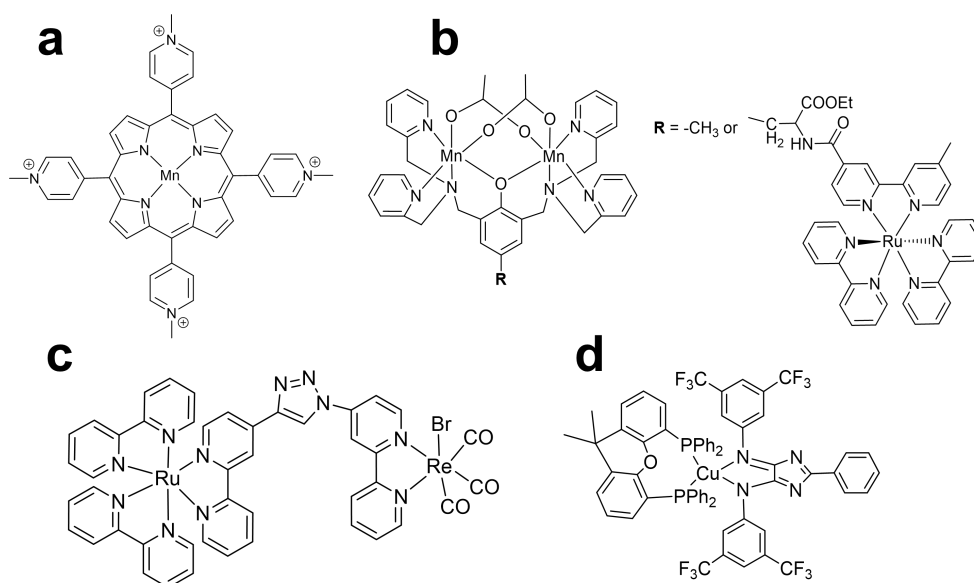


Figure 1.10: **a.** Mn porphyrin as model catalyst for water oxidation. **b.** Binuclear Mn complex for charge accumulation for water oxidation reaction. **c.** Ru-Re dyad for charge accumulation for CO₂ conversion. **d.** Cu complex for charge storage for O₂ reduction.

Light excitation of this couple generates Ru(III) by oxidative quenching, which can in turn transfer the hole onto the Mn porphyrin. The change in the oxidation state of the catalyst was monitored using UV-vis spectroscopy, showing a clear change of absorption spectrum during 7 min of illumination; followed by a slow decay of the oxidized form until full recovery of the starting Mn(III) from back-electron transfer. The experimental techniques reported in this study are still of interest and they will be recalled in the later chapters.

In the context of water oxidation catalysis, many other systems that couple a Ru complex photosensitizer and a Mn complex catalyst have been reported. Akermark and coworkers reported multi-charge accumulation on a Mn^{II}Mn^{II} dimeric complex both through inter and intramolecular electron transfer sensitized by Ru(II) complex (Fig. 1.10, **b**) [83]. In this work, they were able to follow stepwise oxidation until M^{III}Mn^{IV} by coupling flash photolysis with EPR measurements. This successful example mimicks various aspects of PSII, in particular in the structure of the MnMn dimer covalently linked to the Ru unit by a tyrosine unit, however they were not able to detect oxygen formation from water.

A previous study on MnMn dimeric complex had already reported the successful oxidation of water to dioxygen, confirmed by an isotope labelling experiment[84]. On the other hand, the dioxygen production was reported to be quite slow and a very precise and air-tight detection system is necessary to reveal such a small

production of O₂.

Although more direct biomimicking of natural photosynthesis focused on water oxidation, more and more examples of charge accumulation are now developed for other reduction reactions, such as proton reduction, CO₂ reduction, oxygen activation, *etc.*

Our group reported in 2021 two-electron accumulation on a Re complex unit, within a Ru-Re dyad system for CO₂ reduction (Fig. 1.10, **c**) [85]. This was observed by UV-vis absorption spectra and confirmed by comparison with electrochemically and chemically generated species.

An interesting example regarding the stability of the species after charge accumulation was reported in 2020 by Schultz *et al.* [86]. In their study, they combined the chromophore and catalyst unit into a single Cu complex photocatalyst (Fig. 1.10, **d**), capable of accepting two electrons and a proton from a donor upon shining light. The reduced complex showed a stability of 14 hours in the dark in solution, proven by the reduction of added MV²⁺ or O₂ confirming the preservation of the catalyst's reducing power.

Further analysis of molecular systems for CO₂ and O₂ activation, with particular attention to light-induced reactions, will be carried out in the following Sections 1.4 and 1.5. As a general remark to conclude this section, it can be noted that currently the majority of the reported studies on molecular photocatalytic systems makes use of the bimolecular approach. The reasons are to be found in a simpler approach from the synthetic chemistry point of view; together with generally a better catalytic activity than for that of dyad systems[85][87]. The latter can be simply understood from the fact that, differently from natural systems with complex three-dimensional architectures and organization, in solution electron transfers are hardly mono-directional. If the electron transfer is much more rapid in a dyad, then also the back electron transfer will occur at a high rate, and compete with the charge accumulation. In bimolecular systems this problem can be tackled by adjusting species concentration in solution by modulating the concentration of the different components to favour the electron transfer in the desired direction.

1.3.5 . Heterogeneous systems and devices

One last aspect to keep in mind when studying artificial photosynthesis is the interest of translating what was learned at the molecular scale, in a homogeneous medium, into a "device"[49][12]. Indeed, the introduction of a surface in these catalytic systems can bring great advantages, such as higher stability in time, faster electron accumulation, and higher electron flow. A model sys-

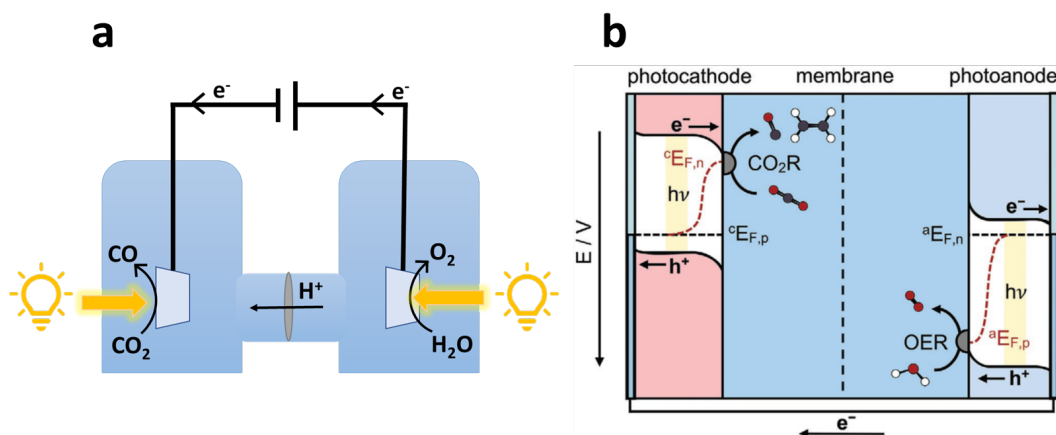


Figure 1.11: **a.** Simplified scheme of a photoelectrochemical cell (PEC) for CO₂ reduction. **b.** Scheme of the energies involved in the functioning of a PEC. Image credits to [89].

tem which scientists often aim at, is the photoelectrochemical cell (PEC). Such device, schematized in Fig. 1.11 **a** consists of an electrochemical cell which is powered by light, with an ideal external bias tending to zero. A combination of different configurations is possible, the one represented is just one possible example. For instance, the half-reactions involved can be CO₂ or proton reduction at the cathode; water oxidation or other reactions at the anode[88]. Also, both sides can be powered by light (as in Fig. 1.11 **a**) or just one of them (only photocathode or only photoanode) and the arrangement of the two electrodes can differ (two half-cells or integrated system). More detailed description of each configuration can be found in dedicated reports[89].

All cases are based on the same operating principle. The photoelectrode is composed of a p-type semiconductor for reduction or n-type for oxidation linked to a photoactive component, which upon light absorption triggers the cascade of electron flow. The light-absorber can either be the semiconductor material itself when it has the good bandgap in the visible region (as in the case of p-type and n-type Si or different metal oxides, as Cu₂O; see Chapter 3), otherwise it can be anchored on the semiconductor, like in the case of molecular photosensitizers covalently linked to the oxide surface. Quite frequently, transparent electrodes are employed as support which leaves the possibility of front or back illumination, these are ITO (indium tin oxide) or FTO (fluorine-doped tin oxide) semiconductors. The other main element needed to build the photoelectrode is the catalyst, that once again can be either a material- often nanostructured- or molecular, which is the focus of the present manuscript. Two examples of strategies to anchor the molecular catalyst to the electrode are covalent linking through specific chemical groups (carboxylic, phosphonic,...) or electro-polymerization. Various

groups have also reported the grafting of chromophore-catalyst dyads, similar to the ones shown in section 1.4.3[90][91].

To explain the principles of this heterogeneous photocatalysis, we can follow for instance, the steps taking place on a photocathode for CO₂ reduction (Fig. 1.11, **b** left side). The scheme represents the interface between the p-type semiconductor and the electrolyte. At a resting state, the difference of potential between the Fermi level ($E_{f,p}$) and the redox potential of the redox couple in solution (indicated as the CO₂R point; at more negative potential) causes a transfer of electrons from the electrolyte to the semiconductor, generating a negatively charged region within the semiconductor that causes the bending of valence and conduction band. Upon irradiation, the semiconductor absorbs light energy greater than the band gap and the quasi-Fermi energy of electrons is raised ($E_{f,n}$) and the electrons can be transferred to the CO₂ reduction catalyst. The band bending favours rapid separation of the electrons and holes when light is absorbed, pushing the electrons to migrate to the interface and the holes to the material's bulk. In the case of a molecular absorber attached to a p-type semiconductor, upon light excitation, the electrons are easily injected from the semiconductor to the chromophore, and then eventually to the catalyst[90]. The opposite dynamics occur at the photoanode side (Fig. 1.11, **b** right side).

In real systems, an applied electrochemical bias is necessary in almost all cases to drive the reaction. The light stimulus helps the directionality of the electron flow going from the anode to the cathode, and this lower the overall energy required for the process.

However, various drawbacks of these systems (i. e. photocorrosion) have hampered their real application and upscaling so far; this and other issues will be discussed more in depth in Chapter 3.

1.4 . CO₂ conversion

1.4.1 . Context

Among the most acknowledged issues that mark the era of the Anthropocene is the dramatic increase of carbon dioxide accumulated in the atmosphere[92]. Many reports exist on this matter[93], the most known being the one from the Intergovernmental Panel on Climate Change (IPCC), established 35 years ago and publishing its First Assessment Report (FAR) in 1990[94]. Already at this time, CO₂ was pointed out as the greenhouse gas of largest impact, due to its long lifetime in the atmosphere (50 to 200 years) and the massive increase in the emissions since the industrial revolution. When looking at the recorded data of CO₂ concentration in the atmosphere, we understand quickly why it should be considered alarming (Fig. 1.12 a). Even though the increasing trend from the 80s seems nearly linear, when we expand to the much larger window that consider our planet's life from the ice ages, we see that from the industrial revolution we have abandoned the stability of the Holocene era, now facing such a rapid variation that resembles phenomena from the ice ages (Fig. 1.12 b)[95][96][97].

Many experts in climate science have been studying this phenomenon and others over the years, its causes, effects and how it interconnects with the complexity of our planet's climate and ecosystems' equilibria[98][99]. Overall, it has been agreed on the importance of lowering dramatically CO₂ emissions in order to mitigate global warming and other related issues, such as oceans acidification. Objectives have been set at international level by establishing agreements, among which the widely known Paris Agreement of 2015 that sets the threshold of temperature increase at a maximum of +1.5°C compared to pre-industrial levels, meaning reaching carbon net-zero by 2050[100].

In this context, many scientific efforts have been made over the last decade to find multiple solutions that can help capture the emitted CO₂ either directly from air (DAC-Direct Air Capture) or from exhausts of factories for devices that require high CO₂ concentrations. Once captured, the two existing strategies envisage either its storage under the form of minerals (CCS-Carbon Capture and Storage) or its conversion into fuels or chemicals (CCU-Carbon Capture and Utilization)[101].

From chemists point of view, there is a high interest in learning ways to convert CO₂ in its more reduced forms, in order to then use it as building block for other chemicals synthesis (such as drugs) or for fuel production (for example

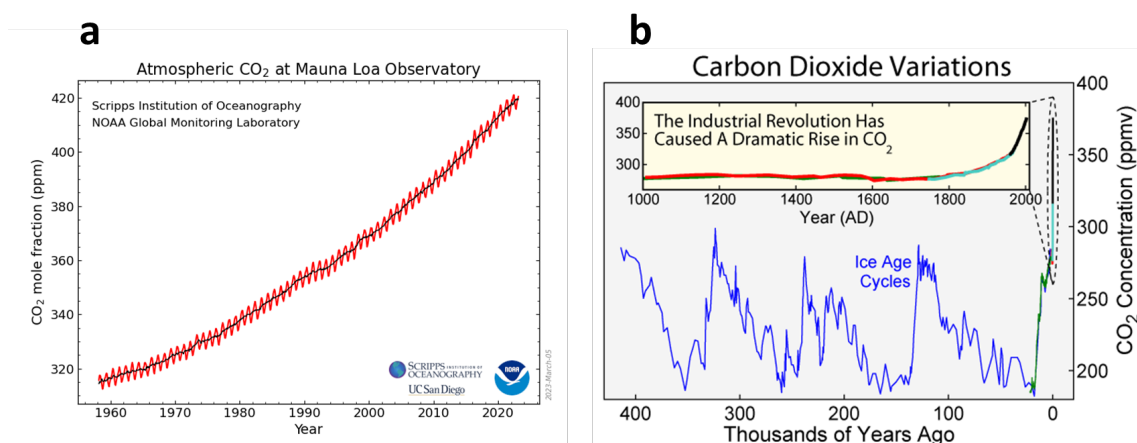


Figure 1.12: **a.** Global monthly means of carbon dioxide in the atmosphere since 1980. From [96] accessed on 23-02-2023. **b.** Carbon dioxide levels determined from 400 thousands years ago. Image credits Robert A. Rohde.

Table 1.1: Apparent standard potentials for CO₂ reductions in water.

Reduction Reaction	E^0_{app}/V vs. NHE[102]
$CO_2 + e^- \rightarrow CO_2^{\cdot -}$	-1.90
$CO_2 + 2H^+ + 2e^- \rightarrow HCO_2H$	-0.61
$CO_2 + 2H^+ + 2e^- \rightarrow CO + H_2O$	-0.53
$2CO_2 + 2H^+ + 2e^- \rightarrow H_2C_2O_4$	-0.49
$CO_2 + 4H^+ + 4e^- \rightarrow HCHO + H_2O$	-0.48
$CO_2 + 6H^+ + 6e^- \rightarrow CH_3OH + H_2O$	-0.38
$CO_2 + 8H^+ + 8e^- \rightarrow CH_4 + 2H_2O$	-0.24

methanol). In fact, this traces a parallel with natural photosynthesis described in Section 1.2, where plants are capable of fixating CO₂ into sugars and other stable forms of chemical energy storage, in a first step through the Calvin-Benson cycle.

Carbon dioxide represents the most oxidized state of carbon(+4) and it is a linear molecule with a high stability and therefore very long lifetime in the atmosphere.

Table 1.1 shows all the possible half-reactions of reduction that CO₂ can undergo and the related potentials. It can be observed that addition of the first electron onto CO₂ demands a high amount of energy as indicated by the very negative potential, but when multi-electron and multi-proton transfers are coupled together the overall thermodynamics become more and more favourable (less negative potentials). At the same time, one can imagine that coupling these multiple transfers altogether is quite kinetically challenging and difficult to realise on a single catalyst, given that already accumulating two-electron transfers on the same catalyst has proven to be experimentally challenging (see

Section 1.3.4). One possible strategy that chemists have followed is the use of tuned molecular catalysts which take inspiration from natural enzymes in the design of very specific secondary interaction, which are thought to stabilize reactive intermediates for further electrons and protons transfers. This and other concepts will be analyzed in the following Section.

1.4.2 . Iron porphyrins for catalytic CO₂ reduction

As discussed in the previous sections, porphyrins can be seen as the synthetic equivalent of chlorophylls, ubiquitous in the proteins involved in the natural photosynthesis. Indeed they have been used in artificial systems both as light harvesting units (in the case of free-base porphyrin or zinc porphyrin) and also as charge accumulating units (when metallated with Mn), see Section 1.3.

Thanks to their synthetic versatility and high absorption in the visible, they have been widely used in different research areas, including organic solar cells, photodynamic therapy, and molecular electronics[103]. In the catalysis field, they are still nowadays quite studied, given their ability to store oxidizing or reducing potential on the macrocyclic structure. When combined with the appropriate metal center, it is possible to access multiple oxidations and reduction states, which is a key step to activate and react with a given substrates.

One simple porphyrin derivative that has been known for a long time is iron - tetraphenyl porphyrin (FeTPP), which presents four phenyl substituents on the *meso* positions and it is stable at ambient conditions in the Fe(III) oxidation state, with one additional axial ligand for charge neutrality. The first electrochemical studies for CO₂ reduction to CO catalyzed by FeTPP date back to the 70s[104]. After the first publications on the subject, these findings were not further investigated until recently, when more public concern of CO₂ accumulation was raised, and therefore also search for innovative solutions for its conversion.

In the last two decades, a number of research groups across the world has been interested in modifying the simple FeTPP to access more efficient electrocatalysts[105][106]. As the first study with FeTPP shows its electrocatalytic ability to convert CO₂, many studies have focused their attention on electrochemical and electrocatalytic properties of the modified iron porphyrins. Often, a first assessment of the electrocatalytic properties of the catalyst is necessary before any further application in photo-induced systems.

When evaluating an electrocatalyst, two main parameters are taken into consideration: how fast the reaction proceeds (reaction rate) and how much energy the system needs in order to perform the reaction (energy needed for activa-

tion). The first term is normally referred as turnover frequency (TOF), whereas the second term is identified as overpotential (η), which corresponds to the difference between the applied potential and the thermodynamic one [106] [107]. Additionally, the performances of a catalyst are also described by the product selectivity (indicated by the Faradaic Efficiency, FE) and by the stability, defined by the turnover number (TON).

Before going into details of molecular design, let us first consider some general aspects of FeTPP and its reactivity with CO₂, which will help a better understanding.

Iron porphyrins generally present three redox waves when going towards more negative potentials, (see Fig. 1.13). In dry organic solvent such as DMF, the three redox waves displayed by FeTPP are attributed to the Fe^{III}P/Fe^{II}P at -0.63 V vs. Fc^{+ / 0}, Fe^{II}P/Fe^{II}P⁻ at -1.51 V vs. Fc^{+ / 0} and Fe^{II}P⁻/Fe^{II}P⁻ at -2.14 V vs. Fc^{+ / 0} redox couples [108]. It is important to notice how after the first metal-centered reduction, the following two are ligand based, once again highlighting its key role [108][109][110][111]. For simplification, in this manuscript, the second and third reductions will be indicated as Fe^{II}/Fe^I and Fe^I/Fe⁰. Also, it should be kept in mind that the axial ligand on the Fe(III) state (often a chloride), is released from the coordination sphere after the first reduction to the Fe(II) oxidation state.

When CO₂ and a proton source (water for example) are added in the electrochemical cell, a typical current increase is observed at the potential of the Fe^I/Fe⁰ wave (Fig. 1.13), indicating that: i) a catalytic reaction is taking place, ii) it is necessary to reach formal Fe⁰ redox state to bind and reduce CO₂ molecule. Proposals about the interaction of CO₂ with the iron porphyrin have been advanced [112], and CO₂ interaction is described as a bond formed between the metal center of the triply reduced catalyst and the carbon atom of CO₂, concomitant with a binding of the CO₂ linear structure that occurs after a first electron transfer. Some recent works [113][114] have opened the possibility of an "early" binding of CO₂ on the Fe(I) state under specific conditions. This aspect will be further discussed in Ch. 2.

Lastly, we shall consider that in the following examples in the literature, the reaction of interest is the two-electron, two-proton reduction of CO₂ to CO (See Table 1.1), unless otherwise specified.

FeTPP has as main disadvantage that the potential needed to activate the catalyst and consequently react with CO₂ substrate is quite negative (around -2 V vs. Fc^{+ / 0}). In other terms a high overpotential is required. In 2016 Azcarate

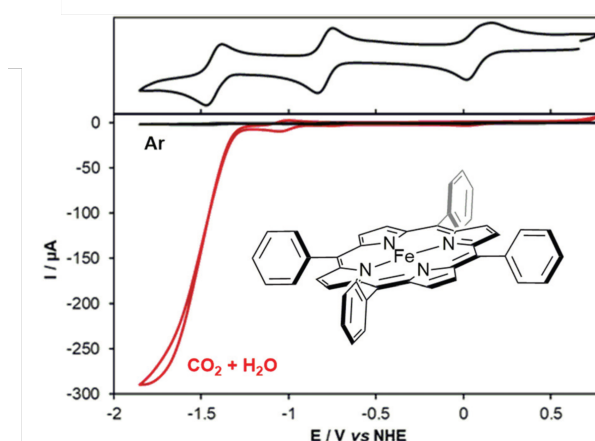


Figure 1.13: FeTPP cyclic voltammogram in Ar (top) and in catalytic conditions (bottom) with a scheme of the molecular structure. Image credit to [106]

et al. [115][116] tackled this issue as a first approach, by introducing electron withdrawing groups (EWG) on the phenyls of FeTPP making it easier to reduce. They could then study the effect of having penta-fluorinated phenyl in one, two or four *meso* positions of the porphyrin. Also our group reported studies on the effect of the number of fluorine atoms for symmetrical porphyrins[117][118]. Both groups reported that addition of EWG such as fluorine atoms, does indeed reduce the overpotential for CO₂ electrocatalysis. On the other hand, the reaction rate decreases in a linear trend with increasing number of EWGs. This effect was named iron-law [105] and it can be understood by analysing the effect that EWG have on the molecule's electronics. In fact, by decreasing the electron density of the iron center, the fluorine atoms render it less nucleophilic with the direct impact being a slower reaction rate. The iron-law effect is presented by the linear trend where improvement on thermodynamics comes with lower kinetic rates and *vice-versa*.

Moving forward from these results, another strategy for catalyst design consisted in using substituents that can act through space, instead of just through bonds as it is the case for electro-donating or withdrawing groups. Examples of these are electrostatic and H-bond interactions. Few examples of those reported in the literature are shown in Fig. 1.14. In general, this strategy is more effective in decreasing the energy requirements, while still keeping good reaction rates. For example insertion of local proton sources through incorporation of hydroxyl groups in the second coordination sphere (molecule **a** in Fig. 1.14) has been reported by the group of Savéant in 2012[119]. Adding multiple local protons enhances the reaction rate of CO₂ reduction to CO ($\log\text{TOF}_{\text{max}} = 5.97$) at low overpotential ($\eta = 0.64$ V) compared to the mono-substituted hydroxyl ana-

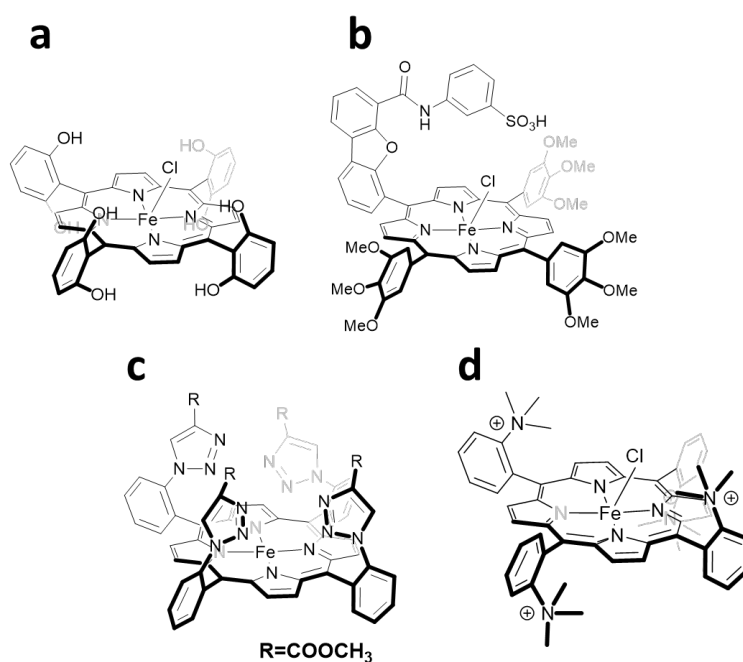


Figure 1.14: Iron porphyrins with second coordination sphere effects: **a.** with hydroxyl local proton source, **b.** with sulfonate local proton source, **c.** with triazole H-bond units, **d.** with ammonium charged groups.

logue ($\log\text{TOF}_{\max} = 2.1$; $\eta = 0.91$ V). Also, when the OH group was replaced by methoxy moieties (OCH₃), the reaction rate became slower ($\log\text{TOF}_{\max} = 2.7$) and at a higher required overpotential ($\eta = 1.00$ V).

Catalyst **b** of Fig. 1.14 was designed by the group of Nocera, implementing the concept of local proton source in the hangman porphyrin widely studied by his group [120][121]. Here, it was studied in parallel with two other substituted hangman porphyrins incorporating guanidinium or phenol groups. Once again improvements on the stabilization of the CO₂-adduct could be obtained for the phenol substituted hangman porphyrin, but in the case of the sulfonic acid one, a lower activity was observed than for the reference unsubstituted porphyrin. This result was ascribed to the fact that the phenol used in the solution as proton source is not acidic enough to re-protonate the sulfonate group after proton transfer to the substrate. The resulting negatively charged sulfonate group is electrostatically and sterically repulsed from the bound CO₂ substrate, resulting in a decrease in the catalytic activity. The results showed the importance of choosing the appropriate proton source in the reaction medium and provided a deeper understanding of the electrocatalytic process for CO₂ conversion.

A. Dey and collaborators have introduced triazole units which provide H-bonding in the distal pocket; this same catalyst was previously used for selective O₂ reduction (molecule **c** Fig. 1.14)[122][123]. When used for CO₂ conversion, they

reported the trapping and characterization of highly reactive intermediates at low temperatures, thanks to the stabilization given by the triazole units. In particular, they could obtain the formal Fe(0) state and the corresponding CO₂ adducts, Fe^I-CO₂⁻ and Fe^I-CO₂H.

One more example mentioned is the introduction of positively charged groups to stabilize reactive intermediates through electrostatic interactions. Catalyst **d** in Fig. 1.14 is an example from a group of catalysts studied by the group of Robert, Costentin and Savéant[116]. In their study, it could be confirmed that the positively charged tri-methyl anilinium groups (TMA) enhance CO₂-to-CO electrochemical conversion. They could also show the effect of the charged moiety position with respect to the CO₂ binding site and indeed they found that *ortho*-substitution with TMA groups has higher activity than the *para*-substituted one. This difference was rationalized by the proximity of the *ortho* position to the CO₂ bound on the iron center.

In our group, the design of second-coordination sphere substituted porphyrins has followed a common strategy coming from bio-inspiration. A known enzyme able to convert CO₂ to CO reversibly and at a very high rate (40 000 s⁻¹ for CO oxidation and 45 s⁻¹ for CO₂ reduction) at near zero overpotential is Carbon monoxide dehydrogenase (CODH) and it is found in both aerobes and anaerobes[124]. The O₂ sensitive CODH of anaerobes has a [Fe₄S₄Ni] cluster in its active site, shown in Fig. 1.15. Of this structure, we shall focus on: i) the close vicinity of the Ni binding site and the second Fe metal center; ii) the histidine residue (H93) and hydroxide/water molecules that can display H-bond interaction with the oxygen atoms of CO₂ to stabilize the intermediate; iii) the possible presence of protonated histidine (H93) and lysine (L563) residues on the second coordination sphere involved in intermediate stabilization through electrostatic interaction [124][125].

These three aspects were addressed one by one in development of modified Fe porphyrins. Molecules **a** and **b** in Fig. 1.16 both make use of H-bond interactions in their second coordination sphere, respectively amide and urea functional groups[117]. As described for the CODH active site, these kind of interactions are thought to help stabilizing the CO₂-adduct and also favouring the binding of substrate, leading to an enhanced catalysis. A comparative study [117] of their electrocatalytic properties showed that indeed the H-bond enhances the reaction rate at a lower overpotential than FeTPP and in particular, the multiple H-bonds induced by the urea arm were proven to be more effective compared to the single H-bond from an amide group.

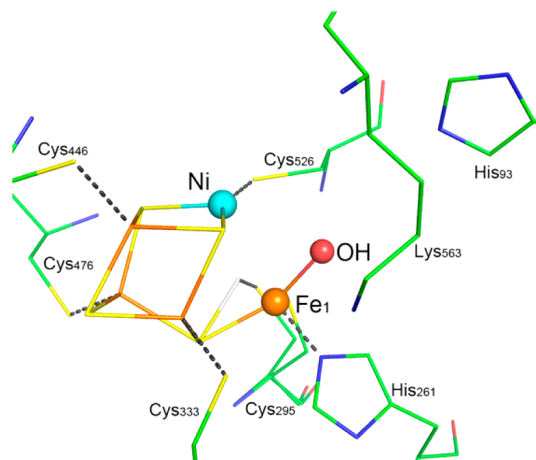


Figure 1.15: Active site of the [NiFe] CO dehydrogenase (CODH) represented with ball-and-stick. Image credits to [124]

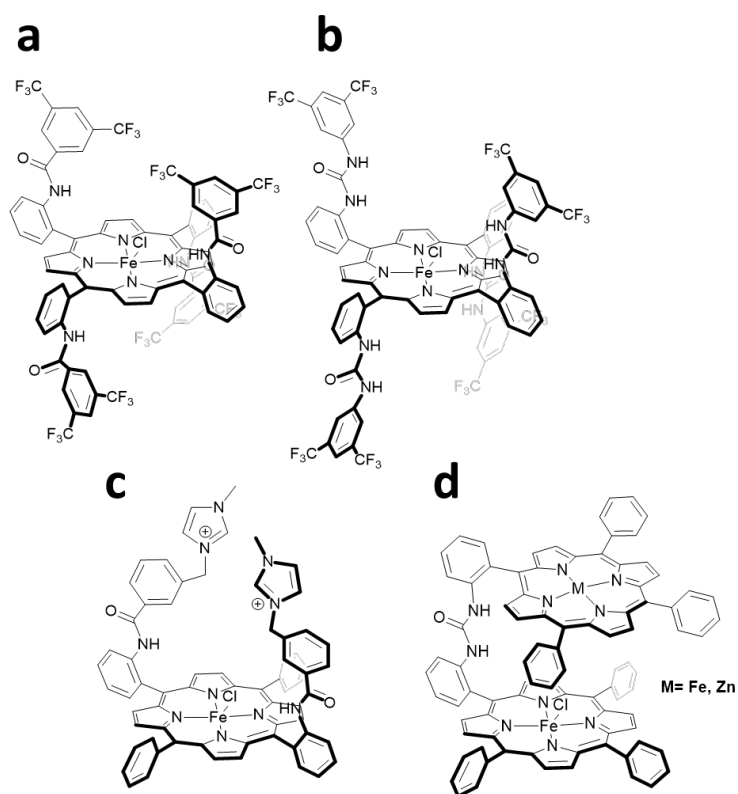


Figure 1.16: Iron porphyrins with through-space effects developed by our group: **a.** with amide H-bond donor groups, **b.** with urea multi H-bond donor groups, **c.** with imidazolium charged groups, **d.** binuclear porphyrin to study metal cooperativity.

As seen in the above examples, positive charges can stabilize negatively charged reactive intermediates. Following this logic, a family of mono-, di- and tetra-substituted imidazolium iron porphyrins were synthesized in the group [118][126]. Catalyst **c** in Fig. 1.16 is an example of di-substituted porphyrin with arms in *αα*-stereoisomer. Once again, the enhancement of catalysis thanks to the second coordination sphere could be highlighted, and interestingly a linear trend "iron law" could be traced also for the effect of the number of charges, with much higher activity than in the previous case of EWG insertion.

Lastly, a more recently studied system in our group involves bimetallic catalysts, where the two metalloporphyrin units are linked by a urea-bridging linker (molecule **d** Fig. 1.16). Other known bimetallic porphyrin systems with different configuration have been analysed by the group of Naruta [127][128]. In this case the goal was to study the two metal cooperativity on CO₂ activation. The study is a comparison between FeFe and FeZn catalysts and it could give evidence, in heterogeneous conditions, the push-pull type mechanism for CO₂ activation [129].

Overall, a better control of the catalyst structure and effects on electrochemical properties has been gained by our group over the last years. The next step was the translation of these results in terms of photocatalysis, for a more direct use of sunlight radiation.

The following section is dedicated to a general view of the state of the art of CO₂ reduction using molecular photocatalysis.

1.4.3 . Photocatalytic CO₂ reduction

Photocatalytic conversion of CO₂ by molecular catalysts has also been known for decades, although less intensively studied compared to electrocatalytic conversion. Indeed, this requires some additional elements in addition to the catalyst. As discussed in the previous sections, such systems need a light-absorbing unit (chromophore or photosensitizer; PS) and a sacrificial source of electrons. The latter comes from the fact that the present studies decouple the half-reactions of reduction and oxidation which would then constitute the ideal device (CO₂ reduction coupled with water oxidation); hence the need of a small molecule which will be easily (and irreversibly) oxidized. This molecule, that replaces the electrode when combined with the chromophore, is named sacrificial electron donor (SED).

At this point, it is important to understand the general mechanisms that take place when the photocatalytic mixture is irradiated. Fig. 1.17 shows two possible pathways for the electron transfers in the catalyst-chromophore-SED tryptic

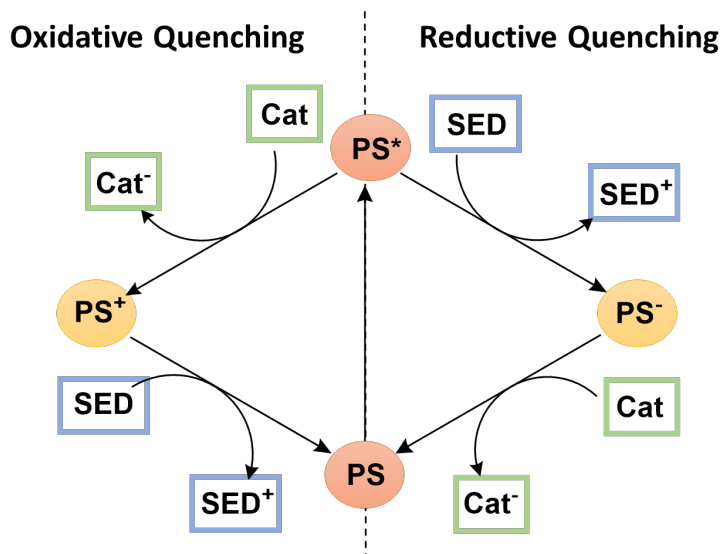


Figure 1.17: Representation of the possible quenching mechanisms.

mixture. In both cases, the first step, as one can guess, is the excitation of the PS by light absorption. Depending on the relative redox potentials of the species involved, the excited chromophore (PS^*) can be quenched either by the SED or by the catalyst (Cat). In the first case, named *reductive quenching*, this will generate the reduced PS^- , and in the other case, named *oxidative quenching*, the catalyst will be reduced (Cat^-), the chromophore oxidized (PS^+). The generated PS^- and PS^+ are then brought back to the ground state by electron transfer to the catalyst or from the SED respectively.

This cycle is repeated until the catalyst reaches an oxidation state able to react with the substrate (three successive reductions are necessary for Fe porphyrins). The need of looping through the cycle multiple times also means that: i) in the cycle, the potentials for the Cat/Cat⁻ couple will keep changing with the successive reductions as a new oxidation state of the catalyst is involved each time, ii) if the oxidative quenching is favoured in the first cycle, this may change when the catalyst will be more difficult to reduce (more negative redox potential), iii) ultimately, it is the reducing power of the PS^- species (in the case of reductive quenching) or of the PS^* species (for oxidative quenching) that determines if it is possible to reach the redox active state of the catalyst to activate the substrate. This last point highlights the importance of an appropriate photosensitizer, and the associated SED. This couple will dictate at which "potential" the catalysis can proceed, as a parallel of setting the right potential in an electrolysis experiment.

Going back to the two mechanisms, it is possible to discriminate which one will be favoured in a given system, both through prediction based on electrochem-

ical and photophysical data, and also it can be easily verified experimentally with quenching experiments. Prediction from collected data is based on the calculation of the thermodynamic drive for each reaction, in terms of Gibbs free energy changes from Rehm-Weller equation (see Eq. 1.4)[130].

$$\Delta G = E_{Ox} - E_{Red} - E_{00} \quad (1.4)$$

E_{Ox} stands for the standard potential of the species getting oxidized (SED for reductive quenching and PS for oxidative quenching), E_{Red} indicates the standard potential of the species being reduced (PS for reductive and Cat for oxidative quenching) and E_{00} is the energy of the excited state of the photosensitizer, which is calculated from absorption and emission spectra. As for all expression of free energy changes, the more negative ΔG term, the more favourable, or spontaneous the reaction will be. Even when the ΔG term is positive, but not too large, it is still possible for the reaction to occur, if a high enough concentration of the quenching species is present, but the rate will be affected. In any case, it is possible to determine experimentally the quenching pathway (at least for the first reduction of the catalyst) qualitatively by monitoring the kinetics of emission of the PS and quantitatively by measuring the quenching constants from fluorescence quenching experiments. When the chromophore is quenched, the visible effect is a shortening of the lifetime of the excited state because of the electron transfer, which has to be rapid enough to compete with the excited state lifetime. This effect also translates into a decrease of the emission intensity linearly with increasing concentration of the quencher. Measuring the chromophore emission in presence of different concentrations of the SED or catalyst one at the time, will determine which process is more efficient. It has also to be taken into account that when considering bimolecular reactions, it is possible to tune concentrations of different species to favour a specific pathway.

In some cases, the catalysts can also absorb in the visible and can trigger an electron transfer, precluding the need of an external photosensitizer, being themselves photocatalysts. However, this removes the possibility of tuning concentrations and reaction conditions to optimize individually light absorption and electron transfer.

As in the case of electrocatalysis, some parameters are used also in photocatalysis to evaluate the efficiency of the overall reaction. The most common value given in molecular photocatalysis is Turnover Number (TON). It is defined

simply by Eq. 1.5.

$$TON = \frac{nmol(product)}{nmol(catalyst)} \quad (1.5)$$

In other words, this number indicates how many moles of product can a single mole of catalyst produce, or rather - how many times the catalyst can cycle before deactivation. This value gives an indication of the stability of the catalyst. Together with TON, also the rate has to be considered, expressed once again in terms of Turnover Frequency (TOF), but here defined in more straightforward terms (Eq. 1.6).

$$TOF = \frac{TON}{time} \quad (1.6)$$

As a rate, it will have units of $time^{-1}$, and it is normally calculated from the linear region of product evolution, before the system starts deactivating and flattening the product evolution curve.

Lastly, quantum yield (QY) determination gives a value of how efficiently the system is absorbing light and transforming it into chemical energy. Two definitions of quantum yield exist: internal quantum yield (IQY) and apparent quantum yield (AQY). They are defined as follows:

$$IQY(\%) = \frac{nmol(product) \cdot e^-}{nmol(photons_{abs})} \quad (1.7)$$

$$AQY(\%) = \frac{nmol(product) \cdot e^-}{nmol(photons_{inc})} \quad (1.8)$$

Where e^- stands for the number of electrons needed for each product molecule, $photons_{abs}$ indicates the number of absorbed photons and $photons_{inc}$ the number of incident photons. For both terms values much far from 100% are to be expected, as a big loss of light energy constantly occurs as competitive deactivations, heat loss, unwanted side reactions and electron transfers, etc. Between the two terms, the first one takes into account the oversaturation of light that occurs at high light power, where the chromophore is not able to absorb all the light received.

When looking into the literature, the first studies made use of Ni and Co cyclam catalyts (Catalyst **a** in Fig. 1.18) [131][132]. It was studied in comparison with its dimeric and dimethylated monomer and dimer in *meso* positions[131]. They were studied in aqueous medium, in the presence of $[Ru(bpy)_3]^{2+}$ PS and represented in Fig. 1.19 and ascorbic acid as sacrificial electron donor. Gas Chromatography (GC) analyses showed activity in CO_2 reduction to CO for

both non-methylated monomer and dimer, but the monomeric complex having quite poor selectivity of CO produced vs. H₂ evolution (less than 50%). On the other hand, the methylated analogues, both monomeric and dimeric showed lower TON for CO production and lower selectivity. Insights on the reasons of the measured photocatalytic activity refer back to the 5 coordination mode of the Ni centers, whether it may be favourable, but do not go deeper at that given moment.

The next example is catalyst **b** in Fig. 1.18 reported for the first time in 2017 by Robert and collaborators. [133]. This was previously synthesized and studied for the effect of the introduction of charged groups at different positions on the porphyrin periphery for electro-catalytic reduction of CO₂. Here, the choice of photosensitizer could not be [Ru(bpy)₃]²⁺, given that the Fe^{I/0} potential is more negative and cannot be reduced by "Ru(I)"³. Few reports exist on the study of this catalyst [133][135][136][137][138], with different PS, molecules **c**, **d** and **e** of Fig. 1.19 represent the main examples. The first study [133] did not make use of any additional chromophore, using the iron porphyrin Fe-*p*-TMA as a photocatalyst in presence of either 1,3-dimethyl-2-phenylbenzimidazole (BIH; see Fig. 1.19) or triethylamine (TEA, Fig. 1.19) as SED and with trifluoroethanol (TFE) or phenol (PhOH) as proton sources in acetonitrile (ACN). A good selectivity was reported for CO over H₂ (nearly 100%) and a robust catalysis (over 2 days) even though at a modest rate (around 1.5 TON h⁻¹); with 3-dimethyl-2-phenyl-2,3-dihydro-1Hbenzo[*d*]imidazole (BIH) outperforming TEA as SED. A more thorough comparison of the catalyst with other iron porphyrins was given in a later report [136], where FeTPP and catalyst **a** in Fig. 1.14 were studied in the same conditions. Here Ir(ppy)₃ was used as an external chromophore (similar to the structure of complex **c** in Fig. 1.19) and TEA was used as SED. In this study a small production of methane together with CO was reported, when catalyst **b** in Fig. 1.18 was illuminated under white light for 47 h. The amount of CH₄ can be increased further with longer irradiation times and by using CO as a starting substrate. This unique production of CH₄ was not reported for any of the other catalysts or in the blank experiments. The evolution of CH₄ was further confirmed by an isotope labelling experiment using ¹³CO₂ and ¹³CO substrates, coupled with GC/MS analysis. Two more studies by the same group further highlighted: i) the evolution of CH₄ in a 70% aqueous medium and the follow-up of the degradation of the Ir(III) PS upon

³[Ru(bpy)₃]²⁺ can be reduced to a formal "Ru(I)" oxidation state, where in reality the metal center is still in its Ru(II) oxidation state and one of the bipyridine ligands holds a radical anion.[134]

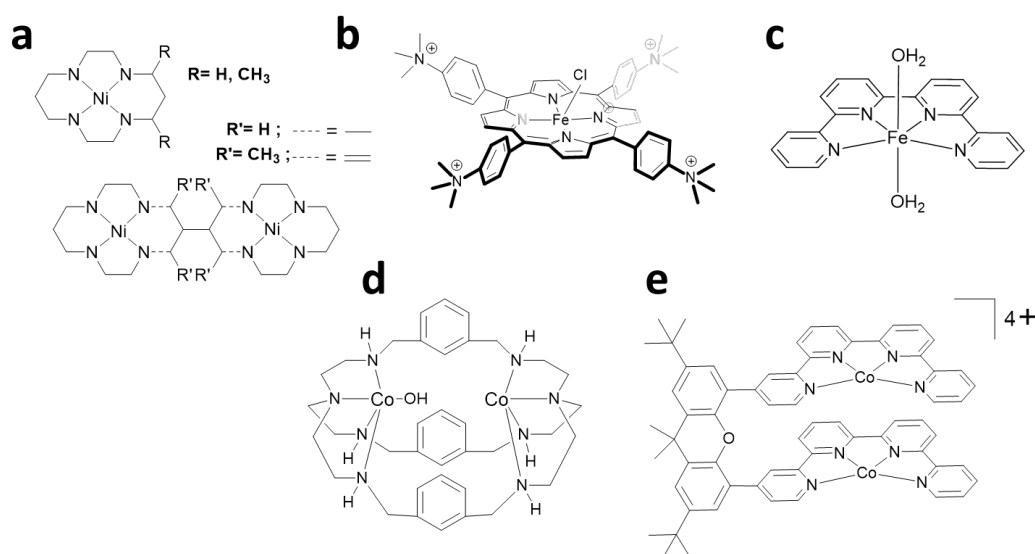


Figure 1.18: Catalysts for CO₂ photoreduction: **a.** Ni cyclam catalyst, **b.** positively charged Fe porphyrin, **c.** Fe quaterpyridine, **d.** binuclear Co cryptate complex, **e.** binuclear Co quaterpyridine complex.

long irradiation[137]; ii) the use of alternative PS (for example molecule **e** Fig. 1.19) which are metal-free ruling out heterogeneous Ir nanoparticles activity [138]. In this latter paper, a first mechanism is also proposed, big questions however still remain, after the CO-adduct formation, how are the remaining 6 electrons and 6 protons transferred.

Interestingly, in a previous report where purpurin is used as chromophore with catalyst **b** in aqueous solution, no mention or detection of CH₄ could be observed, possibly due to the lower reducing power of the chosen photosensitizer[135]. Another class of catalyst studied by the same group for CO₂ photoreduction consists of Fe and Co quaterpyridine and quinquepyridine complexes (complex **c** in Fig. 1.18) [139][140]. Two different photosensitizers were used: [Ru(bpy)₃]²⁺ and the noble-metal free purpurin (Letter **d** Fig. 1.19). In both conditions these catalysts showed a high catalytic activity, with TON= 1879 and TOF= 16 min⁻¹ among the highest reported in the literature at the time. The iron analogue showed in general better activity and similar selectivity for CO.

Among the highest TON numbers ever reported for homogenous molecular photocatalysts, stands out the dinuclear Co cryptate catalyst, shown in letter **d** of Fig. 1.18[141]. The study underlines the effect of metal cooperativity also when applied to photocatalysis. In fact, when the dimer and the monomer are compared, an important effect of the second metal presence is observed, going from 1600 TON(CO) to 16 896 TON(CO) and a TOF of 0.47 s⁻¹ after 10 h of

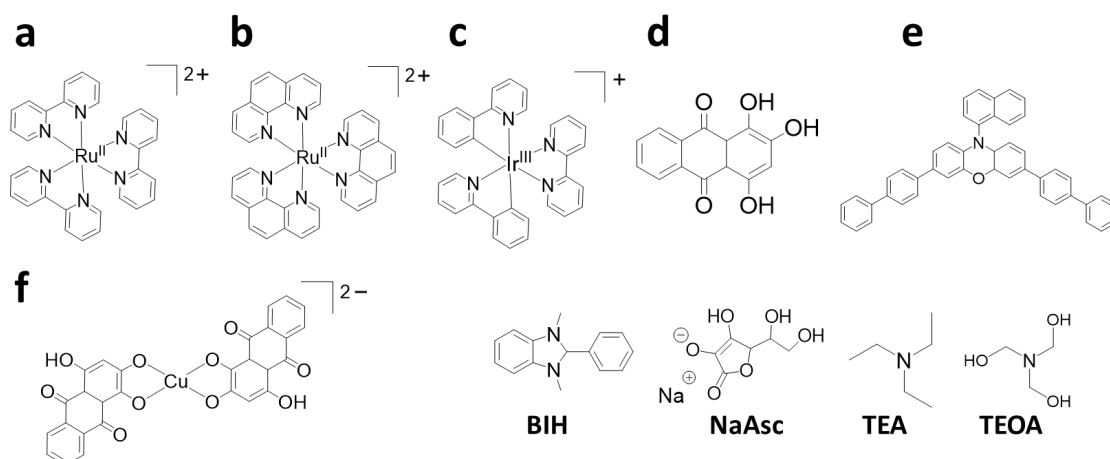


Figure 1.19: Examples of photosensitizers (PS; **a** to **f**) and sacrificial electron donors (SED) generally used.

irradiation. The bimetallic cooperativity hypothesis was consolidated through DFT calculations. In a later work^[142], the second Co center was replaced by a Zn center, giving rise to a further enhancement of catalysis, to reach a TON(CO) of 65 000 and a TOF of 1.8 s⁻¹. This improvement was attributed to the synergistic catalyst effect, where the Zn acts as a Lewis acid, aiding the C-O bond cleavage.

One more interesting example that will come in hand in the later chapter, concerns another dimeric Co complex (letter **e** in Fig. 1.18). In this case, metal cooperativity helps directing product selectivity towards formate (HCOO⁻) instead of CO^[143]. In optimized conditions they could obtain nearly 100% selectivity for HCOO⁻ with varying TON(HCOO⁻) from 110 to 821. The AQY was also estimated as 2.6% for formate. An intriguing result in this work is the characterization by IR of the CO₂ bound intermediate, obtained through a spectroelectrochemical (SEC) experiment, giving a new vibrational band at 1635 cm⁻¹. It was calculated with DFT that this wavenumber well matches asymmetrical stretching of the C=O bond when CO₂ is bound to a metal center.

In this and the previously cited study, the PS used is [Ru(phen)₃]²⁺ (letter **b** of Fig. 1.19). One reason for this choice is to avoid the use of [Ru(bpy)₃]²⁺, considered less stable. Among the examples of chromophores given in Fig. 1.19, the Cu purpurin one has not been discussed yet (letter **f**). This was reported in 2021^[144] used in combination of catalyst **a** of Fig. 1.14 and BIH for photoreduction of CO₂. The idea was to take the cheap and easily available purpurin chromophore and to improve its properties for photocatalysis. For instance, the major absorption of purpurin (letter **d**, Fig. 1.19) is centered in the UV region,

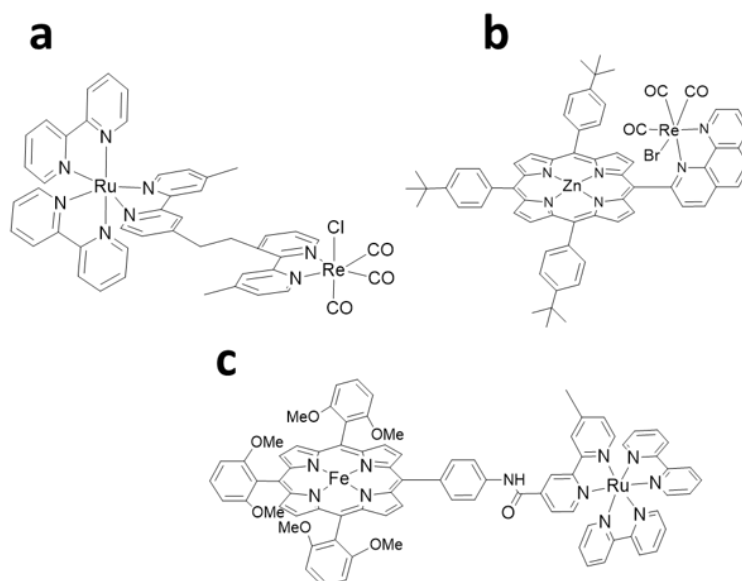


Figure 1.20: Molecular dyads of photosensitizer-catalyst used for CO₂ reduction: **a.** Ru- Re dyad, **b.** Zn porphyrin-Re dyad, **c.** Fe porphyrin - Ru dyad.

which makes it inconvenient for applications with sunlight. A simple coordination with a central Cu(II) enhances the extinction coefficient and red-shifts the absorption. Photophysical and electrochemical studies evidenced that this chromophore can also partly catalyze CO₂ reduction. Photocatalytic experiments showed that without any addition of catalyst, some CO was produced, but when both are mixed together higher production was observed, with TON and TOF varying with the initial concentration of BIH. In particular, with 10 mM BIH 4779 TON(CO) could be achieved with a TOF of 1356 h⁻¹, whereas with a starting concentration of 100 mM BIH, up to 16 109 TON(CO) and 7650 TOF were reached, in both cases with a selectivity of 95% maintained. The authors then tried to give a rationalization of the reaction mechanism, however the concomitant effect of the PS acting as a catalyst makes a full understanding quite complicated.

Molecular dyads have previously been described in Section 1.3.2. The earlier examples dealt with rapid charge transfer between a donor and an acceptor. Here, examples are given where the dyads comprise the PS unit (donor) and the catalyst (acceptor). The key difference here is that multiple electron transfers are necessary within the same dyad, in order to accumulate enough reducing power on the catalyst side, to then activate the substrate. As described earlier, to cycle the electron transfer path, a SED is added in large excess in the reaction mixture, in order to quench rapidly the excited PS* (for reductive quenching) and to keep generating the reduced PS⁻ faster than any side reaction, like in-

tramolecular quenching.

Fig. 1.20 shows some example of dyads used for photocatalytic CO₂ reduction. The first two make use of a Re complex catalytic unit, coupled with different chromophores. [Re(bpy)(CO)₃]⁺ was reported to be an active catalyst for photoreduction of CO₂ since few years.

Dyad **a** was reported in 2015 by the group of Ishitani [145] to perform 2-electron 2-proton reduction of CO₂ to formic acid (HCOOH) in aqueous solution. This selectivity for HCOOH over CO was found to be very specific to the reaction conditions, since when placed in organic medium, the formation of HCOOH was entirely suppressed. Continuing the comparison of the two media, the reaction rate was found to be higher in organic solvent, together with a higher amount of product generated (TON). Photophysical studies allowed rationalization of the observed trend, in terms of faster back-electron transfer (BET) between the oxidized SED. sodium ascorbate (NaAsc) and the reduced Ru PS unit due to a lower cage escape efficiency in water. Addition of external Ru complex chromophore showed an increase in catalytic activity. The same trend was also observed upon increasing the light intensity. Both of these results indicate that the reaction is limited by the generation of reduced chromophore due to a fast BET with the ascorbate. Such conclusion, combined with the observed degradation of the irradiated complex over time, pushed the authors to investigate heterogenization as a way to increase stability and suppress unwanted side reactions [146].

In 2020, Kuramochi *et al.* [147] published a study on a dyad based on the combination of a Re catalyst with a Zn porphyrin as photosensitizer (**b** in Fig. 1.20). Zn - porphyrins examples have already been shown in Section 1.3. They are potentially very good for chromophores, given their strong absorption in the visible region and long-lived triplet state. However, it was shown that under continuous irradiation and with accumulation of electrons, the porphyrin ring can undergo hydrogenation reaction to generate chlorins and bacteriochlorins [148]. Here, the authors aim to suppress this degradation pathway by rapid intramolecular electron transfer to the catalyst side. In this dyad, a strong electronic communication is in play and the excited singlet state of the porphyrin is almost fully quenched in presence of the bound catalyst. At the same time, the light energy is stored in a long-lived triplet state of the Zn porphyrin, which could be observed as an emission at room temperature in absence of a SED (BIH) and O₂. In presence of BIH and PhOH as proton source CO is produced with a TON(CO) of 1300, much greater than with the equivalent bimolecu-

lar system, where the Zn porphyrin underwent visible photodegradation. Two different light sources were used, one focused on the Soret band absorption (around 400 nm) and the other one on the Q bands⁴ (around 560 nm). The calculated AQY gave roughly the same result in the two cases (about 8%), meaning that no important deactivation pathway is present in the decay from the higher excited state (S_2) to the lowest excited singlet state (S_1).

In dyad **c** in Fig. 1.20[150] the porphyrin unit acts as the catalytic site, thanks to its Fe metal center and it is linked through an amide bond to the Ru complex for light harvesting. Unexpectedly, upon excitation the photosensitizing unit suffered from a rapid quenching due to energy transfer to the porphyrin unit. No product was detected when the dyad was irradiated in presence of BIH and proton source. However, when additional Ru chromophore was added in the reaction mixture, a visible production of CO could be evidenced. In particular, when the dyad was tested in presence of 50 μ M external $[\text{Ru}(\text{bpy})_3]^{2+}$, the TON(CO) reached up to almost 450, more than double that obtained when just the Fe porphyrin unit was used in the bimolecular reaction with the same amount of Ru PS (TON(CO) of 180). A boost of the selectivity could also be observed, going from 32% for the Fe porphyrin to 64% for the dyad system. One interesting observation coming from this study is in the proposed mechanism. Indeed, it can be seen from the cyclic voltammograms (CV) that the $\text{Fe}^{I/0}$ reduction potential of the porphyrin is too negative to be reduced by the Ru(I) formal oxidation state. Still, catalytic activity can be observed. The explanation lays in the non-innocence of BIH as electron donor. BIH, as an irreversible electron donor undergoes chemical reactions after first oxidation until deactivation. The pathway that it follows has been reported[151], and it highlights the generation of a radical species, which is in itself highly reducing (around -2 V vs. $\text{Fc}^{+/0}$). This means that BIH gives away two electrons (and one proton), and the second electron can achieve reductions that are inaccessible to the photosensitizer. This effect should always be kept in mind and it will be discussed in the later Chapter 2.

⁴Porphyrins have very characteristic UV-vis absorption spectra. Two main transitions are observed: a high extinction coefficient Soret band which normally ranges between 400 and 430 nm, and lower energy and lower extinction coefficient Q bands (4 bands for metal-free porphyrins and 2 for metallated porphyrins) in the 500-600 nm region of the spectrum. They are both due to π - π^* transitions; a model proposed by Gouterman [149] describes two degenerate π orbitals and two degenerate π^* orbitals, the different dipole combinations give rise to the different intensities of such transitions.

1.5 . O₂ activation

1.5.1 . Context

We often talk about photosynthesis as the most important process that allows our life on Earth, this is because, as it was discussed in Section 1.2, photosynthetic organisms provide us with the dioxygen we breathe and use for the essential functions of our body. Aerobic organisms utilize molecular oxygen for a wide library of reactions in their metabolism[152], at the same time, more than 95% of the O₂ entering the organisms is used for respiration; which consists of a cascade of exergonic electron transfers ultimately producing ATP, the main energy currency in biology. Throughout the evolution, organisms developed the capability of translating previously anaerobic reactions to aerobic ones with a huge gain in reaction efficiency[153].

Also, in the chemical industry, oxidation chemistry plays a central role. The main building blocks of chemical industry are derived from functionalization of simple carbon chains that we can extract from fossil fuels resources. Oil and natural gas are the main source of raw materials and they are mainly composed of hydrocarbons like alkanes and aromatics[154]. Insertion of oxygen atoms to generate oxidized organic molecules is one of the crucial steps to provide a wide variety of products. For instance, monomers used for fibers, plastics and other polymers undergo selective oxidation of hydrocarbons to be produced. On an industrial scale, oxygenation reactions are performed by catalytic processes, both heterogeneous and on a smaller extent homogeneous. Interestingly, a chemical produced on the largest scale by oxidation, terephthalic acid (used for PET synthesis), is oxidized by a homogeneous catalyst.

Like for plants, atmospheric O₂ represents the ideal candidate for "O" atom source for industrial synthesis, given its abundance. The main hurdles for reacting O₂ with organic substrates, is the need of harsh conditions (high temperatures and pressures) in order to activate molecular oxygen. At the same time, once the reaction takes place it may be highly exothermic (full combustion) and difficult to control[155][156]. Why high temperatures and pressures are required? As we know from experience, atmospheric O₂ is not reactive with organic molecules, as our cells are not undergoing undesirable reactions when exposed to air. This is because, when looking at the molecular orbitals of this small molecule, we see that it is best described as a biradical species, with two unpaired electrons in the π^* orbitals, which gives rise to a triplet state. Because of the Wigner's spin conversion rule, the direct consequence is that O₂

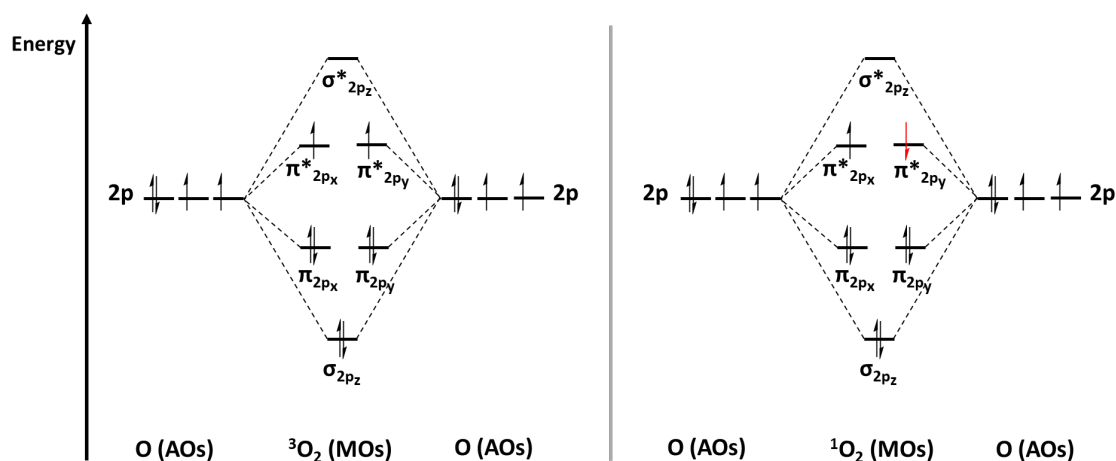


Figure 1.21: Molecular orbitals representations for ground state O_2 (left) and excited singlet O_2 (right).

ground state will have a very small probability of reacting with a singlet state organic molecule. However, upon excitation it is possible to generate so-called *singlet* O_2 having two antiferromagnetically coupled electrons in the π^* orbitals. The two states are represented in Fig. 1.21. Singlet oxygen can be generated photochemically by triplet-triplet energy transfer from the excited photosensitizer[157].

Alternatively, activation of O_2 with paramagnetic centers can be used to initiate the first step of dioxygen activation at lower energy. This approach takes, once again, inspiration from nature, where the class of metalloenzymes capable of activating dioxygen is dominated by iron containing proteins; some famous examples are Cytochrome P450 and Rieske enzymes [158] [159] [160] [161]. Cytochrome P450 is a family of heme- containing metalloenzymes and it is found in bacteria, fungi, plants and animals. Cytochrome P450 (CYP) are oxygenases (enzymes that catalyze oxidation of substrates by molecular oxygen) and their main functions are detoxification from xenobiotics (compounds external to the organism) and biosynthesis of signaling molecules[160]. They are all composed of a single polypeptide ranging between 40 and 55 kDa which surrounds the heme and creates a very specific and flexible pocket that allows the dioxygen and the substrate to enter, and then the product to be released. The H-bond created between the S atom of Cys357 and a peptide NH group modulates the redox potential during the transformation[161]. The mechanism that CYP follows for O_2 activation and "O" atom transfer onto different substrates has been subject of many studies and it includes formation of iron (III) hydroperoxo ($Fe(III)OOH$) and iron (IV) oxo ($Fe(IV)=O$) reactive intermediates (see Fig. 1.22). More specifically, Cytochrome P450 is a fundamental example

to display mechanism of mono-oxygenation of substrate (from R-H to ROH). The first step involves a reduction of the iron center to PorFe(II); step (III), which then reacts with O₂ and upon a second electron transfer coupled with a proton transfer, it generates PorFe(III)OOH; step (IV). This intermediate then undergoes heterolytic bond cleavage to form Por^{•+}Fe(IV)O with release of a water molecule. The heterolytic cleavage was explained by the *push-pull* model, where the S from the axial ligand "pushes" the electron density, and a nearby residue that donates H⁺ "pulls" the water molecule. Finally, the highly active Por^{•+}Fe(IV)O transfers the oxygen atom to the substrate, regenerating the starting complex[158].

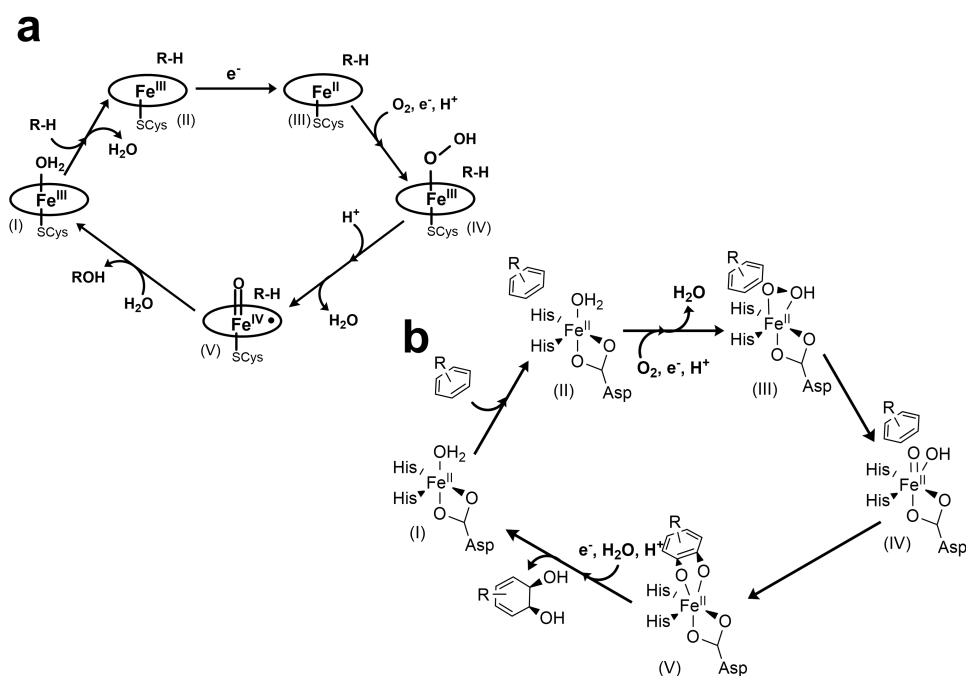


Figure 1.22: Simplified catalytic schemes for the active sites of Cytochrome P450 (a) and Rieske enzyme (b). The circle represents a porphyrin ligand.

Rieske enzymes are a class of non-heme iron-dependent oxidative enzymes and they are involved in the first step of oxidative degradation of aromatic compounds to diols with stereoselectivity control and other oxidative transformations[159]. The enzymes core is composed of three main units: i) a [2Fe-2S] cluster that provides electrons, ii) a mononuclear iron center to activate dioxygen and iii) a bridging aspartate residue, which probably serves as electron transfer shuttle between the two units during catalysis[162]. In this case, the iron complex involved in the activation is non-hemic and the main steps that it undergoes during activation are shown in Fig. 1.22. Similarly to CYP, the first steps involve the generation of an Fe(II) species, with subsequent reaction with

O₂, to generate after a proton and electron transfer an Fe(III)OOH intermediate of which the crystal structure could be obtained; step (III) in Fig. 1.22 **b**[163]. Afterwards, it was theorized that the latter isomerizes to an HO-Fe(V)-oxo (step (IV)), even though no evidence of this intermediate has been reported. From this step, *cis*-insertion of the two oxygen atoms (step (V)) generates the stereoselective diol product.

Based on the second example, chemists have developed different biomimicks of the enzyme active sites, which are discussed in the next section.

1.5.2 . Non-heme Fe complexes for O₂ activation

We have now seen that in biology, both heme and non-heme iron complexes play a central role in dioxygen activation. Chemists have followed two main pathways in the design of iron (or other metals) complexes that can perform substrates oxidation in the same fashion as the enzymes. A more bio-mimetic approach involved the development of different metalloporphyrins, giving the similarity with the active site of CYP[164].

Bio-mimetic models also exist for the non-heme iron complex based enzymes, such as for α -ketoglutarate[165]. However, in this case the stability of the complex upon oxidation was quite moderate and no intermediates could be characterized. This kind of issues lead to investigation of more precisely tuned complexes, which take inspiration from nature, but then extract only the key elements which allows to optimize both their reactivity and stability.

For instance, the coordination environment must be capable of stabilizing high valent oxo species, that were shown in the previous section as the catalytically active ones that transfer the oxygen atom to the substrate. Electron-rich ligands that bind the metal through a N or O atom can help the metal center to sustain its high oxidizing power.

Fig. 1.23 shows two examples of these non heme complexes. Catalyst **a** goes under the name of Jacobsen's catalyst (after Eric N. Jacobsen who first synthesized it in 1991) and it has important industrial applications for asymmetric epoxidation of indole, for the synthesis of Indinavir, an HIV inhibitor[166][167]. This example illustrates how bio-inspired complexes can also play an important role for industrial applications. It is important to notice how in this case the metal center consists of a manganese (Mn) instead of iron. In fact, even if all the above and following examples deal with iron catalysts for O₂ and oxidation of substrates, an equally important library of natural and synthetic catalysts also exists for Mn-based ones. Without going into detail, we can consider that with both of these metal centers, similar reactive intermediates are formed, including

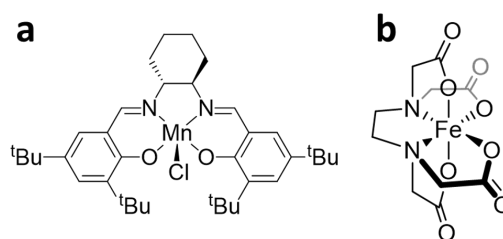


Figure 1.23: **a.** Non-heme Jacobsen's catalyst for O₂ activation. **b.** Non-heme Fe-EDTA complex for O₂ activation.

the above mentioned metal(IV) and metal(V) oxo species.

Complex **b** in Fig. 1.23 is an Fe(III)EDTA that has been known for some decades (discovered in 1956 [168][169]), and it is among the first synthetic non-heme iron complexes to be characterized in its reactive intermediates formed with O₂ [170] [171]. For instance, a Raman spectroscopy study focused on the characterization of the binding mode of O₂ of the Fe(III) peroxy species, [Fe(EDTA)O₂]³⁻. A more in depth study has also been carried by Neese and Solomon [171] where they described a side-on ferric peroxide and identified the more favourable activation mode. In all of these cases, hydroperoxy and peroxy intermediates have been prepared chemically, by using H₂O₂ as the source of oxygen atoms, as it is an already a 2 e⁻ reduced form of O₂.

The ligands described so far, have the common feature of holding negative charges, so that to increase the electron density in the ligand field which can ultimately stabilize high valence metal oxo intermediates. Going back to the Rieske enzyme model, we can notice that the bound histidine (His) residues do not hold negative charge. This lead other chemists to investigate polynitrogen ligands, where the binding unit, such as pyridine, act as π-acceptors and tertiary amines act as σ-donors. This kind of approach may have as drawback the loss of stabilization for the high valence intermediates, but it can also increase their reactivity. Figure 1.24 shows a family of poly-nitrogen ligands that have been studied in the form of iron complexes for O₂ activation. Ligand **a**, the "parent" compound, is often abbreviated as TPEN [*N,N,N',N'*-tetrakis(2-pyridylmethyl)ethane-1,2-diamine] and it was first prepared and studied by Anderegg and Wenk in 1967 [172] and later by Toftlund and Andersen in 1981[173]. The initial interest in this complex was related to the study of spin-transition complexes, related to the understanding of theorized spin-transitions taking place in natural enzymes (like CYP) which play a role in the active site's reactivity.

In 2000, Simaan *et al.* [174] reported a comparative study and intermediates

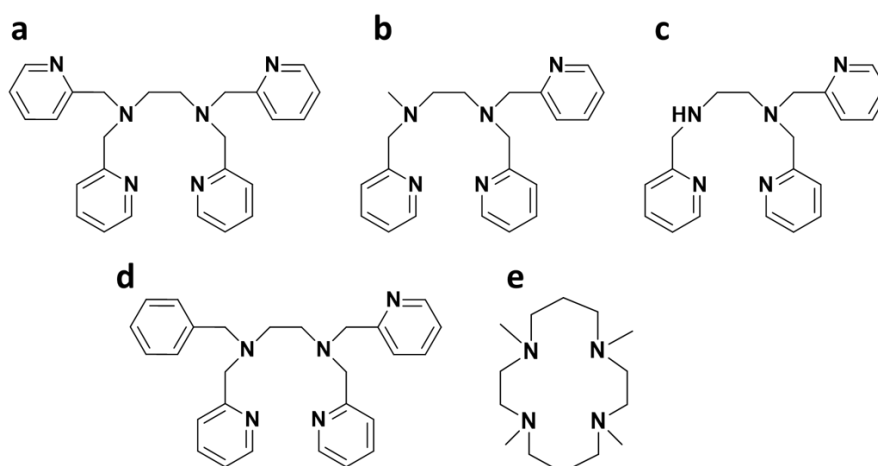


Figure 1.24: Examples of polyaza containing ligands used for the preparation of non-heme iron complexes for O_2 activation. **a.** TPEN parent ligand; **b.** to **d.** modification with 5 coordination sites. **e.** TMC ligand with 4 coordination sites.

characterization of the Fe(II) complexes formed with ligand **a**, **b** and **c**. An important aspect to retain when looking at these ligands, is the number of coordinating N. Except for TPEN (**a** in Fig. 1.24) the removal of one of the binding sites leaves an "incomplete" coordination sphere that allows faster binding of O_2 [175]. In fact, in the case of TPEN, a first decoordination of one pyridine is necessary, which will be an equilibrium based on the metal affinity with the possible ligands (also affected by the nature of solvent). In this study, it was possible to determine using UV-vis, EPR and Resonance Raman (rR) spectroscopies the nature of the Fe(III) hydroperoxo and peroxo intermediates for the three complexes. For $[Fe(TPEN)]^{2+}$ and $[Fe(II)c]$, the $[Fe(III)OOH]^{2+}$ intermediate was prepared in methanol, with addition of a large excess of H_2O_2 at room temperature; from this, deprotonation with triethylamine could generate the $[Fe(III)O_2]^+$ intermediate and their spectroscopic features were compared with reported ones for $[Fe(II)b]$ [176][177][178]. In the case of $[Fe(II)c]$, the peroxo intermediate could not be detected at room temperature, probably due to the sensitivity of the secondary amine group to oxidation. In its hydroperoxo intermediate, higher stretching frequencies for both Fe-O and O-O bonds were found, indicating a different molecular structure, where the steric hindrance of the $-CH_3$ or $-Py$ groups is removed.

More recent studies on the same family of complexes, investigated the electrochemical activation of the Fe(II) complexes as an alternative route to their chemical generation with H_2O_2 [175][179]. The idea behind this approach is to reductively activate O_2 by a first electron injection, which will then react with the Fe(II) metal center to form highly oxidizing intermediates that react with

organic substrates. The advantage of electrochemical activation compared to using chemical reductants or oxidants is a better control of the potential that can be specifically tuned. With this methodology, it was possible to characterize the electrochemical properties of the oxygenated intermediates, giving further insights on the mechanism of the electrochemical activation[180][181].

Another important intermediate that was mentioned in the previous section regarding O₂ activation in enzymes is Fe(IV)-oxo. For non-heme iron complexes, the group of Nam and Que has studied and characterized intermediates of iron complexes with ligand **e** in Fig. 1.24 - abbreviated "TMC"- and its derived forms[182] [183]. In their report of 2005[182], they were able to generate [Fe(IV)O] species with iodosylbenzene (PhIO; an oxo-transfer chemical) and for the first time, to characterize it by rR spectroscopy. They could observe that the [Fe(IV)=O] bond vibration energy is affected by the environment of the ligands (interchanged between N₃⁻, NCS⁻ and acetonitrile).

The same [Fe(II)TMC]²⁺ (ligand **e**) could also activate O₂ in presence of an electron donor (NADH analogue) and perchloric acid (HClO₄) at room temperature in organic solvent[183]. This yielded the formation of the Fe(IV)-oxo species which was characterized by UV-vis spectroscopy and mass spectrometry. Interestingly, the same technique applied to Fe(II) complexes with different ligands, such as ligand **d** of Fig. 1.24 generated the Fe(III)OOH intermediate. In any case, the generation of the Fe(IV)-oxo is considered to proceed through a Fe(III)OOH intermediate, which explains the need for a reductant and a proton donor.

Table 1.2: Reported values for reactive intermediates of non-heme iron complexes; the letters in bold refer to the different ligands reported in Fig. 1.24.

Complex	λ_{\max} (UV-vis)	g-values (EPR)	$\nu(\text{rR})$	Ref.
[aFe(III)OOH]²⁺	541 nm	2.22; 2.15; 1.967	617.2 cm ⁻¹	[174]
[aFe(III)OO]⁺	755 nm	10; 8.1; 5.6; 3.2; 2.4	817 cm ⁻¹	[174]
[bFe(III)OOH]²⁺	537 nm	2.19; 2.12; 1.95	617.2 cm ⁻¹	[176][174]
[bFe(III)OO]⁺	740 nm	7.5; 5.9	819 cm ⁻¹	[176]
[cFe(III)OOH]²⁺	531 nm	2.19; 2.14; 1.96	624.8 cm ⁻¹	[174]
[dFe(III)OOH]²⁺	538 nm	2.34, 2.21, 2.15, 1.97, 1.94		[183]
[eFe(IV)O]²⁺	820 nm		834 cm ⁻¹	[182]

In 2008, Banse, Que and coworkers [184] were able to apply the same methodology to obtain spectroscopic and crystallographic evidence of an Fe(IV)

oxo complex with a modified TMC ligand, holding an additional pyridine as axial ligand.

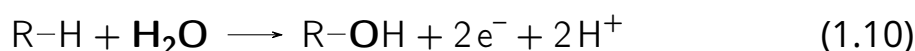
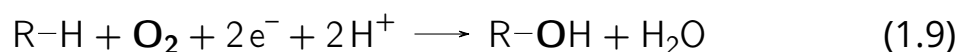
Overall, the examples given, even if not exhaustive, can help understanding the complexity of O₂ activation mechanism, with all its unknowns and undeciphered steps, and at the same time the importance of seizing intermediates that can give hints on the reaction mechanism. A brief summary of the characteristic features of the mentioned complexes is given in table 1.2.

Different methods have been described to generate iron-oxygen active species for oxygen atom transfer reactions, one more option, is to implement a photochemical system, which is described in the following section.

1.5.3 . Light-induced O₂ activation

The use of light can enable specific reactions that are not achieved in more standard conditions. To avoid implementing strong oxidants or oxygen atom donors to activate the catalyst (PhIO, H₂O₂,...), researchers started studying dioxygen activation through light. Two main approaches have been followed in this matter: either coupling a photoredox module with bio-mimetic/bio-inspired molecular catalysts or coupling the photoredox module with an enzyme[185].

Tracing a parallel with what was discussed for CO₂ photocatalytic reduction (see Section 1.4.3), we can recall the photoredox module being composed of a photosensitizer or chromophore (PS) and a quencher. Previously, the quenchers were identified as electron donors, here instead they are mostly electron acceptors (EA). A simple didactic example to describe the mechanism of the photogeneration of oxidizing metal complexes intermediates, is given by the oxidative activation of a Mn porphyrin reported in 2011 by Nam, Fukuzumi and co-workers (Figure 1.25, **a**)[186]. In this case, the reactive intermediates are generated using water as oxygen atom source. The same type of high valent oxo species are formed, and once obtained they will perform the same chemistry as if they were generated through the activation of O₂. The two global equations for these pathways are given in Eq. 1.9 and 1.10[185].



In this study, a mixture of [Ru(bpy)₃]²⁺ photosensitizer, [CoCl(NH₃)₅]²⁺ electron acceptor (EA) and water-soluble Mn porphyrin (PMn) was irradiated for 15 min with visible light in a phosphate buffer. The proposed mechanism starts with a first oxidative quenching of Ru(II) with the EA, generating Ru(III) which in turn oxidizes the PMn(III) to a PMn(IV)O species. The latter can dismutate,

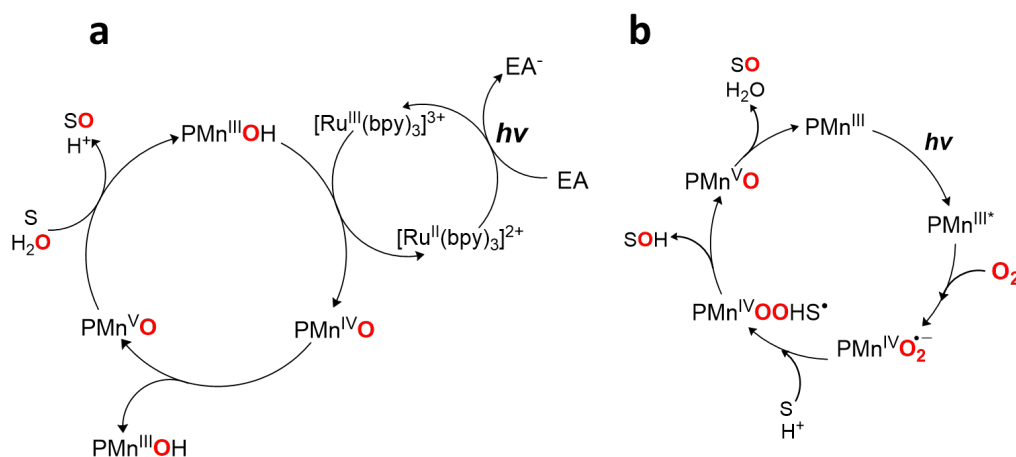


Figure 1.25: Proposed catalytic cycles for high-valence oxo species generation from water as oxygen source (a) or from O₂ as oxygen source (b). See more details in the text.

giving place to a PMn(V)O and the starting PMn(III). The PMn(V)O generated is highly oxidizing and it transfers the oxygen atom to the substrate. In this case either sodium p-styrene sulfonate (NaSS) is oxidized to epoxide or sodium 4-ethylbenzene sulfonate (NaES) is oxidized to alcohol. In the same study, they also compared Mn porphyrins with different substituents and they underlined the importance of the proper electron acceptor.

Few years later, the group of Fukuzumi studied the same family of Mn porphyrins in organic solvent for the photo-activation of O₂ (see Fig. 1.25 letter b)[187]. The proposed mechanism represented in the scheme is quite different from what has been shown until now. The triplet nature of the ground state of O₂ confers on this molecule a very specific chemistry and photochemistry. Thanks to femtosecond transient absorption measurement, it was possible to identify the rapid intersystem crossing (ISC) that the PMn(III) undergoes when excited, forming a long-lived triplet state. The lifetime of the latter decreases when O₂ is added in solution, indicating a reaction between these two triplet states which gives rise to [PMn(IV)(O₂^{•-})] upon electron transfer. A further electron and proton transfer generates PMn(IV)OOH and a substrate radical (S[•], where the substrate is 10-methyl-9,10-dihydroacridine), which they report as the rate-limiting step. At this point, the O-O bond breaking occurs rapidly and it generates the alcohol S-OH and PMn(V)O, that oxidizes further the alcohol to ketone S=O.

Another possible approach that has been reported by different groups to photo-activate O₂ consists of making use of riboflavins derivatives (the most common being riboflavin tetraacetate- RFT; a in Fig. 1.26) as photocatalysts to oxidize a variety of benzylic substrates. For example, in 2010 König and co-workers re-

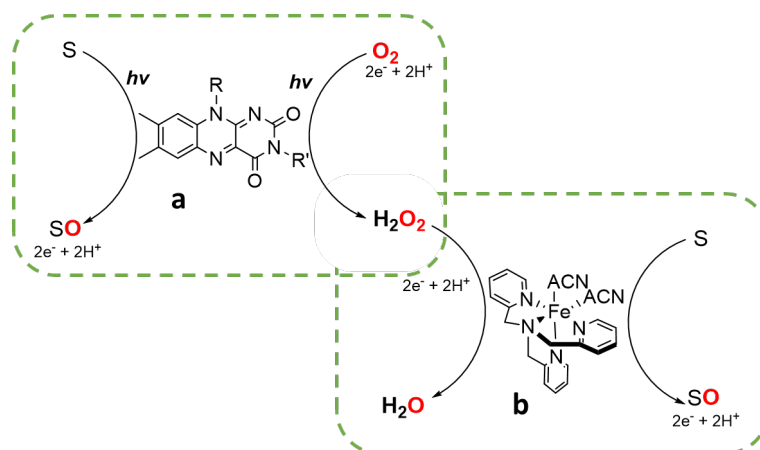


Figure 1.26: Simplified reaction schemes for RFT-based systems described in the literature.

ported the oxidation of various benzylamines to their corresponding aldehydes when irradiating for 10 min with visible light RFT in presence of oxygen[188]. The use of RFT as catalyst gives high product selectivity and the only by-products of the reaction are NH_3 and H_2O_2 . However, the hydrogen peroxide produced in the reaction mixture damages the riboflavin itself and causes a quick decomposition and loss of reactivity.

To bypass this issue, the group of Wolf designed a tandem system where a second catalyst (**b** in Fig. 1.26) was implemented to catalyze H_2O_2 disproportionation and oxygenation of substrate simultaneously[189]. The choice of Fe complex was based on previous literature reporting its activity in H_2O_2 disproportionation[190][191]. With this approach, they demonstrated that it is possible to increase both the lifetime of the riboflavin and the yield of oxidized substrate .

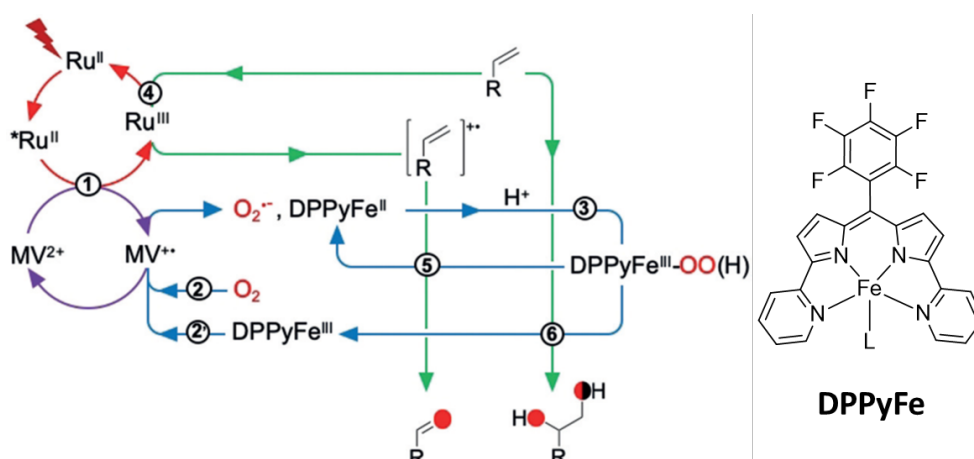


Figure 1.27: Proposed mechanism for O_2 activation by light in presence of a semi-heme iron catalyst. Image adapted from [192]

In 2019 our group reported another way to approach photocatalytic activa-

tion of O₂[192]. In this case, a "classic" photoredox module was employed, however the mechanism is more complex than the previous system of H₂O oxidation (Fig. 1.27). In this case the catalyst consisted in a semi-heme Fe catalyst shown in Fig. 1.27. To avoid the use of sacrificial electron donors for the activation of O₂, the strategy relied on the use of the reversible electron mediator methylviologen (MV²⁺), which can rapidly quench the excited state of Ru(II)* (from the previously seen [Ru(bpy)₃]²⁺) generating its reduced form MV^{•+} (step 1) that transfers one electron to O₂, generating O₂^{•-} (step 2). The superoxide formed in solution can quickly react with the Fe(II) catalyst to generate the Fe(III)OOH oxidizing species (step 3) that can oxidize the styrene sulfonate substrate to diol or aldehyde (steps 5 and 6). The outgoing Fe(III) state of the catalyst can then be reset to Fe(II) thanks to the methyl viologen electron relay (step 2'). Interestingly, the generated Ru(III) can oxidize the substrate (S) to the radical cation (S^{•+}; step 4) favouring the formation of the aldehyde after oxygen atom transfer (step 5). This also allows the resetting of the photosensitizer to its Ru(II) ground state. In a following article, [193] spectroscopic studies on the intermediates formed on the same iron catalyst (MS, EPR, Mössbauer, UV-vis, FTIR) revealed an unexpected active species holding an oxygen atom in between the Fe metal center and the N of the pyridine ligand. Other active intermediates could not be observed in the study.

Overall, these examples display the different approaches for oxygen activation, and even if not exhaustive, they give a view of the complexity of these systems.

1.6 . Goal of the thesis

The aim of this thesis is to investigate different light-induced reactions. Different metal complexes have been used to catalyse substrate conversion. The generation of reactive intermediates by means of light and understanding of their interaction with the substrate is a central focus of this project.

At a fundamental level, insights on the electron pathways during catalytic reactions can provide useful information that can help designing high-performance catalysts, able to tackle the bigger challenges of high-rate and stability in substrate conversion.

In the first part of this manuscript the photocatalytic conversion of CO₂ catalysed by iron porphyrins in homogeneous conditions will be studied (Chapter 2). First, we will focus on the second coordination sphere effect on the photocatalytic performances. Then, the photocatalytic mechanism will be investigated. In Chapter 3, the findings coming from studies in solution are translated to the assembly of a photocathode, with the final goal of increasing the stability and performing CO₂ reduction in aqueous medium at a small applied bias. The results of this section are still preliminary and part of the focus will be on the optimization of the photocathode assembly. The final goal is to generate a photoelectrode modified with the same molecular catalyst, holding second-coordination sphere motives.

Chapter 4 comprises the discussion on the activation of molecular dioxygen for Oxygen Atom Transfers (OAT) reactions by means of light. Once again, the focus will be on the activation through a molecular catalyst, this time a non-heme iron complex. The main focus of this study will be the trapping of reactive intermediates in aqueous solution. In combination with a thorough photophysical study, these findings will help consolidate the proposed mechanism.

Bibliography

- (1) Armaroli, N.; Balzani, V., *Energy for a Sustainable World*, 2010.
- (2) Armaroli, N.; Balzani, V.; Serpone, N., *Powering Planet Earth - Energy Solutions for the Future*; Wiley: 2013.
- (3) Becquerel, H. On Electrode Effect under the Influence of Solar Radiation. *Comptes Rendus de l'Académie Sciences Paris* **1839**, *9*, 561.
- (4) Fritts, C. E. On a new form of selenium photocell. *American Journal of Science* **1883**, *26*, 465.
- (5) Ciamician, G. The Photochemistry of the Future. *Science* **1912**, *36*, 385–394.
- (6) Albini, A.; Fagnoni, M. 1908: Giacomo Ciamician and the Concept of Green Chemistry. *ChemSusChem* **2008**, *1*, 63–66.
- (7) Ciamician, G. Sur les actions chimiques de la lumière. *Bulletin de la Société Chimique de France* **1908**, *IV*, i–xxvii.
- (8) Balzani, V. Photochemistry and Photophysics. **2014**.
- (9) Ritchie, H.; Roser, M.; Rosado, P. *Energy Mix*, 2022.
- (10) Missemmer, A. Un imaginaire fossilisé ? Les représentations économiques de l'énergie au défi de la transition bas-carbone. *Cahiers François Viète* **2022**, *73*–94.
- (11) In *Molecular Mechanisms of Photosynthesis*, Blankenship, R. E., Ed.; Blackwell Science Ltd: Oxford, UK, 2002, pp 26–41.
- (12) Gust, D. In *Advances in Botanical Research*; Elsevier: 2016; Vol. 79, pp 1–42.
- (13) In *Molecular Mechanisms of Photosynthesis*, Blankenship, R. E., Ed.; Blackwell Science Ltd: Oxford, UK, 2002, pp 1–10.
- (14) Emerson, R.; Arnold, W. The photochemical reaction in photosynthesis. *Journal of General Physiology* **1932**, *16*, 191–205.
- (15) In *Molecular Mechanisms of Photosynthesis*, Blankenship, R. E., Ed.; Blackwell Science Ltd: Oxford, UK, 2002, pp 61–94.
- (16) Forster, T. Delocalized excitation and excitation transfer. *Modern Quantum Chemistry Istanbul Lectures* **1965**, *3*, 93–137.
- (17) Van Amerongen, H.; van Grondelle, R.; Valkunas, L., *Photosynthetic Excitons*; World Scientific: London, 2000.
- (18) Pearlstein, R. M. Coupling of exciton motion in the core antenna and primary charge separation in the reaction center. *Photosynthesis Research* **1996**, *48*, 75–82.
- (19) Grondelle, R. v.; Dekker, J. P.; Gillbro, T.; Sundstrom, V. Energy transfer and trapping in photosynthesis. *Biochimica et Biophysica Acta (BBA) - Bioenergetics* **1994**, *1187*, 1–65.
- (20) Schatz, G. H.; Brock, H.; Holzwarth, A. R. Kinetic and Energetic Model for the Primary Processes in Photosystem II. *Biophysics Journal* **1988**, *54*, 397–405.
- (21) Lunde, C.; Jensen, P.; Haldrup, P.; Knoetzel, A.; Scheller, H. The PSI-H subunit of photosystem I is essential for state transitions in plant photosynthesis. *Nature* **2000**, *408*, 613–615.
- (22) In *Molecular Mechanisms of Photosynthesis*, Blankenship, R. E., Ed., 3rd; Blackwell Science Ltd: Oxford, UK, 2021, pp 91–116.
- (23) Clayton, R. Memories of Many Lives. *Photosynthesis Research* **1988**, *19*, 207–224.
- (24) In *Molecular Mechanisms of Photosynthesis*, Blankenship, R. E., Ed., 3rd; Blackwell Science Ltd: Oxford, UK, 2021, pp 117–144.

- (25) Allen, J.; Forsberg, J. Molecular Recognition in Thylakoid Structure and Function. *Trends in Plant Science* **2001**, *6*, 317–326.
- (26) Anderson, J. Changing Concepts About the Distribution of Photosystems I and II between Grana-appressed and Stroma Exposed Thylakoid Membranes. *Photosynthesis Research*, *73*, 157–164.
- (27) Nevo, R.; Charuvi, D.; Tsabari, O.; Reich, Z. Composition, architecture and dynamics of the photosynthetic apparatus in higher plants. *The Plant Journal* **2012**, *70*, 157–176.
- (28) Nagy, G.; Unnep, R.; Zsiros, O.; Tokutsu, R.; Takizawa, K.; Porcar, L.; Moyetg, L.; Petroutsos, D.; Garab, G.; Finazzi, G.; Minagawa, J. Chloroplasts Remodeling During State Transition in *Chlamydomonas reinhardtii* as Revealed by Noninvasive Techniques in vivo. *Proceedings of the National Academy of Sciences* **2014**, *111*, 5042–5047.
- (29) Kirchhoff, H.; Li, M.; Puthiyaveetil, S. Sublocalization of Cytochrome b6f Complexes in Photosynthetic Membranes. *Trends in Plant Science* **2017**, *22*, Publisher: Elsevier, 574–582.
- (30) Höhner, R.; Pribil, M.; Herbstová, M.; Lopez, L. S.; Kunz, H.-H.; Li, M.; Wood, M.; Svoboda, V.; Puthiyaveetil, S.; Leister, D.; Kirchhoff, H. Plastocyanin is the long-range electron carrier between photosystem II and photosystem I in plants. *Proceedings of the National Academy of Sciences* **2020**, *117*, 15354–15362.
- (31) Rhee, K.-H.; Morris, E. P.; Barber, J.; Kühlbrandt, W. Three-dimensional structure of the plant photosystem II reaction centre at 8Å resolution. *Nature* **1998**, *396*, 283–286.
- (32) Kouřil, R.; Dekker, J. P.; Boekema, E. J. Supramolecular organization of photosystem II in green plants. *Biochimica et Biophysica Acta (BBA) - Bioenergetics* **2012**, *1817*, 2–12.
- (33) Van Bezouwen, L. S.; Caffarri, S.; Kale, R. S.; Kouřil, R.; Thunnissen, A.-M. W. H.; Oostergetel, G. T.; Boekema, E. J. Subunit and chlorophyll organization of the plant photosystem II supercomplex. *Nature Plants* **2017**, *3*, 17080.
- (34) Sheng, X.; Watanabe, A.; Li, A.; Kim, E.; Song, C.; Murata, K.; Song, D.; Minagawa, J.; Liu, Z. Structural insight into light harvesting for photosystem II in green algae. *Nature Plants* **2019**, *5*, 1320–1330.
- (35) Anderson, J. M.; Park, Y.-I.; Chow, W. S. Unifying model for the photoinactivation of Photosystem II in vivo under steady-state photosynthesis. *Photosynthesis Research* **1998**, *56*, 1–13.
- (36) Kok, B.; Forbush, B.; McGloin, M. Cooperation of charges in photosynthetic O₂ evolution—I. A linear four step mechanism. *Photochemistry and Photobiology* **1970**, *11*, 457–475.
- (37) McEvoy, J. P.; Brudvig, G. W. Water-Splitting Chemistry of Photosystem II. *Chemical Reviews* **2006**, *106*, 4455–4483.
- (38) Yano, J.; Kern, J.; Sauer, K.; Latimer, M. J.; Pushkar, Y.; Biesiadka, J.; Loll, B.; Saenger, W.; Messinger, J.; Zouni, A.; Yachandra, V. K. Where Water Is Oxidized to Dioxygen: Structure of the Photosynthetic Mn₄Ca Cluster. *Science* **2006**, *314*, 821–825.
- (39) Debus, R. J. The manganese and calcium ions of photosynthetic oxygen evolution. *Biochimica et Biophysica Acta (BBA)/Protein Structure and Molecular Enzymology* **1992**, *1102*, Publisher: Elsevier Science, 269–352.
- (40) Kupitz, C. et al. Serial time-resolved crystallography of photosystem II using a femtosecond X-ray laser. *Nature* **2014**, *513*, 261–265.
- (41) Kern, J. et al. Structures of the intermediates of Kok's photosynthetic water oxidation clock. *Nature* **2018**, *563*, 421–425.
- (42) Suga, M. et al. An oxyl/oxo mechanism for oxygen-oxygen coupling in PSII revealed by an x-ray free-electron laser. *Science* **2019**, *366*, 334–338.
- (43) Ibrahim, M. et al. Untangling the sequence of events during the S₂ → S₃ transition in photosystem II and implications for the water oxidation mechanism. *Proceedings of the National Academy of Sciences* **2020**, *117*, 12624–12635.
- (44) Cox, N.; Pantazis, D. A.; Lubitz, W. Current Understanding of the Mechanism of Water Oxidation in Photosystem II and Its Relation to XFEL Data. *Annual Review of Biochemistry* **2020**, *89*, 795–820.

- (45) Golbeck, J. H. A comparative analysis of the spin state distribution of in vitro and in vivo mutants of Psac. A biochemical argument for the sequence of electron transfer in Photosystem I as $F_X \rightarrow F_A \rightarrow F_B \rightarrow$ ferredoxin/flavodoxin. *Photosynthesis Research* **1999**, *61*, 107–144.
- (46) In *Molecular Mechanisms of Photosynthesis*, Blankenship, R. E., Ed., 3rd; Blackwell Science Ltd: Oxford, UK, 2021, pp 159–190.
- (47) Calvin, M. Forty years of photosynthesis and related activities. *Photosynthesis Research* **1989**, *21*, 3–16.
- (48) Benson, A. A. Following the path of carbon in photosynthesis: a personal story. *Photosynthesis research* **2002**, *73*, Place: Netherlands, 29–49.
- (49) Balzani, V.; Credi, A.; Venturi, M. Photochemical Conversion of Solar Energy. *ChemSusChem* **2008**, *1*, 26–58.
- (50) Barber, J.; Tran, P. D. From natural to artificial photosynthesis. *Journal of The Royal Society Interface* **2013**, *10*, 20120984.
- (51) Wang, Y.; Liu, J.; Wang, Y.; Al-Enizi, A. M.; Zheng, G. Tuning of CO₂ Reduction Selectivity on Metal Electrocatalysts. *Small* **2017**, *13*, 1701809.
- (52) Yamazaki, H.; Shouji, A.; Kajita, M.; Yagi, M. Electrocatalytic and photocatalytic water oxidation to dioxygen based on metal complexes. *Coordination Chemistry Reviews* **2010**, *254*, 2483–2491.
- (53) Boutin, E.; Merakeb, L.; Ma, B.; Boudy, B.; Wang, M.; Bonin, J.; Anxolabéhère-Mallart, E.; Robert, M. Molecular catalysis of CO₂ reduction: recent advances and perspectives in electrochemical and light-driven processes with selected Fe, Ni and Co aza macrocyclic and polypyridine complexes. *Chemical Society Reviews* **2020**, *49*, 5772–5809.
- (54) Melchionna, M.; Fornasiero, P. Updates on the Roadmap for Photocatalysis. *ACS Catalysis* **2020**, *10*, 5493–5501.
- (55) Heidary, N.; Harris, T. G.; Ly, K. H.; Kornienko, N. Artificial photosynthesis with metal and covalent organic frameworks (MOFs and COFs): challenges and prospects in fuel-forming electrocatalysis. *Physiologia Plantarum* **2019**, *166*, 460–471.
- (56) Nocera, D. G. The Artificial Leaf. *Accounts of Chemical Research* **2012**, *45*, 767–776.
- (57) Milgrom, L. R. Synthesis of some new tetra-arylporphyrins for studies in solar energy conversion. *Journal of the Chemical Society, Perkin Transactions 1* **1983**, 2535.
- (58) Cho, H. S.; Rhee, H.; Song, J. K.; Min, C.-K.; Takase, M.; Aratani, N.; Cho, S.; Osuka, A.; Joo, T.; Kim, D. Excitation Energy Transport Processes of Porphyrin Monomer, Dimer, Cyclic Trimer, and Hexamer Probed by Ultrafast Fluorescence Anisotropy Decay. *Journal of the American Chemical Society* **2003**, *125*, 5849–5860.
- (59) Jiang, D.-L.; Aida, T. Morphology-Dependent Photochemical Events in Aryl Ether Dendrimer Porphyrins: Cooperation of Dendron Subunits for Singlet Energy Transduction. *Journal of the American Chemical Society* **1998**, *120*, 10895–10901.
- (60) Campagna, S.; Denti, G.; Serroni, S.; Juris, A.; Venturi, M.; Ricevuto, V.; Balzani, V. Dendrimers of Nanometer Size Based on Metal Complexes: Luminescent and Redox-Active Polynuclear Metal Complexes Containing up to Twenty-Two Metal Centers. *Chemistry - A European Journal* **1995**, *1*, 211–221.
- (61) Hahn, U.; Gorka, M.; Vögtle, F.; Vicinelli, V.; Ceroni, P.; Maestri, M.; Balzani, V. Light-Harvesting Dendrimers: Efficient Intra- and Intermolecular Energy-Transfer Processes in a Species Containing 65 Chromophoric Groups of Four Different Types. *Angewandte Chemie International Edition* **2002**, *41*, 3595–3598.
- (62) Kawasaki, R.; Antoku, D.; Ohdake, R.; Sugikawa, K.; Ikeda, A. Bacterial elimination via the photodynamic activity of a fullerene/light-harvesting antenna molecule assembled system integrated into liposome membranes. *Nanoscale Advances* **2020**, *2*, 4395–4399.

- (63) Antoku, D.; Satake, S.; Mae, T.; Sugikawa, K.; Funabashi, H.; Kuroda, A.; Ikeda, A. Improvement of Photodynamic Activity of Lipid-Membrane-Incorporated Fullerene Derivative by Combination with a Photo-Antenna Molecule. *Chemistry – A European Journal* **2018**, *24*, 7335–7339.
- (64) Tabushi, I.; Koga, N.; Yanagita, M. Efficient intramolecular quenching and electron transfer in tetraphenylporphyrin attached with benzoquinone or hydroquinone as a photosystem model. *Tetrahedron Letters* **1979**, *20*, 257–260.
- (65) Kuciauskas, D.; Liddell, P. A.; Hung, S.-C.; Lin, S.; Stone, S.; Seely, G. R.; Moore, A. L.; Moore, T. A.; Gust, D. Structural Effects on Photoinduced Electron Transfer in CarotenoidPorphyrinQuinone Triads. *The Journal of Physical Chemistry B* **1997**, *101*, Publisher: American Chemical Society, 429–440.
- (66) Marcus, R. A.; Sutin, N. Electron transfers in chemistry and biology. *Biochimica et Biophysica Acta (BBA) - Reviews on Bioenergetics* **1985**, *811*, 265–322.
- (67) Liddell, P. A.; Sumida, J. P.; Macpherson, A. N.; Noss, L.; Seely, G. R.; Clark, K. N.; Moore, A. L.; Moore, T. A.; Gust, D. Preparation and photophysical studies of porphyrin-C₆₀ dyads. *Photochemistry and Photobiology* **1994**, *60*, 537–541.
- (68) Sullivan, B. P.; Abruna, H.; Nagle, J. K.; Meyer, J.; Sprintschnik, H. Multiple emissions from charge transfer excited states of ruthenium(II)- polypyridine complexes. *CHEMICAL PHYSICS LETTERS* **1978**, *58*.
- (69) Gust, D.; Mathis, P.; Moore, A. L.; Liddell, P. A.; Nemeth, G.; Lehman, W.; Chachaty, C. Energy transfer and charge separation in carotenoporphyrins. Photochemistry and Photobiology. *Photochemistry and Photobiology* **1983**, *37S*, S46.
- (70) Moore, T. A.; Gust, D.; Mathis, P.; Mialocq, J.-C.; Chachaty, C.; Bensasson, R. V.; Land, E. J.; Doizi, D.; Liddell, P. A.; Lehman, W. R.; Nemeth, G. A.; Moore, A. L. Photodriven charge separation in a carotenoporphyrin-quinone triad. *Nature* **1984**, *307*, 630–632.
- (71) Flamigni, L.; Baranoff, E.; Collin, J.-P.; Sauvage, J.-P. A Triad Based on an Iridium(III) Bisterpyridine Complex Leading to a Charge-Separated State with a 120- μ s Lifetime at Room Temperature. *Chemistry – A European Journal* **2006**, *12*, 6592–6606.
- (72) Maxwell, K. A.; Sykora, M.; DeSimone, J. M.; Meyer, T. J. One-Pot Synthesis and Characterization of a ChromophoreDonorAcceptor Assembly. *Inorganic Chemistry* **2000**, *39*, 71–75.
- (73) Imahori, H.; Guldi, D. M.; Tamaki, K.; Yoshida, Y.; Luo, C.; Sakata, Y.; Fukuzumi, S. Charge Separation in a Novel Artificial Photosynthetic Reaction Center Lives 380 ms. *Journal of the American Chemical Society* **2001**, *123*, 6617–6628.
- (74) Nakano, A.; Osuka, A.; Yamazaki, T.; Nishimura, Y.; Akimoto, S.; Yamazaki, I.; Itaya, A.; Murakami, M.; Miyasaka, H. Modified Windmill Porphyrin Arrays: Coupled Light-Harvesting and Charge Separation, Conformational Relaxation in the S₁ State, and S₂-S₂ Energy Transfer. *Chemistry - A European Journal* **2001**, *7*.
- (75) Kodis, G.; Terazono, Y.; Liddell, P. A.; Andréasson, J.; Garg, V.; Hambourger, M.; Moore, T. A.; Moore, A. L.; Gust, D. Energy and Photoinduced Electron Transfer in a Wheel-Shaped Artificial Photosynthetic Antenna-Reaction Center Complex. *Journal of the American Chemical Society* **2006**, *128*, 1818–1827.
- (76) Jones, W. E.; Baxter, S. M.; Strouse, G. F.; Meyer, T. J. Intrastrand electron and energy transfer between polypyridyl complexes on a soluble polymer. *Journal of the American Chemical Society* **1993**, *115*, 7363–7373.
- (77) Dupray, L. M.; Devenney, M.; Striplin, D. R.; Meyer, T. J. An Antenna Polymer for Visible Energy Transfer. *Journal of the American Chemical Society* **1997**, *119*, 10243–10244.
- (78) Sykora, M.; Maxwell, K. A.; DeSimone, J. M.; Meyer, T. J. Mimicking the antenna-electron transfer properties of photosynthesis. *Proceedings of the National Academy of Sciences* **2000**, *97*, 7687–7691.

-
- (79) Herrero, C.; Lassallekaiser, B.; Leibl, W.; Rutherford, A.; Aukauloo, A. Artificial systems related to light driven electron transfer processes in PSII. *Coordination Chemistry Reviews* **2008**, *252*, 456–468.
- (80) Gust, D.; Moore, T. A.; Moore, A. L. Solar Fuels via Artificial Photosynthesis. *Accounts of Chemical Research* **2009**, *42*, 1890–1898.
- (81) In *Molecular Mechanisms of Photosynthesis*, Blankenship, R. E., Ed.; Blackwell Science Ltd: Oxford, UK, 2002, pp 95–123.
- (82) Maliyackel, A. C.; Otvos, J. W.; Spreer, L. O.; Calvin, M. Photoinduced oxidation of a water-soluble manganese(III) porphyrin. *Proceedings of the National Academy of Sciences* **1986**, *83*, 3572–3574.
- (83) Huang, P.; Magnuson, A.; Lomoth, R.; Abrahamsson, M.; Tamm, M.; Sun, L.; van Rotterdam, B.; Park, J.; Hammarström, L.; Åkermark, B.; Styring, S. Photo-induced oxidation of a dinuclear $\text{Mn}_2^{II,II}$ complex to the $\text{Mn}_2^{III,IV}$ state by inter- and intramolecular electron transfer to Ru^{III} tris-bipyridine. *Journal of Inorganic Biochemistry* **2002**, *91*, 159–172.
- (84) Limburg, J.; Vrettos, J. S.; Liable-Sands, L. M.; Rheingold, A. L.; Crabtree, R. H.; Brudvig, G. W. A Functional Model for O-O Bond Formation by the O_2 -Evolving Complex in Photosystem II. *Science* **1999**, *283*, 1524–1527.
- (85) Gotico, P.; Tran, T.-T.; Baron, A.; Vauzeilles, B.; Lefumeux, C.; Ha-Thi, M.-H.; Pino, T.; Halime, Z.; Quaranta, A.; Leibl, W.; Aukauloo, A. Tracking Charge Accumulation in a Functional Triazole-Linked Ruthenium-Rhenium Dyad Towards Photocatalytic Carbon Dioxide Reduction. *ChemPhotoChem* **2021**, *5*, 654–664.
- (86) Schulz, M.; Hagemeyer, N.; Wehmeyer, F.; Lowe, G.; Rosenkranz, M.; Seidler, B.; Popov, A.; Streb, C.; Vos, J. G.; Dietzek, B. Photoinduced Charge Accumulation and Prolonged Multielectron Storage for the Separation of Light and Dark Reaction. *Journal of the American Chemical Society* **2020**, *142*, 15722–15728.
- (87) Gotico, P.; Del Vecchio, A.; Audisio, D.; Quaranta, A.; Halime, Z.; Leibl, W.; Aukauloo, A. Visible-Light-Driven Reduction of CO_2 to CO and Its Subsequent Valorization in Carbonylation Chemistry and ^{13}C Isotope Labeling. *ChemPhotoChem* **2018**, *2*, 715–719.
- (88) Ru Ng, A. Y.; Boruah, B.; Chin, K. F.; Modak, J. M.; Soo, H. S. Photoelectrochemical Cells for Artificial Photosynthesis: Alternatives to Water Oxidation. *ChemNanoMat* **2020**, *6*, 185–203.
- (89) Creissen, C. E.; Fontecave, M. Solar-Driven Electrochemical CO_2 Reduction with Heterogeneous Catalysts. *Advanced Energy Materials* **2021**, *11*, 2002652.
- (90) Garcia Osorio, D. A.; Neri, G.; Cowan, A. J. Hybrid Photocathodes for Carbon Dioxide Reduction: Interfaces for Charge Separation and Selective Catalysis. *ChemPhotoChem* **2021**, *5*, 595–610.
- (91) Pellegrin, Y.; Odobel, F. Molecular devices featuring sequential photoinduced charge separations for the storage of multiple redox equivalents. *Coordination Chemistry Reviews* **2011**, *255*, 2578–2593.
- (92) Gaffney, O.; Rockstrom; Thunberg, G., *Breaking Boundaries: The Science of Our Planet*; Penguin Random House LLC.: New York, 2021.
- (93) Moser, S. C. Communicating climate change: history, challenges, process and future directions. *WIREs Climate Change* **2010**, *1*, 31–53.
- (94) IPCC, S. Summary for Policymakers of IPCC Special Report on Global Warming of 1.5°C approved by governments, English, 2018.
- (95) Watson, R. T. et al. Greenhouse Gases and Aerosols. *First Assessment Report* **1990**, *Ch. 1*, 40.
- (96) US Department of Commerce, N. ESRL Global Monitoring Division - Global Greenhouse Gas Reference Network, EN-US, Library Catalog: www.esrl.noaa.gov.
- (97) Bralower, T.; Bice, D. Carbon Dioxide Through Time.
- (98) Hausfather, Z. Explainer: How the rise and fall of CO_2 levels influenced the ice ages, 2020.

- (99) Stips, A.; Macias, D.; Coughlan, C.; Garcia-Gorrioz, E.; Liang, X. S. On the causal structure between CO₂ and global temperature. *Scientific Reports* **2016**, *6*, 21691.
- (100) Nations, U. Paris Agreement, 2015.
- (101) IEA Carbon capture, utilisation and storage, 2022.
- (102) Bonin, J.; Chaussemier, M.; Robert, M.; Routier, M. Homogeneous Photocatalytic Reduction of CO₂ to CO Using Iron(0) Porphyrin Catalysts: Mechanism and Intrinsic Limitations. *ChemCatChem* **2014**, *6*, 3200–3207.
- (103) Shi, Y.; Zhang, F.; Linhardt, R. J. Porphyrin-based compounds and their applications in materials and medicine. *Dyes and Pigments* **2021**, *188*, 109136.
- (104) Takahashi, K.; Hiratsuka, K.; Sasaki, H.; Toshima, S. Electrocatalytic behavior of metal porphyrins in the reduction of carbon dioxide. *Chemistry Letters* **1979**, *8*, 305–308.
- (105) Costentin, C.; Savéant, J.-M. Towards an intelligent design of molecular electrocatalysts. *Nature Reviews Chemistry* **2017**, *1*, 0087.
- (106) Gotico, P.; Halime, Z.; Aukauloo, A. Recent advances in metalloporphyrin-based catalyst design towards carbon dioxide reduction: from bio-inspired second coordination sphere modifications to hierarchical architectures. *Dalton Transactions* **2020**, *49*, 2381–2396.
- (107) Costentin, C.; Drouet, S.; Robert, M.; Savéant, J.-M. Turnover Numbers, Turnover Frequencies, and Overpotential in Molecular Catalysis of Electrochemical Reactions. Cyclic Voltammetry and Preparative-Scale Electrolysis. *Journal of the American Chemical Society* **2012**, *134*, 11235–11242.
- (108) Römel, C.; Song, J.; Tarrago, M.; Rees, J. A.; van Gastel, M.; Weyhermüller, T.; DeBeer, S.; Bill, E.; Neese, F.; Ye, S. Electronic Structure of a Formal Iron(0) Porphyrin Complex Relevant to CO₂ Reduction. *Inorganic Chemistry* **2017**, *56*, 4745–4750.
- (109) Römel, C.; Ye, S.; Bill, E.; Weyhermüller, T.; van Gastel, M.; Neese, F. Electronic Structure and Spin Multiplicity of Iron Tetraphenylporphyrins in Their Reduced States as Determined by a Combination of Resonance Raman Spectroscopy and Quantum Chemistry. *Inorganic Chemistry* **2018**, *57*, 2141–2148.
- (110) Göttle, A. J.; Koper, M. T. M. Determinant Role of Electrogenenerated Reactive Nucleophilic Species on Selectivity during Reduction of CO₂ Catalyzed by Metalloporphyrins. *Journal of the American Chemical Society* **2018**, *140*, 4826–4834.
- (111) Mashiko, T.; Reed, C. A.; Haller, K. J.; Scheidt, W. R. Nature of iron(I) and iron(0) tetraphenylporphyrin complexes. Synthesis and molecular structure of (dibenzo-18-crown-6) bis(tetrahydrofuran) sodium (meso-tetraphenylporphyrinato) ferrate and bis[tris(tetrahydrofuran) sodium] (meso-tetraphenylporphyrinato) ferrate. *Inorganic Chemistry* **1984**, *23*, 3192–3196.
- (112) Davethu, P. A.; de Visser, S. P. CO₂ Reduction on an Iron-Porphyrin Center: A Computational Study. *The Journal of Physical Chemistry A* **2019**, *123*, 6527–6535.
- (113) Kosugi, K.; Kondo, M.; Masaoka, S. Quick and Easy Method to Dramatically Improve the Electrochemical CO₂ Reduction Activity of an Iron Porphyrin Complex. *Angewandte Chemie International Edition* **2021**, *60*, 22070–22074.
- (114) Amanullah, S.; Saha, P.; Dey, A. Activating the Fe(I) State of Iron Porphyrinoid with Second-Sphere Proton Transfer Residues for Selective Reduction of CO₂ to HCOOH via Fe(III/II)–COOH Intermediate(s). *Journal of the American Chemical Society* **2021**, *143*, 13579–13592.
- (115) Azcarate, I.; Costentin, C.; Robert, M.; Savéant, J.-M. Dissection of Electronic Substituent Effects in Multielectron–Multistep Molecular Catalysis. Electrochemical CO₂-to-CO Conversion Catalyzed by Iron Porphyrins. *The Journal of Physical Chemistry C* **2016**, *120*, 28951–28960.
- (116) Azcarate, I.; Costentin, C.; Robert, M.; Savéant, J.-M. Through-Space Charge Interaction Substituent Effects in Molecular Catalysis Leading to the Design of the Most Efficient Catalyst of CO₂-to-CO Electrochemical Conversion. *Journal of the American Chemical Society* **2016**, *138*, 16639–16644.

- (117) Gotico, P.; Boitrel, B.; Guillot, R.; Sircoglou, M.; Quaranta, A.; Halime, Z.; Leibl, W.; Aukauloo, A. Second-Sphere Biomimetic Multipoint Hydrogen-Bonding Patterns to Boost CO₂ Reduction of Iron Porphyrins. *Angewandte Chemie International Edition* **2019**, *58*, 4504–4509.
- (118) Khadhraoui, A.; Gotico, P.; Boitrel, B.; Leibl, W.; Halime, Z.; Aukauloo, A. Local ionic liquid environment at a modified iron porphyrin catalyst enhances the electrocatalytic performance of CO₂ to CO reduction in water. *Chemical Communications* **2018**, *54*, 11630–11633.
- (119) Costentin, C.; Drouet, S.; Robert, M.; Savéant, J.-M. A Local Proton Source Enhances CO₂ Electroreduction to CO by a Molecular Fe Catalyst. *Science* **2012**, *338*, 90–94.
- (120) Margarit, C. G.; Schnedermann, C.; Asimow, N. G.; Nocera, D. G. Carbon Dioxide Reduction by Iron Hangman Porphyrins. *Organometallics* **2019**, *38*, 1219–1223.
- (121) Dogutan, D. K.; Bediako, D. K.; Teets, T. S.; Schwalbe, M.; Nocera, D. G. Efficient Synthesis of Hangman Porphyrins. *Organic Letters* **2010**, *12*, 1036–1039.
- (122) Samanta, S.; Sengupta, K.; Mitra, K.; Bandyopadhyay, S.; Dey, A. Selective four electron reduction of O₂ by an iron porphyrin electrocatalyst under fast and slow electron fluxes. *Chemical Communications* **2012**, *48*, 7631.
- (123) Mondal, B.; Rana, A.; Sen, P.; Dey, A. Intermediates Involved in the 2e⁻/2H⁺ Reduction of CO₂ to CO by Iron(0) Porphyrin. *Journal of the American Chemical Society* **2015**, *137*, 11214–11217.
- (124) Appel, A. M. et al. Frontiers, Opportunities, and Challenges in Biochemical and Chemical Catalysis of CO₂ Fixation. *Chemical Reviews* **2013**, *113*, 6621–6658.
- (125) Can, M.; Armstrong, F. A.; Ragsdale, S. W. Structure, Function, and Mechanism of the Nickel Metalloenzymes, CO Dehydrogenase, and Acetyl-CoA Synthase. *Chemical Reviews* **2014**, *114*, 4149–4174.
- (126) Khadhraoui, A.; Gotico, P.; Leibl, W.; Halime, Z.; Aukauloo, A. Through-Space Electrostatic Interactions Surpass Classical Through-Bond Electronic Effects in Enhancing CO₂ Reduction Performance of Iron Porphyrins. *ChemSusChem* **2021**, *14*, 1308–1315.
- (127) Mohamed, E. A.; Zahran, Z. N.; Naruta, Y. Efficient electrocatalytic CO₂ reduction with a molecular cofacial iron porphyrin dimer. *Chemical Communications* **2015**, *51*, 16900–16903.
- (128) Zahran, Z. N.; Mohamed, E. A.; Naruta, Y. Bio-inspired cofacial Fe porphyrin dimers for efficient electrocatalytic CO₂ to CO conversion: Overpotential tuning by substituents at the porphyrin rings. *Scientific Reports* **2016**, *6*, 24533.
- (129) Zhang, C.; Gotico, P.; Guillot, R.; Dragoe, D.; Leibl, W.; Halime, Z.; Aukauloo, A. Bio-Inspired Bimetallic Cooperativity Through a Hydrogen Bonding Spacer in CO₂ Reduction. *Angewandte Chemie* **2023**, *135*, DOI: [10.1002/ange.202214665](https://doi.org/10.1002/ange.202214665).
- (130) Rehm, D.; Weller, A. Kinetics of Fluorescence Quenching by Electron and H-Atom Transfer. *Israel Journal of Chemistry* **1970**, *8*, 259–271.
- (131) Mochizuki, K.; Manaka, S.; Takeda, I.; Kondo, T. Synthesis and Structure of [6,6'-Bi(5,7-dimethyl-1,4,8,11-tetraazacyclotetradecane)]dinickel(II) Triflate and Its Catalytic Activity for Photochemical CO₂ Reduction. *Inorganic Chemistry* **1996**, *35*, 5132–5136.
- (132) Tinnemans, A. H. A.; Koster, T. P. M.; Thewissen, D. H. M. W.; Mackor, A. Tetraaza-macrocyclic cobalt(II) and nickel(II) complexes as electron-transfer agents in the photo(electro)chemical and electrochemical reduction of carbon dioxide. *Recueil des Travaux Chimiques des Pays-Bas* **1984**, *103*, 288–295.
- (133) Rao, H.; Bonin, J.; Robert, M. Non-sensitized selective photochemical reduction of CO₂ to CO under visible light with an iron molecular catalyst. *Chemical Communications* **2017**, *53*, 2830–2833.
- (134) Mulazzani, Q. G.; Emmi, S.; Fuochi, P. G.; Hoffman, M. Z.; Venturi, M. On the nature of tris(2,2'-bipyridine)ruthenium(1+) ion in aqueous solution. *Journal of the American Chemical Society* **1978**, *100*, 981–983.

- (135) Rao, H.; Bonin, J.; Robert, M. Visible-light Homogeneous Photocatalytic Conversion of CO₂ into CO in Aqueous Solutions with an Iron Catalyst. *ChemSusChem* **2017**, *10*, 4447–4450.
- (136) Rao, H.; Schmidt, L. C.; Bonin, J.; Robert, M. Visible-light-driven methane formation from CO₂ with a molecular iron catalyst. *Nature* **2017**, *548*, 74–77.
- (137) Rao, H.; Bonin, J.; Robert, M. Toward Visible-Light Photochemical CO₂-to-CH₄ Conversion in Aqueous Solutions Using Sensitized Molecular Catalysis. *The Journal of Physical Chemistry C* **2018**, *122*, 13834–13839.
- (138) Rao, H.; Lim, C.-H.; Bonin, J.; Miyake, G. M.; Robert, M. Visible-Light-Driven Conversion of CO₂ to CH₄ with an Organic Sensitizer and an Iron Porphyrin Catalyst. *Journal of the American Chemical Society* **2018**, *140*, 17830–17834.
- (139) Guo, Z.; Cheng, S.; Cometto, C.; Anxolabéhère-Mallart, E.; Ng, S.-M.; Ko, C.-C.; Liu, G.; Chen, L.; Robert, M.; Lau, T.-C. Highly Efficient and Selective Photocatalytic CO₂ Reduction by Iron and Cobalt Quaterpyridine Complexes. *Journal of the American Chemical Society* **2016**, *138*, 9413–9416.
- (140) Qin, Y.; Chen, L.; Chen, G.; Guo, Z.; Wang, L.; Fan, H.; Robert, M.; Lau, T.-C. A highly active and robust iron quinquepyridine complex for photocatalytic CO₂ reduction in aqueous acetonitrile solution. *Chemical Communications* **2020**, *56*, 6249–6252.
- (141) Ouyang, T.; Huang, H.-H.; Wang, J.-W.; Zhong, D.-C.; Lu, T.-B. A Dinuclear Cobalt Cryptate as a Homogeneous Photocatalyst for Highly Selective and Efficient Visible-Light Driven CO₂ Reduction to CO in CH₃CN/H₂O Solution. *Angewandte Chemie International Edition* **2017**, *56*, 738–743.
- (142) Ouyang, T.; Wang, H.-J.; Huang, H.-H.; Wang, J.-W.; Guo, S.; Liu, W.-J.; Zhong, D.-C.; Lu, T.-B. Dinuclear Metal Synergistic Catalysis Boosts Photochemical CO₂-to-CO Conversion. *Angewandte Chemie International Edition* **2018**, *57*, 16480–16485.
- (143) Guo, Z.; Chen, G.; Cometto, C.; Ma, B.; Zhao, H.; Groizard, T.; Chen, L.; Fan, H.; Man, W.-L.; Yiu, S.-M.; Lau, K.-C.; Lau, T.-C.; Robert, M. Selectivity control of CO versus HCOO production in the visible-light-driven catalytic reduction of CO₂ with two cooperative metal sites. *Nature Catalysis* **2019**, *2*, 801–808.
- (144) Yuan, H.; Cheng, B.; Lei, J.; Jiang, L.; Han, Z. Promoting photocatalytic CO₂ reduction with a molecular copper purpurin chromophore. *Nature Communications* **2021**, *12*, 1835.
- (145) Nakada, A.; Koike, K.; Nakashima, T.; Morimoto, T.; Ishitani, O. Photocatalytic CO₂ Reduction to Formic Acid Using a Ru(II)–Re(I) Supramolecular Complex in an Aqueous Solution. *Inorganic Chemistry* **2015**, *54*, 1800–1807.
- (146) Saito, D.; Yamazaki, Y.; Tamaki, Y.; Ishitani, O. Photocatalysis of a Dinuclear Ru(II)–Re(I) Complex for CO₂ Reduction on a Solid Surface. *Journal of the American Chemical Society* **2020**, *142*, 19249–19258.
- (147) Kuramochi, Y.; Fujisawa, Y.; Satake, A. Photocatalytic CO₂ Reduction Mediated by Electron Transfer via the Excited Triplet State of Zn(II) Porphyrin. *Journal of the American Chemical Society* **2020**, *142*, 705–709.
- (148) Windle, C. D.; George, M. W.; Perutz, R. N.; Summers, P. A.; Sun, X. Z.; Whitwood, A. C. Comparison of rhenium–porphyrin dyads for CO₂ photoreduction: photocatalytic studies and charge separation dynamics studied by time-resolved IR spectroscopy. *Chemical Science* **2015**, *6*, 6847–6864.
- (149) Gouterman, M. Study of the Effects of Substitution on the Absorption Spectra of Porphin. *The Journal of Chemical Physics* **1959**, *30*, 1139–1161.
- (150) Trapali, A.; Gotico, P.; Herrero, C.; Ha-Thi, M.-H.; Pino, T.; Leibl, W.; Charalambidis, G.; Coutsolelos, A.; Halime, Z.; Aukauloo, A. Imbroglia at a photoredox-iron-porphyrin catalyst dyad for the photocatalytic CO₂ reduction. *Comptes Rendus. Chimie* **2021**, *24*, 101–114.

-
- (151) Zhu, X.-Q.; Zhang, M.-T.; Yu, A.; Wang, C.-H.; Cheng, J.-P. Hydride, Hydrogen Atom, Proton, and Electron Transfer Driving Forces of Various Five-Membered Heterocyclic Organic Hydrides and Their Reaction Intermediates in Acetonitrile. *Journal of the American Chemical Society* **2008**, *130*, 2501–2516.
- (152) Goldfine, H. The Evolution of Oxygen As a Biosynthetic Reagent. *Journal of General Physiology* **1965**, *49*, 253–268.
- (153) Babcock, G. T. How oxygen is activated and reduced in respiration. *Proceedings of the National Academy of Sciences* **1999**, *96*, 12971–12973.
- (154) *Applied Homogeneous Catalysis with Organometallic Compounds: A Comprehensive Handbook in Four Volumes*, 1st ed.; Cornils, B., Herrmann, W. A., Beller, M., Paciello, R., Eds.; Wiley: 2017.
- (155) *Handbook of Industrial Chemistry and Biotechnology*; Kent, J. A., Bommaraju, T. V., Barnicki, S. D., Eds.; Springer International Publishing: Cham, 2017.
- (156) In *Fundamentals of Industrial Catalytic Processes*; John Wiley & Sons, Inc.: Hoboken, NJ, USA, 2010, pp 560–634.
- (157) Schweitzer, C.; Schmidt, R. Physical Mechanisms of Generation and Deactivation of Singlet Oxygen. *Chemical Reviews* **2003**, *103*, 1685–1758.
- (158) Gamba, I.; Codolà, Z.; Lloret-Fillol, J.; Costas, M. Making and breaking of the O-O bond at iron complexes. *Coordination Chemistry Reviews* **2017**, *334*, 2–24.
- (159) Barry, S. M.; Challis, G. L. Mechanism and Catalytic Diversity of Rieske Non-Heme Iron-Dependent Oxygenases. *ACS Catalysis* **2013**, *3*, 2362–2370.
- (160) Denisov, I. G.; Makris, T. M.; Sligar, S. G.; Schlichting, I. Structure and Chemistry of Cytochrome P450. *Chemical Reviews* **2005**, *105*, 2253–2278.
- (161) Poulos, T. L. Heme Enzyme Structure and Function. *Chemical Reviews* **2014**, *114*, 3919–3962.
- (162) Perry, C.; de los Santos, E. L. C.; Alkhalaf, L. M.; Challis, G. L. Rieske non-heme iron-dependent oxygenases catalyse diverse reactions in natural product biosynthesis. *Natural Product Reports* **2018**, *35*, 622–632.
- (163) Karlsson, A.; Parales, J. V.; Parales, R. E.; Gibson, D. T.; Eklund, H.; Ramaswamy, S. Crystal Structure of Naphthalene Dioxygenase: Side-on Binding of Dioxygen to Iron. *Science* **2003**, *299*, 1039–1042.
- (164) Groves, J. T.; Nemo, T. E.; Myers, R. S. Hydroxylation and epoxidation catalyzed by iron-porphine complexes. Oxygen transfer from iodosylbenzene. *Journal of the American Chemical Society* **1979**, *101*, 1032–1033.
- (165) Mehn, M. P.; Fujisawa, K.; Hegg, E. L.; Que, L. Oxygen Activation by Nonheme Iron(II) Complexes: α -Keto Carboxylate versus Carboxylate. *Journal of the American Chemical Society* **2003**, *125*, 7828–7842.
- (166) Jacobsen, E. N.; Zhang, W.; Muci, A. R.; Ecker, J. R.; Deng, L. Highly enantioselective epoxidation catalysts derived from 1,2-diaminocyclohexane. *Journal of the American Chemical Society* **1991**, *113*, 7063–7064.
- (167) Ghosh, A. K.; Bilcer, G.; Schiltz, G. Syntheses of FDA Approved HIV Protease Inhibitors. *Synthesis* **2001**, *2001*, 2203–2229.
- (168) Cheng, K. L.; Lott, P. F. Reaction of Hydrogen Peroxide with Complexes of (Ethylenedinitrilo)tetraacetic Acid and Nitrilotriacetic Acid. *Analytical Chemistry* **1956**, *28*, 462–465.
- (169) Ringbom, A.; Siitonen, S.; Saxén, B. The Fe(III)-EDTA-H₂O₂ complex and its analytical use. *Analytica Chimica Acta* **1957**, *16*, 541–545.
- (170) Ahmad, S.; McCallum, J. D.; Shiemke, A. K.; Appelman, E. H.; Loehr, T. M.; Sanders-Loehr, J. Raman spectroscopic evidence for side-on binding of peroxide ion to (ethylenediaminetetraacetato)ferrate(1-). *Inorganic Chemistry* **1988**, *27*, 2230–2233.

- (171) Neese, F.; Solomon, E. I. Detailed Spectroscopic and Theoretical Studies on $[\text{Fe}(\text{EDTA})(\text{O}_2)]^{3-}$: Electronic Structure of the Side-on Ferric Peroxide Bond and Its Relevance to Reactivity. *Journal of the American Chemical Society* **1998**, *120*, 12829–12848.
- (172) Anderegg, G.; Wenk, F. Pyridinderivate als Komplexbildner VIII Die Herstellung je eines neuen vier- und sechszähligen Liganden. *Helvetica Chimica Acta* **1967**, *50*, 2330–2332.
- (173) Toftlund, H.; Andersen, S. Y. Spin Equilibria in Octahedral Iron(II) Complexes with Some Hexadentate Ligands of the Tetrakis(2-pyridylmethyl)ethylene-diamine Type and a Spectral Correlation With their Cobalt(III) and Nickel(II) Analogs. *Acta Chemica Scandinavica* **1981**, *A 35*, 575–585.
- (174) Simaan, A. J.; Dopner, S.; Banse, F.; Bourcier, S.; Bouchoux, G.; Boussac, A.; Hildebrandt, P.; Girerd, J.-J. Fe(III)-Hydroperoxo and Peroxo Complexes with Aminopyridyl Ligands and the Resonance Raman Spectroscopic Identification of the Fe-O and O-O Stretching Modes. *European Journal of Inorganic Chemistry* **2000**, 1627–1633.
- (175) Bohn, A. Approche électrochimique de l'activation réductrice du dioxygène à l'aide d'un complexe de fer(II) non hémique, PhD Thesis, 2018.
- (176) Simaan, A. J.; Banse, F.; Mialane, P.; Boussac, A.; Un, S.; Kargar-Grisel, T.; Bouchoux, G.; Girerd, J.-J. Characterization of a Nonheme Mononuclear Peroxoiron(III) Intermediate by UV/Vis and EPR Spectroscopy and Mass Spectrometry. *European Journal of Inorganic Chemistry* **1999**, *1999*, 993–996.
- (177) Bernal, I.; Jensen, I. M.; Jensen, K. B.; McKenzie, C. J.; Toftlund, H.; Tuchagues, J.-P. Iron(II) Complexes of Polydentate Aminopyridyl Ligands and an Exchangeable Sixth Ligand; Reactions with Peroxides. Crystal Structure of $[\text{FeL}(\text{H}_2\text{O})] [\text{PF}_6]_2 \cdot \text{H}_2\text{O}$ [L = N,N'-bis(6-methyl-2-pyridylmethyl)-N,N'-bis(2-pyridylmethyl)ethane-1,2-diamine]. *Journal of Chemical Society, Dalton Transaction* **1995**, 3667–3675.
- (178) Mialane, P. et al. Structures of Fe(II) Complexes with N, N, N'-Tris(2-pyridylmethyl)ethane-1,2-diamine Type Ligands. Bleomycin-like DNA Cleavage and Enhancement by an Alkylammonium Substituent on the N' Atom of the Ligand. *Inorganic Chemistry* **1999**, *38*, 1085–1092.
- (179) Robinson, A. L. New non-heme iron complexes for bioinspired oxidation catalysis: influence of the first or second coordination sphere on the activation of O_2 and H_2O_2 , PhD Thesis, 2022.
- (180) Ségaud, N.; Anxolabéhère-Mallart, E.; Sénéchal-David, K.; Acosta-Rueda, L.; Robert, M.; Banse, F. Electrochemical study of a nonheme Fe(II) complex in the presence of dioxygen. Insights into the reductive activation of O_2 at Fe(II) centers. *Chemical Science* **2015**, *6*, 639–647.
- (181) Robinson, A. L.; Rebilly, J.-N.; Guillot, R.; Herrero, C.; Maisonneuve, H.; Banse, F. A Tale of Two Complexes: Electro-Assisted Oxidation of Thioanisole by an "O₂ Activator/Oxidizing Species" Tandem System of Non-Heme Iron Complexes. *Chemistry – A European Journal* **2022**, *28*, DOI: [10.1002/chem.202200217](https://doi.org/10.1002/chem.202200217).
- (182) Sastri, C. V.; Park, M. J.; Ohta, T.; Jackson, T. A.; Stubna, A.; Seo, M. S.; Lee, J.; Kim, J.; Kitagawa, T.; Münck, E.; Que, L.; Nam, W. Axial Ligand Substituted Nonheme Fe^{IV}O Complexes: Observation of Near-UV LMCT Bands and FeO Raman Vibrations. *Journal of the American Chemical Society* **2005**, *127*, 12494–12495.
- (183) Hong, S.; Lee, Y.-M.; Shin, W.; Fukuzumi, S.; Nam, W. Dioxygen Activation by Mononuclear Nonheme Iron(II) Complexes Generates Iron-Oxygen Intermediates in the Presence of an NADH Analogue and Proton. *Journal of the American Chemical Society* **2009**, *131*, 13910–13911.
- (184) Thibon, A.; England, J.; Martinho, M.; Young, V. G.; Frisch, J. R.; Guillot, R.; Girerd, J.-J.; Münck, E.; Que, L.; Banse, F. Proton- and Reductant-Assisted Dioxygen Activation by a Nonheme Iron(II) Complex to Form an Oxoiron(IV) Intermediate. *Angewandte Chemie International Edition* **2008**, *47*, 7064–7067.
- (185) Mühldorf, B.; Lennert, U.; Wolf, R. Coupling photoredox and biomimetic catalysis for the visible-light-driven oxygenation of organic compounds. *Physical Sciences Reviews* **2019**, *4*, DOI: [10.1515/psr-2018-0030](https://doi.org/10.1515/psr-2018-0030).

-
- (186) Fukuzumi, S.; Kishi, T.; Kotani, H.; Lee, Y.-M.; Nam, W. Highly efficient photocatalytic oxygenation reactions using water as an oxygen source. *Nature Chemistry* **2011**, *3*, 38–41.
- (187) Jung, J.; Ohkubo, K.; Goldberg, D. P.; Fukuzumi, S. Photocatalytic Oxygenation of 10-Methyl-9,10-dihydroacridine by O₂ with Manganese Porphyrins. *The Journal of Physical Chemistry A* **2014**, *118*, 6223–6229.
- (188) Lechner, R.; König, B. Oxidation and Deprotection of Primary Benzylamines by Visible Light Flavin Photocatalysis. *Synthesis* **2010**, *2010*, 1712–1718.
- (189) Mühldorf, B.; Wolf, R. C-H Photooxygenation of Alkyl Benzenes Catalyzed by Riboflavin Tetraacetate and a Non-Heme Iron Catalyst. *Angewandte Chemie International Edition* **2016**, *55*, 427–430.
- (190) Paschke, J.; Kirsch, M.; Korth, H.-G.; de Groot, H.; Sustmann, R. Catalase-Like Activity of a Non-Heme Dibenzotetraaza[14]annulene Fe(III) Complex under Physiological Conditions. *Journal of the American Chemical Society* **2001**, *123*, 11099–11100.
- (191) Ghosh, A.; Mitchell, D. A.; Chanda, A.; Ryabov, A. D.; Popescu, D. L.; Upham, E. C.; Collins, G. J.; Collins, T. J. Catalase Peroxidase Activity of Iron(III)TAML Activators of Hydrogen Peroxide. *Journal of the American Chemical Society* **2008**, *130*, 15116–15126.
- (192) Vo, N. T.; Mekmouche, Y.; Tron, T.; Guillot, R.; Banse, F.; Halime, Z.; Sircoglou, M.; Leibl, W.; Aukauloo, A. A Reversible Electron Relay to Exclude Sacrificial Electron Donors in the Photocatalytic Oxygen Atom Transfer Reaction with O₂ in Water. *Angewandte Chemie International Edition* **2019**, *58*, 16023–16027.
- (193) Vo, N. T.; Herrero, C.; Guillot, R.; Inceoglu, T.; Leibl, W.; Clémancey, M.; Dubourdeaux, P.; Blondin, G.; Aukauloo, A.; Sircoglou, M. Intercepting a transient non-hemic pyridine *N*-oxide Fe(III) species involved in OAT reactions. *Chemical Communications* **2021**, *57*, 12836–12839.

2 - CO₂ REDUCTION IN A HOMOGENEOUS SYSTEM

2.1 . Introduction and objectives

Scientists have been aiming to reproduce the light-triggered electron transfers that plants use to drive redox reactions to ultimately fix CO₂ and oxidize H₂O. In order to achieve this result, a common strategy relies on the optimization of each half-reaction separately, before combining them in a single device. In our group, both half-reactions of CO₂ reduction and H₂O oxidation have been investigated [1] [2] [3] [4] [5]. In particular, iron porphyrins have been implemented as electrocatalysts for CO₂ reduction. As discussed in the previous chapter, different modifications on the second coordination sphere were studied [1] [2] [6]. One interesting result comes from the insertion of H-bond interactions through amide and urea arms, located on the phenyl ring at the *meso* positions of the porphyrin (See Fig. 2.1). These H-bond donating groups are thought to interact directly with the substrate (CO₂) bound to the metal center, aiding the intermediate stabilization and consequently also the reaction to proceed. Previous findings highlighted how the insertion of urea arms instead of amide arms results in better electrocatalytic performances with lower overpotential, thanks to the multiple H-bonds provided by each urea group ($\eta = 0.63$ V for amide and 0.43 V for urea with $\log\text{TOF}_{\text{max}} = 3.85$ for amide and 3.83 for urea). These values, compared to the non-modified **FeTPP**, show a gain in overpotential with a maintained high reaction rate ($\eta = 0.73$ V and $\log\text{TOF}_{\text{max}} = 4.03$ for **FeTPP**)[1].

Furthermore, different atropoisomers were studied for the di-substituted urea porphyrin (Fig. 2.1). The *αα* atropoisomer presents both groups on the same face of the porphyrin ring, whereas the *αβ* atropoisomer has the two groups facing opposite sides of the porphyrin ring. Electrochemical experiments evidenced that with the *αβ* atropoisomer the lower binding affinity of CO₂ due to the absence of a second urea arm on the same face of the porphyrin is counterbalanced by a higher reaction rate (TOF = 5878 s⁻¹ for **αβ-UrFe** and TOF = 1870 s⁻¹ for **αα-UrFe**), due to an easier access for the protons during the protonation step. This interesting result shows the importance of studying the reaction mechanism and understanding what is limiting the reaction rate (rate

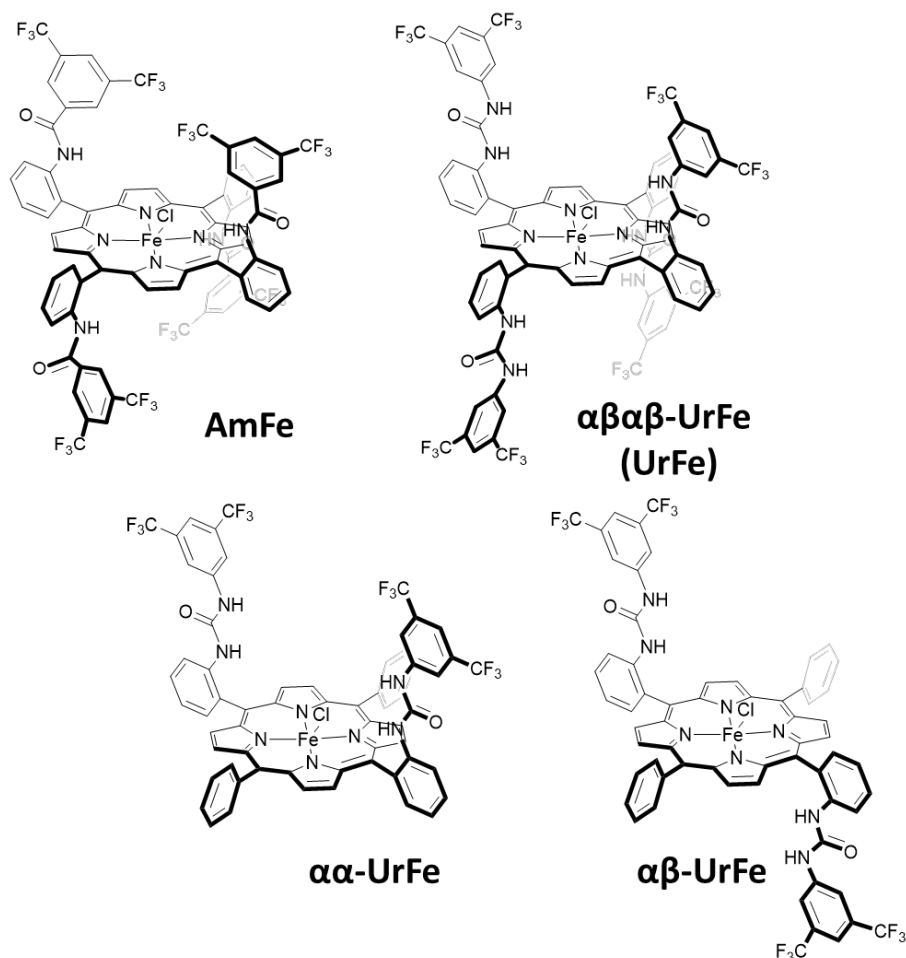


Figure 2.1: Iron porphyrins developed by our group holding H-bond donating groups - four-substituted amide (**AmFe**) and urea (**αβαβ-UrFe** or **UrFe**) porphyrins; di-substituted urea porphyrins with two different atropoisomers (**αα-UrFe** and **αβ-UrFe**).

determining step; RDS).

The promising results obtained with urea-modified iron porphyrins for electrocatalytic CO₂ conversion motivated us to investigate their possible application in light-induced catalysis, to trace a more direct link between natural and artificial photosynthesis, aiming to solar fuels production.

The focus of this chapter is the study of the urea-modified iron porphyrin (**UrFe**) for CO₂ photocatalytic reduction in homogeneous conditions and consequent mechanism investigation. Working in solution allows simple implementation of many different spectroscopic techniques that give insights on the reaction mechanism. At a first level, working in homogeneous conditions provides important information on the catalyst activity and can later be translated in a more stable heterogeneous system.

A step by step description of catalyst synthesis, photocatalysis and spectroscopic characterization is provided in the following sections.

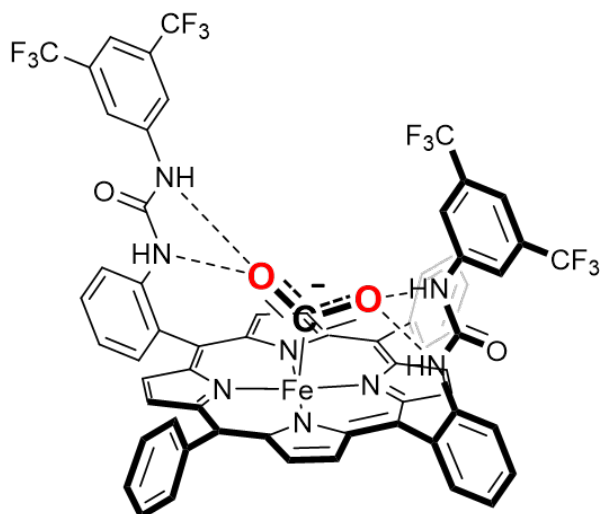


Figure 2.2: Scheme of the interaction between the CO₂ adduct and the H-bond donating groups.

2.2 . Catalyst synthesis and characterizations

The iron porphyrin **UrFe** was synthesized according to previous reports [1] from the precursor porphyrin ***αβαβ*-TPP(NH₂)**, previously prepared through collaboration with the group of Dr. B. Boitrel from the University of Rennes (see Fig. 2.3).

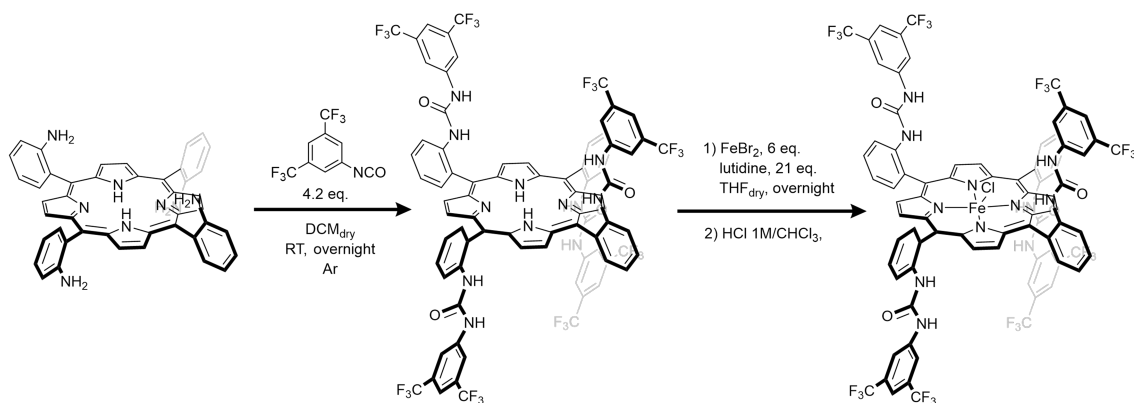


Figure 2.3: Reaction scheme for the synthesis of **UrFe** catalyst.

The first step involves the formation of the urea moieties from the reaction with a slight excess of the commercially available 3,5-Bis(trifluoromethyl) phenyl isocyanate in dry dichloromethane. Then the metal-free ligand was reacted with iron (II) bromide (FeBr₂) for iron insertion, in presence of an excess of lutidine and in inert conditions. A final workup with 1M HCl and column chromatography could ensure a pure compound with chloride anion as an axial ligand. Both the ligand and the iron complex were characterized by UV-vis

spectroscopy and high resolution mass spectrometry (HR-MS); the metal-free porphyrin was also characterized by ¹H-NMR and ¹³C-NMR whereas the iron complex could not be studied with this technique due to its paramagnetic nature. All of the characterizations showed the desired product with good purity and yields of 86% for the first step and 60% for the second step. Related spectra and analysis can be found in more detail in the annex.

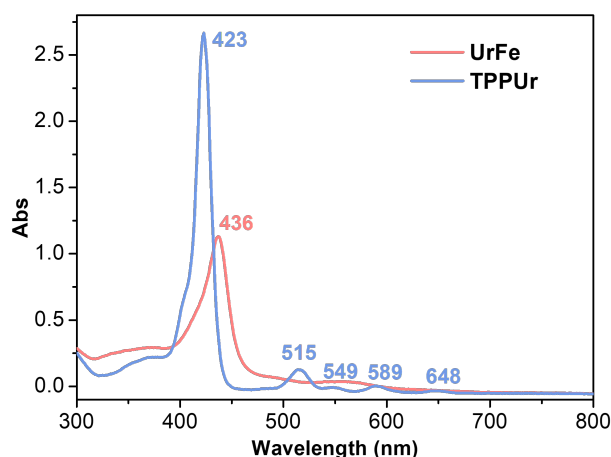


Figure 2.4: UV-vis absorption spectra of a 10 μ M solution of the urea porphyrin ligand (blue) and of the **UrFe** complex in DMF.

Having a look into the UV-vis spectra, it is easy to follow the metal-insertion by the changes in the absorption in the visible region. As shown in Fig. 2.4, the free-base porphyrin presents a Soret band at 423 nm and four Q-bands at 515 nm, 549 nm, 589 nm and 648 nm respectively. When looking at the iron porphyrin, we observe a shift of the Soret band to 436 nm and a decrease in the intensity and the Q-bands turn into two broad peaks at 500 nm and 550 nm. Both Soret and Q-bands are due to ligand-centered transitions to the first excited state (Q-bands) and second excited state (Soret band). The loss of some of the Q-bands is linked to the loss of asymmetry given by the two inner pyrrolic protons of the free-base porphyrin, which affect of the π and π^* degenerate orbitals. The extinction coefficient of **UrFe** was estimated to be 94 000 $\text{M}^{-1}\text{cm}^{-1}$ at 436 nm in DMF. It should be highlighted that axial ligand exchange can occur on the Fe(III) porphyrin, and it is more favoured in highly coordinating solvent, such as ACN or DMF. This will affect the shift and intensity of the Soret band and also result in a widening of the band when a mixture of two iron porphyrins with different ligands is present.

The obtained **UrFe** iron catalyst was also characterized by cyclic voltammetry

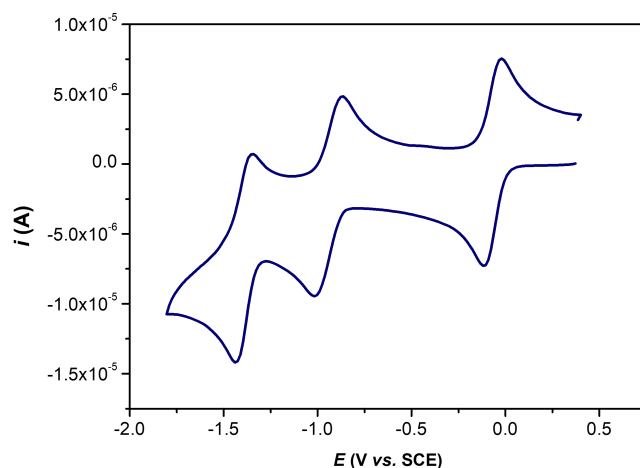


Figure 2.5: Cyclic voltammogram (CV) of the **UrFe** complex at 1 mM concentration in Ar-degassed DMF_{dry} with 0.1 M TBAPF₆. Glassy carbon working electrode; Pt counter electrode and Saturated Calomel Electrode (SCE) as reference electrode; 100 mV s⁻¹ scan rate.

(CV) and compared with the other reported iron porphyrins. As shown in Fig. 2.5, three reversible waves are observed in dry DMF at -0.063 V, -0.934 V and -1.390 V vs. SCE corresponding to the Fe(III/II) and formal Fe(II/I) and Fe(I/0) redox couples respectively.

Other porphyrins used as reference in the study had been previously synthesized in our group and their characterization is reported in the dedicated article [2].

2.3 . Developments and optimizations of the photocatalytic system

To begin the photocatalysis study, the appropriate photosensitizer and sacrificial electron donor should be selected.

Following previous reports [5], the initially selected couple was [Ru(bpy)₃]²⁺ and 3-dimethyl-2-phenyl-2,3-dihydro-1Hbenzo[*d*]imidazole (BIH). [Ru(bpy)₃]²⁺ is one of the most widely used photosensitizer, its photophysical properties are well-known and its advantageous properties include strong absorption in the visible, long-lived excited state (890 ns in ACN) and appropriate redox potentials for both oxidation and reduction reactions ($E_{1/2}$ (Ru^{III/II}) = +1.30 V vs. Ag/AgCl in ACN; $E_{1/2}$ (Ru^{II/I}) = -1.31 V vs. Ag/AgCl in DMF) [7]. In the absorption spectrum it presents a maximum MLCT band around 452 nm with an extinction coefficient of about 13 000 M⁻¹ cm⁻¹ in ACN. When excited, the

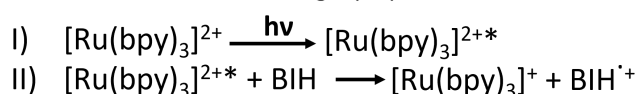
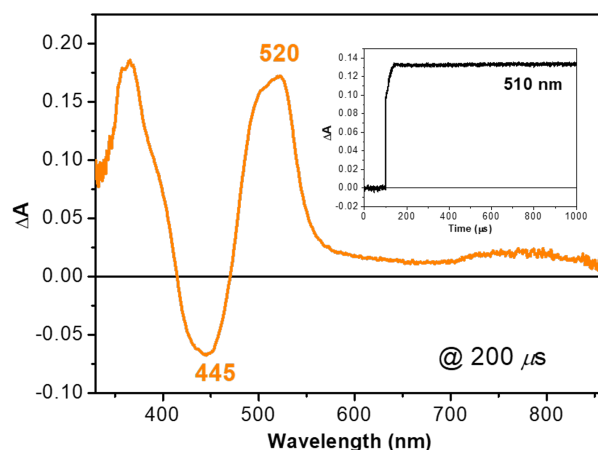


Figure 2.7: Transient absorption measurement at 200 μs delay of a mixture of $[\text{Ru}(\text{bpy})_3]^{2+}$ and BIH. Inset: kinetic trace of Ru(I) formation highlighting the irreversible character of BIH as electron donor.

excited singlet state has a rapid intersystem crossing (ISC) that in less than 100 fs generates the ³MLCT with an emission 620 nm [8] [9].

BIH is a reduced benzimidazole which was synthesized in the laboratory starting from 2-nitroaniline and benzaldehyde (see Annex). It is commonly used in the field of molecular photocatalysis as sacrificial electron donor, thanks to its irreversible oxidation due to a deprotonation reaction that follows the first oxidation. One BIH molecule can give one proton and two electrons, the second coming from a radical generated after the deprotonation step (Fig. 2.6) and with a very negative potential (around -2 V vs. $\text{Fc}^{+/0}$) [10].

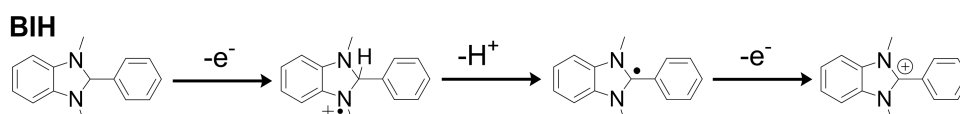


Figure 2.6: Scheme of the steps taking place after BIH first electron transfer to quench the PS.

When $[\text{Ru}(\text{bpy})_3]^{2+}$ and BIH are mixed together and irradiated, clear changes can be seen by UV-vis spectroscopy, both time-resolved (Fig. 2.7) and continuous (Fig. 2.8). In time-resolved UV-vis spectra, also called laser flash photolysis (LFP), after the fast formation of the $\text{Ru}(\text{II})^*$ excited state, a new band around 520 nm can be observed which corresponds to the formal Ru(I) species (see Fig. 2.7). This indicates the successful quenching of the $\text{Ru}(\text{II})^*$ through a reductive pathway to generate its reduced form, which can in turn reduce the

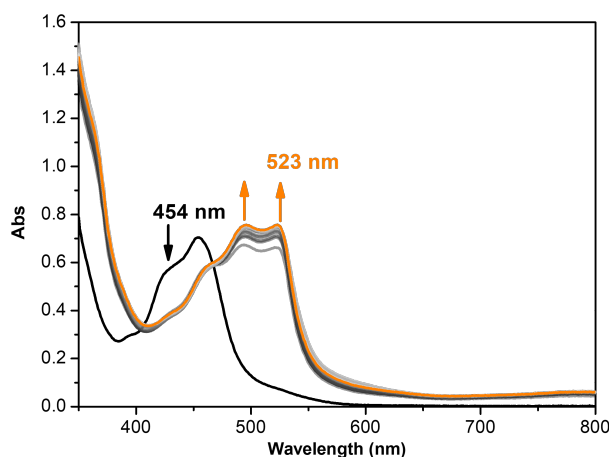


Figure 2.8: UV-vis spectral evolution in photoaccumulation experiment with $[\text{Ru}(\text{bpy})_3]^{2+}$ 30 μM and BIH 7 mM in N_2 -saturated DMF_{dry} , -35°C . The changes highlight the reduction of Ru(II) to Ru(I) with a maximum at 523 nm.

iron catalyst. BIH acts as an irreversible electron donor and in absence of other species to reduce, Ru(I) tends to accumulate in solution in these conditions. For this reason, Ru(I) formation can also be observed using a classic UV-vis spectrophotometry instrument under continuous irradiation (Fig. 2.8). From the kinetic trace of Fig. 2.7, we can observe: i) two different kinetics in the formation of Ru(I) deriving from the first and second electron donation by BIH; ii) the irreversibility of the electron transfer as indicated by the absence of any kinetic decay in the 1 ms time-scale.

To study photocatalytic activity, $[\text{Ru}(\text{bpy})_3]^{2+}$ and BIH were mixed together with the iron porphyrin catalyst, in presence of a proton source (H_2O) and the CO_2 substrate. To measure the photocatalytic activity, vials containing the reaction mixture and degassed with CO_2 were irradiated using a visible LED. Then, small aliquots of gas were sampled automatically from the headspace and injected in a micro-gas chromatography (μGC). The choice of the stoichiometry of the different components is important, as it has a direct impact on the reaction kinetics. For instance, the photosensitizer (PS) should be in excess with respect to the catalyst for two main reasons: i) to favour the successive reductions of the iron porphyrin by accumulation of an excess of reduced Ru(I); ii) to mask the absorption of the porphyrin, given that it has a much higher extinction coefficient than that of the PS. BIH is also in large excess compared to the PS (50 equivalents in standard conditions), to favour the quenching, as well as to have a virtually infinite amount of electrons. For each BIH molecule, one CO_2 molecule can be reduced to CO (two electrons needed), so the electron

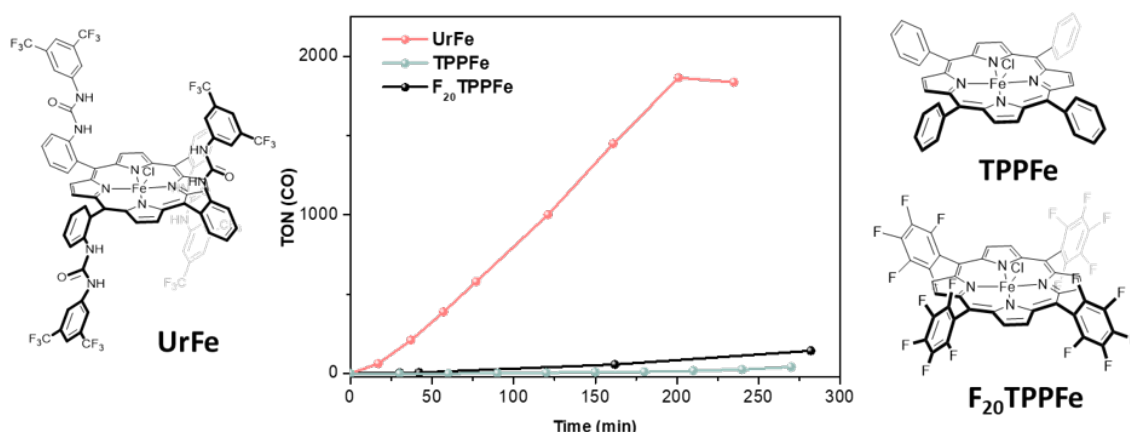


Figure 2.9: Time evolution of CO produced under visible-light irradiation ($\lambda > 405$ nm, 100 Wm^{-2}) with **TPPFe** (green), **F₂₀TPPFe** (black) or **UrFe** (red) as catalyst with $20 \mu\text{M}$ concentration; $[\text{Ru}(\text{bpy})_3]^{2+}$ photosensitizer 1 mM, BIH sacrificial electron donor 50 mM in CO₂-saturated DMF/H₂O 9:1.

donor should always be present in large excess to maintain catalytic conditions. Two other different iron porphyrin catalysts were evaluated in the same conditions as reference and their catalytic performances are shown in Fig. 2.9. **TPPFe** is a non-modified catalyst; and **F₂₀TPPFe** is an important reference for this study because it presents almost overlapping redox potentials with the ones of **UrFe** [1]. The graph shows the product evolution in terms of TON as a function of irradiation time. As we can observe, the **UrFe** catalyst has, from the start, a much higher catalytic activity than the other two reference porphyrins. CO evolution stops after around 3h of irradiation and the small decrease in CO level is due to slight losses into the μGC . **UrFe** could achieve in such conditions up to 1865 TON for CO with a TOF of 580 h^{-1} and no other products were detected (*i.e.* H₂). On the other hand, both **TPPFe** and **F₂₀TPPFe** displayed a lower product evolution, with a TON of 25 and 143 and selectivities of 34% and 85% respectively (see entries 1-3 of Table 2.1). The fact that even **F₂₀TPPFe** shows a modest catalytic activity is significant to highlight the second coordination sphere effect. Indeed, for **TPPFe** the low catalytic activity could be ascribed to the small driving force of the reaction, since the photosensitizer dictates the potential at which the reaction can proceed. For example, Ru(I) has a reduction potential of about -1.33 V vs. SCE [11], which means that the Fe(I/0) reduction is more accessible in the case of **UrFe** (-1.390 V vs. SCE) than for **TPPFe** (-1.695 V vs. SCE). The small catalytic activity of **TPPFe** can be attributed to the generation of the more reducing BI \cdot (around $-2 \text{ V vs. Fc}^{+/0}$ [10]) over a long irradiation time. On the

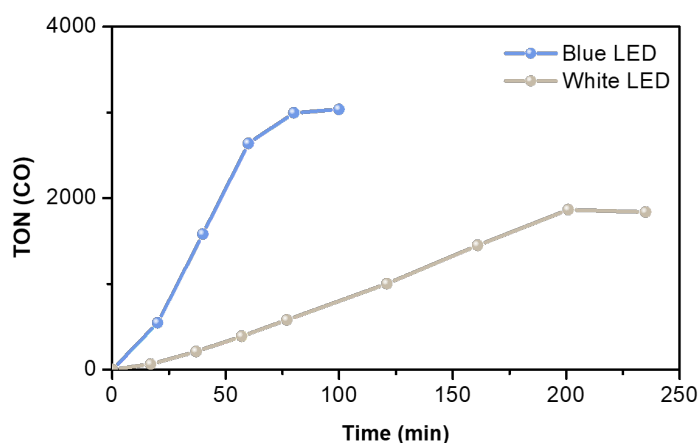


Figure 2.10: Time evolution of CO produced under light irradiation with a blue LED (blue dots, $\lambda_{em}=460$ nm 100 W m^{-2}) and white LED (grey dots, $\lambda > 405$ nm 100 W m^{-2}) of **UrFe** as catalyst with 20 μ M concentration; $[Ru(bpy)_3]^{2+}$ photosensitizer 1 mM, BIH sacrificial electron donor 50 mM in CO_2 -saturated DMF/ H_2O 9:1.

other hand, the results obtained for **F₂₀TPPFe** suggest the important role of the urea functions.

Overall, these first results confirmed the beneficial effect of the second-coordination sphere with H-bond donating groups for the photocatalytic activity of this catalyst. For **F₂₀TPPFe**, with comparable reduction potentials, a lower CO production is observed, suggesting that a secondary effect is coming into play for **UrFe** in addition to the less negative reduction potentials. The results of this comparison, motivated us to investigate further the influence of different parameters on the reactivity of **UrFe**. At the same light power, changing from white LED to blue LED ($\lambda_{em}=460$ nm) induced a further improvement on the photocatalytic activity of the system (Fig. 2.10). With blue LED (entry 4 of Table 2.1), the TON could reach up to 3036, with also a significant improvement of TOF going from 580 to 3141 h^{-1} . This result can be rationalized by considering the light absorbed by the photosensitizer, which has its maximum of absorption (454 nm in DMF) in the same region as the blue LED emission. At the same power, the blue LED is focused only around 460 nm, which means that more photons are emitted in the region where $[Ru(bpy)_3]^{2+}$ absorbs. In other words, in the white light conditions, the rate of the reaction was limited by the absorbed light and consequent light-induced steps; when the rate of incoming photons increases, then the overall reaction rate also increases. This observation confirms the rapid and selective catalytic activity of the **UrFe** catalyst, that was previously limited by the amount of incoming light. The increase of TON can be explained by a shorter irradiation time, limiting any possible

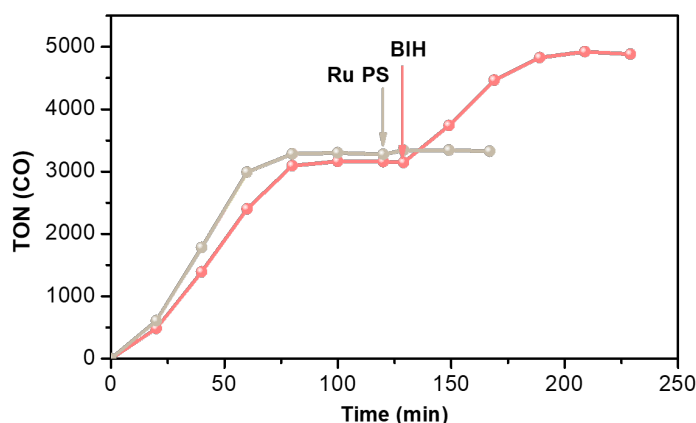


Figure 2.11: Time evolution of CO produced under light irradiation with a blue LED ($\lambda_{em}=460$ nm 100 W m^{-2}) of **UrFe** as catalyst with 20 μ M concentration; $[Ru(bpy)_3]^{2+}$ photosensitizer 1 mM, BIH sacrificial electron donor 50 mM in CO₂-saturated DMF/H₂O 9:1. The arrows indicate the point of reinjection of 1 mL of 2 mM $[Ru(bpy)_3]^{2+}$ (beige) or 1 mL of 0.2 M BIH (red).

photodegradation occurring in the system.

A TON of about 3000 for CO evolved also means that the added BIH (50 mM) was fully consumed. To confirm this, BIH was reinjected in the solution after the first plateau of product evolution. In a similar experiment, $[Ru(bpy)_3]^{2+}$ was also reinjected in the reaction mixture to verify if the photodegradation of the PS is limiting the reaction. These results are shown in Fig. 2.11. From the beige curve, we can see that reinjection of PS does not affect the catalysis, meaning that what stops the activity is not the degradation of the chromophore. On the other hand, when BIH is reinjected (red curve, Fig. 2.11) a recovery of the photocatalytic activity is observed until *quasi*-total consumption of the extra BIH added. Since the amount of electron donor is limiting the reaction under these conditions, the photocatalytic reaction was repeated with even larger excess of BIH, 250 mM (Fig. 2.12). The graph shows how indeed, adding a larger excess of BIH leads to further increase of TON for the **UrFe** catalyst, reaching a value of 7271 , with $TOF = 3720$ h^{-1} and a selectivity of 99% (entry 7 of Table 2.1). These values place **UrFe** among the highest performing molecular catalysts for CO₂ light-induced reduction reported so far in literature. The TON is an index of the catalyst stability (how many cycles the catalyst can perform before deactivation), so the value obtained in such conditions is considered to be intrinsic to the catalyst and not due to other limiting factors, such as light or incoming electrons. In fact, the amount of CO detected is lower than that of BIH present in solution and re-injections of photosensitizer, protons or substrate did not restart the reaction (see Fig. 2.13).

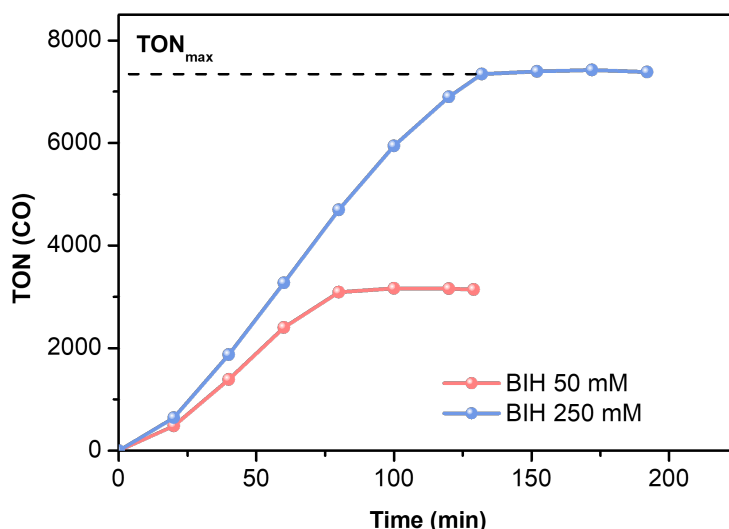


Figure 2.12: Time evolution of CO produced under light irradiation with a blue LED ($\lambda_{em} = 460$ nm, 100 W m^{-2}) of **UrFe** as catalyst with $20 \mu\text{M}$ concentration; $[\text{Ru}(\text{bpy})_3]^{2+}$ photosensitizer 1 mM, BIH sacrificial electron donor 50 mM (red) and 250 mM (blue) in CO_2 -saturated DMF/ H_2O 9:1.

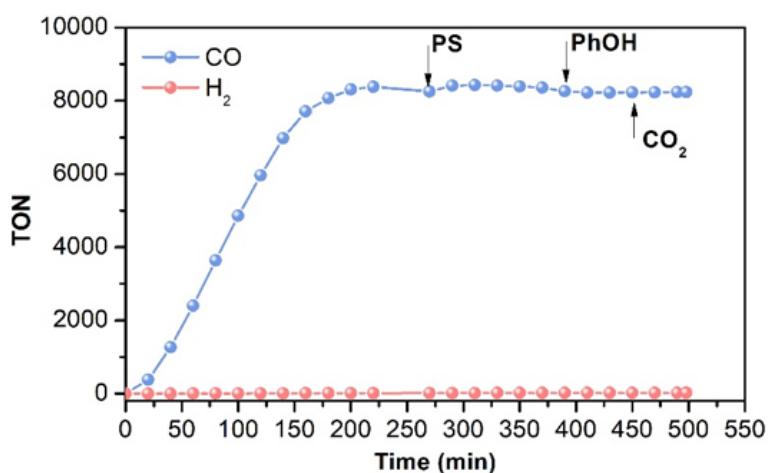


Figure 2.13: Time evolution of CO (blue) and H_2 (red) produced under light irradiation with a blue LED ($\lambda_{em} = 460$ nm 100 W m^{-2}) of **UrFe** as catalyst with $20 \mu\text{M}$ concentration; $[\text{Ru}(\text{bpy})_3]^{2+}$ photosensitizer 1 mM, BIH sacrificial electron donor 250 mM in CO_2 -saturated DMF/ H_2O 9:1. The arrows indicate the re-injections of the photosensitizer (PS), of a proton source (PhOH) and rebubbling of CO_2 .

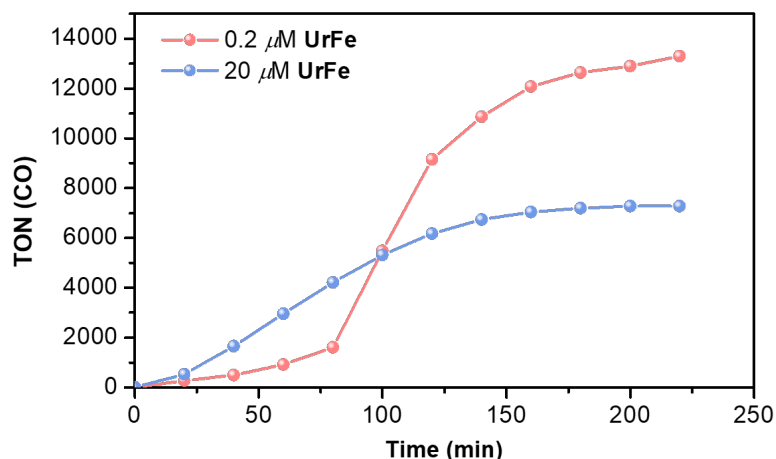


Figure 2.14: Time evolution of CO produced under light irradiation with a blue LED ($\lambda_{em}=460$ nm 100 W m^{-2}) of **UrFe** as catalyst with 20 μ M concentration (blue) and 0.2 μ M concentration (red); $[Ru(bpy)_3]^{2+}$ photosensitizer 1 mM, BIH sacrificial electron donor 250 mM in CO₂-saturated DMF/H₂O 9:1.

Table 2.1: Photocatalysis experiments performed with 20 μ M catalyst, 1 mM $[Ru(bpy)_3]^{2+}$, BIH as SED in DMF/H₂O 9:1 under LED irradiation (100 W m^{-2}) for 200 min.

Entry	Catalyst	[Catalyst] (μ M)	[SED] (mM)	LED type	Selectivity (CO %)	TON _{CO}	TOF _{CO} (h^{-1})
1	UrFe	20	50	White	100	1865	580
2	TPPFe	20	50	White	34	25	5
3	F₂₀TPPFe	20	50	White	85	143	32
4	UrFe	20	50	Blue	99	3036	3141
5	TPPFe	20	50	Blue	81	25	5
6	F₂₀TPPFe	20	50	Blue	65	170	78
7	UrFe	20	250	Blue	99	7271	3720
8	UrFe	0.2	250	Blue	86	13299	1160

For comparison with reported studies [12] [13] [14], a further condition tuning was done by lowering the catalyst concentration by 100 times (0.2 μ M). This resulted in a further increase of TON to reach more than $13\,000$ (entry 8 of Table 2.1). However, we are concerned that such value is artificially increased due to the experimental errors that can be related to error of the catalyst concentration and from the integrated area of the smaller peak on the μ GC response. The comparison between the two different concentrations is shown in Fig. 2.14. Table 2.1 summarizes all the experiments discussed until now and their conditions.

Another interesting experiment with surprising result is the change of the solvent mixture. Until now, the experiments discussed were performed in DMF with 10% water. When the same experiment was conducted in ACN instead

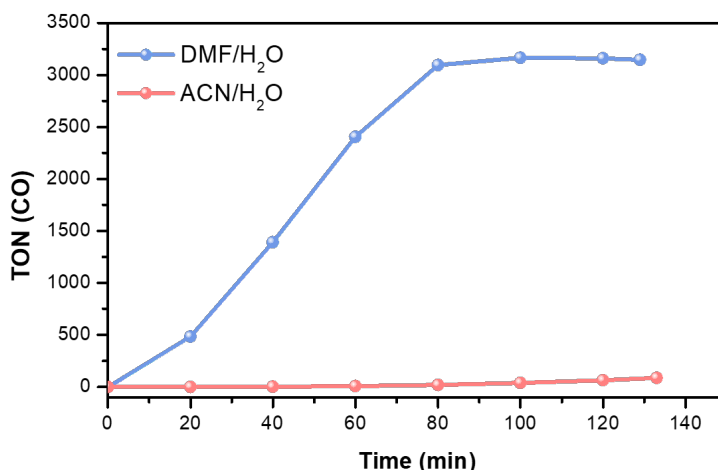


Figure 2.15: Time evolution of CO produced under light irradiation with a blue LED ($\lambda_{em}=460$ nm 100 W m^{-2}) of **UrFe** as catalyst with 20 μ M concentration; $[Ru(bpy)_3]^{2+}$ photosensitizer 1 mM, BIH sacrificial electron donor 50 mM in CO_2 -saturated DMF/ H_2O 9:1 (blue) and CO_2 -saturated ACN/ H_2O 9:1 (red).

of DMF, the photocatalytic activity was dramatically lower (see Fig. 2.15, entry 1 of Table 2.2). This behaviour can be attributed to the nature of BIH irreversibility. It was mentioned before that what gives its property of being an irreversible SED is a deprotonation occurring after the first oxidation. How fast the deprotonation occurs and the possible reversibility of it can be strongly influenced by the solvent nature. To prove this point, we performed a photoaccumulation experiment to generate Ru(I) in presence of BIH in ACN (Fig. 2.16). The monitoring of this photoaccumulation showed that the formation of Ru(I) is slower than in DMF and not complete (top graph of Fig. 2.16), and once the LED is switched off, re-oxidation to Ru(II) is observed even in absence of O_2 (bottom graph Fig. 2.16). This means that after reductive quenching of the PS, the electron can be transferred back to BIH, shortening the lifetime of the Ru(I) and hampering its accumulation. This phenomenon is clearly observed with time-resolved spectroscopy. In Fig. 2.17 we can observe the kinetic traces for the Ru(I) formation in the two different solvents. In both cases, there is a rapid formation of Ru(I), but in ACN this is followed by a first rapid decay and a second slower decay kinetics which indicates reversibility of the electron transfer. Similarly, low catalytic activity was also measured when sodium ascorbate (NaAsc) was used as electron donor instead of BIH. NaAsc is commonly used as reversible electron donor for LFP experiments where it is important for the system to be reversible, since changes are investigated before and after flashing the sample with light. Time-resolved photophysical studies

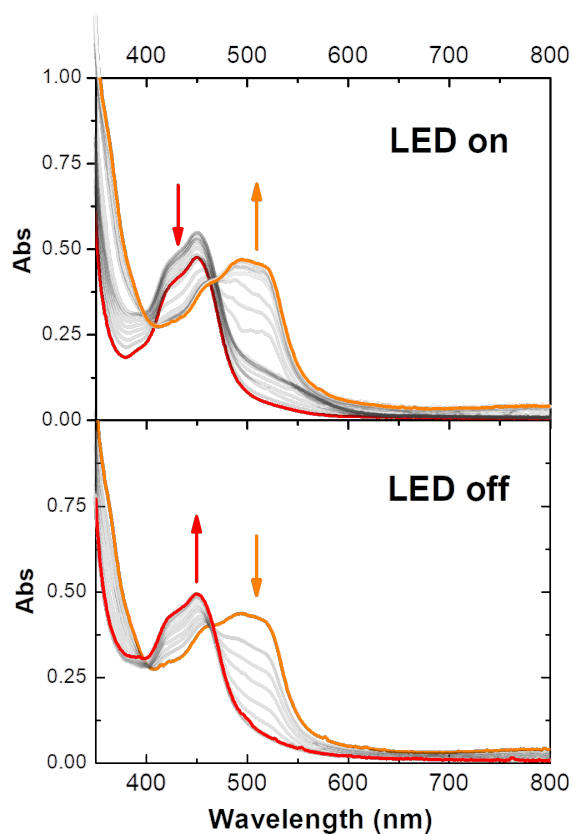


Figure 2.16: UV-vis spectral evolution over time in photoaccumulation experiment with $[\text{Ru}(\text{bpy})_3]^{2+}$ 30 μM and BIH 7 mM in Ar-saturated ACN_{dry} , room temperature. Top: LED turned on ($\lambda_{\text{em}} = 460$ nm; 100 W m^{-2}). The changes highlight the reduction of Ru(II) to Ru(I) with a maximum around 520 nm. Bottom: LED switched off, the process is reversible.

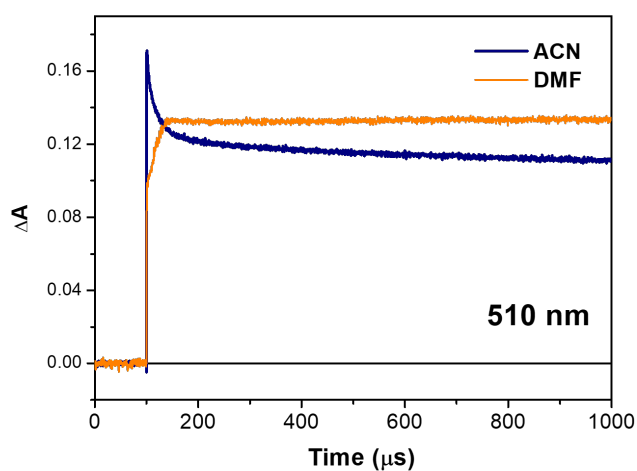


Figure 2.17: Kinetic profiles at 510 nm (corresponding to Ru(I)) obtained with a solution of $[\text{Ru}(\text{bpy})_3]^{2+}$ and BIH in Ar-saturated ACN (blue) and Ar-saturated DMF (orange).

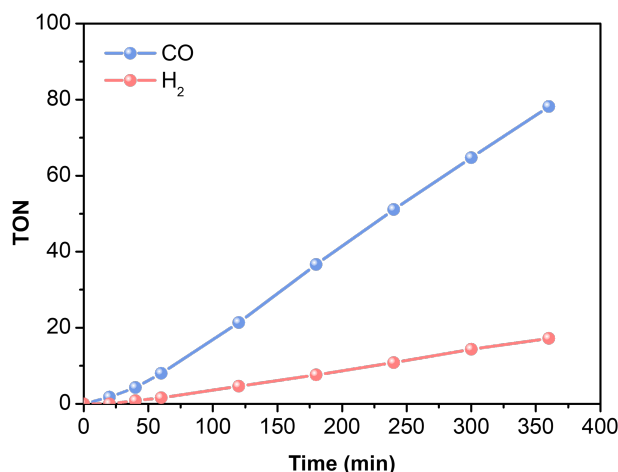


Figure 2.18: Time evolution of CO (blue) and H₂ (red) produced under light irradiation with a blue LED ($\lambda_{em}=460$ nm 100 W m⁻²) of **UrFe** as catalyst with 20 μ M concentration; [Ru(bpy)₃]²⁺ photosensitizer 1 mM, NaAsc sacrificial electron donor 100 mM in CO₂-saturated ACN/H₂O 6:4.

were also performed on the system, and to ensure that switching SED from irreversible to reversible still guarantees catalytic conditions, photocatalysis was measured in the same conditions of LFP experiments. As expected, a striking decrease of CO production could be observed due to SED reversibility, but still a catalytic activity was maintained (Fig. 2.18, entry 2 of Table 2.2).

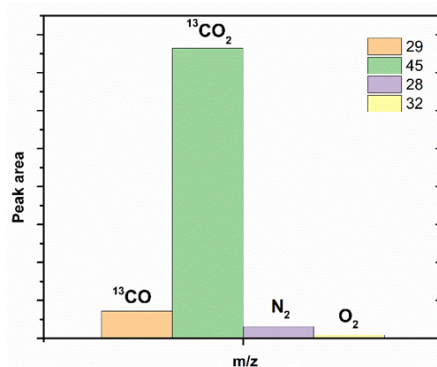
To consolidate the findings discussed above, a series of control experiments was carried out. One at the time, **UrFe**, [Ru(bpy)₃]²⁺, H₂O, CO₂ and BIH were removed from the reaction mixture (entries 3,4,6 of Table 2.2). No catalysis was observed when [Ru(bpy)₃]²⁺, CO₂ or BIH were absent. In the absence of **UrFe**, a much smaller CO evolution was detected after 2h of irradiation. This activity is probably due to the Ru complex that undergoes photodegradation forming a catalytically active complex. It has been previously reported that upon long illumination, [Ru(bpy)₃]²⁺ can lose one of the coordinated bipyridine ligands, generating [Ru(bpy)₂(H₂O)₂]²⁺, that is active for CO₂ conversion [15]. In any case, the degradation pathway will be slower in presence of the catalyst in solution, since less reduced Ru(I) will accumulate, because of electron transfer to the iron porphyrin. When removing H₂O, the catalytic activity is almost entirely suppressed, but still a small amount of CO can be detected, possibly due to the not perfectly dry solvent and the protons coming from BIH.

Another PS/SED couple was also studied for this catalytic reaction to induce this time an oxidative quenching mechanism. Ir(ppy)₃ and triethylamine (TEA) were chosen, because they have been previously reported in literature to follow

Table 2.2: Photocatalysis experiments performed with 20 μM catalyst, 1 mM $[\text{Ru}(\text{bpy})_3]^{2+}$, BIH as SED in DMF/H₂O 9:1 under LED irradiation (100 W m⁻²) for 2h.

Entry	Catalyst	[SED] (mM)	LED type	CO (μmol)	H ₂ (μmol)	CO %	TON _{CO}	TOF _{CO} (h ⁻¹)
1	UrFe ^[a]	50	Blue	8	0.7	92	63	46
2	UrFe ^[b]	100	Blue	2.7	0.6	82	21	14.6
3	-	50	Blue	50	0.4	99	-	-
4	UrFe ^[c]	50	White	0	0	-	-	-
5	UrFe ^[d]	50	White	0.9	0	100	7	3.5
6	UrFe ^[e]	50	Blue	65	0.1	100	623	497

[a] In ACN/H₂O 9:1 solvent mixture. [b] Sodium ascorbate used as SED in ACN/H₂O 6:4. [c] No photosensitizer in the reaction mixture. [d] Ir(ppy)₃ is used as photosensitizer and TEA as electron donor. [e] No water in the solvent mixture.

**Figure 2.19:** GC/MS analysis of 50 μL of gas mixture produced upon 1 h irradiation with blue LED ($\lambda_{\text{em}}=460$ nm 100 W m⁻²) of 20 μM **UrFe** catalyst; 1 mM $[\text{Ru}(\text{bpy})_3]^{2+}$ photosensitizer, 50 mM BIH sacrificial electron donor ¹³CO₂-saturated DMF/H₂O 9:1.

oxidative quenching mechanism [16]. We measured a much lower activity in this case, which indicates that reductive quenching is more efficient since the quencher (SED) is present in larger excess (entry 5 of Table 2.2).

A summary of the conditions of these further control experiments is given in Table 2.2.

¹³C isotope labelling experiments were also performed using ¹³CO₂ to confirm the origin of the detected CO. GC/MS response showed the peak corresponding to ¹³CO with an m/z value of 29. The data is shown in Fig. 2.19. Lastly, DLS measurements were also performed on the solution before and after a catalytic run, to rule out nanoparticles formation. The size distribution from DLS analysis highlights that no changes occurred during the photoinduced reaction (see Fig. 2.20).

No analysis of liquid products was made, however, given that the electrons coming from BIH are quantitatively used for CO production for **UrFe**, no other products are to be expected.

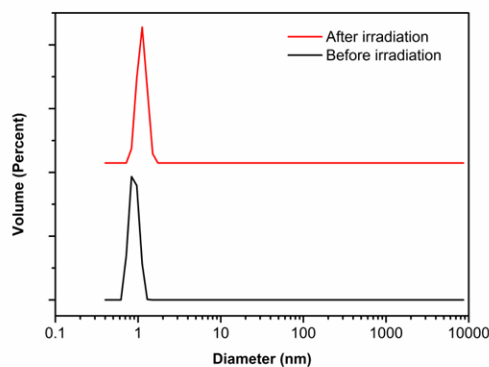


Figure 2.20: DLS measurements of a solution containing 1 mM $[\text{Ru}(\text{bpy})_3]^{2+}$ and 50 mM BIH in DMF/ H_2O 9:1 before (black) and after (red) 2h irradiation with a blue LED ($\lambda_{\text{em}}=460$ nm 100 W m^{-2}).

2.4 . Capturing reaction intermediates and their spectral fingerprints

To further investigate our photocatalytic system, we performed a spectroscopic study on the **UrFe** catalyst in different conditions to unravel the light-induced steps that confer to this iron porphyrin the unmatched photocatalytic activity. A first step to investigate the reaction mechanism is to obtain the reference spectra of the **UrFe** catalyst in its different oxidation states. To do so, different methods can be applied and compared to identify the different species.

2.4.1 . Chemical reductions

The first method described here uses chemical reductants. The advantage of using chemical reductants is that no specific equipment is needed and different reduced species can be obtained by choosing a reductant with an appropriate reducing potential. It is also possible to vary the stoichiometry of the reductant, which can help reaching different oxidation states. However, choosing the appropriate reducing agent, with good solubility, no overlaps of spectral signatures and appropriate reduction potential, may be a difficult challenge. This makes the technique quite limited, but it is a good starting point to obtain the spectra of interest.

Reduction of Fe(III) to Fe(II) is quite accessible given the half-wave potential of -0.06 V vs. SCE. For this reduction, zinc amalgam (ZnHg) was prepared and then added to a solution of **UrFe**, all under inert conditions to avoid re-oxidation by O_2 . ZnHg is a solid that is stable for a period of time if stored away from O_2 . The solution was stirred for 1 to 2 h and then spectra were recorded.

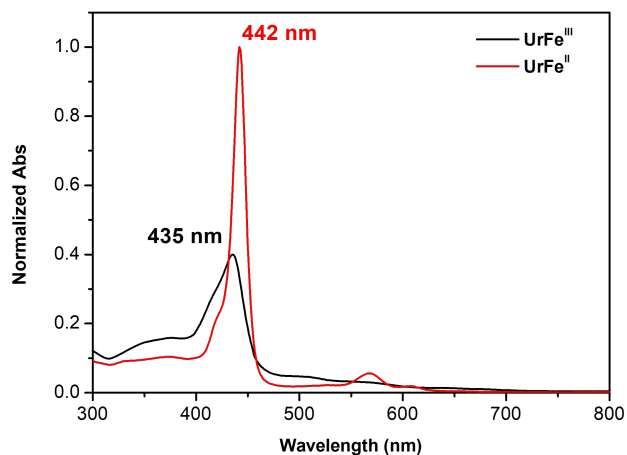


Figure 2.21: UV-vis reference spectra of **UrFe^{III}** (black) in Ar-saturated DMF, and chemically prepared **UrFe^{II}** (red) with ZnHg amalgam in N₂-saturated DMF.

Even before recording the UV-vis spectra, a visible change was observed in the solution going from a yellow-brown color to a brown-green color. Fig. 2.21 shows a significant change of absorption in the visible region, in particular a red-shift of the Soret band from 436 nm to 442 nm and a significant increase of extinction coefficient, which is expected for Fe(II) porphyrins [17].

For further reductions, stronger reducing agents are needed. Reduction to the formal Fe(I) was attempted using cobaltocene (CoCp₂) which has a reported potential of -0.95 V vs. SCE [18]. However, no clean reduction could be observed in this case. Attempts for Fe(0) generation with chemical reductants, such as sodium amalgam (NaHg) or decamethyl cobaltocene (CoCp₂*), were also not successful.

2.4.2 . UV-vis spectroelectrochemistry

Spectroelectrochemistry is a useful technique to monitor spectral evolutions during oxidation or reduction of molecules. It consists in the combination of a three-electrode electrochemical cell and a UV-vis spectrophotometer. The setup used (described in further details in the Annex) allows to detect the changes occurring directly on the working electrode. This is a key feature because the stability of multi-reduced intermediates is often limited by the short lifetime of the species and the measurement should be performed on a short timescale. UV-vis spectroelectrochemical measurements were performed on the **UrFe** catalyst both in DMF and ACN, in order to better compare photophysical data recorded in ACN. As the potential was shifted more negatively with controlled potential method, three sequential spectral changes could be observed, corre-

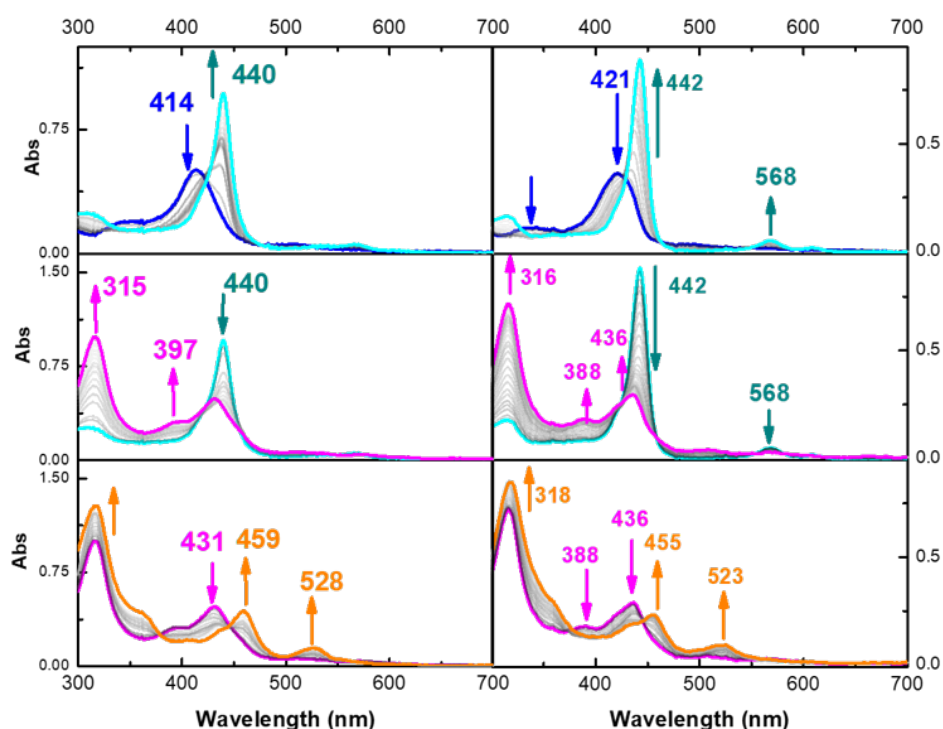


Figure 2.22: UV-Vis spectral evolution in spectroelectrochemistry experiment with **UrFe** 40 μM in Ar-saturated ACN_{dry} (left) and DMF_{dry} (right), 0.1 M TBAPF₆, Pt working electrode, Pt counter electrode and Pt pseudoreference electrode; room temperature. Top: Fe(III) to Fe(II) reduction. Middle: Fe(II) to Fe(I) reduction. Bottom: Fe(I) to Fe(0) reduction.

sponding to the first, second and third reduction that can be seen on the CV (Fig. 2.5). Figure 2.22 shows the obtained results at room temperature in two different solvents. Slight differences in the recorded wavelengths are expected in two different solvents, but the overall trends are comparable in the two cases. The top part of Fig. 2.22 shows the reduction of Fe(III) to Fe(II). This corresponds to an increase of the Soret band intensity, together with a red-shift. Changes are also observed in the Q-band region. Further reduction (middle graphs) highlights a decrease of the extinction coefficient of the Soret band. It was possible to obtain a full conversion of Fe(II) to Fe(I), which is proven by the isosbestic points maintained throughout the whole experiment. Successfully, also the reduction of Fe(I) to Fe(0) could be achieved using this method (bottom graphs). This allowed us to obtain the spectral signature of the Fe(0) species, which has not been frequently reported in the literature, due to its unstable nature [19]. The changes observed were a further red-shift of the Soret band to 455 nm, with a second band increasing around 523 nm. Spectroelectrochemical measurements were also performed for **F₂₀TPPFe**. In

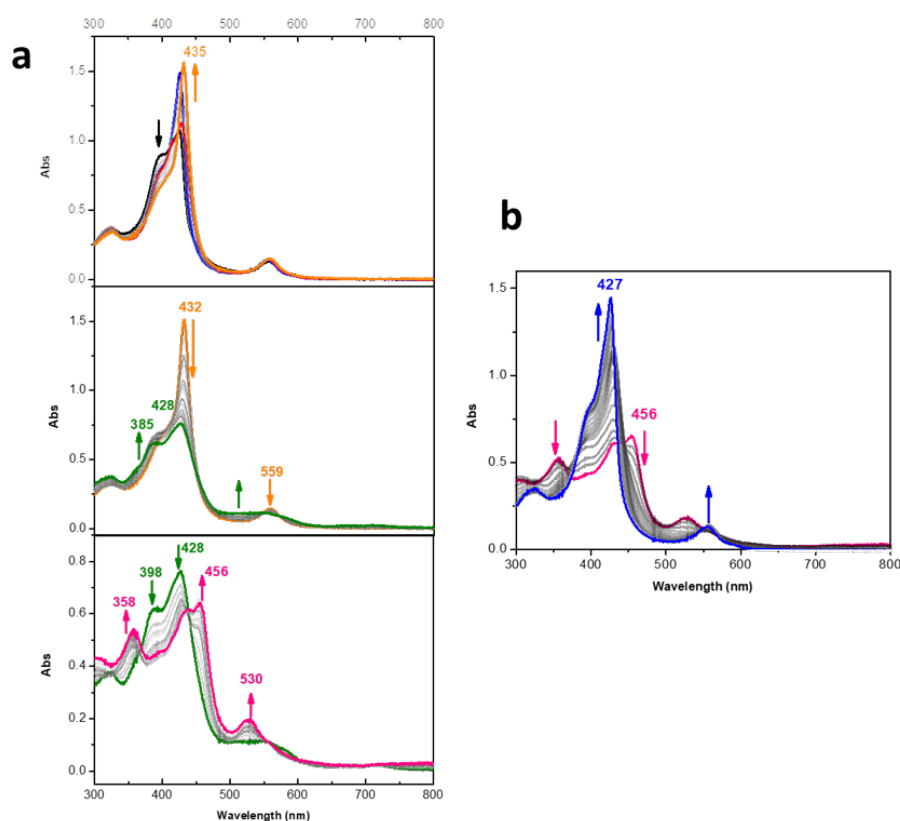


Figure 2.23: **a.** UV-Vis spectral evolution in spectroelectrochemistry experiment with **F₂₀TPPFe** 40 μ M in Ar-saturated DMF_{dry}, 0.2 M TBAPF₆, Pt working electrode, Pt counter electrode and Pt pseudoreference electrode; room temperature. Top: Fe(III) to Fe(II) reduction. Middle: Fe(II) to Fe(I) reduction. Bottom: Fe(I) to Fe(0) reduction. **b.** UV-Vis spectral evolution after spectroelectrochemical measurement, with no applied potential. Same experimental conditions as letter **a.**

this case, the spectra were recorded exclusively in DMF and in presence of 0.2 M of electrolyte, at room temperature. The changes observed were comparable to the ones observed for **UrFe**, with a more intense Soret band for the first reduction and gradual less intense Soret band for the next two oxidation states, accompanied by a red-shift. Possible degradation of the porphyrin during electrolysis was excluded by letting the system recover with no applied potential at the end of the measurement (Fig. 2.23, **b**). The recovery of the Soret band highlights that the changes observed are due to a reduction of the porphyrin and not the degradation of the catalyst. The final spectrum recorded seems to correspond to the intermediate Fe(II) state and not to the fully reoxidized Fe(III). We can rationalize this as the Fe(II) species is already stable enough in this conditions, where the cell has been previously purged with argon, so any further oxidation will be slower than the experiment time and only due to small leaks of the setup.

The spectra obtained in this section seem to be a good reference for the rest of the study. A comparison with the same type of experiment performed in presence of the CO₂ substrate will be provided later in the Chapter.

2.4.3 . Photoaccumulation of reaction intermediates

Another method was used to identify the reduced species. This time, the catalyst reduction was triggered photochemically instead of electrochemically. The term "photoaccumulation" is used to indicate the accumulation of species induced by shining continuous light.

In this case, the same principle used for the photocatalytic study was applied to generate the reduced forms of the **UrFe** catalyst, but in absence of substrate and water. In these conditions, the reduced iron porphyrin cannot transfer its electrons and it will tend to accumulate in solution.

To perform the experiment, a mixture of **UrFe**, [Ru(bpy)₃]²⁺ and BIH was prepared in the dark and in the glovebox to avoid any possible trace of water and oxygen. The measurement was performed both at low and room temperature thanks to a built-in three-window cryostat chamber (see Annex). Once again, the relative concentrations of the different species needed to be adjusted for this type of measurement. The same reasoning followed for photocatalysis also applies here (excess of PS with respect to the catalyst, and excess of SED with respect to the PS). However, the goal here is to observe spectral changes of the catalyst, which restricts us on the amount of [Ru(bpy)₃]²⁺ that can be added in solution. After some optimizations, 1.5 equivalents of ruthenium PS with respect to the iron porphyrin were used.

The measured changes in DMF_{dry} at -35 °C are shown in Fig. 2.24, a. The top graph displays the first recorded spectrum in cyan colour, overlaid with a reference Fe(III) spectrum previously obtained (blue trace). We can observe that the spectrum of the starting species is similar to the Fe(II) spectra recorded using the electrochemical method. Indeed, we estimated that in these conditions BIH is performing the first reduction already in the dark. This was also confirmed by mixing **UrFe** and BIH and recording the obtained spectrum (Fig. 2.25).

Once the blue LED was switched on, clear spectral changes were observed. Accurately lowering the LED intensity allowed us to detect the two further one electron reductions one after the other, as highlighted by the presence of isosbestic points. In the center and bottom graphs of Fig. 2.24, **a** a new band is visible in the 500 nm region when we compare these spectra to the ones of spectroelectrochemistry. This band corresponds to the accumulated Ru(I) (see Fig. 2.8), necessary to perform the successive reductions. All the

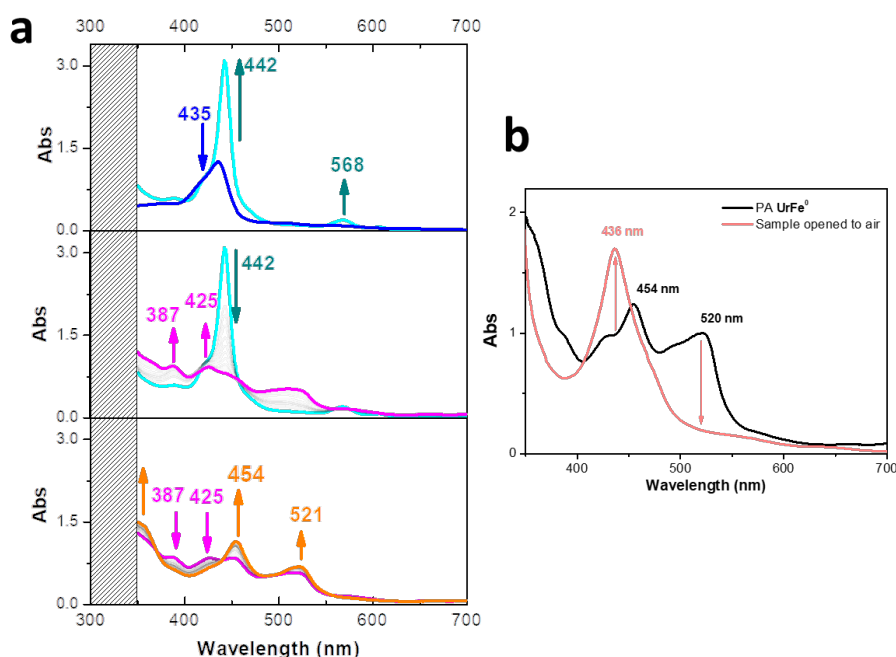


Figure 2.24: a. UV-Vis spectra recorded in photoaccumulation experiment with **UrFe** 10 μM , $[\text{Ru}(\text{bpy})_3]^{2+}$ 15 μM , BIH 7 mM in N_2 -saturated DMF_{dry} at $-35\text{ }^\circ\text{C}$. Top: reference spectra of **UrFe^{III}** under Ar and the first spectrum corresponding to **UrFe^{II}** reduced in the dark. Middle and bottom: spectral evolution with LED on ($\lambda_{\text{em}} = 460\text{ nm}$, 3 Wm^{-2}). b. UV-vis spectra of photoaccumulated (blue LED irradiation) **UrFe** 10 μM , $[\text{Ru}(\text{bpy})_3]^{2+}$ 30 μM , BIH 7 mM in N_2 -saturated DMF_{dry} at $-35\text{ }^\circ\text{C}$ before (black) and after (red) opening the sample to the air.

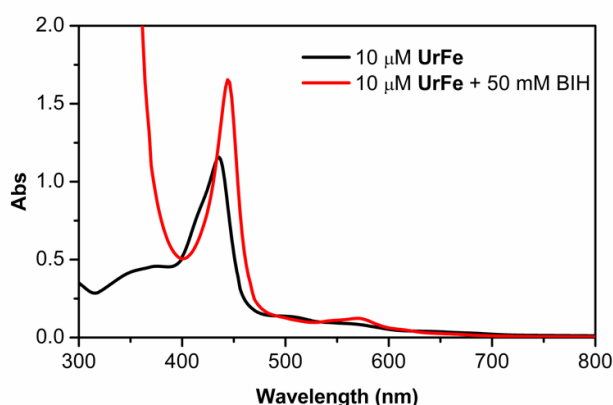


Figure 2.25: UV-vis reference spectra of 10 μM **UrFe** in Ar-saturated DMF alone (black) and with 50 mM BIH added (red).

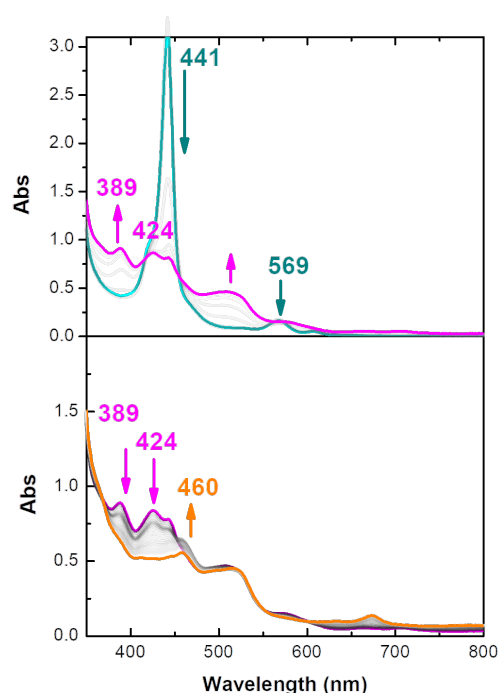


Figure 2.26: UV-Vis spectra recorded in photoaccumulation experiment with **UrFe** 10 μM , $[\text{Ru}(\text{bpy})_3]^{2+}$ 15 μM , BIH 7 mM in N_2 -saturated DMF_{dry} at room temperature. Top: reduction from Fe(II) to Fe(I). Bottom: reduction from Fe(I) to Fe(0). LED used: $\lambda_{\text{em}} = 460 \text{ nm}$, 3 Wm^{-2} .

other features observed in this measurement match well with those previously observed in the SEC, and confirm the origin of such spectral changes. The small shifts in wavelengths can be justified by the different temperature and components in solution between the two methods. Because of the presence of BIH saturating the near-UV region, the band at 320 nm could not be observed. When the Fe(0) species was accumulated, the sample was then left in the dark and re-opened to air to verify that no degradation of the porphyrin had occurred. The red trace of Fig. 2.24, **b** displays the full recovery of the Fe(III) original species, with a maximum absorbance at 436 nm.

The same experiment was also performed at room temperature (Fig. 2.26). Once again, the first species detected corresponds to the Fe(II) state and when the light is switched on, similar trends of changes are observed. The main difference here is that the highly reduced species (Fe(I) and Fe(0)) are less stable over time.

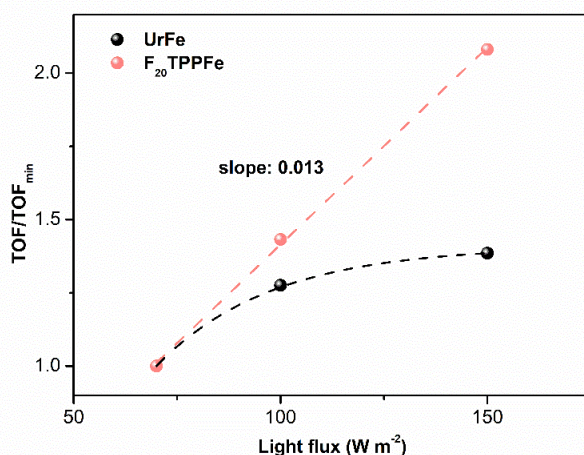


Figure 2.27: Dependency of the reaction kinetics (TOF) on the light flow for **UrFe** (black) and for **F₂₀TPPFe** (red). 20 μ M catalyst, 1 mM [Ru(bpy)₃]²⁺ photosensitizer, 50 mM BIH sacrificial electron donor in CO₂-saturated DMF/H₂O 9:1, blue LED irradiation (λ_{em} = 460 nm).

2.5 . Unravelling the mechanism

With all the data gathered, we now turned to understanding in depth the successive events in the photocatalytic mechanism.

2.5.1 . Limiting factors in the catalysis

To understand what is limiting the photocatalytic reaction rate in the optimized conditions, the same reaction was performed varying light intensity, CO₂ concentration and acid strength.

As described in the previous section, switching the light source from white to blue LED caused an obvious increase of the reaction rate. Further increasing the light power of the blue LED resulted in only a small increase in TOF. Fig. 2.27 shows how the normalized TOF values tend towards a plateau in the case of the **UrFe** catalyst (black trace). On the other hand, the **F₂₀TPPFe** catalyst in the same experimental conditions follows a linear increase of TOF with increasing light flux (red trace). This can be interpreted as the limiting step may be light-induced in the case of **F₂₀TPPFe**.

Studying the effect of the acid strength is also an important control experiment, as protonation had previously been found to be the rate determining step (RDS) in the electrocatalytic reduction of CO₂ by **UrFe** [1]. For this purpose, different proton sources with increasing acid strength were used in comparison with H₂O: trifluoroethanol (TFE) and phenol (PhOH). Comparing the three different proton sources, only a small effect is visible on the reaction rate, suggesting that the protonation is not the main factor limiting the rate (Fig. 2.28). As

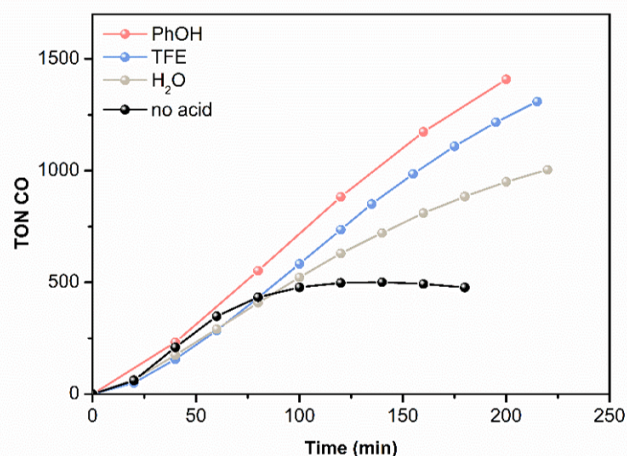


Figure 2.28: Time evolution of CO produced under light irradiation with a white LED ($\lambda > 405$ nm, 100 W m^{-2}) of **UrFe** as catalyst with $20 \mu\text{M}$ concentration; $[\text{Ru}(\text{bpy})_3]^{2+}$ photosensitizer 1 mM, BIH sacrificial electron donor 50 mM in CO_2 -saturated DMF and 100 mM PhOH (red), 100 mM TFE (blue), 100 mM H_2O (grey) or in absence of proton (black).

mentioned earlier, some catalytic activity was recorded also in absence of added proton source thanks to BIH protons until their full consumption that is likely to cause the stop in catalytic activity in less than 100 min. In the first part of the curve, before the catalysis slows down, the rate seems quite comparable for the four different conditions, confirming that the source of proton does not really matter, as it is not the one dictating the reaction rate.

The effect of the protonation step on the reaction kinetics was also investigated in terms of kinetic isotopic effect (KIE) measurement, where the reaction rates in presence of H_2O and D_2O were compared (Fig. 2.29). In electrocatalytic conditions, a KIE value of 5.77 was found for the **UrFe** catalyst, which confirmed that the protonation is RDS [1]. However, in the photocatalytic conditions studied here, a KIE of 1.17 was determined, which supports the limited contribution of the protonation step to the overall reaction rate. This outcome is an interesting point to prove how electro- and light-induced catalysis may follow two different pathways, even with the same molecular catalyst. Lastly, the effect of substrate concentration on the photocatalytic rate was studied. We found here a clear linear dependency of the reaction rate (TOF) on the substrate concentration until standard saturated conditions (see Fig. 2.30). Such a result suggests that CO_2 binding onto the catalyst is involved in the RDS of the photocatalytic cycle in the optimized conditions.

We then aimed to investigate further the interaction of the **UrFe** catalyst with the CO_2 substrate, by performing different *in situ* spectroscopies, as described in the next section.

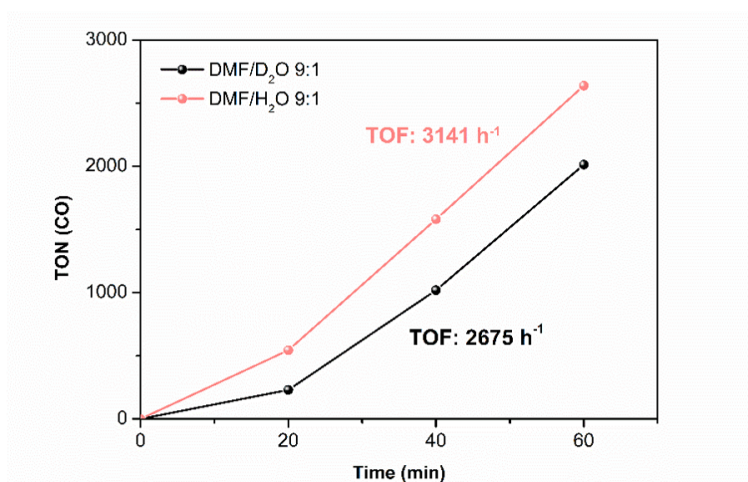


Figure 2.29: Time evolution of CO produced under light irradiation with a blue LED ($\lambda_{em}=460$ nm 100 Wm^{-2}) of **UrFe** as catalyst with $20 \mu\text{M}$ concentration; $[\text{Ru}(\text{bpy})_3]^{2+}$ photosensitizer 1 mM , BIH sacrificial electron donor 50 mM in CO_2 -saturated DMF/ H_2O 9:1 (red) and CO_2 -saturated DMF/ D_2O 9:1 (black).

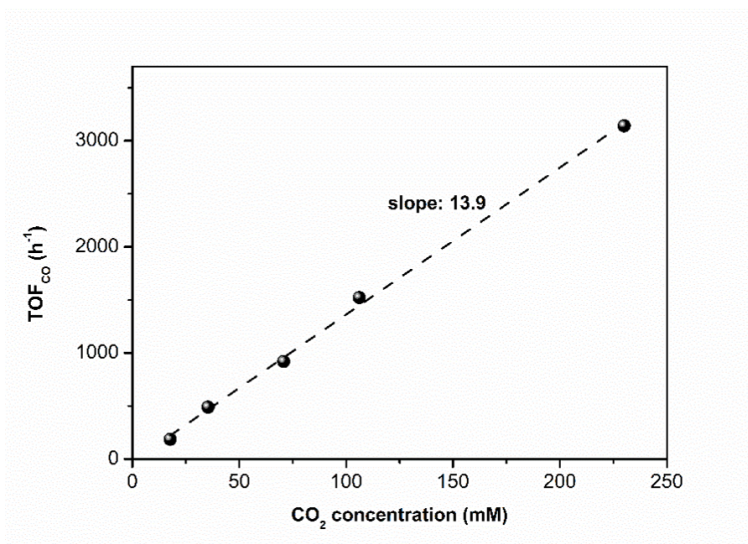


Figure 2.30: Dependency of the reaction kinetics (TOF) on the amount of CO_2 added for **UrFe** $20 \mu\text{M}$ catalyst, 1 mM $[\text{Ru}(\text{bpy})_3]^{2+}$ photosensitizer, 50 mM BIH sacrificial electron donor in DMF/ H_2O 9:1, blue LED irradiation ($\lambda_{em}=460$ nm 100 Wm^{-2}).

2.5.2 . *In situ* investigation of CO₂ binding to UrFe

From the above experiments, we deduced that the substrate binding is limiting the photocatalytic reaction rate. In the first place, we aimed to monitor the UV-vis changes *in situ* to determine if we observe the iron porphyrin species before CO₂ binding during the photocatalytic cycle. To do so, we performed the same type of experiment as for the photoaccumulation described above, with the only difference being that now protons and CO₂ were also added, in order to be in catalytic conditions. It should be pointed out once again that the conditions are somewhat different in photoaccumulation compared to photocatalysis, as the PS and SED concentrations are lower, to allow the observation of the catalyst's UV-vis changes.

In steady-state conditions, we expect to detect only the signals of the species that precedes the rate determining step, being the slowest of the cycle. The formation and decay of all other intermediates are faster and not observable in these conditions. In this given case, we expected to observe the iron porphyrin species just before the binding of CO₂, in its Fe(0) state. The outcome of the experiment was unexpected and it suggested us to rethink the reaction mechanism for the **UrFe**-catalyzed photocatalysis. In Fig. 2.31 we can see the spectral evolution of **UrFe** over time when the LED is switched on. Here, the initial spectrum (black trace) corresponds to the Fe(III) species, possibly because the presence of water hampers the removal of oxygen traces and keep the iron porphyrin in the more oxidized state. A quick evolution to Fe(II) is observed as soon as the light is turned on (blue trace) to then decay to a state that remains stable (red trace) until the full consumption of substrate (orange trace). In the experiment, a small amount of CO₂ was added (less than the BIH amount) to ensure that all of it could be converted to products. By doing so, we can follow the "end" of the reaction by accumulation of Ru(I) in solution (orange trace). The steady-state spectrum does not seem to match with the Fe(0) spectral fingerprints described in the previous sections. Instead the spectrum seems to correspond to what was found to be the Fe(I) state, suggesting that CO₂ binding occurs already at the Fe(I) oxidation state.

Another hypothesis that has been advanced in reported studies, is that Fe(II)-CO can accumulate in solution during photocatalytic reactions as steady-state [20]. The reference spectrum of Fe(II)-CO for **UrFe** is shown in Fig. 2.32. When CO is added on the Fe(II) solution, Fe(II)-CO is formed quickly and it is quite stable thanks to the affinity for CO of Fe(II) porphyrins. In the visible region, a blue-shift is observed for the Soret band, still maintaining high extinc-

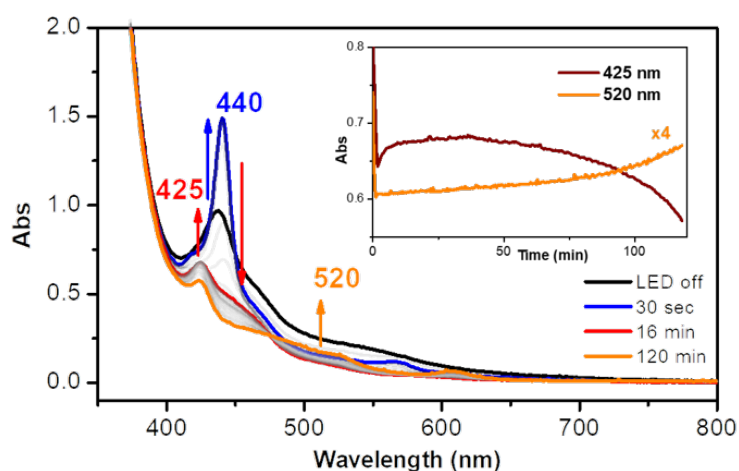


Figure 2.31: UV/Vis spectra recorded in photoaccumulation experiment with **UrFe** 5 μM , $[\text{Ru}(\text{bpy})_3]^{2+}$ 20 μM , BIH 70 mM in DMF/H₂O 9:1 and 60 mM CO₂. Blue LED ($\lambda_{\text{em}} = 460 \text{ nm}$, 70 Wm^{-2}), 25 °C. Inset: Kinetic profile of Fe(I) (brown) and Ru(I) (orange) species.

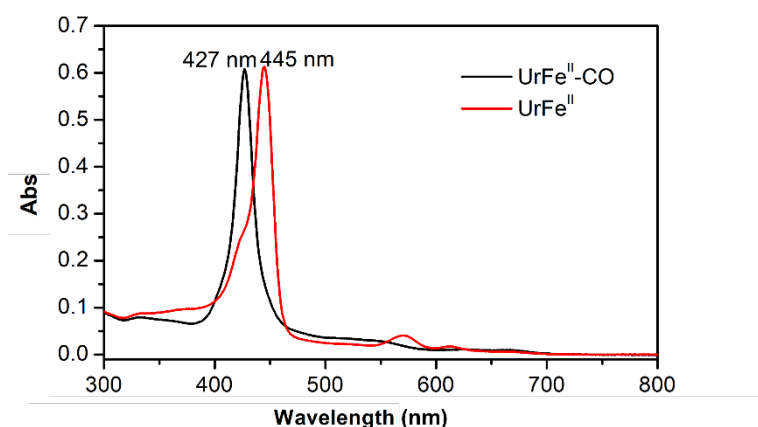


Figure 2.32: UV-vis reference spectra of chemically prepared **UrFe^{II}** in N₂-saturated DMF (red) and with CO-saturated DMF (black).

tion coefficient.

The wavelength measured in the steady state experiment (Fig. 2.31) is quite close to the reference for Fe(II)-CO. However, this hypothesis is considered less likely, since upon shining light, a rapid photolysis of the Fe-CO bond was recorded (Fig. 2.33 and 2.34). In time-resolved LFP experiment (Fig. 2.33), the generation of Fe(II) upon flashing is underlined by the appearance of the band at 436 nm, together with the bleaching of the Fe(II)-CO signal at 419 nm. It should be noted that this experiment was performed in ACN so the wavelength values may be slightly affected. The inset on the same figure also shows that re-coordination of the CO to the Fe(II) is also quite rapid.

In continuous light irradiation, the effect of de-coordination and re-coordination,

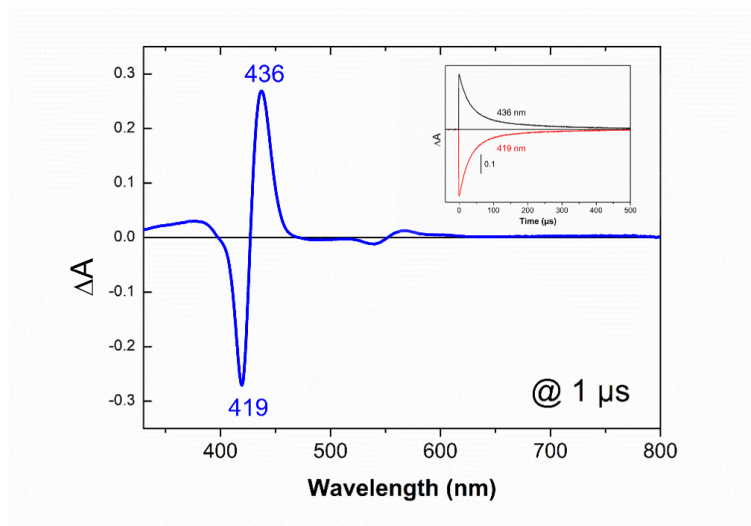


Figure 2.33: UV-vis laser flash photolysis of **UrFe** (OD 420=1) at 1 μ s delay, in CO-saturated ACN/H₂O 9:1, 25 mM NaAsc, exc 460 nm, 15 mJ. Inset: kinetic traces at 419 nm and 436 nm.

is purely an equilibrium which will be affected also by CO concentration in solution. The evolution upon continuous irradiation of an Fe(II)-CO solution is shown in Fig. 2.34. A coexistence of the two species can be evidenced. Also, we assume that in catalytic conditions, de-coordination of CO will be more favoured as the CO₂ reduction catalysis proceeds, otherwise product evolution would quickly stop. With these reasons we argue that Fe(II)-CO should not be the steady-state species in our system.

We then investigated possible binding of CO₂ on the **UrFe^I** state. We performed once again spectroelectrochemical measurements, but this time in CO₂ atmosphere. The obtained changes are presented in Fig. 2.35. When comparing the changes between Ar and CO₂, no particular effect was seen on Fe(III) and Fe(II) states. However, some differences can be seen when comparing Fe(I) spectral fingerprints under Ar and under CO₂ (pink traces in Fig. 2.35 bottom graphs), the most obvious being the disappearance of the band at 320 nm. The same set of results is also displayed in Fig. 2.36, where the traces under CO₂ and Ar are overlaid for better comparison. This first evidence supports the hypothesis of possible binding of CO₂ before reaching the Fe(0) redox state.

For comparison, the same experiment was also performed on **F₂₀TPPFe**. The spectral evolution in presence of CO₂ is illustrated in Fig. 6.14. The spectra until the Fe(0) state seem quite similar with what was obtained under Ar and shown previously in this Chapter. No clear changes were observed in the spectra of the Fe(I) state when compared to the same species under Ar (see overlay of Fig. 2.37).

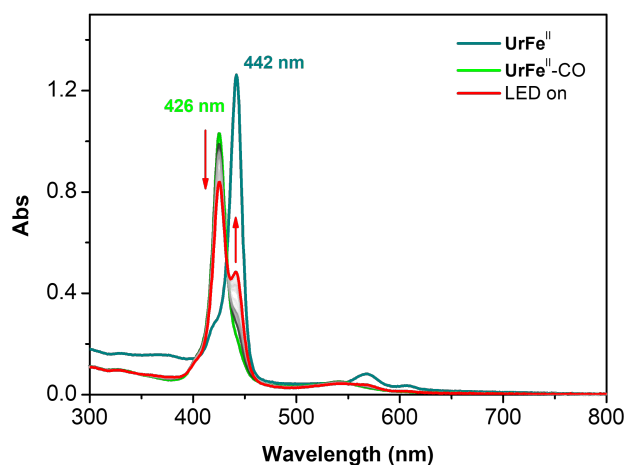


Figure 2.34: UV-vis spectral evolution of 4 μM $\text{UrFe}^{\text{II}}\text{-CO}$ solution in DMF_{dry} irradiated with blue LED (100 W m^{-2}) at room temperature. In blue: reference spectrum of UrFe^{II} .

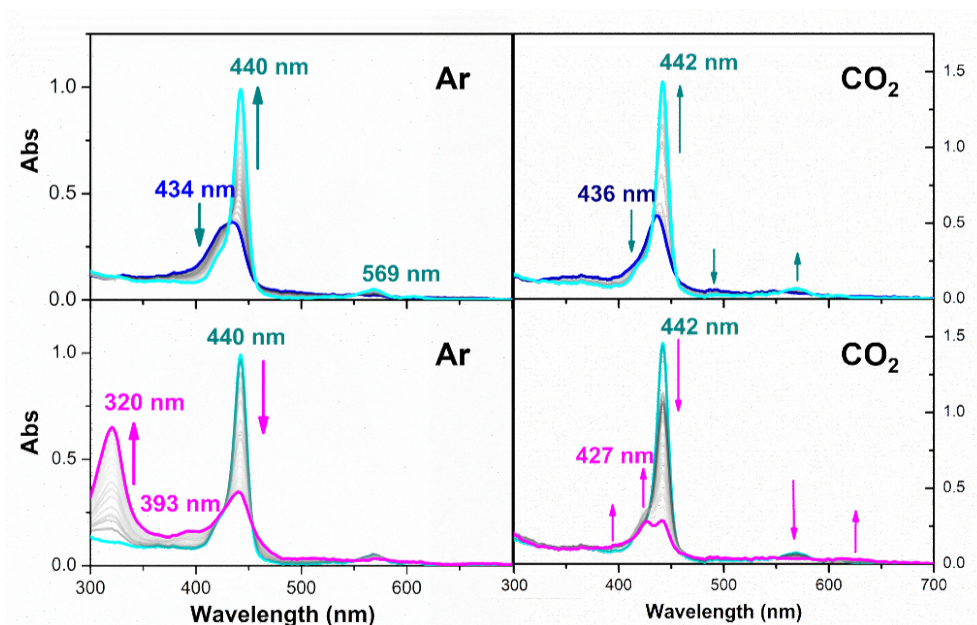


Figure 2.35: UV-vis spectral evolution in spectroelectrochemistry experiment with UrFe 40 μM in Ar-saturated DMF_{dry} (left) and CO_2 -saturated DMF_{dry} (right), 0.2 M TBAPF_6 , Pt Working Electrode, Pt Counter Electrode and Ag pseudo-Reference Electrode; Room Temperature. Top: Fe(III) to Fe(II) reduction; Bottom: Fe(II) to Fe(I) reduction.

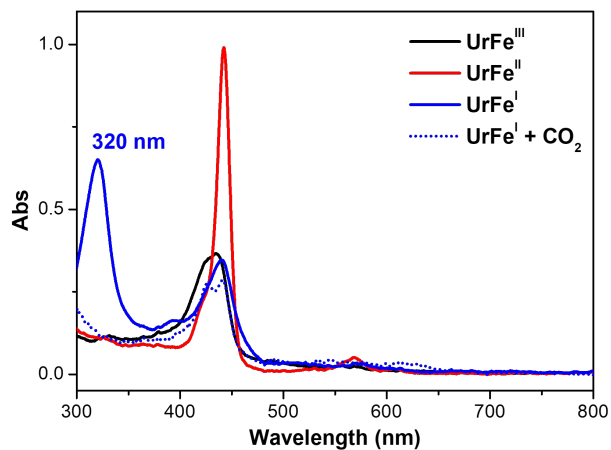


Figure 2.36: CO₂ influence on the **UrFe^I** reduced states monitored by spectroelectrochemistry in the UV-Visible region in DMF. **UrFe^{III}** (black), **UrFe^{II}** (red) and **UrFe^I** state (blue solid line) in Ar and comparison of **UrFe^I** in presence of CO₂ (blue dashed line).

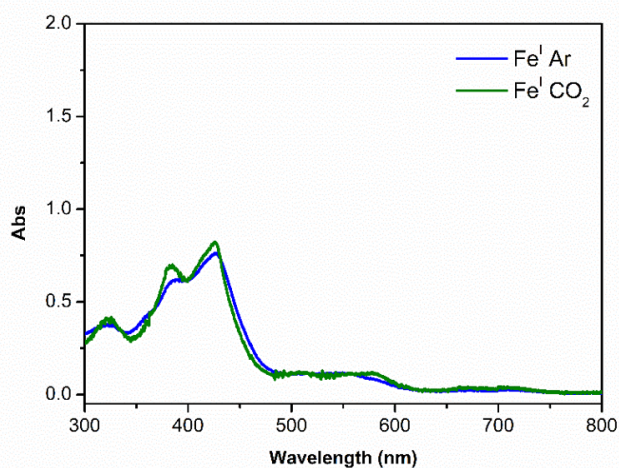


Figure 2.37: Comparison of the Fe(I) state of **F₂₀TPPFe** in Ar (blue) and CO₂ (green) obtained in spectroelectrochemistry.

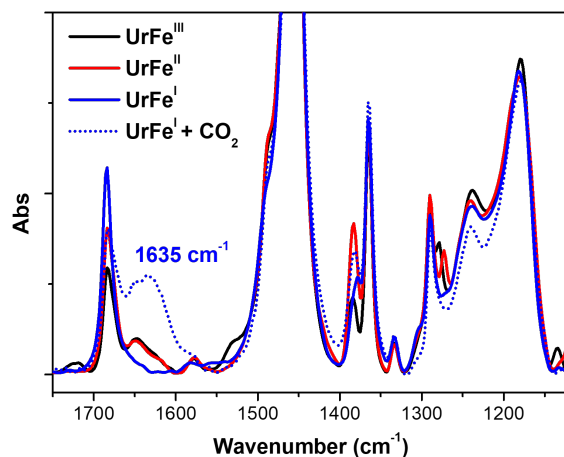


Figure 2.38: CO₂ influence on the **UrFe^I** reduced states monitored by spectroelectrochemistry in the infrared region in THF. **UrFe^{III}** (black), **UrFe^{II}** (red) and **UrFe^I** state (blue solid line) in Ar and comparison of **UrFe^I** in presence of CO₂ (blue dashed line).

One more evidence for CO₂ binding to **UrFe^I** comes from infrared spectroelectrochemistry (IR-SEC). To perform this measurement we used an ATR-FTIR instrument (see Annex) with the working glassy carbon electrode as close as possible to the ATR prism. Controlled potentials electrolysis were performed in a step-wise manner and it was possible to monitor the IR changes until the Fe(I) oxidation state under Ar and under CO₂. Once again, comparison on the first reduction under Ar and under CO₂ did not evidence any significant change. Instead, when the reduction was continued further to reach Fe(I) oxidation state, a clear band started rising around 1635 cm⁻¹ (see Fig. 2.38). A previous study, mentioned in the introduction chapter, had also reported a vibration coming from the asymmetric stretching of the C=O bond of a CO₂ molecule sandwiched between two Co centers of a bimetallic catalyst around the same spectral region [21].

Such encouraging result supported once more our hypothesis of CO₂ binding before the Fe(0) oxidation state for the **UrFe** catalyst. We then attempted to assign the observed vibrational signature using Density Functional Theory (DFT). This was performed using B3LYP hybrid functional with dispersion correction for solvent interaction. DFT calculations were conducted by Dr. M. Sircoglou from our research group. The **UrFe^I-CO₂** intermediate was computed and more detailed discussion will be given in the section just after. Fig. 2.39 shows the simulated IR spectrum for such intermediate, with the new bands characteristic of the CO₂ interacting with the Fe(I) complex highlighted by red dots. Even though the most intense band expected at 1293.9 cm⁻¹ was

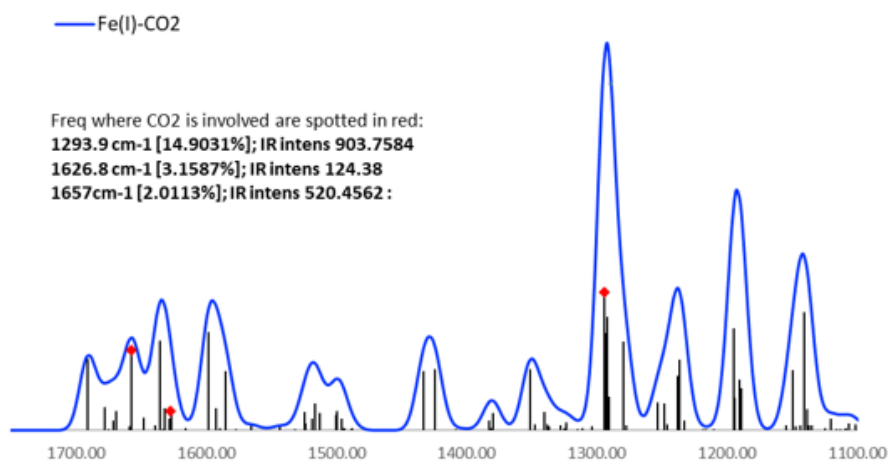


Figure 2.39: Theoretical IR stick and band spectrum (gaussian fit $w_{1/2}=15\text{ cm}^{-1}$) obtained for $\alpha\alpha\text{UrFe}^{\text{I}}\text{-CO}_2$.

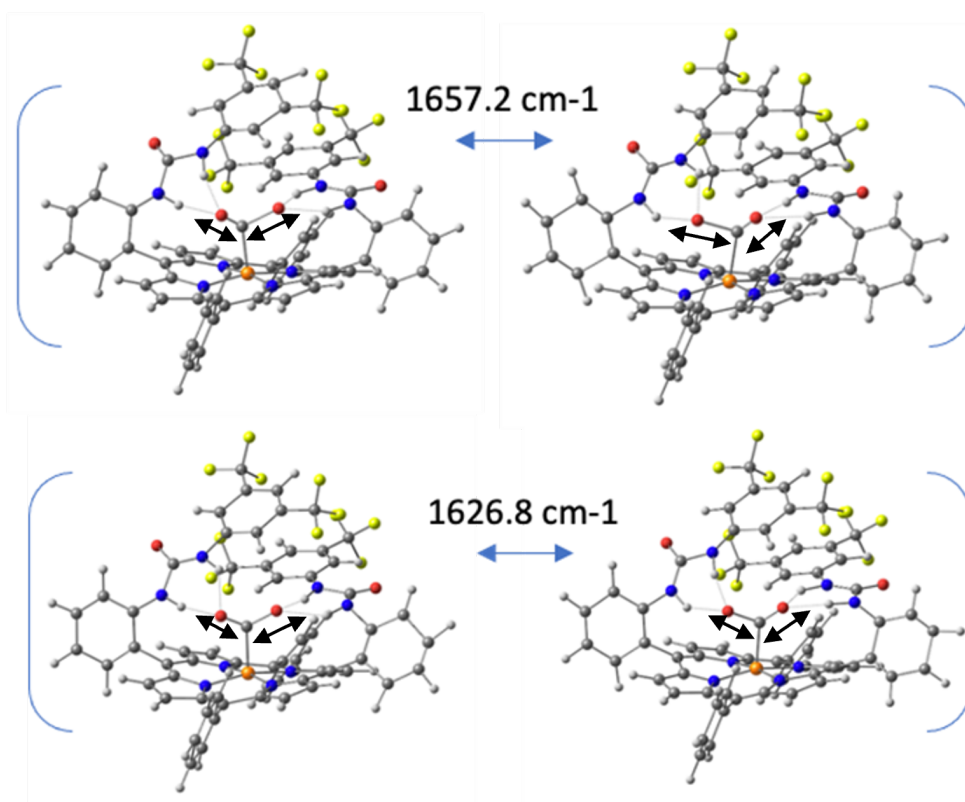


Figure 2.40: Vibration modes associated to the CO₂ fragment in $\alpha\alpha\text{UrFe}^{\text{I}}\text{-CO}_2$.

covered by the electrolyte, we could still see the correspondence of experimental and theoretical values from the frequencies estimated at 1626.8 cm⁻¹ and 1657 cm⁻¹. These were assigned as two asymmetric stretching modes of the C=O bond, depicted in Fig. 2.40.

2.5.3 . DFT and mechanism proposal

As it was just acknowledged above, DFT calculations enabled us to have a comparison on the likelihood and stability of the proposed Fe(I)-CO₂ intermediate, both for **UrFe** and **F₂₀TPPFe** catalysts. For both iron complexes it was possible to describe the tentative Fe(I)-CO₂ intermediate with DFT. The stable geometries for the Fe(I) state with and without bound-CO₂ are shown in Fig. 2.41 and 2.42. It should be specified that to reduce the calculation time, two of the **UrFe** porphyrin arms were removed (**ααUrFe**). The two faces of the porphyrin are indeed equivalent and the opposite face should not affect the interaction with the CO₂ substrate. Comparing the structures by partial charges and spin density distribution on the different elements of the intermediate, no significant changes are observed between **ααUrFe^I-CO₂** and **F₂₀TPPFe^I-CO₂**. However, when looking at the coordination free energy of these intermediates (Table 2.3), we found that the CO₂ adduct for **UrFe^I** lays at 0.78 kcal mol⁻¹ above the dissociated pair, whereas the same coordination for **F₂₀TPPFe^I** is 10.46 kcal mol⁻¹ higher in energy than the dissociated couple. This results in a quite unfavourable binding of CO₂ on Fe(I) for **F₂₀TPPFe** ($k_A = 9.19 \times 10^{-8} \text{ M}^{-1}$), with an association constant 8 orders of magnitude smaller than for **UrFe^I**. Such huge difference has to be attributed to the effect of the donating H-bond urea arms. In the PBE0 geometry of Fig. 2.42, we can see that the urea arms in the η¹ coordination of CO₂ to the metal center induced a bending of the OCO with an angle of 128.4°, compared to the 139.5° for **F₂₀TPPFe**. The further bending of the CO₂ substrates also corresponds to a substantial activation.

Table 2.3: Predicted coordination energetics in the Fe(I) oxidation state at 298K

	ΔG coord (kcal/mol)	k_D (M ⁻¹)	k_A (M ⁻¹)	ΔE (V)
ααUrFe(I)	0.78	0.87	1.16	0.006
F₂₀TPPFe(I)	10.46	1.09·10 ⁷	9.19·10 ⁻⁸	0.000

From the partial charges calculated (Fig. 2.42) we can deduce that a more accurate description of this intermediate would be **UrFe^{II}-CO₂⁻**, given the -0.67 charge transferred from the metal to the CO₂. Overall, DFT calculations

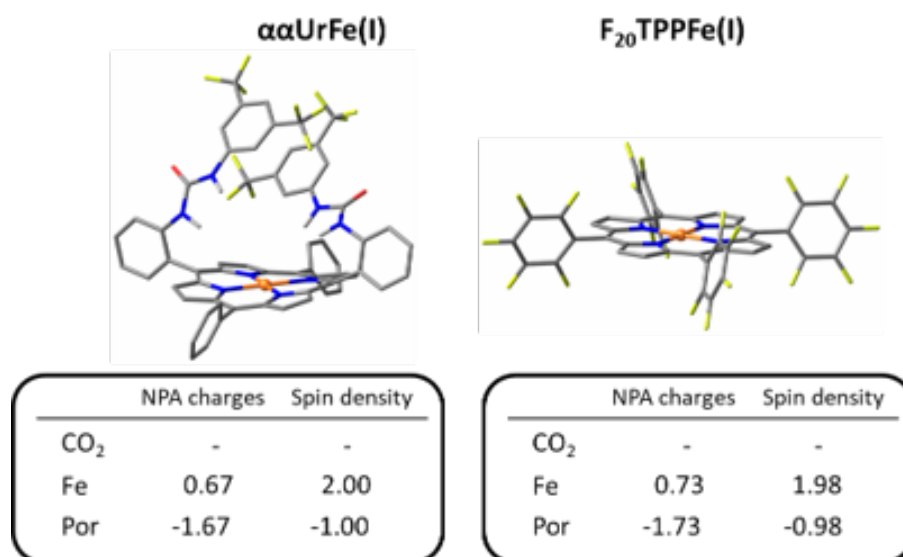


Figure 2.41: PBE0 geometries, partial charges and spin densities of $\alpha\alpha\text{UrFe}^{\text{I}}$ and $\text{F}_{20}\text{TPPFe}^{\text{I}}$.

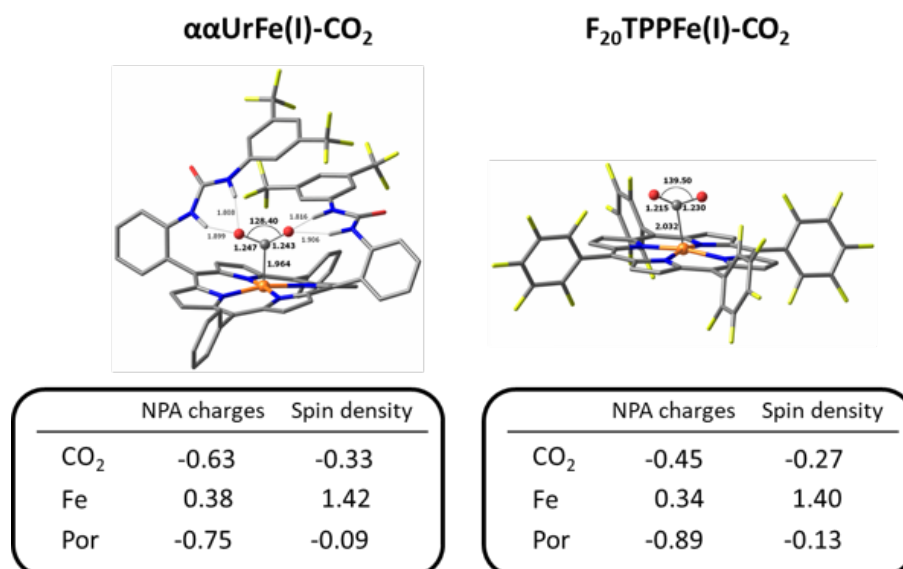


Figure 2.42: PBE0 geometries, partial charges and spin densities of $\alpha\alpha\text{UrFe}^{\text{I}}\text{-CO}_2$ and $\text{F}_{20}\text{TPPFe}^{\text{I}}\text{-CO}_2$.

support the possibility of interaction of CO₂ on the Fe(I) state in the case of **UrFe**, whereas the earlier binding at Fe(I) oxidation state seems much more unfavourable for **F₂₀TPPFe**.

With all this information, we attempted to give an explanation behind the striking difference in photocatalytic activity for the iron porphyrins studied. In the case of **TPPFe**, it was argued in the previous section that the driving force to reach the Fe(0) state is very small, given the redox potentials, quite more negative than the Ru(II)/Ru(I) couple of the photosensitizer (-1.695 V vs. SCE). However, **UrFe** and **F₂₀TPPFe** have very comparable CVs under Ar. We have seen in Section 2.5.1, that what limits the rate of the photocatalytic reaction in our experimental conditions is most likely the substrate binding. We therefore hypothesize that the introduction of urea arms in the second coordination sphere of the catalyst induces a great enhancement of photocatalytic activity, by unlocking a new reaction pathway where the Fe(I) state can already interact and activate the substrate.

Going back to the cyclic voltammograms of the three catalysts under Ar and under CO₂, which we had previously reported (Fig. 2.43) [1]. We had already observed that when CO₂ is added in solution, but still not in catalytic regime (absence of protons), the last reduction of **UrFe** has an anodic shift of around 70 mV. This phenomenon was not observed for the other iron porphyrins (Fig. 2.43). With our new findings of the Fe(I)-CO₂ we may now say that this new species formed is more easily reduced than when the bound-CO₂ is not present. Such gain in reduction potential can therefore increase the reaction driving force, resulting in one of the highest reaction rates reported for molecular photo-induced CO₂ reduction.

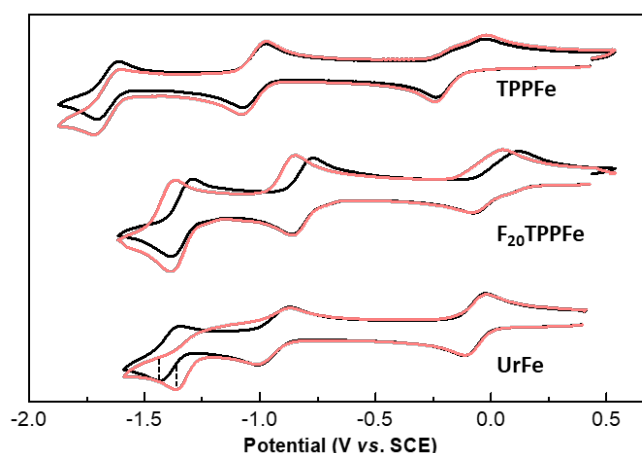


Figure 2.43: Cyclic voltammograms of the studied iron porphyrins in Ar (black) and CO₂ (red) atmospheres, 1 mM catalyst, 0.1 M TBAPF₆ in DMF_{dry}, 100 mV s⁻¹.

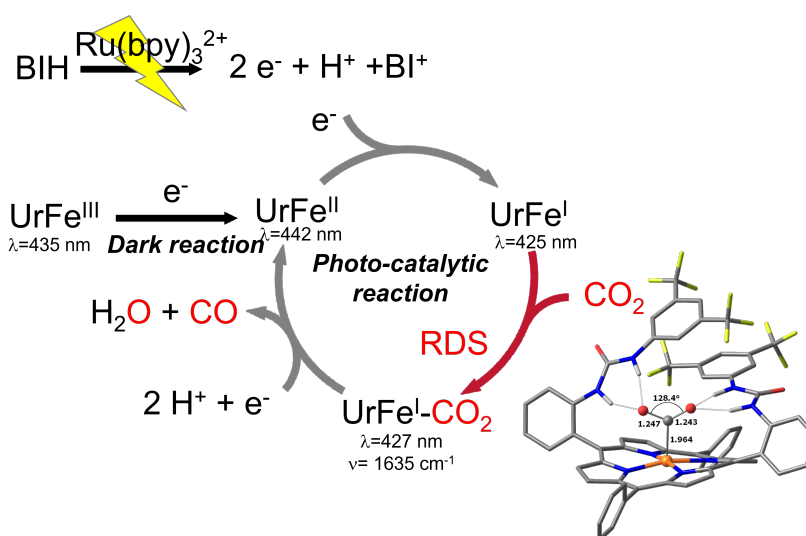


Figure 2.44: Proposed mechanism for the light-induced CO₂ reduction to CO with **UrFe** with the species characterized.

Finally, we summarized our efforts in the understanding of the photocatalytic mechanism by proposing a mechanism for the reaction of the catalytic reduction of CO₂ to CO by **UrFe**. As represented in Fig. 2.44, **UrFe^{II}** enters the catalytic cycle after reduction in the dark of **UrFe^{III}** by BIH. The first light-induced step involves the reductive of the excited state of [Ru(bpy)₃]²⁺, to form the reducing [Ru(bpy)₃]⁺ which transfers one electron to the catalyst to generate **UrFe^I**. UV-vis monitoring of the reaction seems to suggest that this latter is the steady-state of the catalytic cycle, preceding the rate determining step (RDS) of catalysis, that consists in the CO₂ binding to form the formal [**UrFe^I-CO₂**] adduct. Given the small KIE value found, we cannot assess that the protonation is involved in the RDS. The following steps involve one more electron inputted and two proton transfers to release the product, CO. The sequence of the reduction and protonations and possible coupling of the two has not been fully determined yet, but more studies are undergoing in our research group. Finally after cleaving the Fe(II)-CO bond, the product is released and **UrFe^{II}** enters again the catalytic cycle.

2.6 . Conclusions

Light-induced CO₂ reduction can be quite complex to monitor and understand, since many different elements are present in the reaction mixture. In this study, we were able to understand the role that different factors play in photocatalytic activity. By choosing the appropriate chromophore, we could study the reactivity of a family of iron porphyrins, in particular by highlighting the crucial role that the second coordination sphere can play in catalysis.

The urea-modified **UrFe** catalyst shows excellent activity for CO production for a homogeneous system, in terms of stability (TON), rate (TOF) and product selectivity (nearly 100%). This system was further studied with different spectroscopic techniques, in order to identify reactive intermediates and the rate determining step. Working with a homogeneous setup allowed a rather facile application of these techniques that allowed us to obtain important pieces of information. The reduced forms of the porphyrin could be identified, and an unexpected interaction of CO₂ with the Fe(I) state was evidenced. Throughout the study, we aimed to compare this catalyst with **F₂₀TPPFe**, having the same reduction potentials, but lacking the second coordination sphere. For the latter, we could not detect any interaction of CO₂ at the Fe(I) state, which brought us to think that the early binding of substrate for **UrFe** is crucial to increase the driving force of the reaction, unlocking a new species that is more easily reduced. From our results we also deduced that substrate binding may be determining the reaction rate in our photocatalytic conditions.

Overall, a lot still has to be learnt to follow-up multiple electron-transfer processes, but we were able to set up some simple methods to already extract some important information on the reaction mechanism.

Bibliography

- (1) Gotico, P.; Boitrel, B.; Guillot, R.; Sircoglou, M.; Quaranta, A.; Halime, Z.; Leibl, W.; Aukauloo, A. Second-Sphere Biomimetic Multipoint Hydrogen-Bonding Patterns to Boost CO₂ Reduction of Iron Porphyrins. *Angewandte Chemie International Edition* **2019**, *58*, 4504–4509.
- (2) Khadhraoui, A.; Gotico, P.; Boitrel, B.; Leibl, W.; Halime, Z.; Aukauloo, A. Local ionic liquid environment at a modified iron porphyrin catalyst enhances the electrocatalytic performance of CO₂ to CO reduction in water. *Chemical Communications* **2018**, *54*, 11630–11633.
- (3) Patel, J.; Yuan, X.; Marinho, S. M.; Leibl, W.; Remita, H.; Aukauloo, A. Visible light-driven simultaneous water oxidation and quinone reduction by a nano-structured conjugated polymer without co-catalysts. *Chemical Science* **2020**, *11*, 7324–7328.
- (4) Herrero, C.; Lassallekaiser, B.; Leibl, W.; Rutherford, A.; Aukauloo, A. Artificial systems related to light driven electron transfer processes in PSII. *Coordination Chemistry Reviews* **2008**, *252*, 456–468.
- (5) Gotico, P.; Del Vecchio, A.; Audisio, D.; Quaranta, A.; Halime, Z.; Leibl, W.; Aukauloo, A. Visible-Light-Driven Reduction of CO₂ to CO and Its Subsequent Valorization in Carbonylation Chemistry and ¹³C Isotope Labeling. *ChemPhotoChem* **2018**, *2*, 715–719.
- (6) Khadhraoui, A.; Gotico, P.; Leibl, W.; Halime, Z.; Aukauloo, A. Through-Space Electrostatic Interactions Surpass Classical Through-Bond Electronic Effects in Enhancing CO₂ Reduction Performance of Iron Porphyrins. *ChemSusChem* **2021**, *14*, 1308–1315.
- (7) Cerfontaine, S.; Troian-Gautier, L.; Wehlin, S. A. M.; Loiseau, F.; Cauët, E.; Elias, B. Tuning the excited-state deactivation pathways of dinuclear ruthenium(II) 2,2'-bipyridine complexes through bridging ligand design. *Dalton Transactions* **2020**, *49*, 8096–8106.
- (8) Arias-Rotondo, D. M.; McCusker, J. K. The photophysics of photoredox catalysis: a roadmap for catalyst design. *Chemical Society Reviews* **2016**, *45*, 5803–5820.
- (9) Durham, B.; Caspar, J. V.; Nagle, J. K.; Meyer, T. J. Photochemistry of tris(2,2'-bipyridine)ruthenium(II) ion. *Journal of the American Chemical Society* **1982**, *104*, 4803–4810.
- (10) Zhu, X.-Q.; Zhang, M.-T.; Yu, A.; Wang, C.-H.; Cheng, J.-P. Hydride, Hydrogen Atom, Proton, and Electron Transfer Driving Forces of Various Five-Membered Heterocyclic Organic Hydrides and Their Reaction Intermediates in Acetonitrile. *Journal of the American Chemical Society* **2008**, *130*, 2501–2516.
- (11) Prier, C. K.; Rankic, D. A.; MacMillan, D. W. C. Visible Light Photoredox Catalysis with Transition Metal Complexes: Applications in Organic Synthesis. *Chemical Reviews* **2013**, *113*, 5322–5363.
- (12) Ouyang, T.; Huang, H.-H.; Wang, J.-W.; Zhong, D.-C.; Lu, T.-B. A Dinuclear Cobalt Cryptate as a Homogeneous Photocatalyst for Highly Selective and Efficient Visible-Light Driven CO₂ Reduction to CO in CH₃CN/H₂O Solution. *Angewandte Chemie International Edition* **2017**, *56*, 738–743.
- (13) Yuan, H.; Cheng, B.; Lei, J.; Jiang, L.; Han, Z. Promoting photocatalytic CO₂ reduction with a molecular copper purpurin chromophore. *Nature Communications* **2021**, *12*, 1835.
- (14) Thoi, V. S.; Kornienko, N.; Margarit, C. G.; Yang, P.; Chang, C. J. Visible-Light Photoredox Catalysis: Selective Reduction of Carbon Dioxide to Carbon Monoxide by a Nickel N-Heterocyclic Carbene-Isoquinoline Complex. *Journal of the American Chemical Society* **2013**, *135*, 14413–14424.
- (15) Hawecker, J.; Lehn, J.-M.; Ziesel, R. Photochemical reduction of carbon dioxide to formate mediated by ruthenium bipyridine complexes as homogeneous catalysts. *Journal of the Chemical Society, Chemical Communications* **1985**, 56.

- (16) Rao, H.; Bonin, J.; Robert, M. Toward Visible-Light Photochemical CO₂-to-CH₄ Conversion in Aqueous Solutions Using Sensitized Molecular Catalysis. *The Journal of Physical Chemistry C* **2018**, *122*, 13834–13839.
- (17) Lexa, D.; Momenteau, M.; Mispelter, J. Characterization of the reduction steps of Fe(III) porphyrins. *Biochimica et Biophysica Acta (BBA) - General Subjects* **1974**, *338*, 151–163.
- (18) Connelly, N. G.; Geiger, W. E. Chemical Redox Agents for Organometallic Chemistry. *Chemical Reviews* **1996**, *96*, 877–910.
- (19) De Silva, C.; Czarnecki, K.; Ryan, M. D. Visible and resonance Raman spectra of low valent iron porphyrins. *Inorganica Chimica Acta* **1999**, *287*, 21–26.
- (20) Rao, H.; Lim, C.-H.; Bonin, J.; Miyake, G. M.; Robert, M. Visible-Light-Driven Conversion of CO₂ to CH₄ with an Organic Sensitizer and an Iron Porphyrin Catalyst. *Journal of the American Chemical Society* **2018**, *140*, 17830–17834.
- (21) Guo, Z.; Chen, G.; Cometto, C.; Ma, B.; Zhao, H.; Groizard, T.; Chen, L.; Fan, H.; Man, W.-L.; Yiu, S.-M.; Lau, K.-C.; Lau, T.-C.; Robert, M. Selectivity control of CO versus HCOO production in the visible-light-driven catalytic reduction of CO₂ with two cooperative metal sites. *Nature Catalysis* **2019**, *2*, 801–808.

3 - HETEROGENEOUS PHOTOCATALYSIS FOR CO₂ REDUCTION

3.1 . Introduction and objectives

It is possible to develop catalysts highly specific to the substrate through molecular design that can significantly boost the reaction of interest. In the previous chapter, we discussed how modifications of the second coordination sphere of an iron porphyrin catalyst enhance the binding of the CO₂ substrate resulting in higher reaction rate and catalyst turnovers in a photocatalytic system.

Given the positive outcome of our study on photocatalytic activity in a homogeneous medium, we aimed to implement the urea-modified iron porphyrin **UrFe** in a device for heterogeneous photocatalysis. Heterogenization of the molecular catalyst is desirable to increase the system stability (less (photo) degradation) pathways on a surface than in solution [1]), to reduce the amount of catalyst needed (in solution we are limited by the diffusion of the species) and to ideally constitute a device that is more easily scalable and reusable. In addition, immobilizing the catalyst onto a surface enables us to operate in aqueous medium, avoiding often toxic organic solvents where generally this kind of catalysts is soluble.

With these advantages in mind, we addressed the construction of a photocathode assembly, where the light-assisted electron transfer is integrated in an electrochemical cell to perform CO₂ reduction. Such device allows to reduce the potential needed to perform CO₂ reduction thanks to the additional energy provided by the sunlight and converted to an electrochemical potential [2] [3]. As it was mentioned in the introduction chapter, the photocathode assembly is constituted mainly by three parts: i) a conductive support to deposit the top layers; ii) a light absorbing unit with the parallel function of the photosensitizer discussed in Chapter 2 and iii) a catalyst to perform the reaction of interest. To build a photoelectrode, we can consider two possible approaches (see Fig. 3.1). On the one hand (Fig. 3.1, **a**) we can keep both the photosensitizer (P) and the catalyst (Cat) as molecular components and covalently link them to

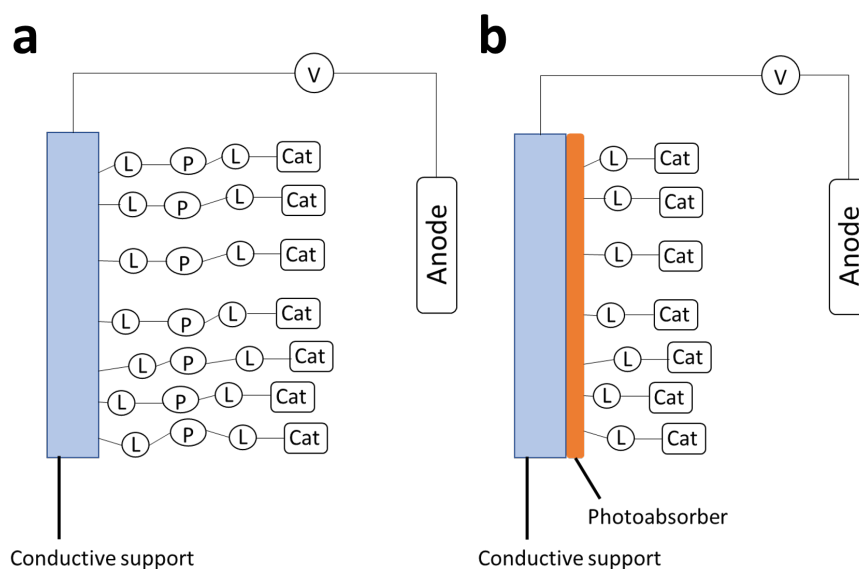


Figure 3.1: Simplified scheme for the assembly strategies of a photocathode based on molecular catalyst.

the surface and to each other with linking groups (L); on the other hand (Fig. 3.1, **b**) we can use a small band gap semiconductor material that absorbs visible light and transfers electrons to the catalyst. On top of the semiconductor, the catalyst (Cat) is immobilized by covalent bonds through specific functional groups (L). It is noteworthy to highlight the importance of using covalent bonds to immobilize the molecular catalyst, which provides a well-defined and stable interface compared to having the catalyst in solution [4].

For reasons of synthetic simplicity, we opted for the second approach, where a modification of the porphyrin ligand is necessary for the final assembly. Different covalent linking groups have already been reported in literature, the most common ones being carboxylic and phosphonic groups [5] [6]. Based on a study by Gong *et al.* [6] on the stability of different linking groups at different pH values, we opted for a hydroxamate group modification on the phenyl rings at the extremities of the catalyst arms (Fig. 3.2).

3.1.1 . Cuprous oxide as semiconductor and photoabsorber

The choice of the appropriate semiconductor material as photoabsorber has to follow specific criteria. First of all, as we are concerned with a reduction reaction, we need to use a p-type semiconductor, where the minority carriers are electrons. This can be better understood by looking at the band-bending phenomenon, which occurs for a semiconductor in solution when the Fermi level (E_F) of the semiconductor equilibrates with the potential of the species in solu-

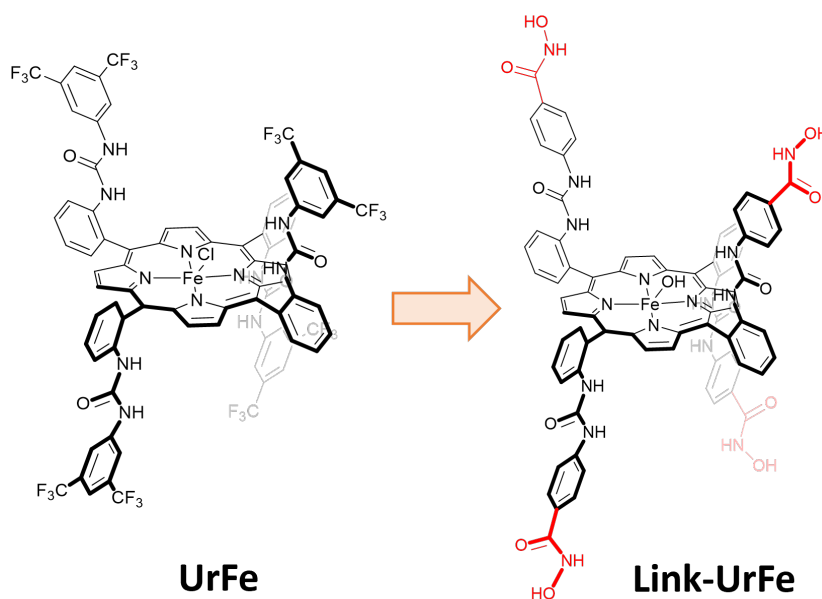


Figure 3.2: Scheme of the structural modification done on the **UrFe** catalyst to insert hydroxamate covalent linking groups (**Link-UrFe**).

tion (E_{red} , Fig. 3.3). In a p-type semiconductor, the electron that is excited into the conduction band upon photon absorption is driven to the surface because of the thermodynamic drive generated by the band-bending, while the hole is driven towards the electrode. This will enable the electrons to be injected onto the substrate or catalyst to perform the desired reduction reaction. This property of semiconductors is desirable to perform photochemistry, since it pushes the separation of hole and electron in the desired direction. As we can see in the scheme (Fig. 3.3), this is true only in the region near the solution, where the band bending occurs. The depth of this region can be further modulated by applying an external electrochemical bias [4]. On the other hand, for an n-type semiconductor we observe the opposite behaviour bringing holes to the surface, in order to perform oxidation reactions.

The second important criterion concerns the reduction potential of the semiconductor indicated by the conduction band positions, which should be negative enough to be able to transfer the electrons to the molecular catalyst. Fig. 3.4 shows an overview of the main semiconductors of interest for photoreduction of CO₂ with their associated band gaps and energy levels of valence and conduction bands. We chose to focus our interests on cuprous oxide (Cu₂O, in orange). Indeed, this material presents both a band gap small enough to absorb visible light (ranging from approximately 1.6 to 3.2 eV) and a highly reducing conduction band (-1.4 V vs. NHE [7]). When we compare this reduction potential to the CO₂/CO couple (-0.53 V vs. NHE [8]) or to the **UrFe** catalyst Fe(I) to

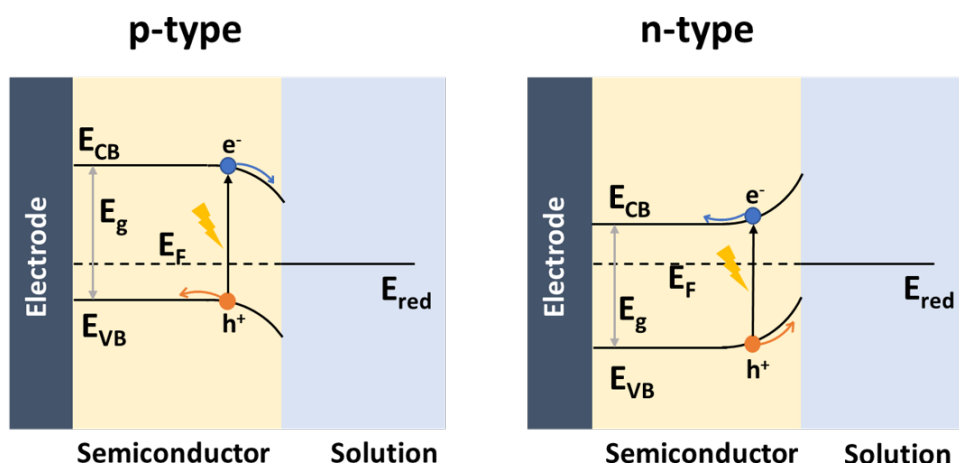


Figure 3.3: Simplified scheme of the band levels and band bending in p- and n-type semiconductors when in contact with the electrolyte solution. E_g : band gap; E_{VB} : valence band potential; E_{CB} : conduction band potential; E_F : Fermi level; E_{red} : solution potential.

Fe(0) reduction (-1.146 V vs. NHE) , for instance, we see that this material has the potential to perform CO₂ reduction on its own. However, we need to take into account that such negative potentials also promote its degradation, which under irradiation can reduce itself from Cu(I) to Cu(0) undergoing the phenomenon called photocorrosion. For this reason it is crucial to associate Cu₂O to a catalyst that can efficiently store and transfer electrons to the substrate and to the protective layers that help the transfer of the electron to the surface of the electrode, minimizing self-reduction.

Cu₂O has been investigated as a photocatalyst for water splitting reaction since the late 90s [10] [11] [12] [13] [14] [15]. In more recent years, the group of Grätzel has also implemented this p-type semiconductor for photoelectrocatalytic (PEC) CO₂ reduction [16] [17]. In these reports, the Cu₂O layer is prepared by electrodeposition in specific conditions which will be described in more details in Section 3.4. This preparation has been optimized to yield a high and stable photocurrent response, by varying the applied current, duration of the deposition, temperature and pH conditions [18]. The overall assembly for the photocathode for CO₂ reduction is further composed of two or three different buffer layers prepared by Atomic Layer Deposition (ALD) that form buried p-n heterojunctions and prevents undesirable interfacial charge recombination. For the catalyst immobilization, they then add an additional mesoporous layer of TiO₂ which serves to increase the loading of the catalyst, as compared to just having a flat surface [17].

It should be emphasized that by adding the buffer layers on Cu₂O, the reducing

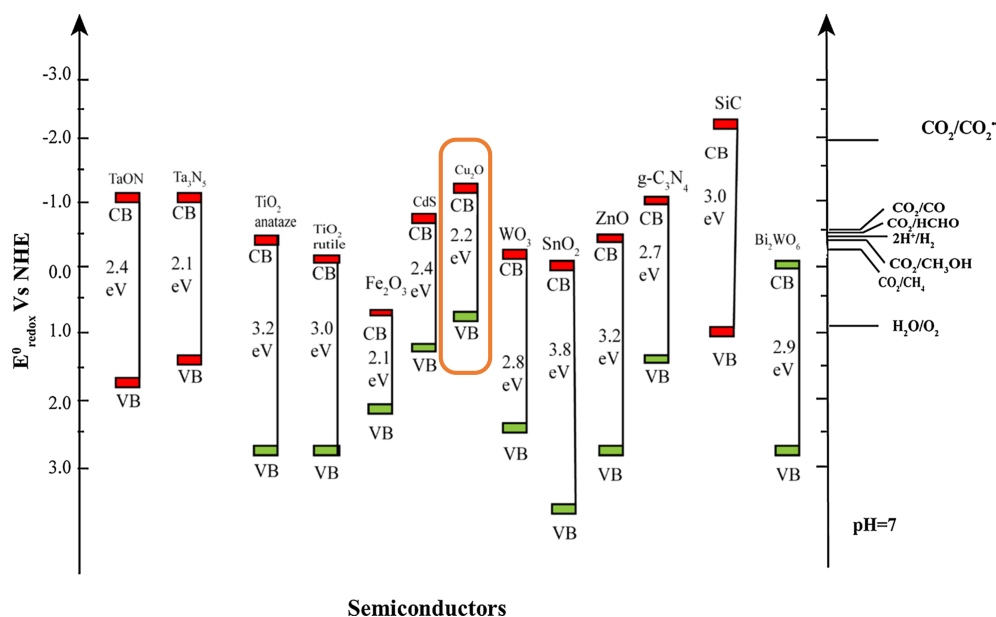


Figure 3.4: Conduction band, valence band potentials, and band gap energies of various semiconductors in comparison to the thermodynamic potentials of various CO_2 reduction reactions at pH 7. Credits to [9]

potential is significantly lowered as a penalty of the downhill cascade of conduction band through the buffer layers. This has as an unfortunate consequence that the initial highly reducing potential of Cu_2O is lost, but this is necessary to gain material stability and to avoid photocorrosion. If we look back at the thermodynamic landscape of Fig. 3.4, we can notice that the conduction band of TiO_2 has a similar potential as of that of the CO_2/CO couple, which means that we can have just enough reducing power to perform CO_2 reduction.

With these examples in mind, we aimed to construct a photocathode constituted by Cu_2O photoabsorber, TiO_2 protective and anchoring layer, and our hydroxamate-modified catalyst (**Link-UrFe**). Our goal was to initially simplify the overall design as much as possible, but we then implemented additional ALD layers to improve stability and electron transport. More specifically, our assembly relies on the implementation of a urea-modified catalyst, which we know is highly active for CO_2 reduction, and that we immobilized on the photoelectrode surface through covalent bonds. Fig. 3.5 shows a scheme of the overall assembly of our photocathode.

3.2 . Catalyst synthesis and characterization

To insert the hydroxamate functional groups on the **UrFe** porphyrin, we used the same precursor porphyrin **$\alpha\beta\alpha\beta$ -TPP(NH₂)** described in Chapter

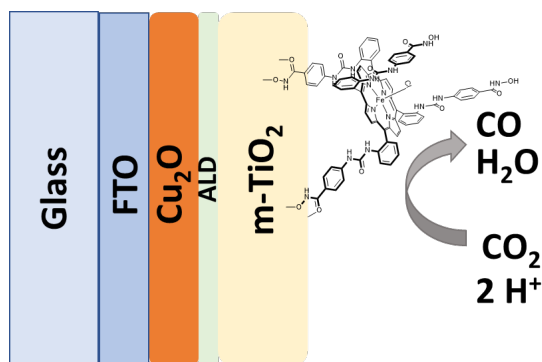


Figure 3.5: Scheme of the photocathode assembly described in this Chapter.

2 (see Fig. 3.6). Here, we performed the first reaction with an excess of the commercially available methyl 4-isocyanatobenzoate to form the urea arms and with an additional methyl ester group on the para position as precursor for the hydroxamate group [19].

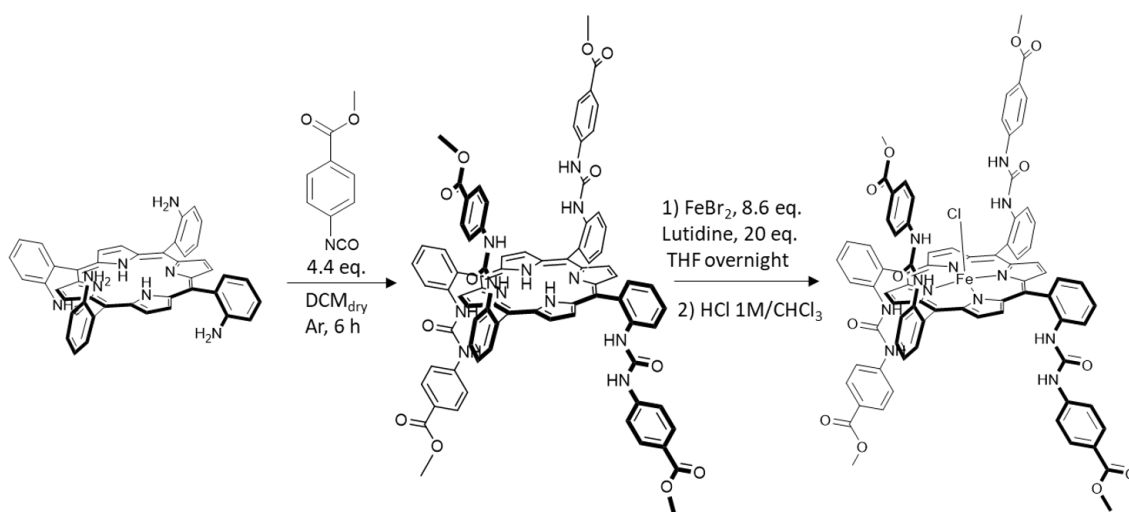


Figure 3.6: Reaction scheme for the synthesis of **OMeUrFe** (**Link-UrFe** precursor).

After the reaction was completed, the crude was evaporated and precipitated with DCM/pentane to yield a purple powder in a yield of about 80%. ¹H-NMR and HR-MS analysis showed the desired product. Fig. 3.7 shows the recorded ¹H-NMR with some of the assigned peaks.

We then inserted the iron metal in the free-base porphyrin at this stage since the formation of the hydroxamate moieties will considerably change the porphyrin solubility. Metallation was carried out overnight in the glovebox in THF with an excess of FeBr₂ and lutidine. The crude was then evaporated and treated with 1 M HCl in order to exchange the axial ligand and insert chloride to obtain a brown powder in a quantitative yield. HR-MS showed the desired peaks for this reaction step (Fig. 3.8), while we could not perform ¹H-NMR due to the

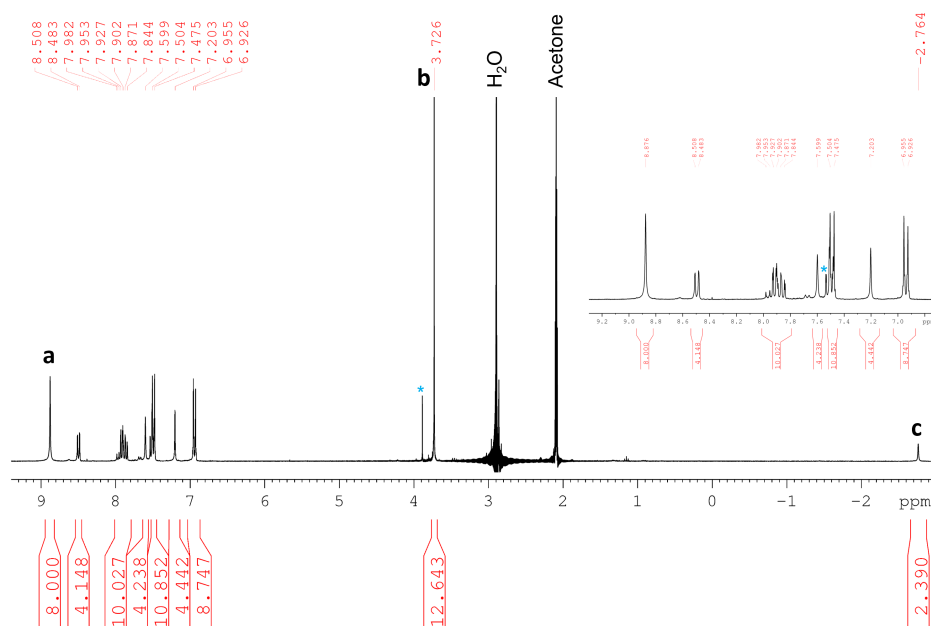


Figure 3.7: ¹H-NMR spectrum of **TPPOMe** in deuterated acetone, 300 MHz. **a**: pyrrolic protons, **b**: -CH₃ protons of the methyl esters, **c**: -NH protons inside the porphyrin ring.

paramagnetic Fe center. This complex (**OMeUrFe**) was further characterized by UV-vis spectroscopy (Annex) and cyclic voltammetry. The electrochemical analysis is important to determine the potentials needed to reduce the catalyst to its catalytically active oxidation state. In fact, it is necessary to verify that the structural modifications to the **UrFe** catalyst do not affect significantly the redox potentials. Fig. 3.9 shows the CV obtained in Ar (blue), CO₂ (red) and in catalytic conditions (green) for the iron porphyrin intermediate holding the ester groups (**OMeUrFe**). As it was discussed in Chapter 2, also here we can observe three reversible waves corresponding to the Fe(III)/Fe(II) and the formal Fe(II)/Fe(I) and Fe(I)/Fe(0) reductions at 0.236 V, -0.605 V and -1.17 V vs. NHE respectively. By comparison with the CV of unmodified **UrFe** (0.181 V, -0.690 V and -1.146 V vs. NHE for Fe(III)/Fe(II), Fe(II)/Fe(I) and Fe(I)/Fe(0)), we see that these values are indeed quite close, meaning that with the structural modification the redox potential of the Fe(0) state is well-aligned with the conduction band of the semiconductor. Like for the **UrFe**, we also observe here an anodic shift of the third reduction wave when CO₂ is added in solution. This has been attributed to an efficient CO₂ capture. Upon addition of the proton source (water), we observe the expected increase of current due to the CO₂ reduction reaction taking place.

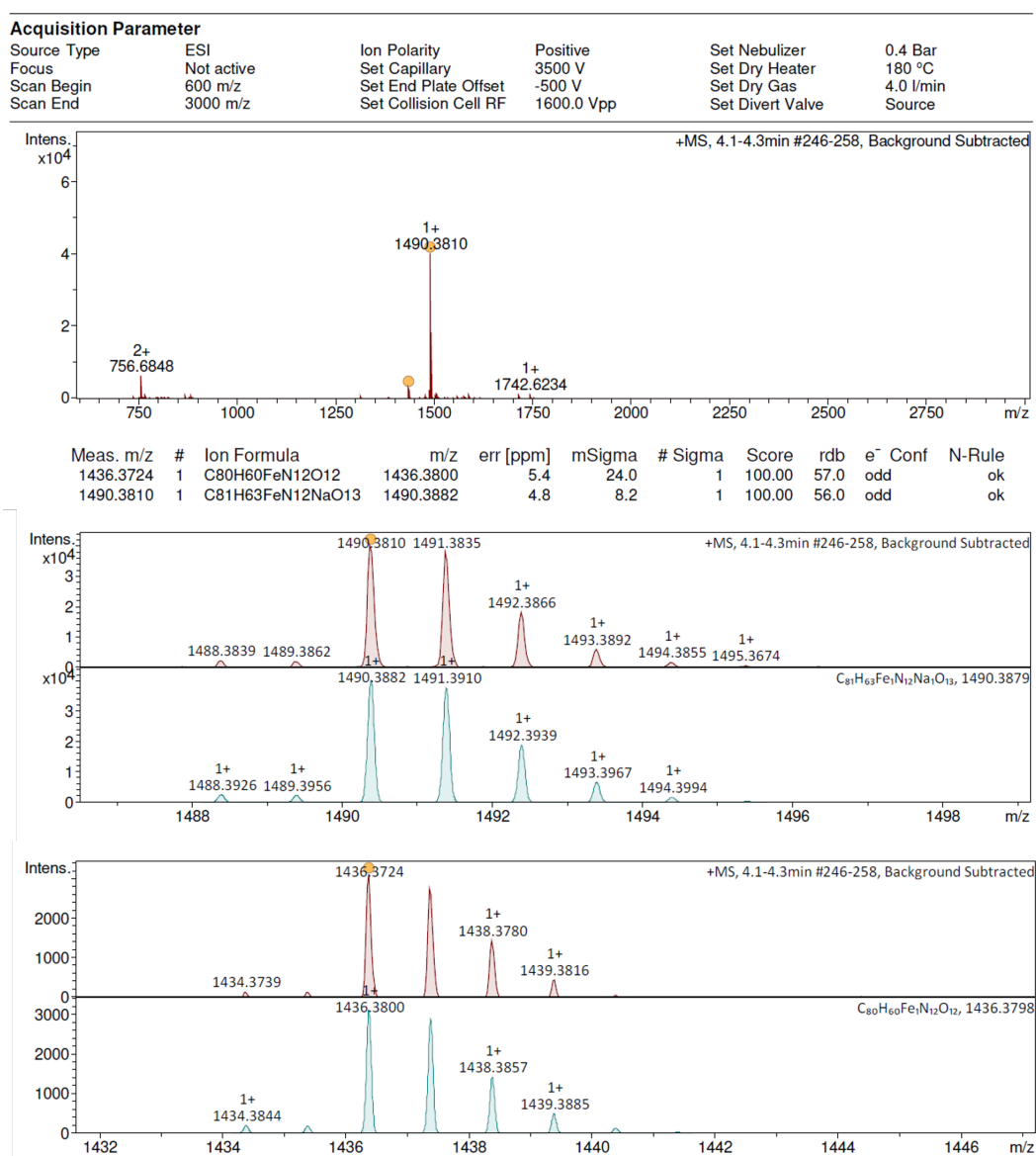


Figure 3.8: ESI-HR mass spectrum of **OMeUrFe** (top), showing the experimental and simulated isotope patterns for the 1490.3810 (center) and 1436.3724 (bottom) peaks.

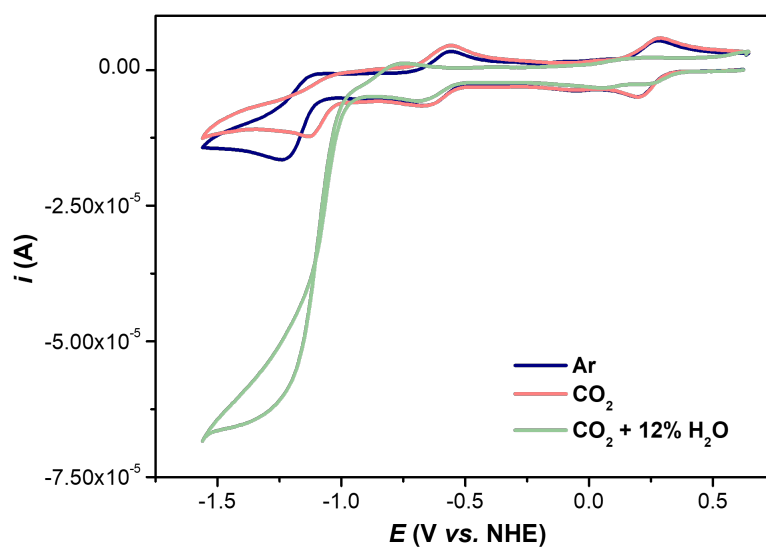


Figure 3.9: Cyclic voltammogram (CV) of the **OMeUrFe** complex at 1 mM concentration in Ar-degassed dry DMF with 0.1 M TBAPF₆. Glassy carbon working electrode; Pt counter electrode and Saturated Calomel Electrode (SCE) as reference electrode; 100 mV s⁻¹ scan rate.

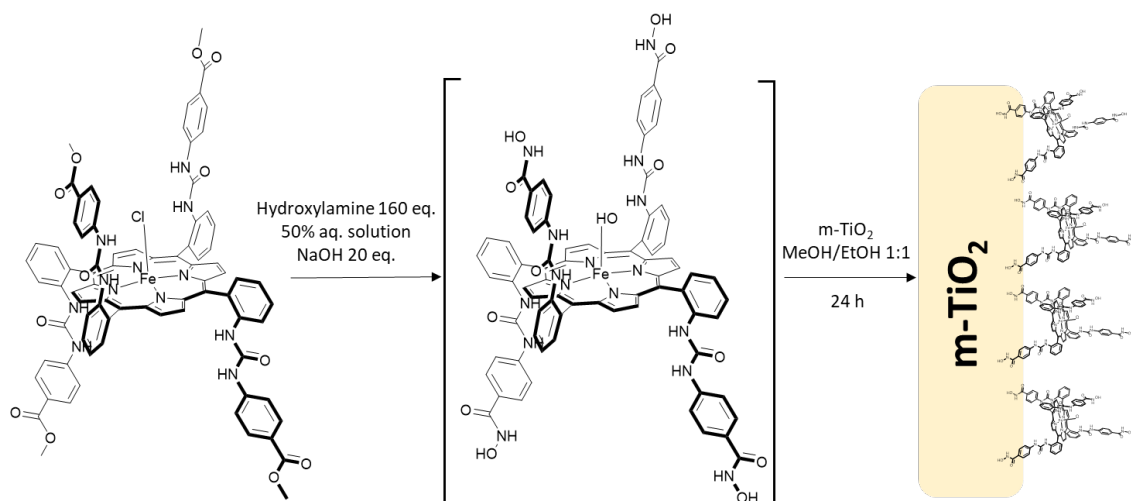


Figure 3.10: Scheme of the catalyst activation step and immobilization on TiO₂.

3.3 . Catalyst immobilization

To immobilize the iron catalyst, a two-step procedure is necessary (see Fig. 3.10). In the first step, the methyl ester groups were activated using hydroxylamine to form hydroxamate groups. Then, in the second step, the activated catalyst was immobilized on the FTO electrode with a mesoporous TiO₂ layer prepared by drop-casting. The electrode was dipped for 24 h in a 0.35 mM solution of the catalyst (**Link-UrFe**) in 1:1 MeOH/EtOH mixture. For comparison, a similar experiment was also performed using the non-modified **UrFe** catalyst. Afterwards, the electrodes were taken out of the solution, rinsed thoroughly with EtOH and dried. The electrode containing **Link-UrFe** showed a darker colour compared to the one with **UrFe**, indicating successful catalyst attachment in the case of **Link-UrFe** (see Fig. 3.11). Thanks to the electrode transparency, we could perform transmission UV-vis spectra for the two electrodes, which clearly showed the peak corresponding to the Soret band of the iron porphyrin at 426 nm in the case of **Link-UrFe** (Fig. 3.11). To further confirm the immobilization of the catalyst on the TiO₂ layer, we performed Attenuated total reflectance Fourier-transform infrared spectroscopy (ATR-FTIR) and X-ray photoelectron spectroscopy (XPS) analyses. We recorded the infrared spectra by directly pressing the electrode surface against the ATR silicon crystal. For reference, we also recorded the spectra of the FTO surface alone (on which the TiO₂ layer is deposited) and of the catalyst powder. By overlaying the spectra (Fig. 3.12), we can observe that the electrode containing the FTO electrode with TiO₂ and **Link-UrFe** catalyst (blue trace) is an overlap of the other two reference spectra. In particular, we can see the peaks

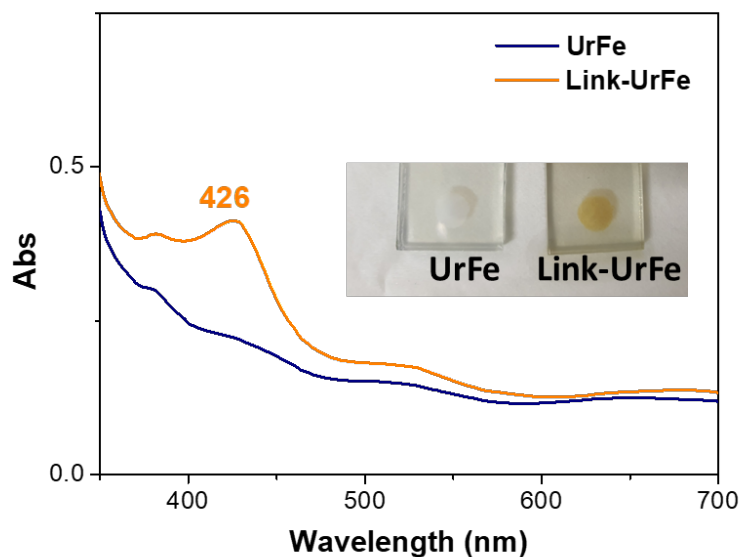


Figure 3.11: UV-vis absorption spectrum obtained for the FTO electrode with mesoporous TiO_2 after being left in the catalyst solution of **UrFe** (blue) and **Link-UrFe** (orange). Inset: Photograph of the two electrodes analyzed.

corresponding to the catalyst vibrations (red asterisks). On the other hand, when the same measurement was performed for the electrode with FTO, TiO_2 and **UrFe** (Fig. 3.13), we could not clearly distinguish any of the characteristic peaks of the catalyst.

XPS analyses of the two samples confirmed once again the successful immobilization of the catalyst in the case of **Link-UrFe** but not in absence of the covalent anchoring groups (**UrFe**). From the survey (Fig. 3.14) we can observe in both cases the predominant signals of Ti and O, as the main elements of the top mesoporous layer. For both samples, we can see peaks of C and N, corresponding to the molecular catalyst on the surface of the electrode. However, in the case of the **Link-UrFe** containing electrode, they are much more intense. For the same electrode, we can also see additional peaks of Fe and F. The F peak is due to the underlying FTO substrate, while the Fe signal, again, is indicative of the molecular catalyst presence on the electrode. Fig. 3.15 shows the spectrum obtained for the Fe 2p region, which indicates that introducing covalent anchoring groups can significantly increase the amount of catalyst immobilized on the surface of the electrode. The XPS analysis confirms for both electrodes the presence of molecular catalyst on the surface, however the greater peak intensities detected in presence of **Link-UrFe** underlines the importance of introducing anchoring groups.

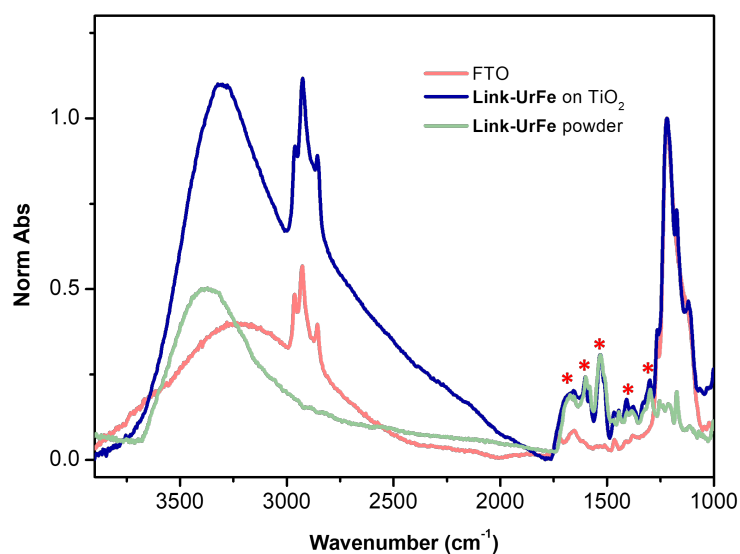


Figure 3.12: ATR-FTIR normalized spectra (for the peak at 1200 cm⁻¹) of the FTO on glass support (red), of the **Link-UrFe** catalyst powder (green) and of the FTO electrode with mesoporous TiO₂ after being 24 h in the **Link-UrFe** catalyst solution.

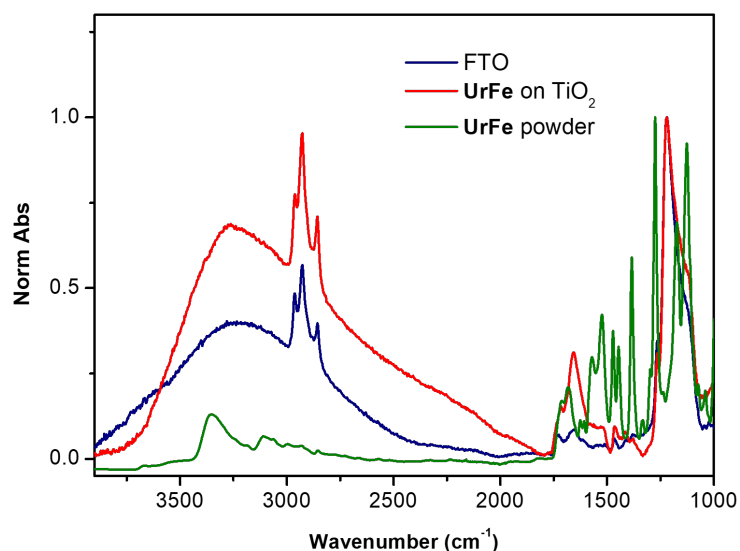


Figure 3.13: ATR-FTIR normalized spectra (for the peak at 1200 cm⁻¹) of the FTO on glass support (red), of the **UrFe** catalyst (green) and of the FTO electrode with mesoporous TiO₂ after being 24 h in the **UrFe** catalyst solution.

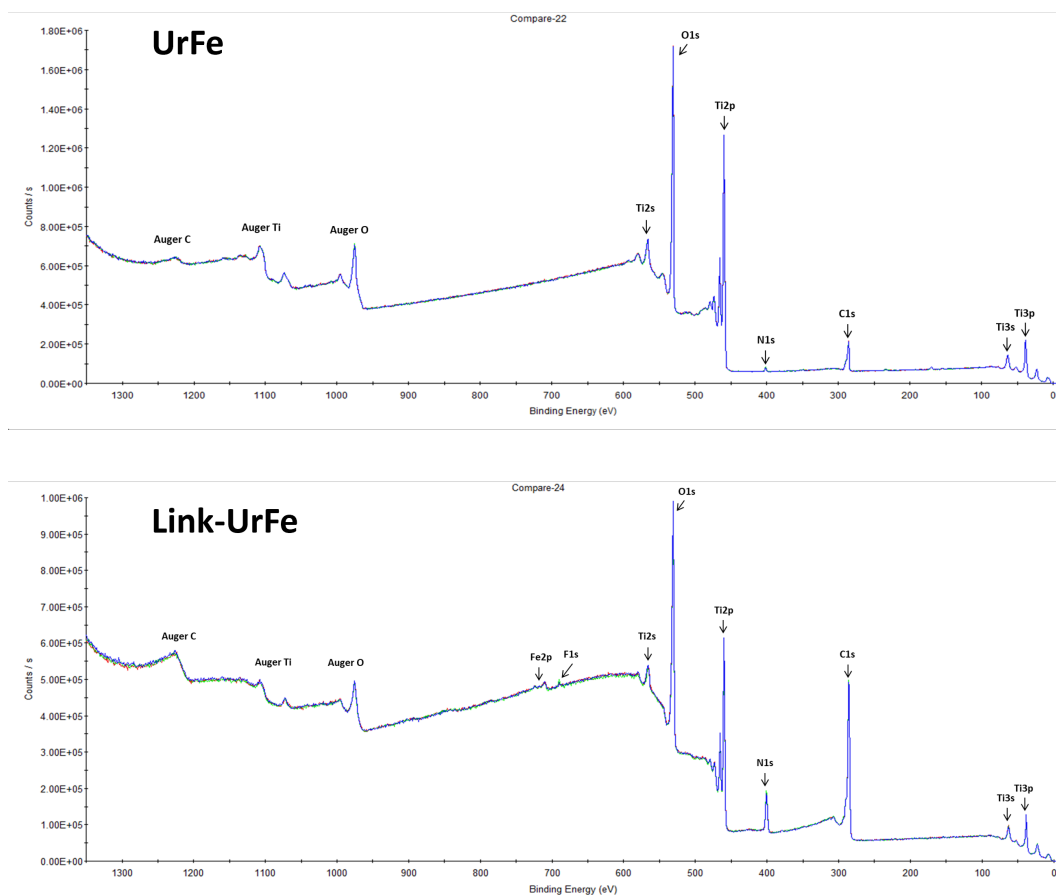


Figure 3.14: XPS spectra of the FTO electrode with mesoporous TiO₂ and after being placed for 24 h in the **UrFe** (top) and **Link-UrFe** (bottom) catalyst solutions; survey scans.

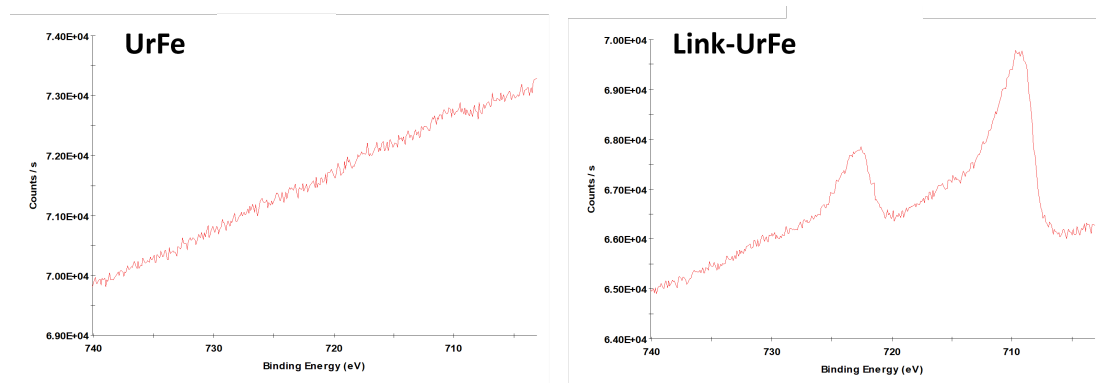


Figure 3.15: XPS spectra of the FTO electrode with mesoporous TiO₂ and after being placed for 24 h in the **UrFe** (left) and **Link-UrFe** (right) catalyst solutions in the Fe 2p region.

3.4 . Photoelectrode preparation

We then turned to the more challenging task of assembling the photoelectrode with its various layers. As discussed above, the main component is constituted by the Cu₂O layer. To prepare this photoelectrode, we followed the previously optimized electrodeposition conditions reported in the literature [18] [16]. In particular, we used FTO as substrate on glass support with low resistance (TEC 7, between 7 and 10 Ω), which served as a working electrode during the deposition. Careful cleaning of the substrate was performed by sonication in soapy water, acetone, EtOH and distilled water for 15 min each. The clean surfaces were stored in distilled water and rinsed again with EtOH before use. For the electrodeposition we used a three-electrode set-up with the FTO as working electrode, Pt grid as counter electrode and Ag/AgCl as reference electrode at 30 °C. We then applied a constant current density of 0.1 mA cm⁻² for 105 min to a solution of 0.2 M CuSO₄, 0.5 M K₂HPO₄ and 3 M lactic acid, and the solution is brought to pH 12 with addition of KOH 2 M solution. It is important to use lactate ligand to avoid the precipitation of Cu(OH)₂. These parameters are used to deposit approximately a 500 nm layer, which optimally gives high photocurrent. At the end of the deposition, the Cu₂O layer was rinsed with water and acetone.

By following these steps, we initially encountered reproducibility and uniformity problems for our depositions. Fig. 3.16 shows an example of the electrode obtained following this method, where some areas of the substrate have much thicker layers (darker color) and others seem to not have an effective deposition (lighter color). After few unsuccessful trials, we decided to add a layer of gold (Au) on the FTO substrate to increase the conductivity of the substrate and improve the deposition.

To deposit the Au layer we used a Chemical Vapour Deposition (CVD) setup, where we first deposited 10 nm of Cr and then add on top of it 100 nm of Au. The Cr layer is used to increase the adherence of the thick Au layer on the FTO support. When the electrodeposition was performed on the FTO with Cr and Au layers, a more uniform layer of Cu₂O could be obtained. To further analyze the difference of the Cu₂O layers obtained in the two different cases, we tested the photoelectrochemical response by sweeping potential with LSV method (linear sweep voltammetry) while pulsing a white LED on and off. In both cases, we could notice a photocurrent response, corresponding to an increase of current when the light is on, and then going back to nearly zero when

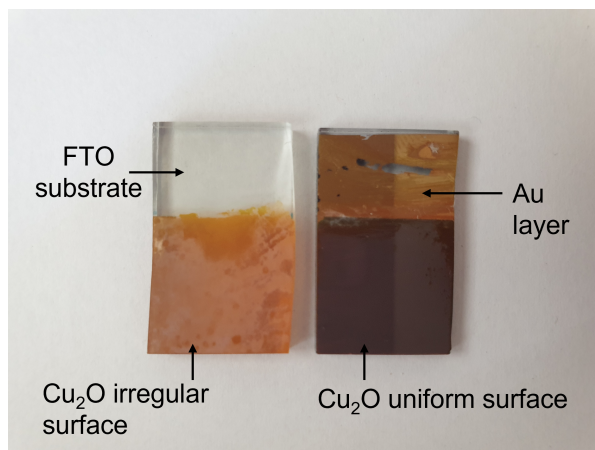


Figure 3.16: Photograph of the electrodeposited Cu_2O layers directly on FTO substrate (left) and on 10 nm Cr and 100 nm Au layers (right).

the light is off (see Fig. 3.17). Comparing the curves of Fig. 3.17, we can notice that electrodeposition on gold surface allows not only to have a more uniform Cu_2O layer, but also to significantly increase the photocurrent response from $-0.315 \text{ mA cm}^{-2}$ to -2.98 mA cm^{-2} at $-0.2 \text{ V vs. Ag/AgCl}$. These values are calculated by subtracting the current measured in the dark from the one measured with the light on.

Importantly, it should be highlighted that the current response in the dark should ideally stay nearly zero. The phenomenon observed for the curves in Fig. 3.17 where the dark current tends to slowly increase by scanning more negative potentials is associated to photocorrosion, meaning that an electrochemical transformation is taking place and giving rise to a current response even without excitation of the semiconductor; in this case the self reduction of the material from Cu(I) to Cu(0) . Monitoring the extent of photocorrosion can be used to determine the photoelectrode stability.

We then moved to characterize further the obtained electrode by XPS (Fig. 3.18). As expected, the spectra clearly show the presence of Cu and O peaks, together with the presence of potassium, hydroxide and carbonate, probably to be ascribed to the electrodeposition solution (see Fig. 3.18 and 3.19). During the measurement, the signals corresponding to carbonate and hydroxide diminish, confirming that they are due to pollution of the surface. The XPS analysis confirms the nature of the copper oxide deposited being Cu(I) as previously described in literature. One more analysis to confirm the nature of the material deposited on the electrode is the band gap measurement. This was performed by measuring the absorbance and by plotting the Tauc diagram based on the experimental data. Fig. 3.20 displays the experimental direct band gap esti-

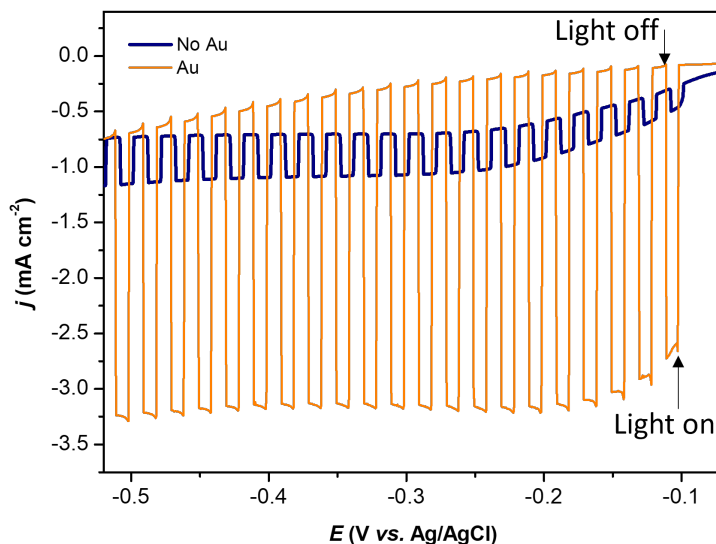


Figure 3.17: Photocurrent response obtained upon Linear Sweep Voltammetry (LSV) while pulsing white LED light (100 W m^{-2} , 1s/1s on/off inputs) for Cu₂O electrodeposited directly on FTO TEC 7 substrate (blue) or in presence of a 10 nm Cr and 100 nm Au layers (orange). 0.5 M Na₂SO₄ and 0.1 M KH₂PO₄ electrolyte, pH 4.4, N₂ atmosphere.

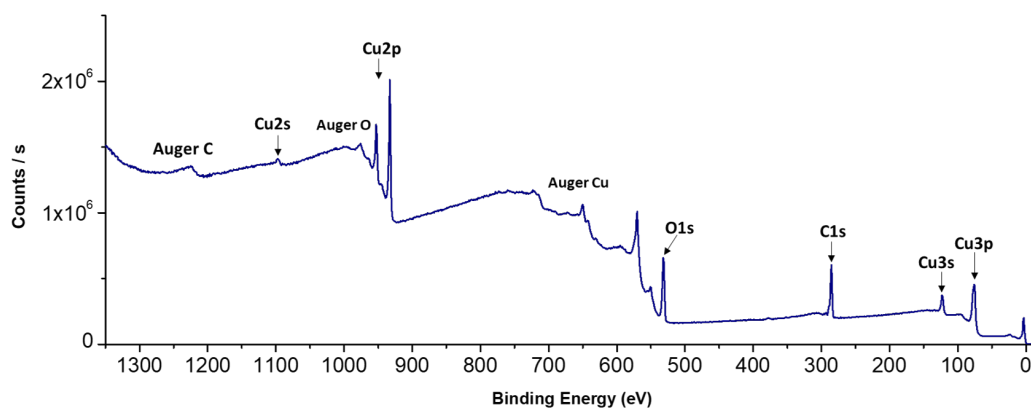


Figure 3.18: XPS spectra of Cu₂O electrodeposited on FTO electrode with 10 nm Cr and 100 nm Au layers; survey scans.

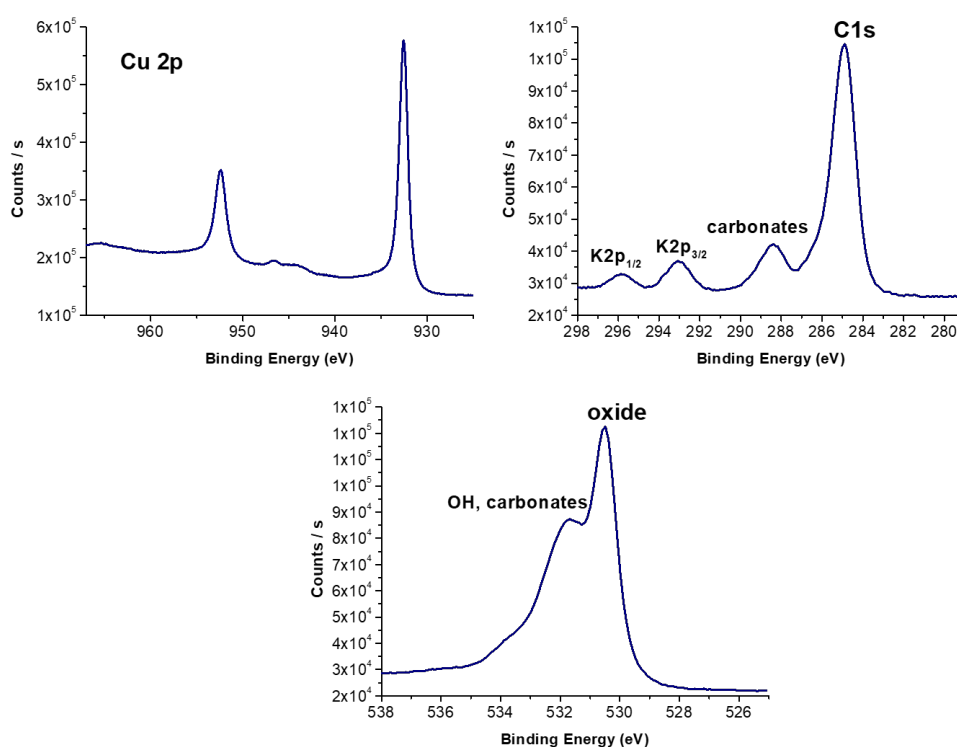


Figure 3.19: XPS spectra of Cu₂O electrodeposited on FTO electrode with 10 nm Cr and 100 nm Au layers; Cu 2p, C 1s and O 1s regions.

mated from the Tauc plot, corresponding to 2.39 eV. To find this value, we applied the KubelkaMunk function [20] [21]. This value slightly differs from the reported value of 2.2 eV [22], but it is considered to be an acceptable variation.

After having optimized the Cu₂O deposition and verified that we can obtain a good photocurrent response (nearly -3 mA cm^{-2} at $-0.2 \text{ V vs. Ag/AgCl}$ for proton reduction), we moved to integrating the mesoporous TiO₂ layer on the photocathode, where the catalyst can be immobilized. Indeed, few buffer layers could be integrated to the electrode assembly as described in Fig. 3.5, but we also addressed the construction of a simplified assembly, where the TiO₂ layer is directly in contact with the Cu₂O semiconductor.

Different preparations of the mesoporous TiO₂ are possible. Our first attempt was by using blade coating (BC) technique starting from the Solaronix titania paste for high transparency (HT) films. This methodology allows to obtain a highly transparent film, with the additional binders being removed by heat treatment or by UV light [17]. However, we observed an unexpected degradation of the Cu₂O layer upon contact with the titania paste, possibly due to a chemical reaction with the binders present in the paste.

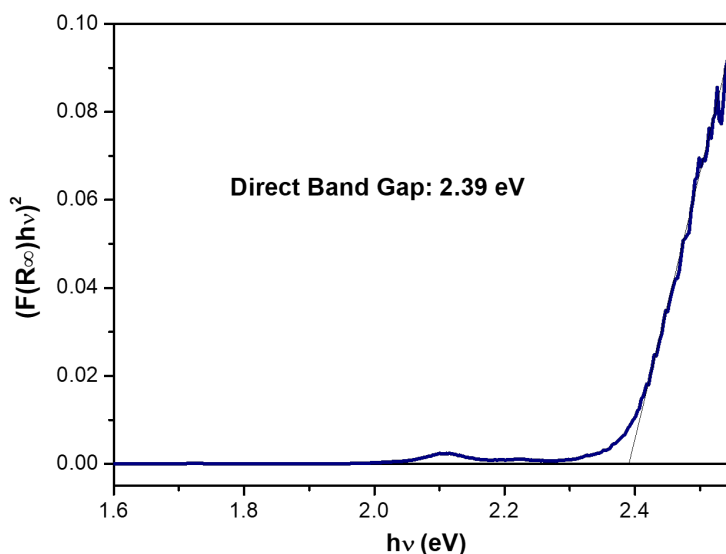


Figure 3.20: Tauc plot obtained from the absorption spectrum of an FTO TEC 7 substrate with Cu₂O layer. The data was best fitted in the direct band-gap equation, the intercept shows the experimental band-gap value.

To overcome this hurdle, we proceeded in parallel to i) develop an alternative way to constitute the TiO₂ mesoporous layer and ii) integrate ALD layers to protect the Cu₂O in the final device. For the former, we chose a simple method reported by Marica *et al.* [23] where a TiO₂ suspension is simply prepared from 21 nm TiO₂ particles and water and then drop-casted (DC) on the surface. The choice of solvent is important for both preventing damages on the surface and allowing a slow evaporation to obtain a homogeneous film. However, this methodology yields a rather white colored film, which causes a decrease of the light absorption of the semiconductor. Optimization of this preparation may be a key point for further development; further analysis is discussed in the next sections.

Integration of ALD layers in the electrode seems promising as this technique allows to access a wide range of materials and to deposit them in a highly controlled way in terms of both conformity and thickness. Depositions were made in collaboration with *L'Institut Photovoltaïque d'Île-de-France* (IPVF) and the specific conditions used can be found in the Annex. Three different combinations of ALD layers were prepared and tested in terms of photocurrent (see next Section). In particular, a first batch included a 10 nm TiO₂ layer between the Cu₂O and the mesoporous TiO₂ (Cu₂O/ALD-TiO₂/DC-TiO₂), whereas the other two included one additional ALD layer for a more favourable p-n hetero-

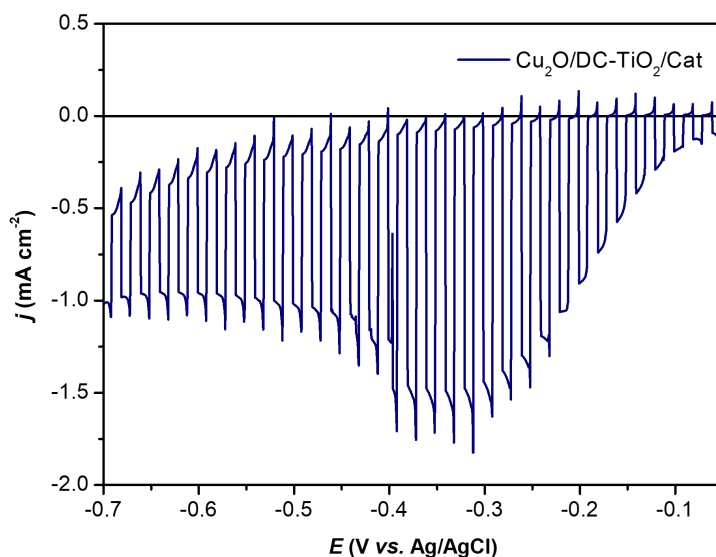


Figure 3.21: Photocurrent response obtained upon Linear Sweep Voltammetry (LSV) while pulsing white LED light (600 W m^{-2} or 0.6 sun, 1s/1s on/off inputs) for the $\text{Cu}_2\text{O}/\text{DC-TiO}_2/\text{Link-UrFe}$ electrode. CO_2 -saturated KHCO_3 0.5 M electrolyte. CE: Pt; RE: Ag/AgCl.

junction: Al-doped ZnO ($\text{Cu}_2\text{O}/\text{ALD-AZO}/\text{ALD-TiO}_2/\text{DC-TiO}_2$) and Al_2O_3 ($\text{Cu}_2\text{O}/\text{ALD-Al}_2\text{O}_3/\text{ALD-TiO}_2/\text{DC-TiO}_2$). The thicknesses of the different layers were chosen in order to limit the insulating effect that these materials can inevitably induce; for Al_2O_3 a single ALD cycle was performed, whereas AZO was deposited with a 20 nm thickness, given its higher conductivity. On top of the ALD layers, mesoporous TiO_2 was drop-casted as described above. On the mesoporous layer, the catalyst was immobilized simply by dipping the electrode in the catalyst solution, as described in Section 3.3.

3.5 . Photoelectrochemical study

To study the different assemblies of the photocathode described in the Section above, we mainly compared the photocurrent response in catalytic conditions, in presence of CO_2 . First of all, we evaluated the PEC performances of the simpler assembly without ALD layers. Fig. 3.21 shows the current response of the $\text{Cu}_2\text{O}/\text{DC-TiO}_2/\text{Link-UrFe}$ electrode under chopped light while applying negative bias. Quite interestingly, we see an increase of the photocurrent recorded until around $-0.35 \text{ V vs. Ag/AgCl}$ (-1.48 mA cm^{-2}) of applied potential, followed by a decrease of photocurrent together with an increase of dark current. These symptoms indicate that photocorrosion is taking place.

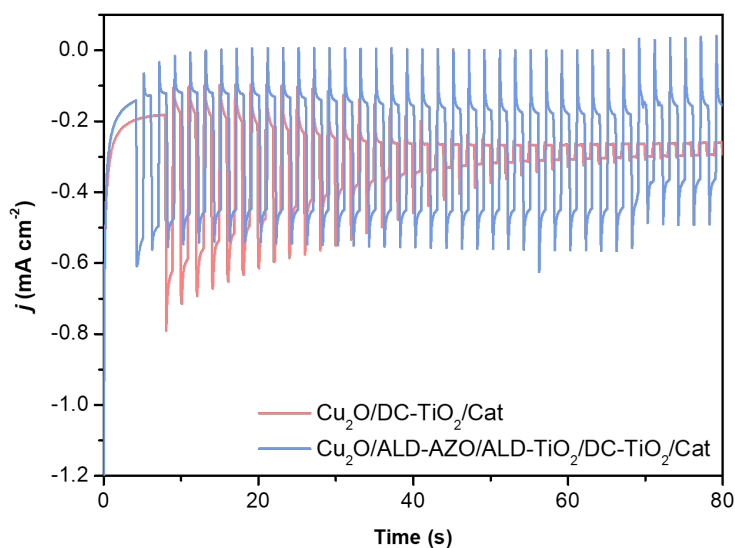


Figure 3.22: Photocurrent response obtained upon Chronoamperometry (CA) while pulsing white LED light (600 W m^{-2} or 0.6 sun , $1\text{s}/1\text{s}$ on/off inputs) for the $\text{Cu}_2\text{O}/\text{ALD-AZO}/\text{ALD-TiO}_2/\text{DC-TiO}_2/\text{Link-UrFe}$ electrode at $-0.6 \text{ V vs. Ag/AgCl}$ (blue) and for the $\text{Cu}_2\text{O}/\text{DC-TiO}_2/\text{Link-UrFe}$ electrode at $-0.4 \text{ V vs. Ag/AgCl}$ (red). CO_2 -saturated KHCO_3 0.5 M electrolyte. CE: Pt; RE: Ag/AgCl.

The photocurrent obtained seems to be quite promising in terms of PEC response when compared to values found in the literature [17], however, when testing the stability of the photocurrent response (red curve of Fig. 3.22), we can observe a quick decay of photocurrent density upon prolonged electrolysis at $-0.4 \text{ V vs. Ag/AgCl}$ when pulsing the light. In fact, in less than one minute, almost all the photocurrent is lost and the electrode is damaged, as we can see from the dark current behaviour. This observation highlights the importance of introducing protective layers before mesoporous TiO_2 to prevent the photocorrosion phenomenon and increase the photocathode stability over time.

Comparing the three different ALD preparation batches in catalytic conditions (with CO_2 substrate and the **Link-UrFe** catalyst on the surface), we can determine which buffer layer composition is more appropriate for the efficiency of the final device. Fig. 3.23 displays the results obtained for the electrodes with the different ALD layers assembly. As a general observation, we noticed the decrease in photocurrent density compared to the previous case (Fig. 3.21), which is to be expected since we inserted additional interfaces that may increase the probability of charge recombination. Having a closer look, we see that the addition of only ALD- TiO_2 layer gives the worst performances (-0.24 mA cm^{-2} at $-0.6 \text{ V vs. Ag/AgCl}$). This can be rationalized by the large gap between the conduction bands of the $\text{Cu}_2\text{O}/\text{TiO}_2$ junction, meaning that recombination

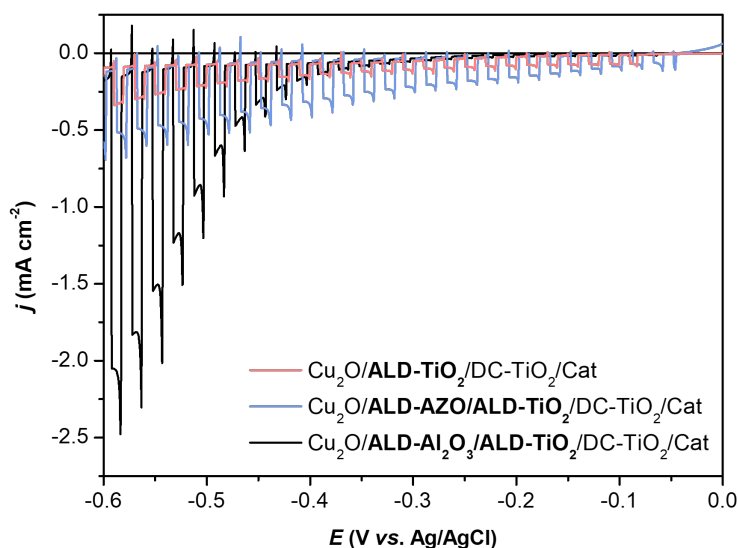


Figure 3.23: Photocurrent response obtained upon Linear Sweep Voltammetry (LSV) while pulsing white LED light (600 W m^{-2} or 0.6 sun, 1s/1s on/off inputs) for the electrodes $\text{Cu}_2\text{O}/\text{ALD-TiO}_2/\text{DC-TiO}_2/\text{Link-UrFe}$ (red), $\text{Cu}_2\text{O}/\text{ALD-AZO}/\text{ALD-TiO}_2/\text{DC-TiO}_2/\text{Link-UrFe}$ (blue) and $\text{Cu}_2\text{O}/\text{ALD-Al}_2\text{O}_3/\text{ALD-TiO}_2/\text{DC-TiO}_2/\text{Link-UrFe}$ (black). CO_2 -saturated KHCO_3 0.5 M electrolyte. CE: Pt; RE: Ag/AgCl.

between the valence band (VB) of Cu_2O and the conduction band (CB) of TiO_2 may not be successfully minimized (see Fig. 3.24). If the recombination takes place (electron from CB of TiO_2 replenishing the hole in the VB of Cu_2O), the electrons will not be efficiently drawn to the electrode surface as desired and the catalysis will not occur. Next, the photocurrent density obtained when an AZO layer is added before TiO_2 was measured to be -0.39 mA cm^{-2} at $-0.6 \text{ V vs. Ag/AgCl}$ (blue curve in Fig. 3.23). To further confirm that the observed current is coming from the catalytic reaction, we compared the LSV obtained in identical conditions but in the absence of the catalyst (green curve of Fig. 3.25). Indeed, we observed an increase of $180 \mu\text{A cm}^{-2}$ in the current density when the catalyst is integrated in the system, likely an index of the CO_2 reduction reaction occurring on the surface that increases the photocurrent response. When we investigated the stability of this electrode at a constant potential (blue curve in Fig. 3.22) we observed a significant improvement compared to the $\text{Cu}_2\text{O}/\text{DC-TiO}_2/\text{Link-UrFe}$ electrode. Even though we can observe some dark current the additional ALD layer can clearly enhance the photocathode stability both in terms of photocorrosion and photocurrent density stability over time.

From Fig. 3.23, the electrode containing the Al_2O_3 buffer layer seems to be the

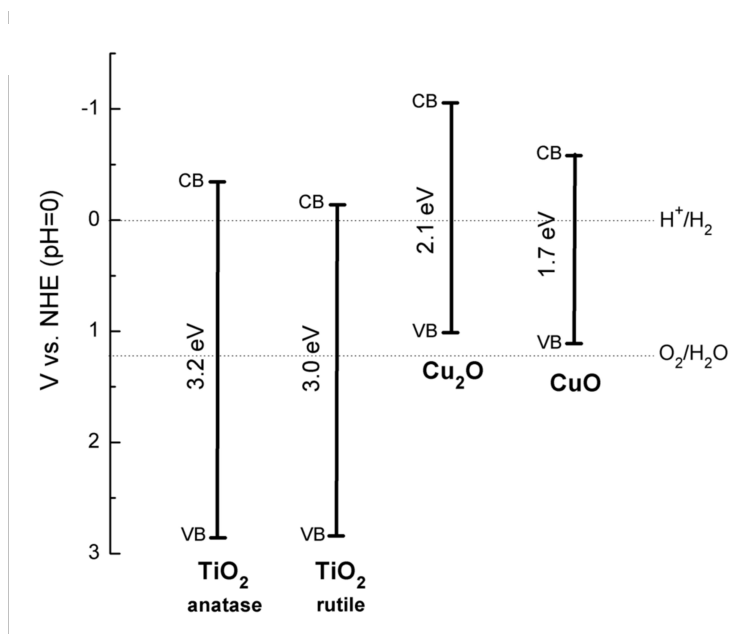


Figure 3.24: Comparison scheme of the band levels for Ti oxide and Cu oxides. Credits to [24]

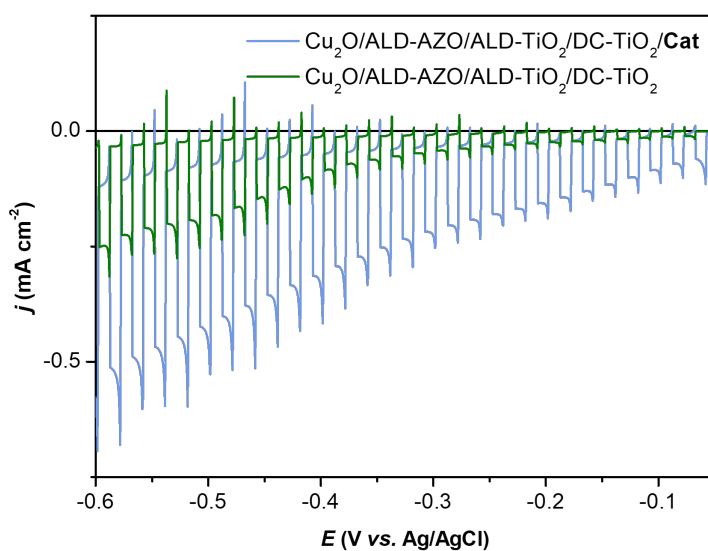


Figure 3.25: Photocurrent response obtained upon Linear Sweep Voltammetry (LSV) while pulsing white LED light (600 W m^{-2} or 0.6 sun, 1s/1s on/off inputs) for the Cu₂O/ALD-AZO/ALD-TiO₂/DC-TiO₂ electrode in presence (blue) and absence of the **Link-UrFe** catalyst (green). CO₂-saturated KHCO₃ 0.5 M electrolyte. CE: Pt; RE: Ag/AgCl.

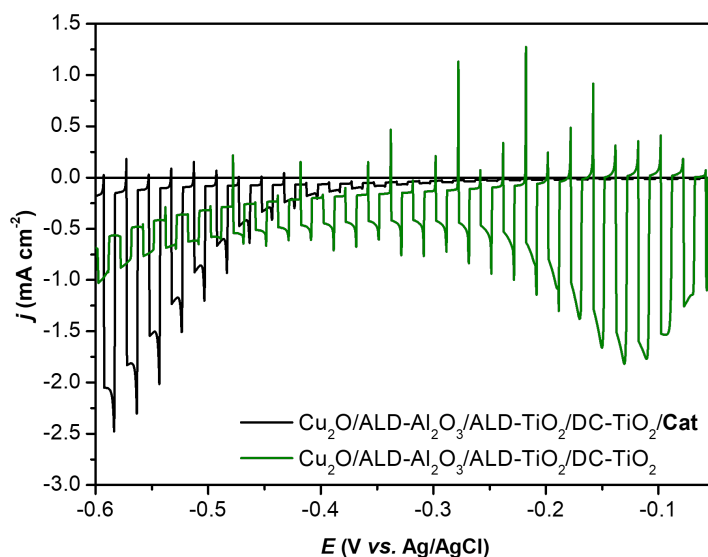


Figure 3.26: Photocurrent response obtained upon Linear Sweep Voltammetry (LSV) while pulsing white LED light (600 W m^{-2} or 0.6 sun, 1s/1s on/off inputs) for the $\text{Cu}_2\text{O}/\text{ALD-Al}_2\text{O}_3/\text{ALD-TiO}_2/\text{DC-TiO}_2$ electrode in presence (black) and absence of the **Link-UrFe** catalyst (green). CO_2 -saturated KHCO_3 0.5 M electrolyte. CE: Pt; RE: Ag/AgCl.

most active for CO_2 reduction given the current density of -1.86 mA cm^{-2} at $-0.6 \text{ V vs. Ag/AgCl}$. Strangely, we also observed a quite negative onset potential when compared to the other cases (around $-0.4 \text{ V vs. Ag/AgCl}$). Analogously to the AZO electrode, we compared the LSV curves in presence and absence of catalyst (Fig. 3.26) and once again we noticed an unexpected behaviour. The green curve in Fig. 3.26 displays a much more positive onset potential than in the presence of catalyst (black trace) and the current intensities seem to be comparable. This observation is not yet clearly understood, but it is indicative that secondary processes are taking place on the electrode and not necessarily linked to the catalytic reaction of interest. With these preliminary remarks we conclude that the introduction of the AZO layer seems to be the most promising for the electrode assembly.

We now turned to question the stability of the catalyst immobilization in operating conditions. Are the covalent bonds stable at reducing potentials and light irradiation? To verify this, we analyzed with XPS the sample with $\text{Cu}_2\text{O}/\text{ALD-Al}_2\text{O}_3/\text{ALD-TiO}_2/\text{DC-TiO}_2/\text{Link-UrFe}$ after recording the photocurrent. Fig. 3.27 shows the survey scans obtained for the sample. Because of the multi-layer assembly, the results are more complex than what was shown in Section 3.3 for the electrode containing simply FTO, TiO_2 and the catalyst. In addition to what was detected in Fig. 3.14, we can see additional signals related to the

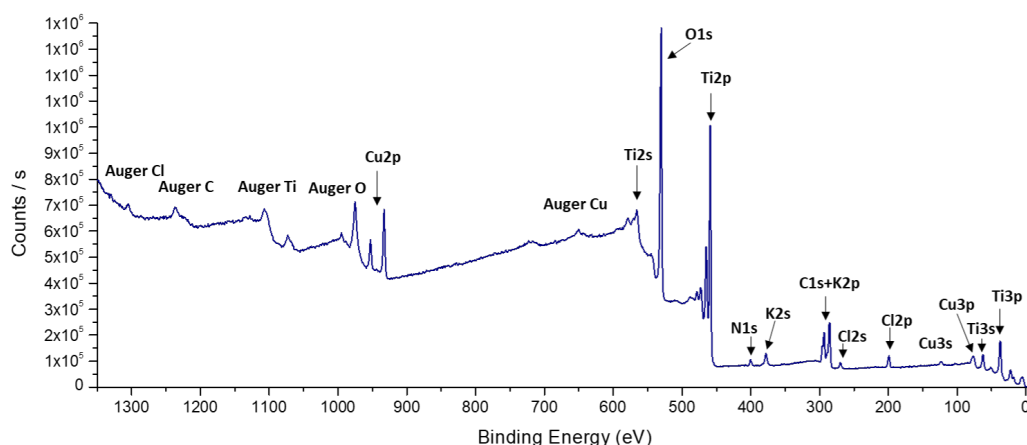


Figure 3.27: XPS spectra of the Cu₂O/ALD-Al₂O₃/ALD-TiO₂/DC-TiO₂/Link-UrFe electrode after photocurrent measurements; survey scans.

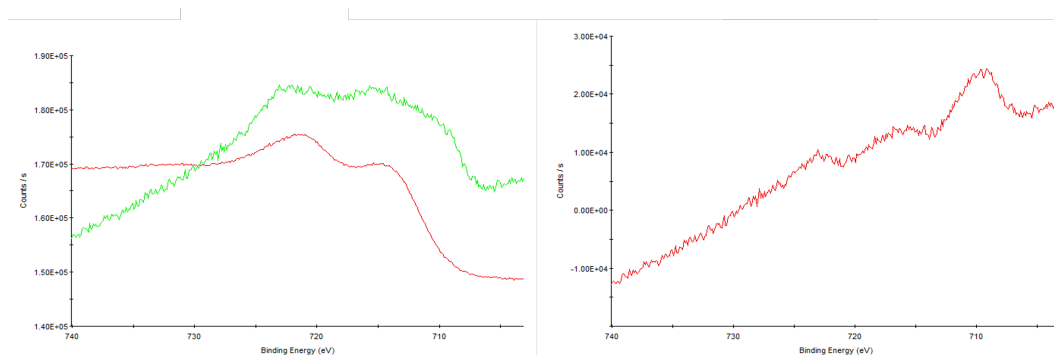


Figure 3.28: XPS spectra of the Cu₂O/ALD-Al₂O₃/ALD-TiO₂/DC-TiO₂/Link-UrFe electrode after photocurrent measurements in the Fe 2p region. Left: experimental spectrum (green) and Auger peak of Cu of the Cu₂O layer alone (red). Right: subtraction spectrum of the recorded spectrum (green on the left) minus the Auger peak of Cu (red on the left).

underlying Cu₂O layer and to the electrolyte (KHCO₃ solution). Nevertheless, we can still observe the presence of C and N peaks, corresponding to the molecular catalyst, indicating that at least part of the **Link-UrFe** is still present on the surface. A closer analysis in the Fe 2p region (Fig. 3.28) shows that the main signal is coming from the Auger peak of Cu, but when subtracting it from the recorded spectrum, we can observe the Fe 2p signals. These results show that Fe catalyst is still present on the surface, but a deeper study of the same sample before and after the electrochemical experiment with a quantification technique would be more appropriate to monitor the stability of the covalent bonds over time.

Furthermore, we investigated the effect of the nature of the TiO₂ mesoporous layer on the overall performances by taking the assembly containing only ALD-TiO₂ on top of the Cu₂O layer as a model electrode. Blade coating (BC) of

the TiO₂ paste still caused some partial issues in terms of Cu₂O stability, since we could observe few spots on the electrode area slowly turning black, possibly due to some diffusion of the paste upon friction through the 10 nm layer of TiO₂. However, the majority of the surface was still intact to proceed with the preparation. As described by Schreier *et al.* [17], this was treated by UV radiation for 72 h in order to remove the organic binders, before soaking it in the **Link-UrFe** solution. The photocurrent obtained with this electrode was then compared to that obtained using the drop casting (DC) TiO₂ method (Fig. 3.29). We can observe the significant change when the BC-TiO₂ layer is used, with a photocurrent density reaching -1.1 mA cm⁻² at -0.6 V vs. Ag/AgCl, compared to the -0.24 mA cm⁻² recorded for DC-TiO₂. As mentioned in the previous section, this can be ascribed partially to the light screening by the white film formed by DC-TiO₂. Also, it is possible that more catalyst can be loaded on the BC-TiO₂ when soaked for the same period of time (24 h) in the catalyst's solution. One more explanation could be that there is a better contact between the incoming electrons and the catalyst because of the extra sintering step ensuring good contact of the mesoporous layer.

The purple curve of Fig. 3.29 also shows a greater extent of photocorrosion when compared to DC-TiO₂. We think that this could arise from the small imperfections generated on the surface of the blade-coated sample, visually observed as dark spots.

From this last comparison we can remark that the used mesoporous layer is not optimal for the photocathode efficiency, and ways to overcome issues during BC of TiO₂ should be foreseen for future improvements. This includes i) having optimized and thicker ALD overlayer or ii) searching for alternative ways to deposit transparent mesoporous TiO₂ that does not corrode the underlying Cu₂O.

Detection of CO₂ reduction product by μ -GC was not yet possible with the light-assisted electrode; most likely due to the instability of the photocurrent that quickly decreases after few minutes. However, bulk electrolysis in the dark (using a FTO electrode with BC-TiO₂ and **Link-UrFe**) yielded CO with a small faradaic efficiency of about 4%, probably due to the competing proton reduction reaction by TiO₂ and partial electrode degradation affecting the recorded current. This result together with the CV discussed earlier confirm the effective CO₂ reduction taking place, even though critical optimizations of the mesoporous layer and the photoelectrode in general need to be implemented.

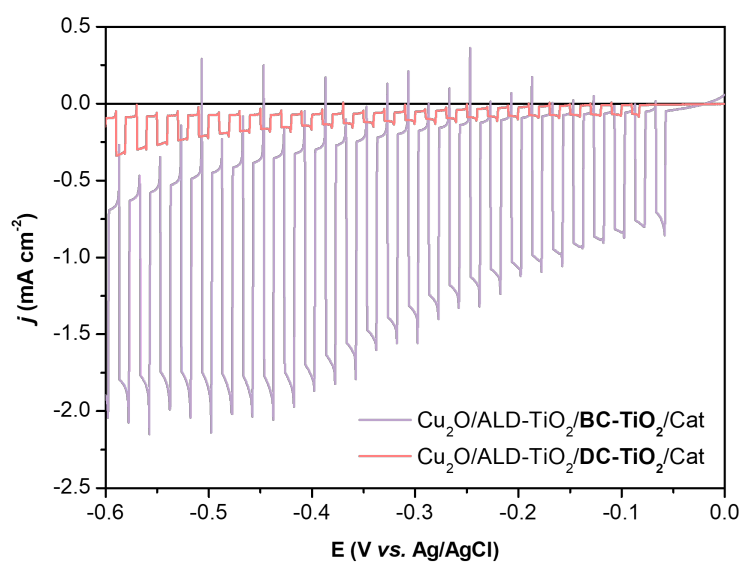


Figure 3.29: Photocurrent response obtained upon Linear Sweep Voltammetry (LSV) while pulsing white LED light (600 W m^{-2} or 0.6 sun, 1s/1s on/off inputs) for the $\text{Cu}_2\text{O}/\text{ALD-TiO}_2/\text{m-TiO}_2/\text{Link-UrFe}$ electrodes, where the mesoporous layer (m-TiO_2) is obtained by drop-casting (red) or blade-coating (purple). CO_2 -saturated KHCO_3 0.5 M electrolyte. CE: Pt; RE: Ag/AgCl.

3.6 . Conclusions and perspectives

Assembling a heterogeneous device for light-assisted CO₂ reduction is an interesting perspective that can bring several advantages compared to a homogeneous photocatalytic system (aqueous medium, catalyst recycling, smaller catalyst loading, device stability, *etc.*). However, building such device can be quite challenging given that each layer needs to be optimized to maximize the photocurrent while minimizing photocorrosion and charge recombination. In this study we showed the construction of a PEC hybrid system for CO₂ reduction, where we studied the Cu₂O p-type semiconductor with a molecular catalyst **Link-UrFe** for CO₂ reduction. We could demonstrate the importance of optimizing the Cu₂O deposition method and its consequences on the PEC performance. Also, we highlighted the crucial role that covalent anchoring groups play in immobilizing the catalyst on the surface. We could still detect the catalyst on the surface after applying voltage and irradiation to the sample. This gives a first indication of the stability of hydroxamate groups for molecular immobilization.

To anchor the molecular catalyst, we implemented a mesoporous TiO₂ layer, where the porosity is fundamental to ensure an optimized loading of the catalyst. TiO₂ was chosen as a well-known material both to form transparent films and to allow covalent anchoring of molecules. We encountered some difficulties in this step, as the paste of TiO₂ can degrade the Cu₂O layer. We implemented instead a drop-casting technique that will need further improvements in particular for the transparency.

Different ALD layers were also added to the device to improve the stability and minimize photocorrosion. We remarked a more stable current compared to an electrode where Cu₂O is directly in contact with TiO₂ mesoporous layer. Even though the photocurrent density can be decreased due to the added interfaces, we believe that a gain in stability is more important to constitute a practical device.

Electrochemical studies on "dark" electrodes confirmed that even immobilized on the surface, **Link-UrFe** catalyst can perform CO₂ reduction, although the presence of TiO₂ could affect the product selectivity.

Overall, this preliminary study offers a panorama on the challenges that we face when assembling a photocathode for CO₂ reduction. Implementing a highly reducing semiconductor is advantageous in terms of reducing potentials that we can access, but requires a careful stabilization to avoid self-reduction. Further

work is envisioned in order to optimize the stacking of different layers and to take advantage of the modified second-coordination sphere that the molecular catalyst offers.

Bibliography

- (1) Groeneveld, I.; Kanelli, M.; Ariese, F.; Van Bommel, M. R. Parameters that affect the photodegradation of dyes and pigments in solution and on substrate – An overview. *Dyes and Pigments* **2023**, *210*, 110999.
- (2) Li, J.; Wu, N. Semiconductor-based photocatalysts and photoelectrochemical cells for solar fuel generation: a review. *Catalysis Science & Technology* **2015**, *5*, 1360–1384.
- (3) Grätzel, M. Photoelectrochemical cells. **2001**, 414.
- (4) Garcia Osorio, D. A.; Neri, G.; Cowan, A. J. Hybrid Photocathodes for Carbon Dioxide Reduction: Interfaces for Charge Separation and Selective Catalysis. *ChemPhotoChem* **2021**, *5*, 595–610.
- (5) Zhang, L.; Cole, J. M. Anchoring Groups for Dye-Sensitized Solar Cells. *ACS Applied Materials & Interfaces* **2015**, *7*, 3427–3455.
- (6) Gong, L.; Yin, H.; Nie, C.; Sun, X.; Wang, X.; Wang, M. Influence of Anchoring Groups on the Charge Transfer and Performance of p-Si/TiO₂/Cobaloxime Hybrid Photocathodes for Photoelectrochemical H₂ Production. *ACS Applied Materials & Interfaces* **2019**, *11*, 34010–34019.
- (7) Aguirre, M. E.; Zhou, R.; Eugene, A. J.; Guzman, M. I.; Grela, M. A. Cu₂O/TiO₂ heterostructures for CO₂ reduction through a direct Z-scheme: Protecting Cu₂O from photocorrosion. *Applied Catalysis B: Environmental* **2017**, *217*, 485–493.
- (8) Bonin, J.; Chaussemier, M.; Robert, M.; Routier, M. Homogeneous Photocatalytic Reduction of CO₂ to CO Using Iron(0) Porphyrin Catalysts: Mechanism and Intrinsic Limitations. *ChemCatChem* **2014**, *6*, 3200–3207.
- (9) Khan, A. A.; Tahir, M. Recent advancements in engineering approach towards design of photo-reactors for selective photocatalytic CO₂ reduction to renewable fuels. *Journal of CO₂ Utilization* **2019**, *29*, 205–239.
- (10) Hara, M.; Kondo, T.; Komoda, M.; Ikeda, S.; Kondo, J. N.; Domen, K.; Hara, M.; Shinohara, K.; Tanaka, A. Cu₂O as a photocatalyst for overall water splitting under visible light irradiation. *Chemical Communications* **1998**, 357–358.
- (11) De Jongh, P. E.; Vanmaekelbergh, D.; Kelly, J. J. Photoelectrochemistry of Electrodeposited Cu[sub 2]O. *Journal of The Electrochemical Society* **2000**, *147*, 486.
- (12) Siripala, W.; Ivanovskaya, A.; Jaramillo, T. F.; Baeck, S.-H.; McFarland, E. W. A Cu₂O/TiO₂ heterojunction thin film cathode for photoelectrocatalysis. *Solar Energy Materials and Solar Cells* **2003**, *77*, 229–237.
- (13) Hu, C.-C.; Nian, J.-N.; Teng, H. Electrodeposited p-type Cu₂O as photocatalyst for H₂ evolution from water reduction in the presence of WO₃. *Solar Energy Materials and Solar Cells* **2008**, *92*, 1071–1076.
- (14) Nian, J.-N.; Hu, C.-C.; Teng, H. Electrodeposited p-type Cu₂O for H₂ evolution from photoelectrolysis of water under visible light illumination. *International Journal of Hydrogen Energy* **2008**, *33*, 2897–2903.
- (15) Barreca, D.; Fornasiero, P.; Gasparotto, A.; Gombac, V.; Maccato, C.; Montini, T.; Tondello, E. The Potential of Supported Cu₂O and CuO Nanosystems in Photocatalytic H₂ Production. *ChemSusChem* **2009**, *2*, 230–233.
- (16) Schreier, M.; Gao, P.; Mayer, M. T.; Luo, J.; Moehl, T.; Nazeeruddin, M. K.; Tilley, S. D.; Grätzel, M. Efficient and selective carbon dioxide reduction on low cost protected Cu₂O photocathodes using a molecular catalyst. *Energy & Environmental Science* **2015**, *8*, 855–861.
- (17) Schreier, M.; Luo, J.; Gao, P.; Moehl, T.; Mayer, M. T.; Grätzel, M. Covalent Immobilization of a Molecular Catalyst on Cu₂O Photocathodes for CO₂ Reduction. *Journal of the American Chemical Society* **2016**, *138*, 1938–1946.

- (18) Paracchino, A.; Brauer, J. C.; Moser, J.-E.; Thimsen, E.; Graetzel, M. Synthesis and Characterization of High-Photoactivity Electrodeposited Cu_2O Solar Absorber by Photoelectrochemistry and Ultrafast Spectroscopy. *The Journal of Physical Chemistry C* **2012**, *116*, 7341–7350.
- (19) Tavares, M. T.; de Almeida, L. C.; Kronenberger, T.; Monteiro Ferreira, G.; Fujii de Divitiis, T.; Franco Zannini Junqueira Toledo, M.; Mariko Aymoto Hassimotto, N.; Agostinho Machado-Neto, J.; Veras Costa-Lotufo, L.; Parise-Filho, R. Structure-activity relationship and mechanistic studies for a series of cinnamyl hydroxamate histone deacetylase inhibitors. *Bioorganic & Medicinal Chemistry* **2021**, *35*, 116085.
- (20) Makuła, P.; Pacia, M.; Macyk, W. How To Correctly Determine the Band Gap Energy of Modified Semiconductor Photocatalysts Based on UV-Vis Spectra. *The Journal of Physical Chemistry Letters* **2018**, *9*, 6814–6817.
- (21) Kubelka, P.; Munk, F. A Contribution to the Optics of Pigments. *Zeit Tech Phys* **1931**, *12*, 593–599.
- (22) Zhang, L.; McMillon, L.; McNatt, J. Gas-dependent bandgap and electrical conductivity of Cu_2O thin films. *Solar Energy Materials and Solar Cells* **2013**, *108*, 230–234.
- (23) Marica, I.; Stefan, M.; Boca, S.; Falamaş, A.; Farcău, C. A simple approach for coffee-ring suppression yielding homogeneous drying patterns of ZnO and TiO_2 nanoparticles. *Journal of Colloid and Interface Science* **2023**, *635*, 117–127.
- (24) Janczarek, M.; Kowalska, E. On the Origin of Enhanced Photocatalytic Activity of Copper-Modified Titania in the Oxidative Reaction Systems. *Catalysts* **2017**, *7*, 317.

4 - PHOTOCATALYSIS FOR OXYGEN ATOM TRANSFER REACTIONS

4.1 . Introduction and objectives

Performing oxidation reactions is crucial for a variety of chemicals' preparation in the chemical industry. Atmospheric dioxygen has great potential to be one of the most environmentally compatible oxidants. However, because of its triplet state a first activation step is necessary to allow it to react with organic molecules in their ground singlet states.

Coordination chemists have taken inspiration from nature in designing iron complexes (heme and non-heme) that can carry the function of dioxygen activation. If the ligands are correctly tuned, an Fe(II) complex is capable of binding dioxygen upon sharing of electrons, to first generate a superoxide which turns to peroxide with the second electron transfer, generating Fe(III) peroxide intermediate. Non-heme iron complex $[\text{L}_5\text{Fe}^{\text{II}}-\text{OH}_2]^{2+}$ (later abbreviated as $[\text{L}_5\text{Fe}^{\text{II}}]^{2+}$) is one of the model complexes that have been studied for the formation of reactive intermediates (Fig. 4.1). Its activation with an already reduced form of dioxygen, H_2O_2 has been previously reported [1] [2] [3]. This chemical method allows to form intermediates such as Fe(III) hydroperoxo ($\text{Fe}^{\text{III}}-\text{OOH}$) and Fe(III) peroxo ($\text{Fe}^{\text{III}}-\text{OO}^-$) which are key intermediates in the transfer of an oxygen atom to an organic substrate.

On the other hand, different strategies can be addressed to find ways to implement directly dioxygen in the catalytic cycle. The option that we investigate in this chapter includes the use of a photoredox module to generate *in-situ* superoxide ($\text{O}_2^{\cdot-}$) which can then bind to the $[\text{L}_5\text{Fe}^{\text{II}}]^{2+}$ complex to perform oxygen atom transfer on a model substrate. This strategy relies on the use of methyl viologen (MV^{2+}) as electron relay; also known to readily transfer one electron to dioxygen when in the $\text{MV}^{\cdot+}$ form [4].

It should be emphasized that in this system we are dealing with *reductive* activation of O_2 (since electrons need to be injected for activation) to then perform *oxidation* of an organic substrate. This notion may seem counter-intuitive at first, but it means that a first transfer of electrons to O_2 is necessary to allow

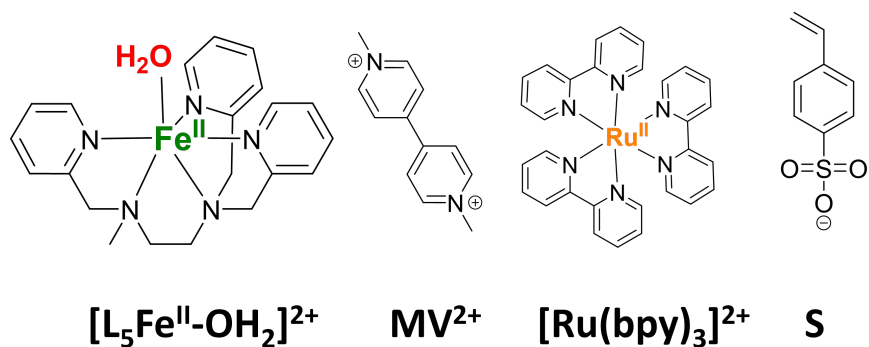


Figure 4.1: Structures of the components used in this study: $[L_5Fe^{II}-OH_2]^{2+}$ as catalyst, methylviologen (MV^{2+}) as electron relay, $[Ru(bpy)_3]^{2+}$ as photosensitizer and styrene sulfonate sodium salt as substrate (S).

its binding to the iron complex; at the same time the metal center that transfers electrons to the oxygen accumulates enough oxidizing power to insert the oxygen atom into the substrate's double bond.

The choice of these components has allowed us to work in aqueous medium, which is advantageous in terms of soft conditions for performing oxidation.

The goal of this study is to understand the photophysical events occurring in this system, in order to follow the formation of reactive intermediates and piece them together in a proposal of mechanism. The catalytic activity and related controls are also investigated to assess the presence catalytic regime in the mechanistic studies. We also study the effect of pH both on catalysis and on the intermediates formed.

4.2 . Understanding the photophysical events

As a first step of the study, investigation of the photophysical events was performed in our group, following LFP experiments on a mixture of $[\text{Ru}(\text{bpy})_3]^{2+}$, MV^{2+} , $[\text{L}_5\text{Fe}^{\text{II}}]^{2+}$ in presence of O_2 and an organic substrate. As a model substrate we chose 4-styrene sulfonate, sodium salt (abbreviated as S, see Fig. 4.1), where the sulfonate group allows its solubility in an aqueous medium. For a better understanding, we followed one event at the time from a simplified system and then gradually increased its complexity.

When $[\text{Ru}^{\text{II}}(\text{bpy})_3]^{2+}$ and MV^{2+} were mixed together and irradiated in anaerobic conditions, we observed quenching of the PS excited state ($[\text{Ru}^{\text{II}}(\text{bpy})_3]^{2+*}$) with a shortening of its lifetime from 600 ns to 270 ns, and the formation of reduced methyl viologen ($\text{MV}^{\bullet+}$), with the characteristic absorption maxima at 390 nm and 605 nm. In Fig. 4.2 we can see the absorption spectrum at 1 μs delay of such LFP measurement. The bleaching at 460 nm indicates the disappearance of the Ru(II) species absorption (450 nm), at the same time with formation of the $\text{MV}^{\bullet+}$ bands. On a longer timescale, back-electron transfer is observed with a decay of the light-generated Ru(III) and $\text{MV}^{\bullet+}$ species. These steps are described in Eq. 4.2 and 4.3.

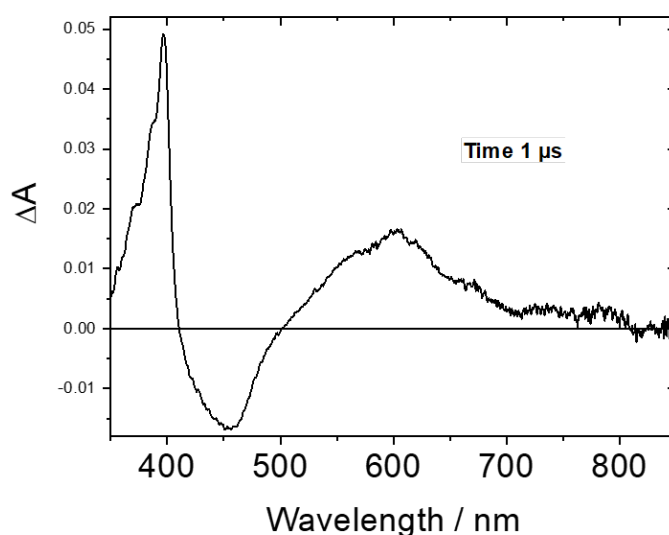
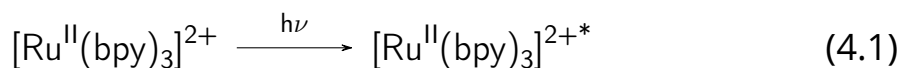


Figure 4.2: Transient absorption spectrum from a Britton and Robinson (B&R) pH 4 buffer solution of $[\text{Ru}^{\text{II}}(\text{bpy})_3]^{2+}$ (30 μM), MV^{2+} (4 mM) in Ar at 1 μs delay after excitation.



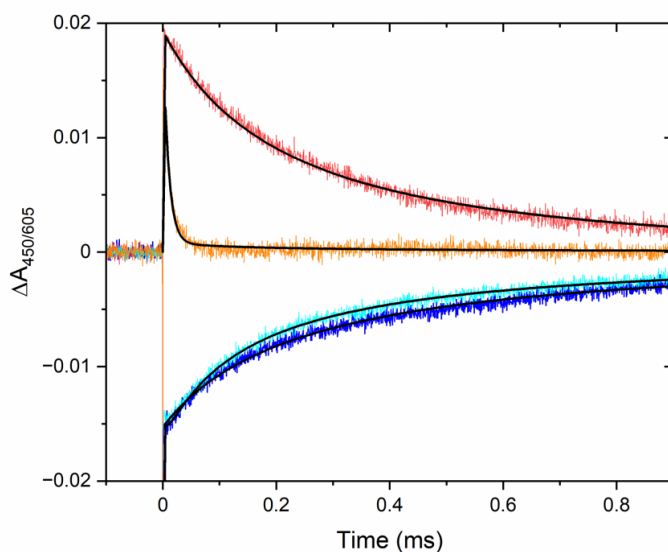
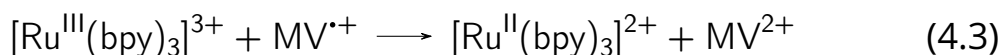


Figure 4.3: Time-resolved absorption changes of a solution of $[\text{Ru}^{\text{II}}(\text{bpy})_3]^{2+}$ ($30 \mu\text{M}$) and MV^{2+} (4 mM) at 450 nm (blue) and 605 nm (red) in argon saturated B&R pH 4 buffer; at 450 nm (cyan) and 605 nm (orange) in B&R pH 4 buffer under aerobic conditions. Solid black lines are best fit traces.



When the same experiment was repeated in aerobic conditions, the lifetime of the $\text{MV}^{\bullet+}$ species was significantly shortened, due to its reaction with O_2 .

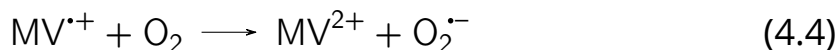
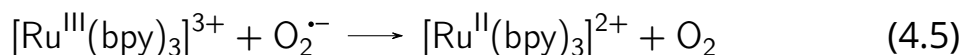


Fig. 4.3 shows the comparison of the kinetic traces of the $\text{MV}^{\bullet+}$ and $\text{Ru}(\text{II})$ species in the two conditions described above (with and without O_2). We can observe that the lifetime of $\text{MV}^{\bullet+}$ is indeed shortened (red and orange traces). No big changes are observed for the kinetic trace of the recovery of $\text{Ru}(\text{II})$ (blue and cyan traces). In the introduction chapter it was mentioned that singlet oxygen can be formed upon triplet-triplet energy transfer from an excited chromophore, such as $[\text{Ru}^{\text{II}}(\text{bpy})_3]^{2+}$. However, by increasing the concentration of MV^{2+} as quencher, it is possible to minimize this effect, given that MV^{2+} was at a concentration nearly two orders of magnitude greater than the dissolved O_2 . After the electron is transferred following eq. 4.4, recovery of $\text{Ru}(\text{II})$ occurs following the reaction in eq. 4.5.



We then investigated the interaction of our model substrate S with the other light-induced events. When $[\text{Ru}^{\text{II}}(\text{bpy})_3]^{2+}$, MV^{2+} and S were irradiated in a

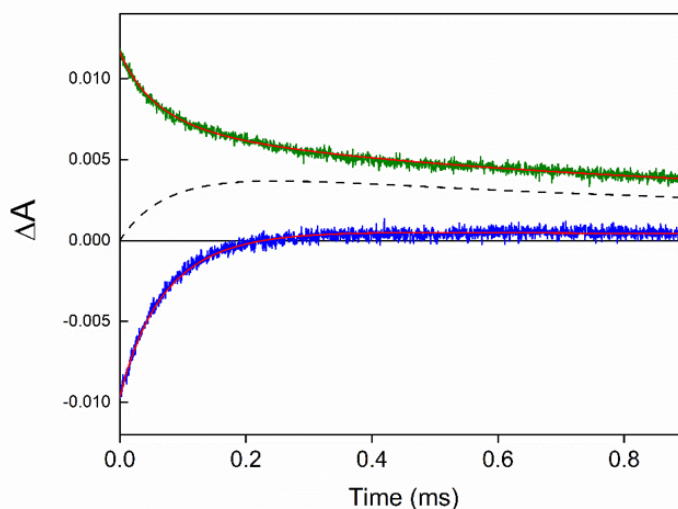
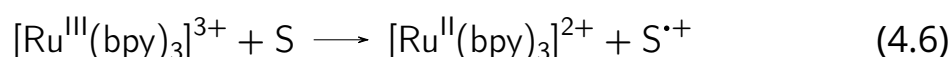


Figure 4.4: Time-resolved absorption changes of a solution of $[\text{Ru}^{\text{II}}(\text{bpy})_3]^{2+}$ ($30 \mu\text{M}$) and MV^{2+} (4 mM) at 450 nm (blue) and 605 nm (green) in Ar-saturated B&R buffer (pH 4) in presence of sodium 4-styrenesulfonate (100 mM). Red traces: kinetic analysis yielding second order rate constants for charge recombination between $[\text{Ru}^{\text{III}}]$ and MV^{*+} ($9.5 \cdot 10^9 \text{ M}^{-1}\text{s}^{-1}$; this rate is increased by about a factor of 2 and attributed to the very high concentration of styrene in this particular experiment), sodium 4-styrenesulfonate oxidation by $[\text{Ru}^{\text{III}}]$ ($7.3 \cdot 10^4 \text{ M}^{-1}\text{s}^{-1}$) and charge recombination between MV^{*+} and oxidized sodium 4-styrenesulfonate ($1.9 \cdot 10^9 \text{ M}^{-1}\text{s}^{-1}$). The dashed line indicates the concentration of oxidized styrene, with the maximum corresponding to a concentration of $0.4 \mu\text{M}$. Initial concentration of Ru(III) and MV^{*+} : $0.85 \mu\text{M}$.

deaerated solution, we observed once again the oxidative quenching of Ru(II) to form Ru(III) and MV^{*+} ; but this time the back-electron transfer kinetics were affected by the presence of the substrate. Fig. 4.4 shows that the decay of the 605 nm species (MV^{*+} , green trace) is slower compared to the Ru(II) recovery (450 nm , blue trace). This means that the recovery of Ru(II) not only occurs via Eq. 4.3, but a second electron transfer is taking place concomitantly, which involves extraction of an electron from the substrate to generate its radical cation (see Eq. 4.6). We could also simulate the estimated concentration of oxidized substrate (dashed line in Fig. 4.4) from fittings of the kinetic traces.



The same kind of verification was performed for possible interaction of $[\text{L}_5\text{Fe}^{\text{II}}]^{2+}$ with other photo-induced species. In the first place, the mixture of $[\text{Ru}^{\text{II}}(\text{bpy})_3]^{2+}$ and $[\text{L}_5\text{Fe}^{\text{II}}]^{2+}$ was irradiated in anaerobic conditions. No changes of the $[\text{Ru}^{\text{II}}(\text{bpy})_3]^{2+*}$ emission were observed (see Fig. 4.5), meaning that the excited state is not being quenched by the Fe complex. When MV^{2+} was also added in solution, the result was comparable to what had already been seen

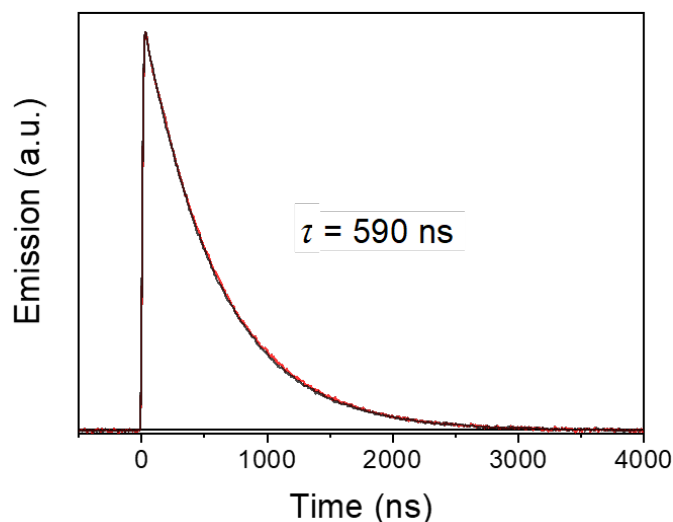


Figure 4.5: Normalized traces of the kinetics of $\text{Ru}^{\text{II}*}$ emission measured at 610 nm in a B&R pH 4 solution of $[\text{Ru}^{\text{II}}(\text{bpy})_3]^{2+}$ ($30 \mu\text{M}$) (red) in the absence and (black) presence of $[\text{L}_5\text{Fe}^{\text{II}}]^{2+}$ ($30 \mu\text{M}$).

in absence of $[\text{L}_5\text{Fe}^{\text{II}}]^{2+}$. Fig. 4.6 shows once again the bleaching of $\text{Ru}(\text{II})$ around 450 nm, together with the appearance of $\text{MV}^{\bullet+}$ at 390 nm and 605 nm. The electron transfer steps are described as above, by Eq. 4.2 and 4.3, for the oxidative quenching and recombination, respectively. From these observations, we could deduce that no oxidation or reduction of $[\text{L}_5\text{Fe}^{\text{II}}]^{2+}$ is occurring in these conditions. Oxidation could be possible from the photo-produced $\text{Ru}(\text{III})$ species, and also thermodynamically feasible. However, we hypothesize that it is not observed due to its slow kinetics when compared to the recombination with $\text{MV}^{\bullet+}$ (See Eq. 4.3). The slower kinetics may be related to unfavourable deprotonation step ($\text{L}_5\text{Fe}^{\text{II}}-\text{OH}_2$ to $\text{L}_5\text{Fe}^{\text{III}}-\text{OH}$) that accompanies oxidation given the pH 4 of the experiment. On the other hand, reduction of $[\text{L}_5\text{Fe}^{\text{II}}]^{2+}$ by the photo-generated $\text{MV}^{\bullet+}$ (with a reduction potential of -1.0 V vs. SCE [5]) seems to be inaccessible, as it is indicated by the absence of a reduction wave in the CV until -1.0 V vs. SCE (Fig. 4.7).

Lastly, when the $[\text{Ru}^{\text{II}}(\text{bpy})_3]^{2+} / [\text{L}_5\text{Fe}^{\text{II}}]^{2+} / \text{MV}^{2+}$ mixture was studied in aerobic solution clear changes in the kinetics for $\text{Ru}(\text{II})$ and $\text{MV}^{\bullet+}$ were observed. Fig. 4.8 highlights the faster recovery of MV^{2+} in presence of O_2 together with a slower of recovery $\text{Ru}(\text{II})$. The former can be explained, as we mentioned previously, by Eq. 4.4, where the $\text{MV}^{\bullet+}$ quickly reacts with O_2 . However, the latter indicated that recombination of $\text{Ru}(\text{III})$ with $\text{O}_2^{\bullet-}$ is inhibited. We interpreted this observation by the possibility of a rapid binding of the superoxide formed with the $\text{Fe}(\text{II})$ complex, giving rise to $\text{Fe}(\text{III})$ hydroperoxo intermediates, given

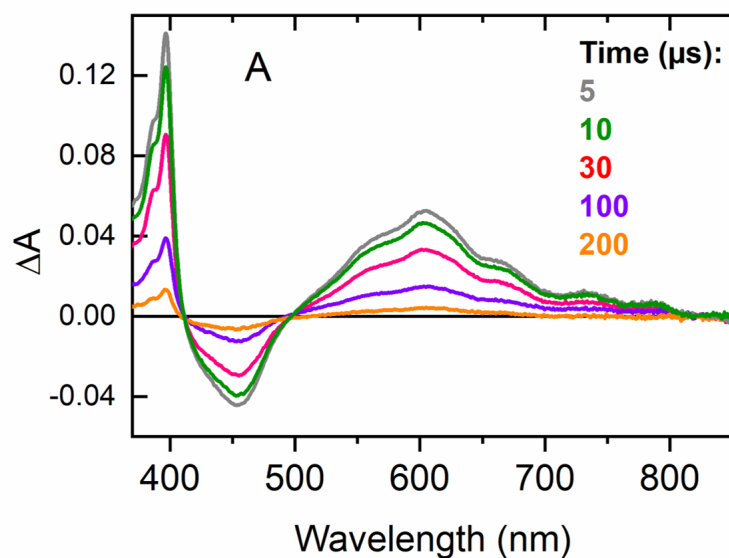


Figure 4.6: Transient absorption spectra from an Ar-saturated B&R pH 4 buffer solution of $[\text{Ru}^{\text{II}}(\text{bpy})_3]^{2+}$ ($30 \mu\text{M}$), MV^{2+} (20mM), and $[(\text{L}_5)\text{Fe}^{\text{II}}]^{2+}$ ($100 \mu\text{M}$) at the indicated delay times after excitation.

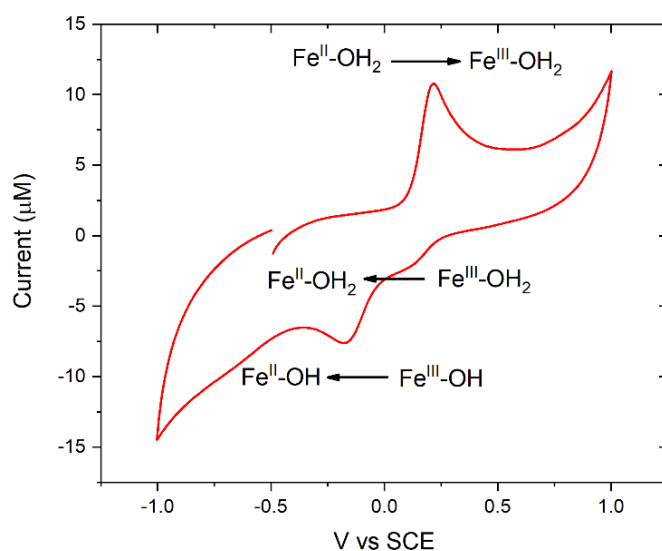


Figure 4.7: Cyclic voltammetry of $1 \text{mM} [(\text{L}_5)\text{Fe}^{\text{II}}]^{2+}$ at 0.1V/s in an aqueous medium buffered at pH 6. Supporting electrolyte: 0.1M NaClO_4 , working electrode: glassy carbon. The redox couples were attributed to the presence of a water molecule in the coordination sphere of the iron center. The loss in reversibility of the electrochemical oxidation wave was attributed to a proton coupled electron transfer process.

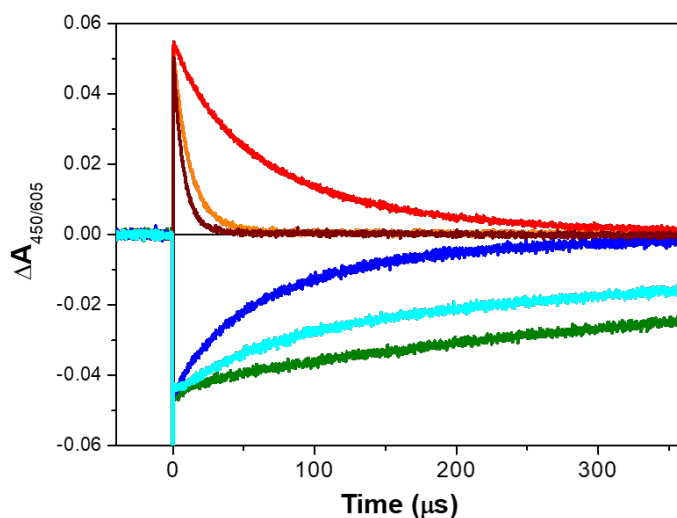
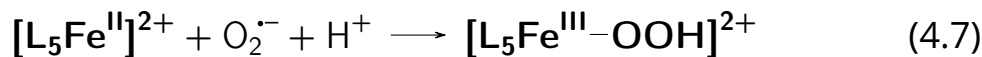
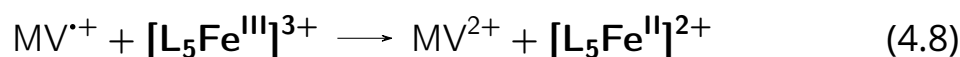


Figure 4.8: Time-resolved absorption changes at 605 nm (warm colors) and 450 nm (cold colors) in argon-saturated pH 4 buffer (red and blue lines), under aerobic conditions (brown and cyan lines), and after renewed excitation under anaerobic conditions of the previous solution (orange and green lines). Solution containing $[\text{Ru}^{\text{II}}(\text{bpy})_3]^{2+}$ ($30 \mu\text{M}$), MV^{2+} (20mM), and $[(\text{L}_5)\text{Fe}^{\text{II}}]^{2+}$ ($100 \mu\text{M}$).

the pH 4 of these conditions (see Eq. 4.7).



Interestingly, when the same solution was then degassed again with Ar and the same laser photolysis experiment is repeated in anaerobic conditions (orange and green lines of Fig. 4.8), the kinetics are different from the first anaerobic measurement. The lifetime of $\text{MV}^{\cdot+}$ remains almost as short as in aerobic conditions and the recovery of Ru(II) is even slower than in aerobic conditions. This can be rationalized by assuming the formation of a new species that can be reduced by $\text{MV}^{\cdot+}$ and hampering its recombination with Ru(III). Indeed the $[\text{Fe}^{\text{III}}-\text{OOH}]^{2+}$ formed in presence of O_2 can generate $\text{Fe}(\text{V})=\text{O}$ to then reduce back to an Fe(III) species, which is then reduced to Fe(II) by $\text{MV}^{\cdot+}$ (see Eq. 4.8). This will be confirmed in later sections by EPR analysis.



The rate constants were estimated from analysis of the kinetic traces and the observed decay times and taking into account the order of each reaction with relative concentrations of each species involved. The values found are summarized in Table 4.1.

Table 4.1: Summary of bimolecular rate constants deduced from laser flash photolysis^a.

Equation	Reaction	Rate constant (M ⁻¹ s ⁻¹)
4.2	$[\text{Ru}^{\text{II}}(\text{bpy})_3]^{2+\ast} + \text{MV}^{2+} \longrightarrow [\text{Ru}^{\text{III}}(\text{bpy})_3]^{3+} + \text{MV}^{\bullet+}$	$0.45 \cdot 10^9$
4.3	$[\text{Ru}^{\text{III}}(\text{bpy})_3]^{3+} + \text{MV}^{\bullet+} \longrightarrow [\text{Ru}^{\text{II}}(\text{bpy})_3]^{2+} + \text{MV}^{2+}$	$3.1 \cdot 10^9$
4.4	$\text{MV}^{\bullet+} + \text{O}_2 \longrightarrow \text{MV}^{2+} + \text{O}_2^{\bullet-}$	$0.6 \cdot 10^9$
4.5	$[\text{Ru}^{\text{III}}(\text{bpy})_3]^{3+} + \text{O}_2^{\bullet-} \longrightarrow [\text{Ru}^{\text{II}}(\text{bpy})_3]^{2+} + \text{O}_2$	$3 \cdot 10^9$
4.6	$[\text{Ru}^{\text{III}}(\text{bpy})_3]^{3+} + \text{S} \longrightarrow [\text{Ru}^{\text{II}}(\text{bpy})_3]^{2+} + \text{S}^{\bullet+}$	$8 \cdot 10^4$
4.8	$\text{MV}^{\bullet+} + [\text{L}_5\text{Fe}^{\text{III}}]^{3+} \longrightarrow \text{MV}^{2+} + [\text{L}_5\text{Fe}^{\text{II}}]^{2+}$	$0.9 \cdot 10^9$

^a The rate of quenching of the $[\text{Ru}^{\text{II}}(\text{bpy})_3]^{2+\ast}$ excited state by MV^{2+} is an apparent rate including the effect of escape yield of about 20%. The bimolecular rate constant for reaction 4.7 is difficult to estimate given the weak signal of $[\text{L}_5\text{Fe}^{\text{III}}-\text{OOH}]^{2+}$ under the LFP conditions.

The study of the photophysical events seems to support the interaction of $[\text{L}_5\text{Fe}^{\text{II}}]^{2+}$ with superoxide generated *in-situ* by light-induced electron transfers. We could also demonstrate that the reaction of the photo-generated Ru(III) with the substrate allows to reset the Ru(II) ground state, an important step in catalytic conditions. These first results indicate a possible interaction of $[\text{Fe}^{\text{III}}-\text{OOH}]^{2+}$ with the substrate to perform oxidation reactions. To confirm our hypothesis we aimed first of all to verify the expected photocatalytic activity.

4.3 . Photocatalysis

In order to ensure that the system is catalytic, we irradiated a mixture of $[\text{L}_5\text{Fe}^{\text{II}}]^{2+}$, $[\text{Ru}(\text{bpy})_3]^{2+}$, MV^{2+} in presence of O_2 and the styrene sulfonate substrate.

Experiments conducted in our group have confirmed the formation of oxidized products, comprising aldehyde, diol and epoxide, depending on the pH conditions (see Fig. 4.9) [6]. The results observed with the assigned peaks are shown in Fig. 4.10. Since the catalysis occurs in a homogeneous system yielding water-soluble products, analysis of the products was performed using ¹H-NMR.

Control experiments in absence of Fe catalyst (blue and green spectra), MV^{2+} (cyan spectrum) or with an iron salt (FeCl_3 , brown spectrum) did not yield any significant amount of detectable products, except for some small trace of aldehyde in absence of $[\text{L}_5\text{Fe}^{\text{II}}]^{2+}$ (green spectrum). This confirms the sequence of reactions proposed in the previous section, where each element is necessary for the cascade of light-induced electron transfers that ultimately favours the formation of high-valent oxygen-metal adducts, capable of transferring the oxygen atom onto the double bond of the styrene. The presence of $[\text{L}_5\text{Fe}^{\text{II}}]^{2+}$ is necessary to have a great enhancement of the catalytic reaction and it rules out

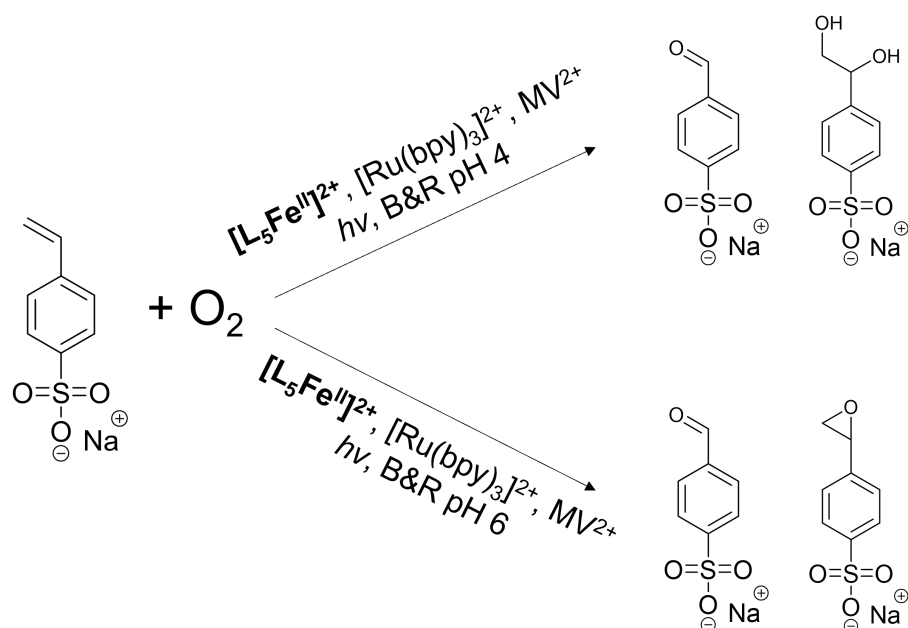


Figure 4.9: Scheme of the substrate oxidation reaction in the studied conditions.

the contribution of singlet oxygen formation to the substrate's oxidation. With an iron salt as catalyst, the negligible catalytic activity confirms that there is no prominent radical chemistry taking place. Table 4.2 reports conditions and calculated TON for these experiments. The found TON of about 70 is comparable with those reported for molecular iron complexes using H_2O_2 instead of O_2 [7].

Interestingly, a difference in products selectivity was also observed depending on pH. In all cases, aldehyde was detected in larger amounts than the other products, however in acidic conditions (pH 4) the diol was detected instead of the epoxide found at pH 6. This can be related to a preferential ring-opening operating in more acidic conditions, the second oxygen atom deriving from water [8]. Some possible pathways that can be involved in the transfer of oxygen from the iron complex to the double bond are shown in Fig. 4.11. We can see at the top two different hypothesis of events occurring after the formation of $Fe(III)\text{-OOH}$ intermediate, both leading to a state where a highly reactive $Fe(V)=O(OH)$ is formed. At this stage, the three detected products can be formed (lower part of Fig. 4.11) depending on pH conditions, or if the oxygen atom is transferred to the substrate as alkene (left side) or as radical cation (right side).

Importantly, isotope-labelling experiments had also been carried out using $^{18}O_2$ to confirm the source of oxygen atom on the oxidized products (see annex).

Furthermore, we calculated here the apparent quantum yield obtained in the

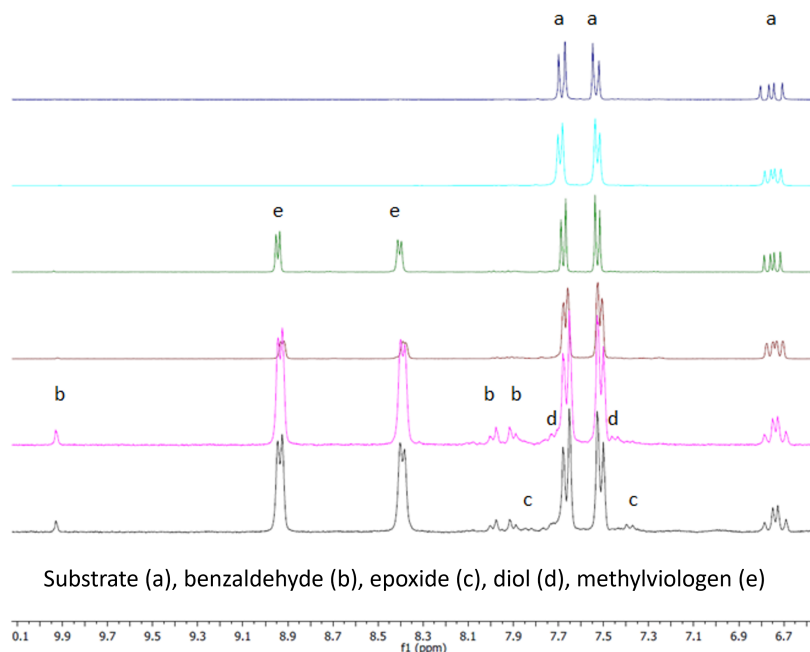


Figure 4.10: Extracts of the $^1\text{H-NMR}$ spectra of crude reaction mixtures in H_2O and 10 % D_2O obtained upon light irradiation of sodium 4-styrenesulfonate (10 mM) for 22 hours under aerobic conditions. (Blue) with $[\text{Ru}^{\text{II}}(\text{bpy})_3]^{2+}$ (30 μM) in B&R pH 4; (Cyan) with $[\text{Ru}^{\text{II}}(\text{bpy})_3]^{2+}$ (30 μM) and $[\text{L}_5\text{Fe}^{\text{II}}]^{2+}$ (30 μM) in B&R pH 4; (Green) with $[\text{Ru}^{\text{II}}(\text{bpy})_3]^{2+}$ (30 μM) and MV^{2+} (4 mM) in B&R pH 4; (Brown) with $[\text{Ru}^{\text{II}}(\text{bpy})_3]^{2+}$ (30 μM), FeCl_3 (60 μM), MV^{2+} (4 mM) in B&R pH 4; (Pink) with $[\text{Ru}^{\text{II}}(\text{bpy})_3]^{2+}$ (30 μM), $[\text{L}_5\text{Fe}^{\text{II}}]^{2+}$ (30 μM), MV^{2+} (4 mM) in B&R pH 4; (Black) with $[\text{Ru}^{\text{II}}(\text{bpy})_3]^{2+}$ (30 μM), $[\text{L}_5\text{Fe}^{\text{II}}]^{2+}$ (30 μM), MV^{2+} (4 mM) in B&R pH 6. Credits to [6].

Table 4.2: Substrate conversion under different conditions. Oxygenation reactions were carried out under irradiation for 22 hours (backlight white LED = 1.3 mW cm^{-2} equipped with a Wratten filter 2E, $\lambda > 450 \text{ nm}$), under aerobic conditions, in B&R buffer at pH 4. Substrate initial concentration: 10 mM.

$[\text{Ru}^{\text{II}}(\text{bpy})_3]^{2+}$	$[\text{L}_5\text{Fe}^{\text{II}}]^{2+}$	MV^{2+}	Product (mM)			TON	φ (%)
			Diol	Aldehyde	Epoxide		
30 μM	0	0	0	0	0	0	-
30 μM	0	4 mM	0	traces	0	nd	-
0	30 μM	4 mM	0	0	0	0	-
30 μM	30 μM	0	0	0	0	0	-
30 μM	30 μM	4 mM	0.83	1.27	traces	70	2.0
30 μM	60 $\mu\text{M}^{\text{[a]}}$	4 mM	0	traces	0	nd	-
30 μM	30 $\mu\text{M}^{\text{[b]}}$	4 mM	traces	1.17	0.66	61	1.7

[a] FeCl_3 is used as catalyst instead of the $[\text{L}_5\text{Fe}^{\text{II}}]^{2+}$ complex [b] B&R buffer at pH 6.

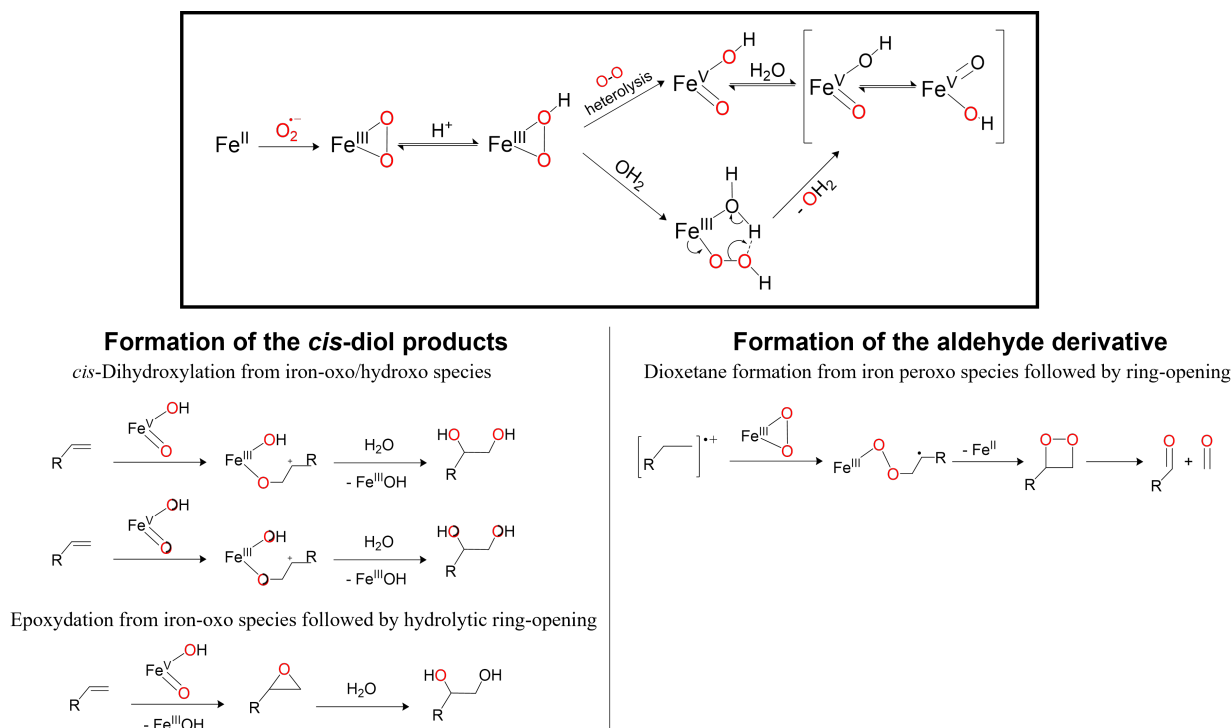


Figure 4.11: Proposed mechanisms for iron catalyzed sodium styrene-4-sulfonate oxidation based on literature reports [9] [10] [11] [12].

different cases. The general equation was discussed in the first chapter, but it is recalled here for this specific case (Eq. 4.9).

$$\varphi = [(2 \cdot N_{diol} + 2 \cdot N_{epoxide} + N_{aldehyde}) / N_{photons}] \cdot 100 \quad (4.9)$$

N indicates the number of moles of the different quantities, where $N_{photons}$ stands for incident photons. The factor multiplying the products moles corresponds to the number of photons necessary per catalytic cycle (two for diol and epoxide and one for aldehyde). The global quantum yield for all the detected products was estimated to be around 2 % for both pH conditions (see Table 4.2). These values are not exceptional, as it often occurs in experimental photocatalytic systems, where big losses of energy in secondary processes cause huge drops of quantum yield. For further developments of our system, it will be undoubtedly useful to understand such secondary processes and aim to improve the yield of the reaction.

Some more studies were conducted to optimize the reaction conditions. The main purpose was to verify the catalytic activity in the conditions in which photophysics experiments were performed. The red spectrum in Fig. 4.13 was obtained by blue light irradiation of a mixture containing $[L_5Fe^{II}]^{2+}$, $[Ru^{II}(bpy)_3]^{2+}$ and MV^{2+} at the same concentrations of the experiments described in the previous section and in presence of substrate and O_2 . As ex-

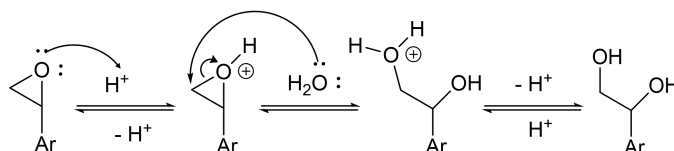


Figure 4.12: Mechanism scheme for the epoxide ring-opening in acidic medium.

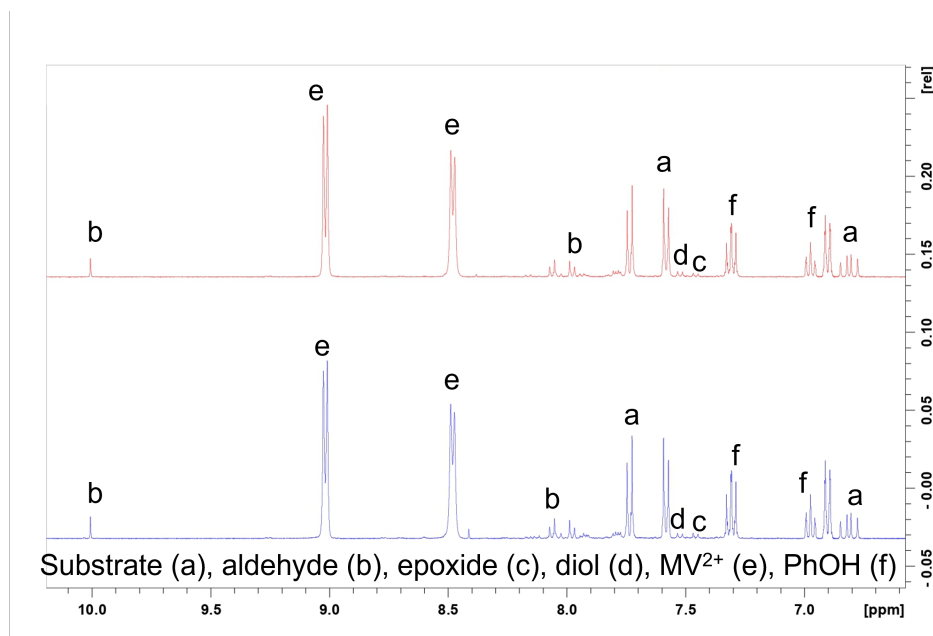


Figure 4.13: Extracts of the ¹H-NMR spectra of crude reaction mixtures in H₂O and 10% of standard for calibration (50 mM PhOH and 10 mM DMSO in D₂O) obtained upon light irradiation of sodium 4-styrenesulfonate (10 mM), [Ru^{II}(bpy)₃]²⁺ (30 μM), MV²⁺ (10 mM), [L₅Fe^{II}]²⁺ (100 μM) for 22 hours with blue LED (λ_{em} = 460 nm; 50 W m⁻²) under aerobic conditions in B&R pH 4. (Blue) With 2.5 mM EDTA addition and (Red) without.

pected, we could detect the presence of aldehyde and diol, given the pH 4 of this experiment. EDTA was then added also in the mixture (blue trace Fig. 4.13). Its function will be better discussed in the next session, for now it will suffice to say that it is added as electron donor. EDTA is known for its affinity for chelating metal ions, including Fe [13]; by following the catalytic activity in presence of such donor we can determine if the chelating power is affecting the catalysis due to Fe removal. Comparing the two spectra in Fig. 4.13, we do not observe a big difference, with the same products detected in comparable amount. Surprisingly, we could also observe a small peak due to the epoxide. This could be linked to an equilibrium between the two forms, where the diol is favoured at this pH value, but no full conversion of the epoxide has occurred (Fig. 4.12).

We then moved to study the effect of the substrate concentration on the catalytic activity. Increasing by a factor of 10 the styrene sulfonate amount and

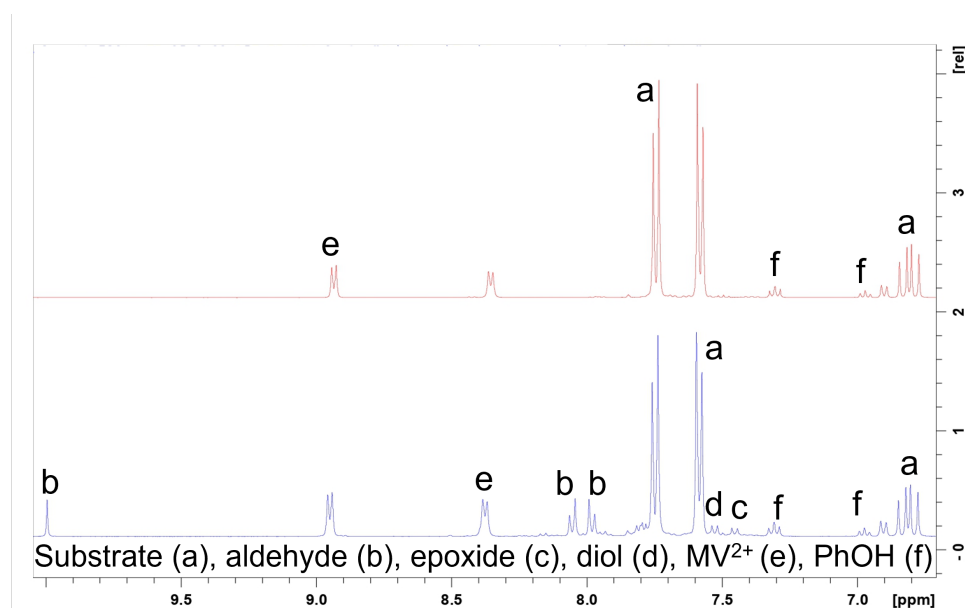


Figure 4.14: Extracts of the $^1\text{H-NMR}$ spectra of crude reaction mixtures in H_2O and 10% of standard for calibration (50 mM PhOH and 10 mM DMSO in D_2O) with sodium 4-styrenesulfonate (100 mM), $[\text{Ru}^{\text{II}}(\text{bpy})_3]^{2+}$ (30 μM), MV^{2+} (10 mM), $[\text{L}_5\text{Fe}^{\text{II}}]^{2+}$ (100 μM) under aerobic conditions in B&R pH 4. (Red) Control kept in the dark, (Blue) under light irradiation for 22h with blue LED ($\lambda_{\text{em}} = 460 \text{ nm}$; 50 W m^{-2}).

keeping the other values unchanged gave the resulting spectrum shown in the blue line of Fig. 4.14. We can notice an increase in the amount of both the aldehyde and diol products.

An important control is shown in the red trace in Fig. 4.14, where the same mixture was kept in the dark for the same time duration. As it can be observed, no traces of products can be detected, confirming the importance of light-induced cascade reactions to trigger oxygen atom transfer to the substrate.

The quantification of the products in these catalytic runs are shown in Table 4.3. In entries 1 and 2, we can see a clear decrease of catalysis in terms of TON compared to what we reported in Table 4.2. This could be rationalized by the more than three-fold increase of catalyst concentration, which may cause "over saturation", with not all the metal sites being effectively used. On the other hand, entry 3 of Table 4.3 shows a remarkable increase in terms of TON. However, when the conversion percentage is compared in the two cases of substrate concentration, we observe almost equal values. This interesting finding can be explained in terms of the oxidation of the substrate by the $\text{Ru}(\text{III})$ being a slow reaction, in competition with other back reactions (such as with MV^+). Having a larger concentration of the substrate will therefore favor the catalytic steps.

Table 4.3: Substrate conversion under different reaction conditions. Oxygenation reactions were carried out under irradiation for 22 hours (blue LED = 50 W m⁻² λ_{em} = 460 nm), under aerobic conditions, in B&R buffer at pH 4, [Ru^{II}(bpy)₃]²⁺ 30 μM, [L₅Fe^{II}]²⁺ 100 μM, MV²⁺ 10 mM.

Entry	Substrate (mM)	EDTA (mM)	Product (mM)			TON	Conversion (%)
			Diol	Aldehyde	Epoxide		
1	10	2.5	0.387	0.865	0.335	15.9	15.9
2	10	0	0.492	0.977	0.279	17.5	17.5
3	100	0	4.30	9.02	3.34	166.6	16.7
4 ^[a]	100	0	0	0	0	0	-

[a] No irradiation.

4.4 . Trapping reactive intermediates

After confirming the catalytic activity of our system, we aimed to obtain further insights on the mechanism using intermediates trapping and characterization. The ideal case for reactive intermediates study is to generate and characterize them in the same conditions as those during catalysis. In this case, using light-induced electron transfers.

In the first place, we monitored changes in the electronic spectra in the visible region. Previous works [14] [15] reported an absorption of the $[\text{L}_5\text{Fe}^{\text{III}}-\text{OOH}]^{2+}$ intermediate in methanol and at low temperatures at 537 nm. Such intermediate was generated chemically using H_2O_2 .

In our case, we irradiated a mixture of $[\text{L}_5\text{Fe}^{\text{II}}]^{2+}$, $[\text{Ru}^{\text{II}}(\text{bpy})_3]^{2+}$ and MV^{2+} in presence of an electron donor and O_2 at different pH. We chose to use EDTA as electron donor, to be able to reset to the Ru(II) ground state of the Ru(III) photo-generated through an oxidative quenching with MV^{2+} . In the catalytic system, this reaction is carried out using the styrene substrate **S**. However, given the lower rate constant of such step (see Table 4.1), we chose EDTA for the more rapid electron transfer to Ru(III), to be able to accumulate quickly a maximum amount of the iron intermediate.

When we irradiated this solution at pH 4, we noticed from the beginning a bleaching of absorption around 390 nm, which correspond to the loss of $[\text{L}_5\text{Fe}^{\text{II}}]^{2+}$. Concomitantly, we observed the growth of a new band in the 500 nm region, which could correspond to the Fe(III)-OOH state reported before (See Fig. 4.15). The difference in wavelength compared to the reported one, can be explained by the different solvent and temperature conditions. We accumulated this intermediate by shining continuous light with blue LED for 10 s. When the light is switched off, we can observe a rapid decay of the formed species, due to its instability in aqueous medium at room temperature (inset of Fig. 4.15).

To highlight the importance of the electron donor choice, we performed the same experiment using the substrate in the place of EDTA. The result (Fig. 4.16) showed a very similar trend of bleaching at 390 nm and a growing band in the 500 nm region; however, the signal recorded in these conditions is much smaller, probably due to the smaller amount of $[\text{L}_5\text{Fe}^{\text{III}}-\text{OOH}]^{2+}$ formed.

When the same experiment was repeated in more basic conditions (in B&R buffer at pH 6), we observed once again the bleaching of the Fe(II) species around 390 nm, but with a different growing wide band, with a maximum ab-

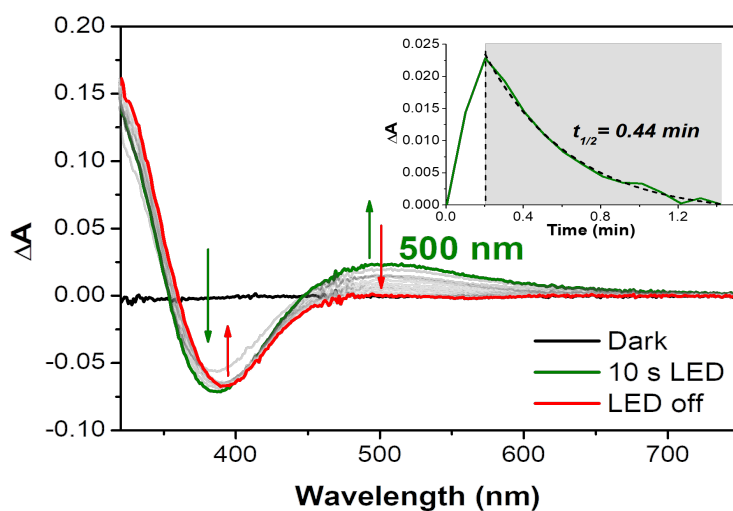


Figure 4.15: Spectral evolution of the absorption of a B&R pH 4 buffer solution containing $[\text{Ru}^{\text{II}}(\text{bpy})_3]^{2+}$ ($30 \mu\text{M}$), MV^{2+} (10 mM), EDTA (20 mM), and $[\text{L}_5\text{Fe}^{\text{II}}]^{2+}$ ($100 \mu\text{M}$) upon irradiation (100 W m^{-2} for 10 s) under aerobic conditions and no stirring. The difference of absorbance from the solution in the dark and during irradiation. Inset: kinetic profile of the 500 nm band.

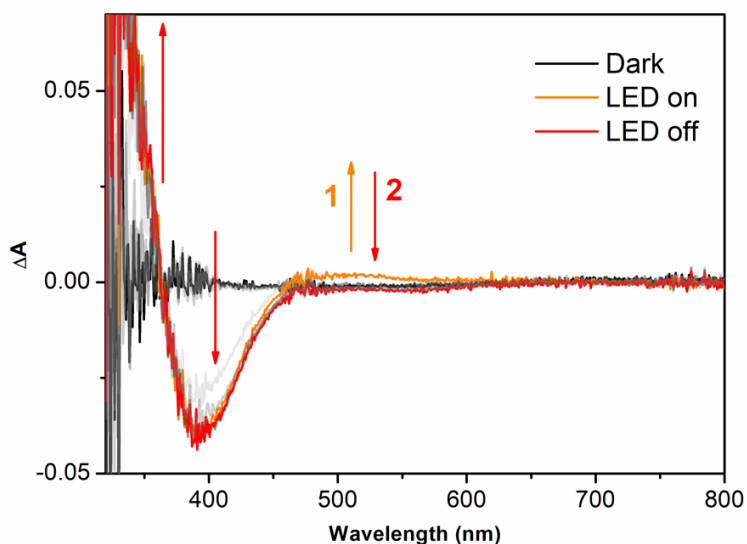


Figure 4.16: Photoaccumulation of $100 \mu\text{M}$ $[\text{L}_5\text{Fe}^{\text{II}}]^{2+}$ in pH 4 buffer in presence of $30 \mu\text{M}$ $[\text{Ru}^{\text{II}}(\text{bpy})_3]^{2+}$, 10 mM MV^{2+} and 100 mM styrene sulfonate, at room temperature under aerobic conditions, blue LED, 100 W m^{-2} for 5 s , no stirring.

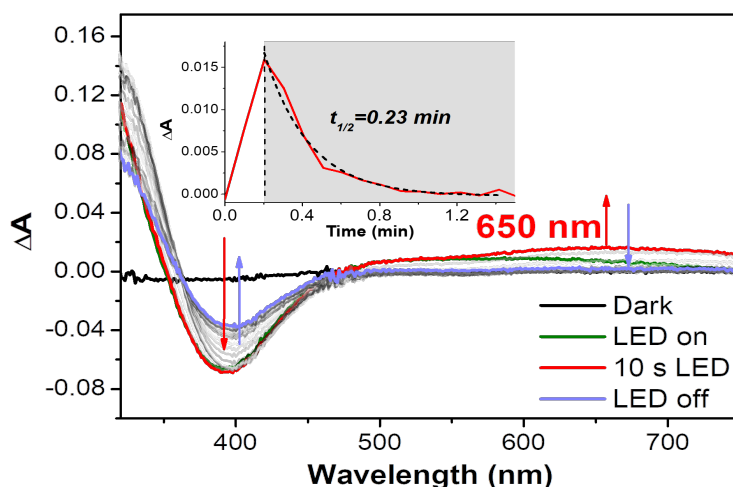


Figure 4.17: Spectral evolution of the absorption of a B&R pH 6 buffer solution containing $[\text{Ru}^{\text{II}}(\text{bpy})_3]^{2+}$ ($30 \mu\text{M}$), MV^{2+} (10 mM), EDTA (20 mM), and $[\text{L}_5\text{Fe}^{\text{II}}]^{2+}$ ($100 \mu\text{M}$) upon irradiation (100 W m^{-2} for 10 s) under aerobic conditions and no stirring. The difference of absorbance from the solution in the dark and during irradiation. Inset: kinetic profile of the 650 nm band.

sorption around 650 nm (Fig. 4.17). This red-shift matches well with what has been reported for the deprotonated peroxy form $[\text{L}_5\text{Fe}^{\text{III}}-\eta^2\text{O}_2]^+$ [3]. Once again, the lifetime of the intermediate is very short and it decays completely in less than 1 min under these experimental conditions.

When the irradiation was prolonged further (Fig. 4.18), we observed the bands of this intermediate decreasing, to leave place to the accumulation of $\text{MV}^{\bullet+}$ with characteristic peaks at 390 nm and 605 nm (see Section 4.2). We explained this phenomenon by the full consumption of the O_2 present in the solution, which gives rise to accumulation of the reduced methylviologen.

The above results show the possible trapping of reactive intermediates in catalytic conditions. To confirm that the detected bands correspond to the $[\text{L}_5\text{Fe}^{\text{III}}-\text{OOH}]^{2+}$ and $[\text{L}_5\text{Fe}^{\text{III}}-\eta^2\text{O}_2]^+$ species, we characterized by Electron Paramagnetic Resonance (EPR) spectroscopy the photo-generated intermediates. EPR spectroscopy is a useful tool to gain information on the oxidation state of a metal center and on its coordination environment. The initial EPR spectrum of the $[\text{Ru}^{\text{II}}(\text{bpy})_3]^{2+}/\text{MV}^{2+}/[\text{L}_5\text{Fe}^{\text{II}}]^{2+}$ mixture (black trace of Fig. 4.19) has signals at g values of 4.41 and 4.04. The expected Fe(II) initial species should be EPR silent, however these signals are assigned to a high spin (HS) $[\text{L}_5\text{Fe}^{\text{III}}-\text{X}]^{2+}$ species, where X is an axial ligand that can come from the buffer or the solvent. This means that a small fraction of the initial catalyst is in the Fe(III) state, but this will not affect the system, as it can be reduced to Fe(II) by the

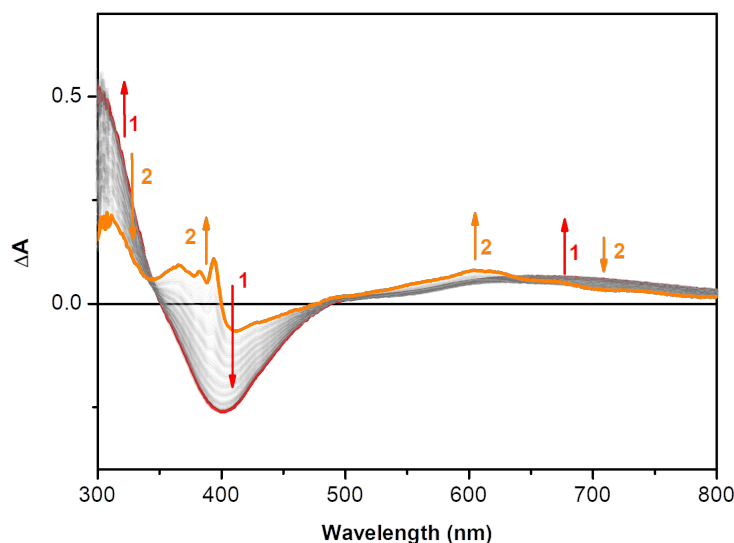


Figure 4.18: Photoaccumulation of 250 μM $[\text{L}_5\text{Fe}^{\text{II}}]^{2+}$ in pH 4 buffer in presence of 30 μM $[\text{Ru}^{\text{II}}(\text{bpy})_3]^{2+}$, 4 mM MV^{2+} and 200 mM TEOA at 5°C under aerobic conditions, blue LED, 100 W m^{-2} continuous light.

photo-generated $\text{MV}^{\bullet+}$ (recall Fig. 4.8 and Eq. 4.8). The signal at 4.27 was attributed to some trace of Fe^{3+} impurity from iron salts.

When the mixture was irradiated for a prolonged period of time in presence of EDTA and O_2 (red trace of Fig. 4.19), the recorded spectrum showed a fading of the 4.41 and 4.04 signal, with appearance of an intense signal at 2.00. This matches well with what was mentioned just above (Fig. 4.18) where the accumulation of $\text{MV}^{\bullet+}$ was detected upon prolonged irradiation. In fact, a signal in this EPR region is very likely to originate from an organic radical, like in the case of $\text{MV}^{\bullet+}$. Such result proves one more time that any trace of $\text{Fe}(\text{III})$ can be reduced in presence of reduced methylviologen.

The same solution mixture was also irradiated for 1 s directly in the EPR tube and the spectra were recorded. It should be noted that the irradiation times in UV-vis and EPR photo-accumulation experiments are different because of the different cell configurations of the cuvette and the EPR tube, in which the light can be focused accelerating the reaction. At pH 4, we recorded a spectrum with g values of 2.21, 2.15 and 1.97 (red spectrum of Fig. 4.20). These correspond to a typical low spin (LS) $\text{Fe}(\text{III})\text{-OOH}$ species which had been previously characterized [1]. The signal's morphology supports the presence of different rotational isomers giving rise to the observed asymmetry. We can also notice that the signals of the HS $[\text{L}_5\text{Fe}^{\text{III}}\text{-X}]^{2+}$ (4.41 and 4.04) increase upon irradiation (see Fig. 4.21 for better comparison). We can rationalized this as the

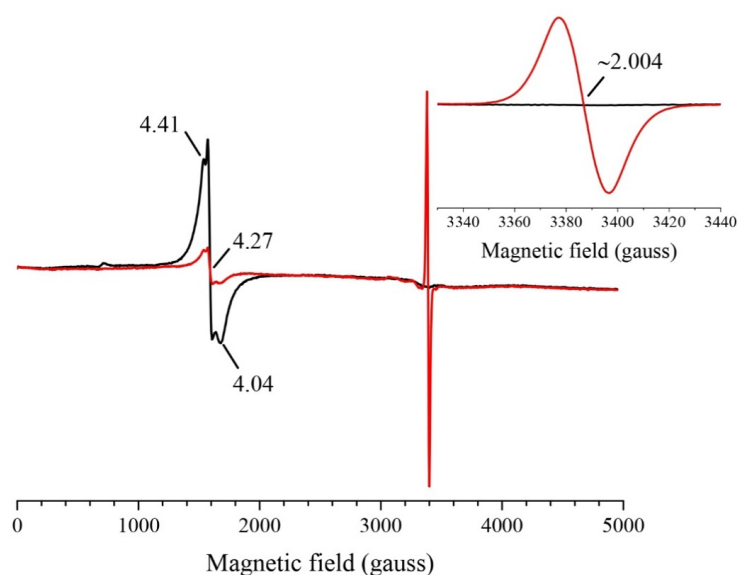


Figure 4.19: EPR spectra of a B&R pH 4 solution containing $[\text{Ru}^{\text{II}}(\text{bpy})_3]^{2+}$ ($30 \mu\text{M}$), MV^{2+} (20 mM), $[\text{L}_5\text{Fe}^{\text{II}}]^{2+}$ ($100 \mu\text{M}$) with traces of $[\text{L}_5\text{Fe}^{\text{III}}]^{3+}$ species and 20 mM EDTA in the dark (black) and after 30 s irradiation with 100 W m^{-2} blue LED (red). The spectra were recorded at 15 K with a modulation amplitude of 25 gauss and a microwave power of 5 mW . The microwave frequency was 9.4 GHz .

decay of the $\text{Fe}(\text{III})\text{-OOH}$ intermediate that generates more $\text{Fe}(\text{III})$ species, as it was proposed in Section 4.2 (Fig. 4.8).

Switching electron donor from EDTA to triethanolamine (TEOA) brings the overall solution pH to a value of 7.26 . When the EPR spectrum was recorded upon irradiation in these conditions, we could detect a HS species with g values of 7.64 and 5.72 (green spectrum of Fig. 4.20). These values correspond to the reported ones for $[\text{L}_5\text{Fe}^{\text{III}}-\eta^2\text{O}_2]^+$, where η^2 describes the coordination mode of the dioxygen as side-on with respect to the Fe center (see scheme in Fig. 4.20) [1].

Overall, EPR spectral signatures give the undeniable proof of the formation of iron (III) hydroperoxo and peroxo intermediates in photocatalytic conditions (room temperature and aqueous medium). This confirms the signal recorded in the visible region and it is further support for the hypothesized light-induced steps.

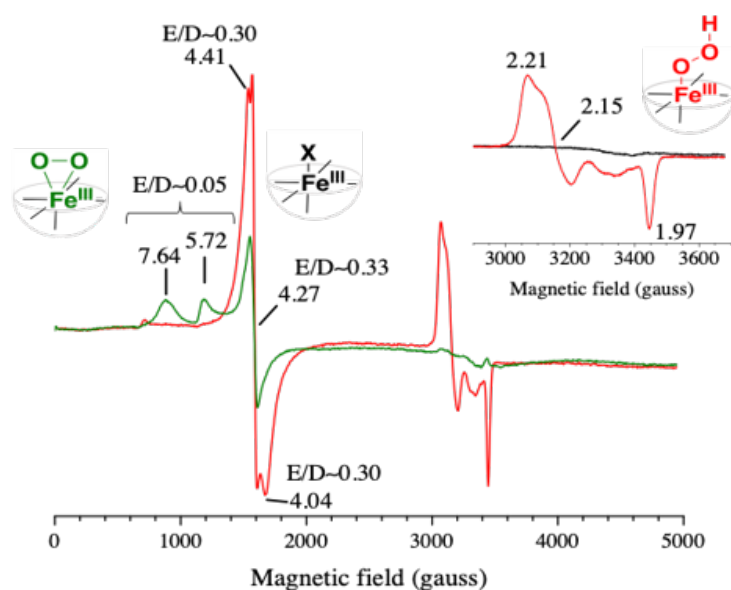


Figure 4.20: EPR spectra of a B&R pH 4 buffer solution containing $[\text{Ru}^{\text{II}}(\text{bpy})_3]^{2+}$ ($30 \mu\text{M}$), MV^{2+} (20 mM), $[\text{L}_5\text{Fe}^{\text{II}}]^{2+}$ ($100 \mu\text{M}$) and 20 mM EDTA (red) or 200 mM TEOA (green) irradiated for 1 s with a 100 W m^{-2} blue LED. The spectra were recorded at 15 K with a modulation amplitude of 25 gauss and a microwave power of 20 mW (5 mW for the inset). The microwave frequency was $\approx 9.49 \text{ GHz}$. In red, the EPR spectrum of the photo-generated low spin $[\text{L}_5\text{Fe}^{\text{III}}-\text{OOH}]^{2+}$ species, and in green the EPR spectrum of the photo-generated high spin $[\text{L}_5\text{Fe}^{\text{III}}-\eta^2\text{O}_2]^+$ species. In the inset, the black spectrum was recorded before the illumination.

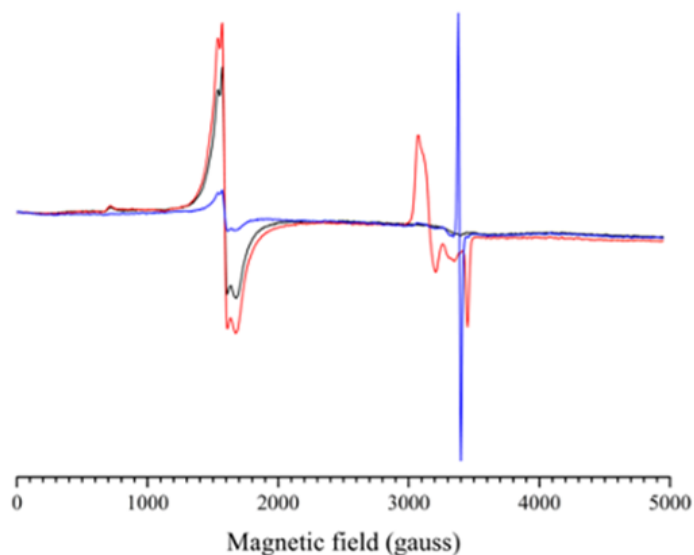


Figure 4.21: EPR spectral evolution of a B&R pH 4 solution containing $[\text{Ru}^{\text{II}}(\text{bpy})_3]^{2+}$ ($30 \mu\text{M}$), MV^{2+} (20 mM), $[\text{L}_5\text{Fe}^{\text{II}}]^{2+}$ ($100 \mu\text{M}$) with traces of $[\text{L}_5\text{Fe}^{\text{III}}]^{3+}$ species and 20 mM EDTA, upon irradiation. In the dark (black spectrum), after 1 s (red) and after 20 s (blue) irradiation with 100 W m^{-2} blue LED. The spectra were recorded at 15 K with a modulation amplitude of 25 gauss and a microwave power of 5 mW . The microwave frequency was 9.4 GHz .

4.5 . Mechanism proposal

Being able to trap one of the key intermediates in both its protonated and deprotonated forms, gave us a solid proof of the main the steps involved in the photocatalytic mechanism.

We then put together all of the investigated photophysical events in a mechanism proposal, represented in Fig. 4.22. We should highlight that, even if dealing with reductive activation of O_2 , no sacrificial electron donor is necessary in this system to perform oxygen atom transfer (OAT). In fact, methylviologen plays the important role of electron relay but it is constantly regenerated in the looping cycles. Thanks to the reaction of Ru(III) with the substrate, no external source of electrons is necessary.

Having a more detailed look into the proposed scheme, we can follow the light-induced steps, recalling also the reactions described in section 4.2. As a first event, $[Ru^{II}(bpy)_3]^{2+}$ absorbs visible light (1) and it quenched by methylviologen generating $MV^{\bullet+}$ and Ru(III) (2). Now, the reduced methylviologen can react with dioxygen generating superoxide ($O_2^{\bullet-}$) and resetting itself to MV^{2+} (3). The $O_2^{\bullet-}$ species will quickly bind to the Fe(II) complex in solution to generate $[L_5Fe^{III}-OOH]^{2+}$ after protonation (6) or $[L_5Fe^{III}OO]^+$ in more basic conditions (6'). These are the reactive intermediates characterized by UV-vis and EPR spectroscopies. In the meantime, Ru(III) is set back to its initial state by reacting with the styrene substrate and giving the radical cation (5).

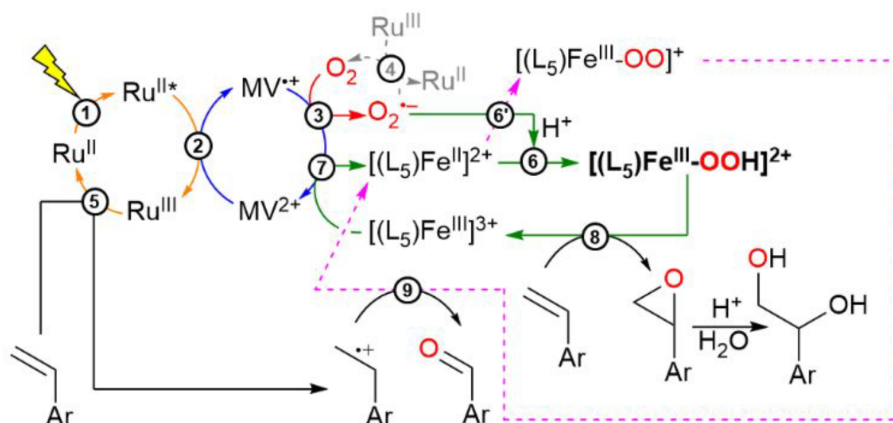


Figure 4.22: Photocatalytic OAT to an alkene substrate in the absence of a sacrificial electron donor using light, O_2 as the oxygen source, $[L_5Fe^{II}]^{2+}$ as the catalyst, $[Ru^{II}(bpy)_3]^{2+}$ as the photosensitizer (written as Ru^{II} for simplification) and MV^{2+} as the electron relay.

In depth studies in organic solvents showed that the Fe(III) hydroperoxo species can evolve to an iron oxo enabling oxygen atom transfer to the alkene substrate to generate an epoxide or diol (8) [9] [10] [11]. The isotope labelling

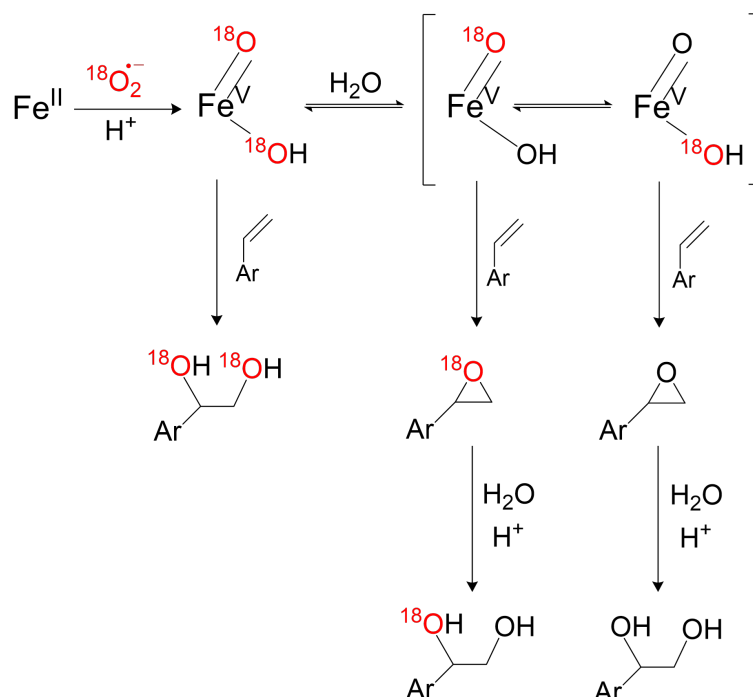


Figure 4.23: Simplified scheme of the formation of isotope labelled products detected by mass spectrometry.

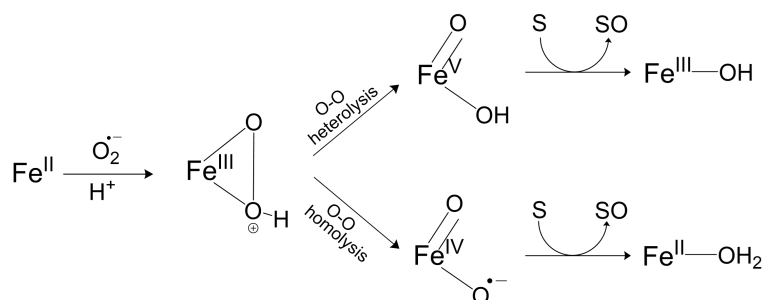


Figure 4.24: Scheme of the formation of the possible iron oxo intermediates and their final states after two-electron substrate oxidation.

experiments (see Fig. 4.23 and Annex) proved the formation of both labelled and unlabelled epoxide, coming from a high valent Fe-oxo species that can exchange O-atom with water (see Fig. 4.23 and 4.11). The diol labelling also showed mixed products, rising from O-atom of water molecules involved in the ring-opening process. The aldehyde can be formed by reaction of the radical cation with the $[\text{L}_5\text{Fe}^{\text{III}}\text{OO}]^+$ species (9), which generates an unstable dioxetane ring cleaved to an aldehyde (Fig. 4.11).

Another question on the mechanistic aspect concerns the oxidation state of the high valent iron oxo intermediate being formed. Indeed, depending on the homolytic or heterolytic cleavage of the O-O bond in Fe(III) hydroperoxo, Fe(IV)-oxo or Fe(V)-oxo can be generated, respectively [12]. Depending on

this, we can obtain either an Fe(II) or and Fe(III) redox state after the OAT reaction (see Fig. 4.24). Because of what was observed in EPR (Fig. 4.21) and photophysics experiments (Fig. 4.8), we assume that Fe(III) is formed as a decay of high valent iron-oxo species, which supports the formation of an Fe(V)-oxo as reactive intermediate. This hypothesis is supported by previous studies, where the presence of water seems to favour heterolytic cleavage of the O-O bond. The Fe(III) so generated can then be set back to its Fe(II) state by reaction with the photo-generated $MV^{\bullet+}$ (7).

4.6 . Conclusions

Performing dioxygen activation for OAT reactions in a photocatalytic setup can be advantageous thanks to the *in-situ* generation of reducing species that can transfer electrons to O₂. However, controlling the multiple light-induced electron transfers and their directionality can be a challenging task.

In this study we chose to combine a photoredox module based on [Ru(bpy)₃]²⁺ and MV²⁺ as electron relay, with the [L₅Fe^{II}]²⁺ catalyst to oxidize styrene sulfonate (S) as model substrate using dioxygen. Individual study of the photophysical events helped us follow the chain of reactions taking place in this system. We then moved to study the photocatalytic activity, to find three possible products: aldehyde, epoxide and diol. The TON found here are in line with other reports with similar catalysts using H₂O₂ as oxygen atom source and the selectivity of diol vs. epoxide seems to be pH sensitive, as the epoxide is less stable in acidic conditions.

After the confirmation of the catalytic regime of our system, we aimed to characterize reactive intermediates in the same catalytic conditions. We successfully captured both the [L₅Fe^{III}OOH]²⁺ and [L₅Fe^{III}OO]⁺ intermediates using photoaccumulation, in aqueous medium and at room temperature. These species were characterized by UV-vis and EPR spectroscopies. It is particularly interesting to generate reactive intermediates in the same conditions as the catalysis because it provides a direct proof of their involvement in the catalytic cycle.

Overall, we were able to gather all of the collected data in a mechanism proposal, where two of the main intermediates were identified experimentally. More studies will be needed for a further insight into the catalytic cycle, where high valent iron-oxo species are most likely involved, but no direct evidence could be found for the moment. These results give a proof of concept of the application of light-induced reactions to perform oxidation of organic substrates using the abundant O₂ as oxygen source. This can allow us to operate in soft conditions, even though a lot still has to be mastered to control the complex chemistry of O₂.

Bibliography

- (1) Simaan, A. J.; Dopner, S.; Banse, F.; Bourcier, S.; Bouchoux, G.; Boussac, A.; Hildebrandt, P.; Girerd, J.-J. FeIII-Hydroperoxo and Peroxo Complexes with Aminopyridyl Ligands and the Resonance Raman Spectroscopic Identification of the Fe-O and O-O Stretching Modes. *European Journal of Inorganic Chemistry* **2000**, 1627–1633.
- (2) Simaan, A. J.; Banse, F.; Mialane, P.; Boussac, A.; Un, S.; Kargar-Grisel, T.; Bouchoux, G.; Girerd, J.-J. Characterization of a Nonheme Mononuclear Peroxoiron(III) Intermediate by UV/Vis and EPR Spectroscopy and Mass Spectrometry. *European Journal of Inorganic Chemistry* **1999**, 1999, 993–996.
- (3) Bohn, A. Approche électrochimique de l'activation réductrice du dioxygène à l'aide d'un complexe de fer(II) non hémique, PhD Thesis, 2018.
- (4) Thorneley, R. N. A convenient electrochemical preparation of reduced methyl viologen and a kinetic study of the reaction with oxygen using an anaerobic stopped-flow apparatus. *Biochimica et Biophysica Acta (BBA) - Bioenergetics* **1974**, 333, 487–496.
- (5) Steckhan, E.; Kuwana, T. Spectroelectrochemical Study of Mediators I. Bipyridylum Salts and Their Electron Transfer Rates to Cytochrome c. *Berichte der Bunsengesellschaft für physikalische Chemie* **1974**, DOI: <https://doi.org/10.1002/bbpc.19740780307>.
- (6) Vo, N. T. Bioinspired semi-hemic iron(III) complex for chemical and photochemical oxygen atom transfer reactions, fr, Ph.D. Thesis, Université Paris-Saclay, 2019.
- (7) Olivo, G.; Cussó, O.; Borrell, M.; Costas, M. Oxidation of alkane and alkene moieties with biologically inspired nonheme iron catalysts and hydrogen peroxide: from free radicals to stereoselective transformations. *JBIC Journal of Biological Inorganic Chemistry* **2017**, 22, 425–452.
- (8) Parker, R. E.; Isaacs, N. S. Mechanisms Of Epoxide Reactions. *Chemical Reviews* **1959**, 59, 737–799.
- (9) Oloo, W. N.; Que, L. Bioinspired Nonheme Iron Catalysts for C–H and CC Bond Oxidation: Insights into the Nature of the Metal-Based Oxidants. *Accounts of Chemical Research* **2015**, 48, 2612–2621.
- (10) Gamba, I.; Codolà, Z.; Lloret-Fillol, J.; Costas, M. Making and breaking of the O–O bond at iron complexes. *Coordination Chemistry Reviews* **2017**, 334, 2–24.
- (11) Feng, Y.; England, J.; Que, L. Iron-Catalyzed Olefin Epoxidation and cis-Dihydroxylation by Tetraalkylcyclam Complexes: the Importance of cis-Labile Sites. *ACS Catalysis* **2011**, 1, 1035–1042.
- (12) Oloo, W. N.; Fielding, A. J.; Que, L. Rate-Determining Water-Assisted O–O Bond Cleavage of an Fe^{III}-OOH Intermediate in a Bio-inspired Nonheme Iron-Catalyzed Oxidation. *Journal of the American Chemical Society* **2013**, 135, 6438–6441.
- (13) Mohammadi, Z.; Shalavi, S.; Jafarzadeh, H. Ethylenediaminetetraacetic acid in endodontics. *European Journal of Dentistry* **2013**, 07, S135–S142.
- (14) Bohn, A.; Chinaux-Chaix, C.; Cheaib, K.; Guillot, R.; Herrero, C.; Sénéchal-David, K.; Rebilly, J.-N.; Banse, F. Base-controlled mechanistic divergence between iron(IV)-oxo and iron(III)-hydroperoxo in the H₂O₂ activation by a nonheme iron(II) complex. *Dalton Transactions* **2019**, 48, 17045–17051.
- (15) Bernal, I.; Jensen, I. M.; Jensen, K. B.; McKenzie, C. J.; Toftlund, H.; Tuchagues, J.-P. Iron(II) Complexes of Polydentate Aminopyridyl Ligands and an Exchangeable Sixth Ligand; Reactions with Peroxides. Crystal Structure of [FeL1(H₂O)] [PF₆], H₂O [L1 = N,N'-bis(6-methyl-2-pyridylmethyl)-N,N'-bis(2-pyridylmethyl)ethane-1,2-diamine]. *Journal of Chemical Society, Dalton Transaction* **1995**, 3667–3675.

5 - CONCLUSIONS AND PERSPECTIVES

In this PhD thesis, we investigated light-induced molecular catalysis for activation of small molecules, in particular CO₂ reduction and O₂ activation for oxygen atom transfer (OAT) reactions.

Following the natural model of photosynthesis, we integrated a charge- separation module (photosensitizer or light absorber) with a catalyst unit, able to store oxidizing or reducing power until effective activation of the substrate molecule. This approach can enable us to use an abundant energy source (sunlight) to trigger chemical reactions that can generate valuable products from "waste" or abundant ones.

In Chapters 2 and 3, we studied CO₂ reduction as it is a strategy of interest for carbon capture and utilization (CCU) plans. In particular we studied photocatalytic conversion of CO₂ as one of the direct ways of converting sunlight to stocked chemical energy. Our research interest focuses on the careful tuning of the molecular catalyst by creating specific interaction between the catalyst and the substrate. We chose to work with iron porphyrins given their reported activity for CO₂ reduction electrocatalysis [1] [2] [3] and because they provide a stable platform for electron storage that can be easily modified on the second coordination sphere. We had previously studied the urea-substituted **UrFe** iron porphyrin as electrocatalyst for CO₂ reduction. The urea moieties strategically placed in the vicinity of the Fe active site have the advantage of facilitating CO₂ molecules binding through H-bond interactions. This characteristic will promote a stronger interaction between the iron site and the substrate.

In Chapter 2, the same **UrFe** catalyst was implemented in a photocatalytic system that shows high TON and TOF, especially when compared to the simpler analogs **TPPFe** and **F₂₀TPPFe**. This efficient photocatalysis was optimized by studying the effect that different elements have on the catalytic turnover and rate. We then moved to a more in-depth mechanistic study, where the combination of different spectroscopies allowed us to draft a first mechanism proposal. We found here proofs of the unexpected interaction of CO₂ with the formal Fe(I) state of the catalyst, we believe being a specificity of the urea-substituted porphyrin, supported both by spectroelectrochemical measurements and DFT calculations. This "early" interaction can help rationalizing the enhanced pho-

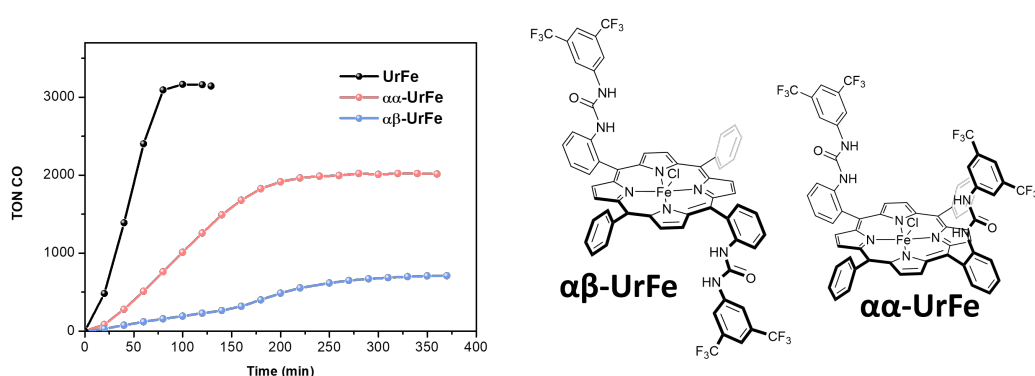


Figure 5.1: Left: Time evolution of CO produced under light irradiation with a blue LED ($\lambda_{em}=460$ nm 100 W m^{-2}) of a mixture of 20 μ M catalyst, 1 mM $[Ru(bpy)_3]^{2+}$ photosensitizer, 50 mM BIH sacrificial electron donor CO_2 -saturated DMF/ H_2O 9:1. Black: **UrFe** catalyst, Red: **αα-UrFe** catalyst, Blue: **αβ-UrFe** catalyst. Right: structure of the related catalysts.

tocatalytic activity both in terms of catalyst stability and reaction rate.

Some open questions still remain from this part of the study, such as the fate of the iron catalyst when deactivation occurs (around 7000 TON of CO). Further studies on the reaction intermediates occurring after the $Fe(I)-CO_2$ formation are ongoing in the group, both by chemical, electrochemical and photochemical methods.

Some first investigations have also been carried out on the di-substituted urea porphyrin in its two atropisomers, **αα-UrFe** and **αβ-UrFe** (see Fig. 5.1). Once again, we studied the photocatalytic activity for CO_2 reduction in presence of $[Ru(bpy)_3]^{2+}$ photosensitizer and BIH electron donor. We could observe that in comparison with the tetra-substituted **UrFe**, there is an obvious decrease of photocatalytic activity. This can be explained by the fact that the reduction potentials are now more negative than **UrFe** because of the lower number of urea functions. For this reason reduction by $Ru(I)$ is less favourable.

Interestingly, the rate of CO evolved by the two atropisomers follows the opposite trend of what was found in electrocatalytic conditions (**αβ-UrFe** having the highest reaction rate). In electrocatalysis protonation was found to be the rate determining step in these systems, therefore the **αβ-UrFe** atropisomer allows faster catalysis thanks to the more accessible protonation site [4]. We may explain the results of photocatalysis, once again in terms of CO_2 binding. Because of the two urea groups on the same face of the porphyrin for **αα-UrFe**, the substrate binding will be more favoured. We discussed in the previous sections how it is such binding to govern our catalytic rate, so the same reasoning may apply here. Further studies will be necessary to confirm our hypothesis.

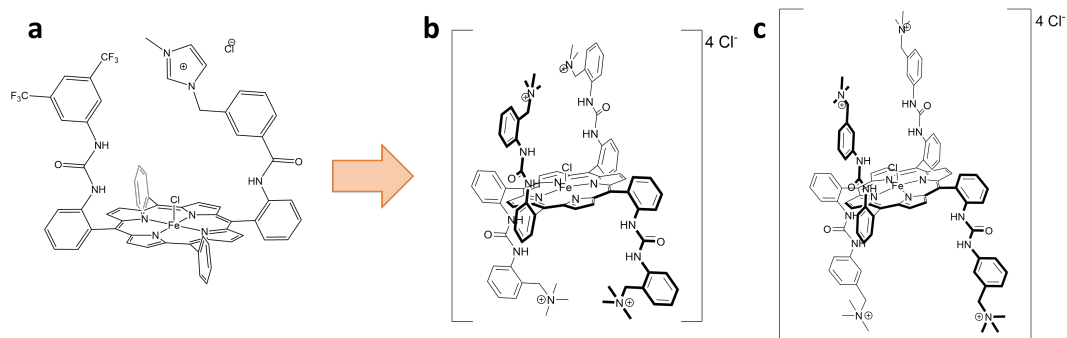


Figure 5.2: Structures the iron porphyrin catalysts with mixed second-coordination sphere effects: electrostatic and H-bond interactions.

As another perspective related to this part of the thesis we foresee the development of another class of molecular catalysts, where different effects of the second coordination sphere are mixed on the same ligand. As hydrogen-bond effects and charged groups have been individually synthesized in the group, we aim to obtain a second-coordination sphere that regroups both of these substituents, to possibly have a further enhancement of catalytic activity. More specifically, we aimed to prepare catalyst **a** in Fig. 5.2, consisting in an asymmetric iron porphyrin with an imidazolium and an urea function. The first attempts for this preparation indicated a tedious synthesis with difficulties to have good separations of side products and consequently very low yields. To overcome this, we now prospect the preparation of tetra-substituted symmetrical iron porphyrins **b** and **c** (Fig. 5.2) where the two functions are present on the same arm.

Chapter 3 follows logically the findings of Chapter 2, where we seek the translation of the light-induced CO₂ conversion into a heterogenized system, with the molecular catalyst anchored onto a photocathode surface. For this purpose, we chose to assemble the photocathode starting with a light-absorbing semiconductor which acts as a charge separator, replacing the expensive ruthenium photosensitizer. Cuprous oxide (Cu₂O) is described in the literature as a promising candidate for light-driven CO₂ reduction [5] [6] [7], given the highly reducing conduction band, which at the same time can provoke photocorrosion of the material itself. It is crucial to optimize the photoelectrode assembly in a way that the electrons are efficiently transferred from the Cu₂O conduction band to eventually the molecular catalyst on the electrode surface. For this reason, protective layers were put in between the Cu₂O surface and the catalyst. A mesoporous layer at the top of the device is essential to maximize the catalyst loading. The catalyst is anchored on the surface by covalent bonds,

as the urea-substituted **UrFe** catalyst structure was modified to obtain the **Link-UrFe** catalyst with hydroxamate groups. The immobilization on TiO₂ surface was confirmed by different techniques and it was proven the necessity of implementing the covalent linkers. The final assembly was studied in terms of recorded photocurrent and an effect of the catalyst was clearly observed. In order to obtain higher currents and better device stability, different improvements are to be foreseen. Firstly, the mesoporous TiO₂ layer needs to show higher transparency and possibly catalyst loading can be optimized further. The added protective layers cause definitely a loss in current, but already a visible increase in stability, which could be acceptable if the final device can be stable for several hours and enough products can be accumulated. To further consolidate our system, it will be necessary to optimize both the current stability and the cell configuration to detect CO₂ reduction products. Preliminary results tell us that the catalyst is still active once immobilized on the surface, but it should be ensured that the presence of TiO₂ does not cause a loss in selectivity in the aqueous medium.

In Chapter 4 we shifted our focus on a different light-induced reaction, oxygen activation for OAT reactions. Finding new ways to perform chemical oxidation of substrates is of high interests among chemists in order to give alternative to high-energy demanding industrial processes. Molecular oxygen is the ideal candidate for OAT reactions given its abundance and easy availability, however its direct interaction with organic substrate is spin forbidden (ground triplet state). To activate dioxygen we decided to take once again a light-induced pathway, where the chosen photoredox module, [Ru(bpy)₃]²⁺ and MV²⁺, can generate *in situ* superoxide to quickly bind an Fe(II) non-heme catalyst. In fact, the [L₅Fe^{II}]²⁺ molecular complex has been chosen as it has already been studied for its chemical activation with H₂O₂, a reduced form of O₂, and its reactive intermediates have been characterized in organic media [8] [9] [10]. Here, we took advantage of the photochemical activation of O₂ to form reactive species with the iron complex, which are then capable of transferring the O atom to a model organic substrate, styrene sulfonate. Photophysical study allowed us to follow the various light-induced steps on ns time resolution. Putting different information together, we were able to construct a global picture of the mechanism, which was consolidated by the proven catalytic activity. We could detect oxygenation of styrene sulfonate to form aldehyde and diol and epoxide depending of pH conditions. Most importantly, we were able to capture Fe(III)-OOH as a key intermediate in OAT reaction and to characterize it by UV-vis

and EPR spectroscopies. Future developments could include tandem oxidation reactions in order to tackle the fate of the photoproduced alkenyl radical and in general a widening of the substrates scope, here restricted to one model reaction.

From all of these lessons we can have an overview of the advantages and challenges of molecular photocatalysis, which can offer at times alternative reaction pathways to "ground state chemical reactions", but also induce faster degradation due to uncontrolled electron transfers upon light-excitation. The natural system teaches us how every single transfer needs to be specifically tailored to the overall chain reactions and surely chemists still find a great challenge into tackling this aspect in the artificial systems. Nevertheless, every step forward in mechanism understanding can guide us to build more robust systems which can hopefully one day be integrated in light-powered devices to trigger challenging chemical reactions to store the solar energy into the form of chemical bonds.

Bibliography

- (1) Takahashi, K.; Hiratsuka, K.; Sasaki, H.; Toshima, S. Electrocatalytic behavior of metal porphyrins in the reduction of carbon dioxide. *Chemistry Letters* **1979**, *8*, 305–308.
- (2) Costentin, C.; Savéant, J.-M. Towards an intelligent design of molecular electrocatalysts. *Nature Reviews Chemistry* **2017**, *1*, 0087.
- (3) Gotico, P.; Halime, Z.; Aukauloo, A. Recent advances in metalloporphyrin-based catalyst design towards carbon dioxide reduction: from bio-inspired second coordination sphere modifications to hierarchical architectures. *Dalton Transactions* **2020**, *49*, 2381–2396.
- (4) Gotico, P.; Roupnel, L.; Guillot, R.; Sircoglou, M.; Leibl, W.; Halime, Z.; Aukauloo, A. Atropisomeric Hydrogen Bonding Control for CO₂ Binding and Enhancement of Electrocatalytic Reduction at Iron Porphyrins. *Angewandte Chemie International Edition* **2020**, *59*, 22451–22455.
- (5) Paracchino, A.; Laporte, V.; Sivula, K.; Grätzel, M.; Thimsen, E. Highly active oxide photocathode for photoelectrochemical water reduction. *Nature Materials* **2011**, *10*, 456–461.
- (6) Paracchino, A.; Brauer, J. C.; Moser, J.-E.; Thimsen, E.; Graetzel, M. Synthesis and Characterization of High-Photoactivity Electrodeposited Cu₂O Solar Absorber by Photoelectrochemistry and Ultrafast Spectroscopy. *The Journal of Physical Chemistry C* **2012**, *116*, 7341–7350.
- (7) Paracchino, A.; Mathews, N.; Hisatomi, T.; Stefik, M.; Tilley, S. D.; Grätzel, M. Ultrathin films on copper(i) oxide water splitting photocathodes: a study on performance and stability. *Energy & Environmental Science* **2012**, *5*, 8673.
- (8) Simaan, A. J.; Dopner, S.; Banse, F.; Bourcier, S.; Bouchoux, G.; Boussac, A.; Hildebrandt, P.; Girerd, J.-J. FeIII-Hydroperoxo and Peroxo Complexes with Aminopyridyl Ligands and the Resonance Raman Spectroscopic Identification of the Fe-O and O-O Stretching Modes. *European Journal of Inorganic Chemistry* **2000**, 1627–1633.
- (9) Bohn, A. Approche électrochimique de l'activation réductrice du dioxygène à l'aide d'un complexe de fer(II) non hémique, PhD Thesis, 2018.
- (10) Simaan, A. J.; Banse, F.; Mialane, P.; Boussac, A.; Un, S.; Kargar-Grisel, T.; Bouchoux, G.; Girerd, J.-J. Characterization of a Nonheme Mononuclear Peroxoiron(III) Intermediate by UV/Vis and EPR Spectroscopy and Mass Spectrometry. *European Journal of Inorganic Chemistry* **1999**, *1999*, 993–996.

6 - ANNEX

6.1 . Chapter 2: CO₂ reduction in a homogeneous system

6.1.1 . Synthesis and characterization

The general synthetic procedure for **UrFe** was described in Chapter 2. Additional characterizations of the free-base porphyrin and the final complex are provided below (Fig. 6.1, Fig. 6.2).

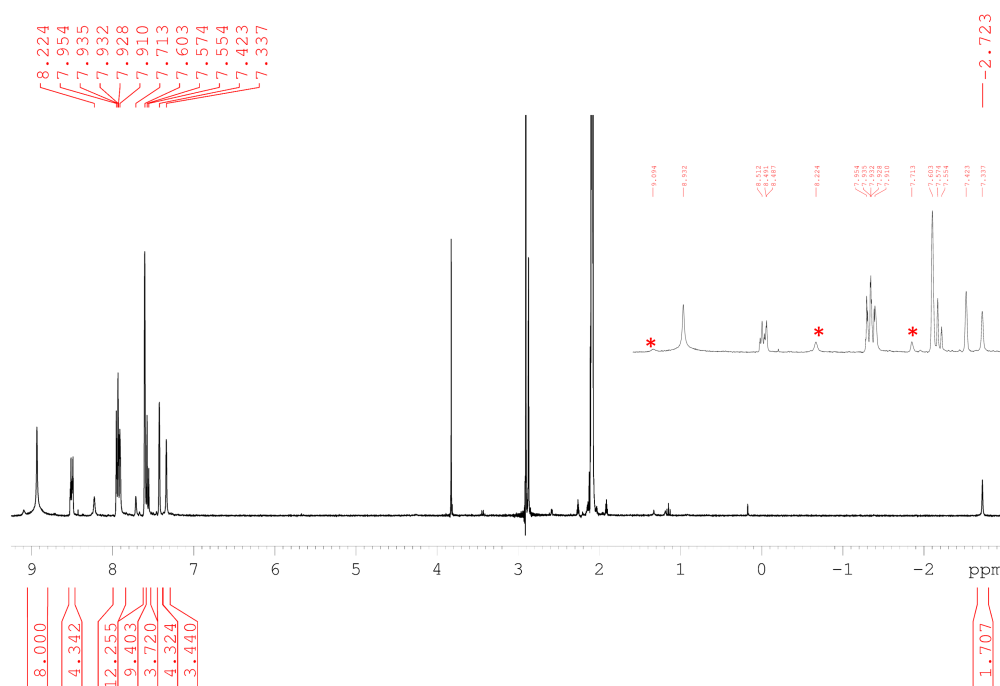


Figure 6.1: ¹H-NMR spectrum of $\alpha\beta\alpha\beta$ -UrTPP in deuterated acetone. Inset: zoom in the aromatic region; the asterisks indicate an impurity coming from the reagent, removed in the next step.

$\alpha\beta\alpha\beta$ -UrTPP

¹H-NMR ((CD₃)₂CO, 298 K, 400 MHz): δ_{H} 8.92 (8H, s, β_{pyrrole}), 8.48 (4H, d, $J = 8.0$ Hz), 7.91 (12H, m), 7.59 (8H, s), 7.56 (4H, td, $J_1 = 7.6$ Hz, $J_2 = 0.8$ Hz), 7.40 (4H, s), 7.31 (4H, s), -2.72 (2H, s, NH_{pyrrole}).

¹³C-NMR ((CD₃)₂CO, 298 K, 100 MHz): δ_{C} 152.2, 141.3, 139.1, 134.8, 132.4, 131.2 (q, $J = 32$ Hz), 129.6, 123.2 (q, $J = 269.7$ Hz), 123.1, 122.9,

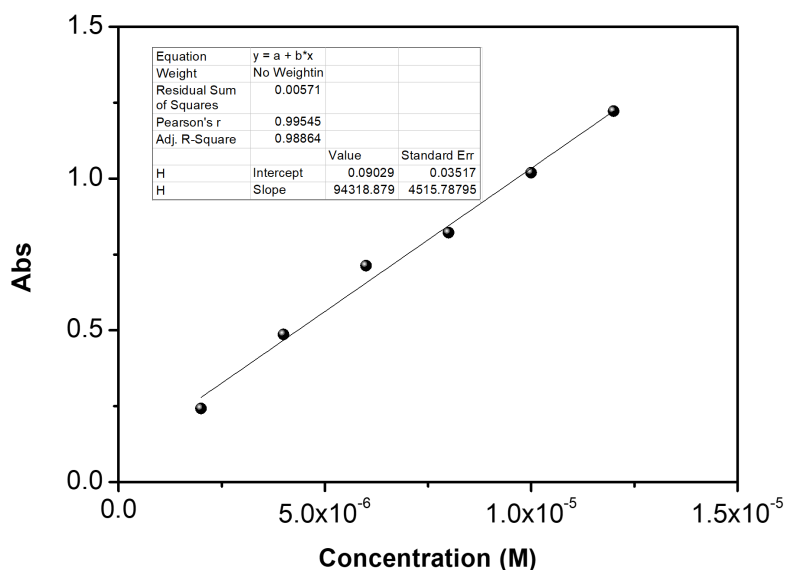


Figure 6.2: Determination of the extinction coefficient for the Soret band (436 nm) of **UrFe** in DMF; giving a value of about $94\,000\text{ M}^{-1}\text{ cm}^{-1}$.

117.53, 115.5, 114.5.

ESI-HRMS calculated $m/z = 1695.3455 [M+H^+]^+$ for $C_{80}H_{47}F_{24}N_{12}O_4$, found 1695.3455; calculated $m/z = 1717.3274 [M+Na^+]^+$ for $C_{80}H_{46}F_{24}N_{12}O_4Na$, found 1717.3236.

UV-vis absorption peaks, λ in nm: 423, 515, 549, 589, 648.

UrFe

ESI-HRMS calculated $m/z = 1802.2654 [M-ClH^- + MeO^- + Na^+]^+$ for $C_{81}H_{47}F_{24}FeN_{12}NaO_5$, found 1802.2644.

UV-vis absorption peaks, λ in nm: 436, 496, 565.

The sacrificial electron donor 3-dimethyl-2-phenyl-2,3-dihydro-1Hbenzo [*d*]imidazole (BIH) was synthesized in four steps following literature reports [1], described in the reaction scheme (Fig. 6.3). For the first step, 0.1 mol of 2-nitroaniline was dissolved in EtOH and benzaldehyde was introduced in stoichiometric amounts. In parallel, sodium thiosulfate was dissolved in water and then added to the reaction mixture. A reflux was set at 90 °C for 5 h, then cooled down and a white precipitate was filtered out of the solution and washed with water. $^1\text{H-NMR}$ analysis in DMSO confirmed the formation of the first intermediate (Fig. 6.4).

For the second step, 2 equivalents of KOH were crushed and dissolved in excess DMSO, to then slowly add the benzylimidazole intermediate to the flask. After 1 h of stirring at room temperature, a colour change from yellow/orange

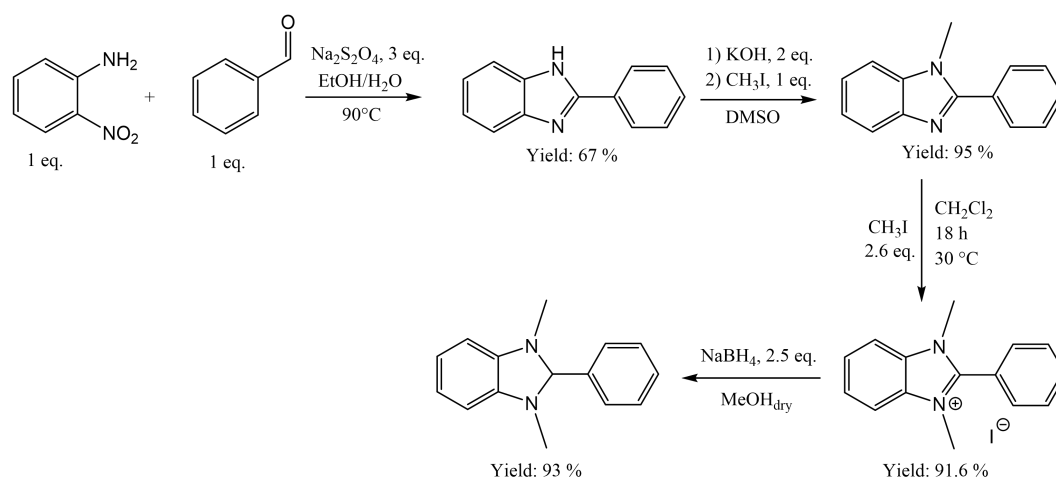


Figure 6.3: Reaction scheme for the synthesis of 3-dimethyl-2-phenyl-2,3-dihydro-1Hbenzo[*d*]imidazole (BIH) electron donor used in photocatalysis.

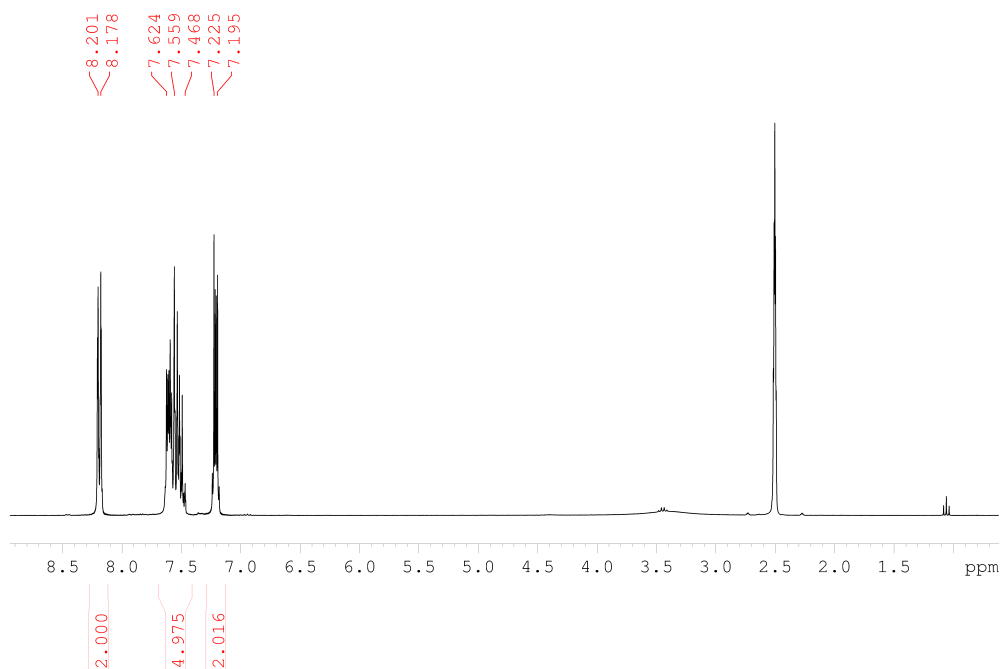


Figure 6.4: ¹H-NMR of benzimidazole (after the first reaction step) in deuterated DMSO, 300 MHz.

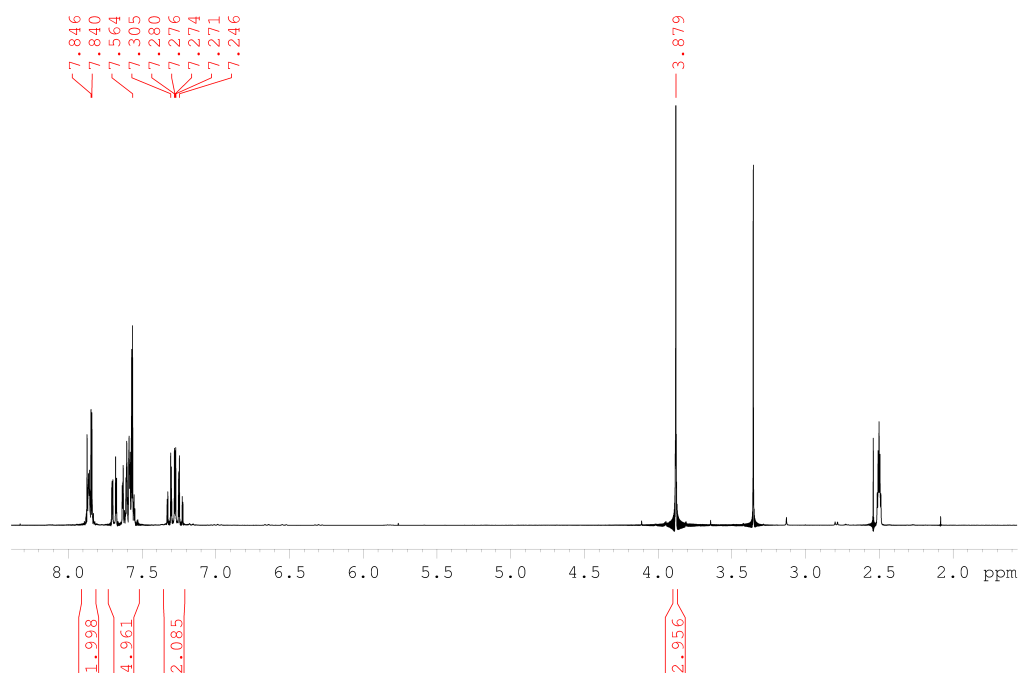


Figure 6.5: ¹H-NMR of mono methylated benzimidazole (after the second reaction step) in deuterated DMSO, 300 MHz.

to dark red was observed, indicating deprotonation of the compound. At this stage, 1 eq. of iodomethane was slowly added to the flask and the reaction was left stirring overnight. For the workup, the crude was first neutralized with a 0.15 M KOH aqueous solution, then Et₂O was added and the organic phase was extracted and evaporated until obtaining a dark brown oil which solidifies upon cooling back to room temperature. ¹H-NMR spectrum was recorded in DMSO and it showed the desired peaks (Fig. 6.5).

For the second methylation, the mono-methylated benzimidazole was dissolved in DCM and 2.6 equivalents of iodomethane were slowly added to the reaction mixture. The temperature was set at 30 °C and the solution was left stirring overnight. The next day, a precipitate was formed at the bottom of the flask. To maximize the yield, the solvent was evaporated and Et₂O was then added in the flask to eliminate the organic phase with unreacted reagents (partial solubility of the desired compound in DCM). The precipitate was filtered and washed to obtain a white-grey solid, analyzed by ¹H-NMR (Fig. 6.6).

The last reaction step consisted in the double bond reduction. To do so we placed the compound under inert atmosphere and dissolved it in MeOH_{dry}. Once solubilized, sodium borohydride was slowly added to the flask previously

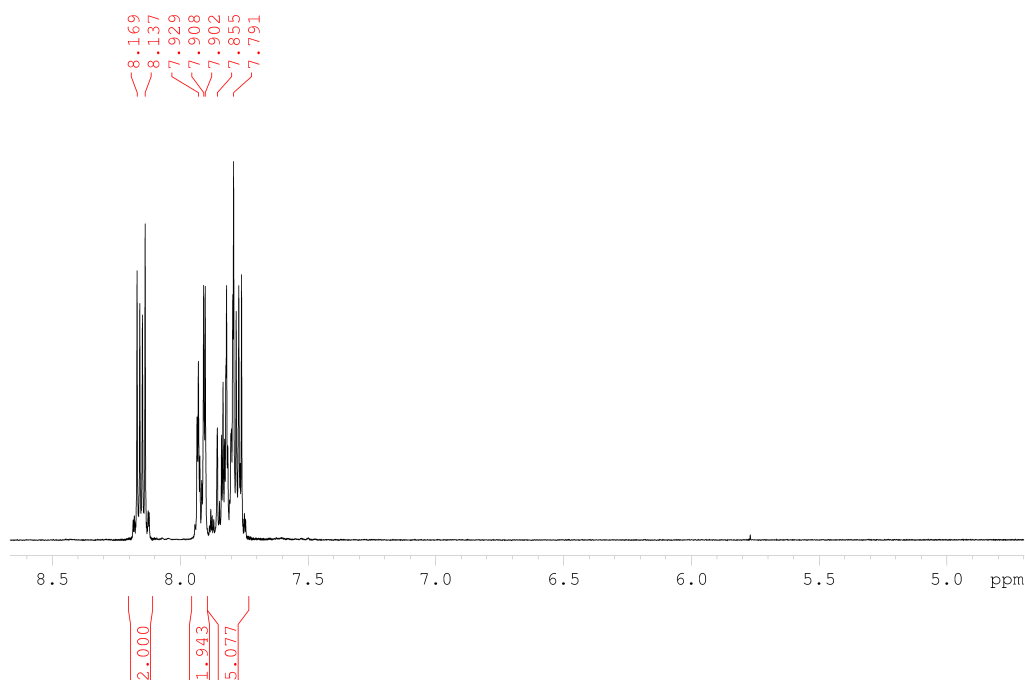


Figure 6.6: ¹H-NMR of charged di-methylated benzimidazole (after the third reaction step) in deuterated DMSO, 300 MHz.

placed in an ice-water bath. Gas release was observed. After the addition, the flask was brought back to room temperature and left stirring for 2 h. For the workup, the solvent was evaporated (formation of a white-yellow solid), then the crude was extracted with Et₂O/H₂O and recrystallized in EtOH/H₂O 2:1 to obtain white crystals. After recrystallization, the ¹H-NMR analysis in CDCl₃ showed the desired product with good purity (Fig. 6.7).

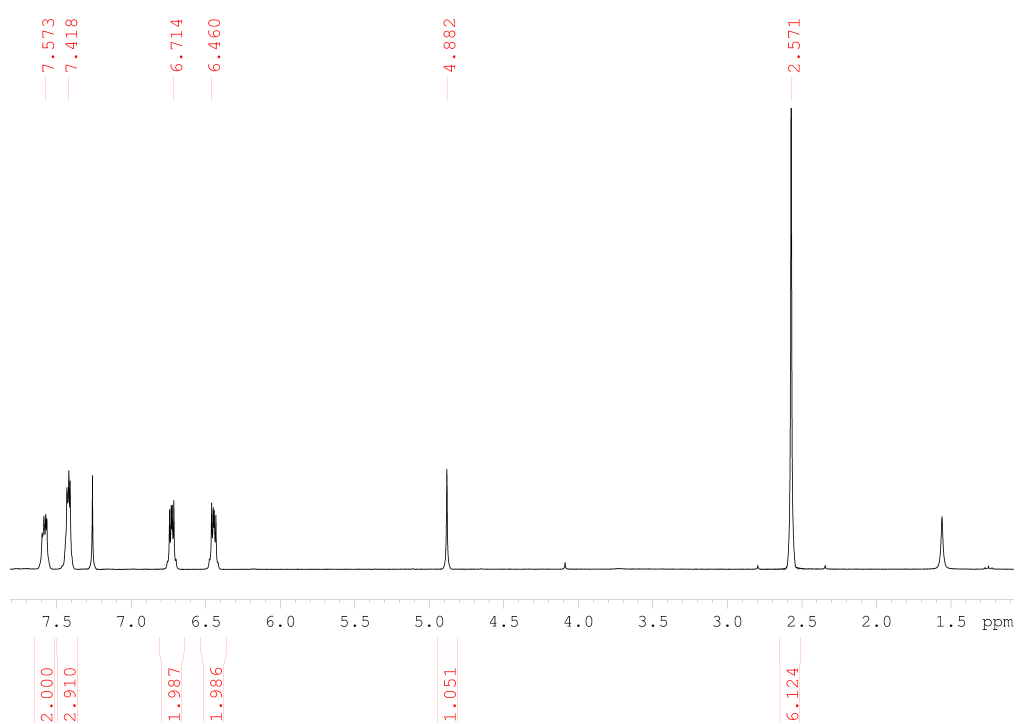


Figure 6.7: ¹H-NMR of BIH (after the reduction step) in CDCl₃, 300 MHz.

Table 6.1: Electrochemical potentials in Volts of the studied compounds vs. NHE in 0.1 M TBAPF₆ Ar-saturated DMF_{dry} solution.

Entry	Compound	E ^{1/2} (M/M ⁻)	E ^{1/2} (M ⁻ /M ²⁻)	E ^{1/2} (M ²⁻ /M ³⁻)	Ref.
1	UrFe	0.23	-0.63	-1.12	[2]
2	TPPFe	0.09	-0.79	-1.42	[2]
3	F ₂₀ TPPFe	0.25	-0.59	-1.11	[2]
4	[Ru(bpy) ₃] ²⁺ [a]	-1.09			[3]
5	[Ir(ppy) ₃] ⁺ [a]	-1.95			[3]

[a] In acetonitrile solution.

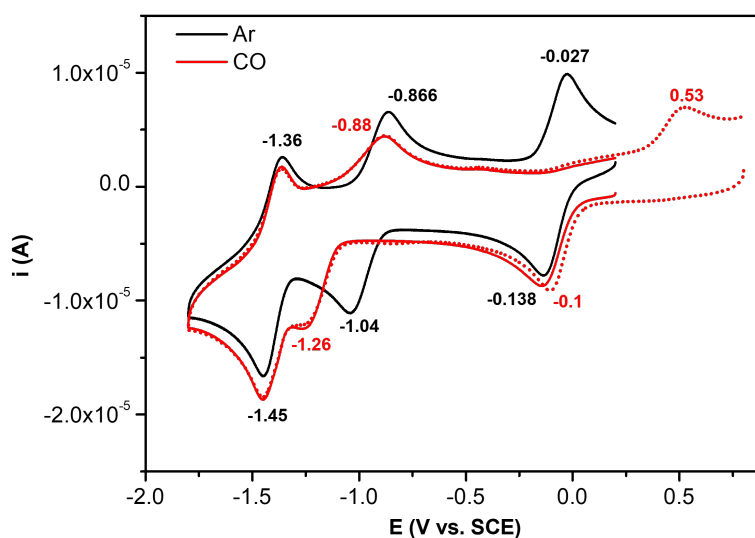


Figure 6.8: Cyclic voltammogram (CV) of 1 mM **UrFe** in Ar-saturated (black) and CO-saturated (red) 0.1 M TBAPF₆ in DMF_{dry}. Dashed line: scan continued to more positive potential for the 3rd oxidation wave. WE: Glassy carbon, CE: Pt, RE: SCE; 0.1 V s⁻¹ scan rate.

6.1.2 . Electrochemical characterizations

To complete the data discussed in the Chapter, we display here a table summarizing the electrochemical potentials taken into account in the study. In addition to what described in Chapter 2, few more electrochemical studies were done to study the system.

To follow the interaction of the **UrFe** iron porphyrin with CO, we performed the CV in presence of CO (Fig. 6.8). We could observe more than 200 mV of negative shift for the Fe(II/I) wave, due to the formation of the stable Fe(II)-CO adduct. Similarly, reoxidation of Fe(II) to Fe(III) becomes harder, with a potential of +0.53 V vs. SCE, indicating the stability of Fe(II)-CO.

We also questioned if the interaction of the Fe(I) of **UrFe** with CO₂ could be detected in a CV. To do so, we scanned the potential only on the first two

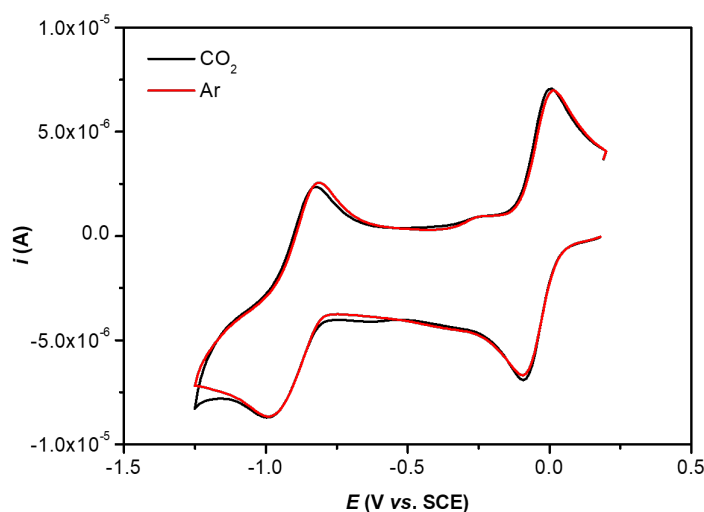


Figure 6.9: Cyclic voltammogram (CV) of 1 mM **UrFe** in Ar-saturated (red) and CO₂-saturated (black) 0.1 M TBAPF₆ in DMF_{dry}. WE: Glassy carbon, CE: Pt, RE: SCE; 0.1 V s⁻¹ scan rate.

reduction waves (until Fe(I)) in Ar and CO₂ saturated electrolyte. In dry solvent (Fig. 6.9), no changes could be observed comparing the two gas atmospheres. However, when water was added in the cell (Fig. 6.10) we could observe a splitting of the Fe(II/I) wave in presence of CO₂ instead of Ar. This could be considered an additional index of the Fe(I)-CO₂ interaction for the **UrFe** catalyst. The wave splitting observed for the Fe(III/II) wave on the same figure can be rationalized as an exchange of axial ligand, initially being chloride, but the latter gets cleaved upon reduction to Fe(II), giving place to a competition of possible axial ligands on reoxidation.

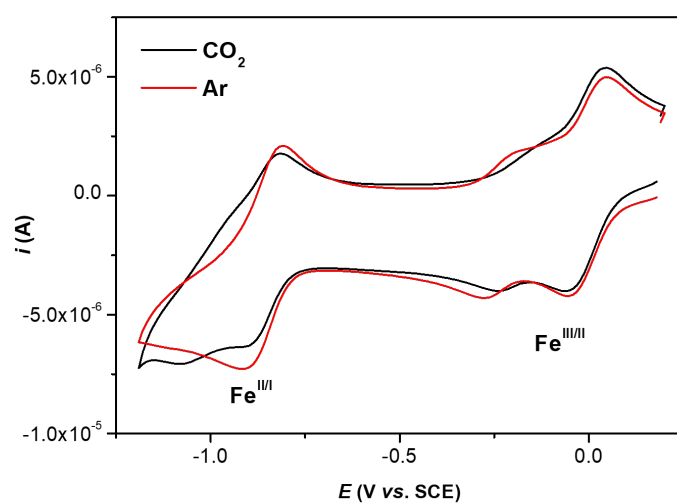


Figure 6.10: Cyclic voltammogram (CV) of 1 mM **UrFe** in Ar-saturated (red) and CO_2 -saturated (black) 0.1 M TBAPF_6 in DMF and 10% water. WE: Glassy carbon, CE: Pt, RE: SCE; 0.1 V s^{-1} scan rate.

6.1.3 . Photocatalysis

Photocatalysis experiments were performed in 41.5 mL glass vials hermetically closed with a septum and containing 6.5 mL of solution and an 8 mm stir bar. The reaction mixture was first purged with CO₂ during 30 min, while kept in the dark, and then irradiated with LED light source (SugarCube). The gas phase was automatically injected and analyzed by a Micro GC Fusion Gas Analyser (Inficon). In module A (PLOT column with molecular sieve and 10 m length) a 9 s backflush is applied to separate H₂, O₂, N₂, CH₄ and CO. Module B (RT-Q-bond column of 12 m) allows the detection of heavier molecules, such as CO₂, H₂O vapor and C₂ products. The setup is equipped of an Ar carrier gas with 99.999% purity and a TCD detector. For experiments with limited amount of CO₂, the reaction vial was first degassed with Ar, then different amounts of a solution of 10 mL of DMF previously purged for 20 min with CO₂ were injected. The solubility of CO₂ in DMF was taken to be 230 mM [4]. To quantify products, calibration was manually performed injecting fixed aliquots (100 or 500 μ L) of reference gasses in the same vial used in a typical run, filled with 6.5 mL of the same solvent mixture and an 8 mm stirring bar, and purged for 30 min with CO₂. Calibration curves were fitted with 10 points choosing the same range of area peaks obtained experimentally.

Below are shown the calibration curves obtained for CO (Fig. 6.11) and H₂.

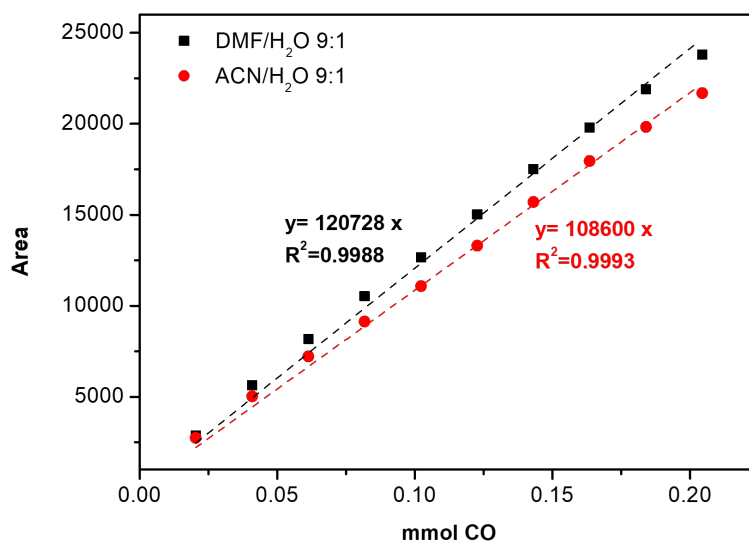


Figure 6.11: Calibration curve for CO obtained in the photocatalytic setup, in CO₂ atmosphere.

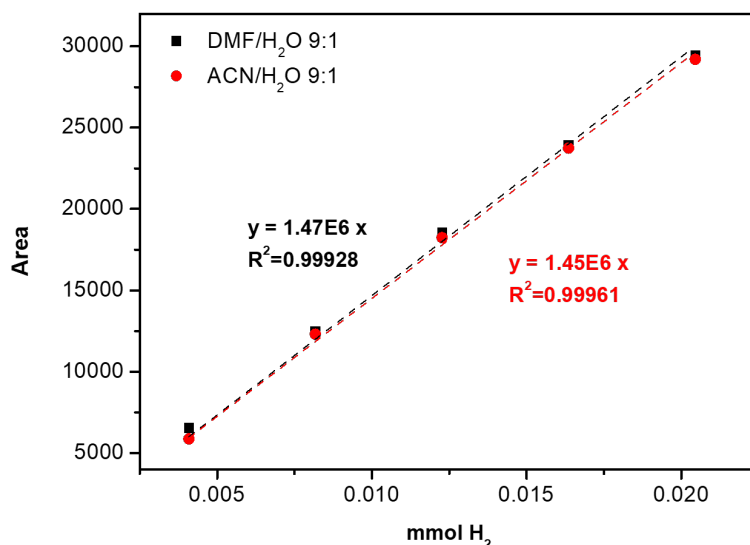


Figure 6.12: Calibration curve for H₂ obtained in the photocatalytic setup, in CO₂ atmosphere.

In addition to the data displayed in Chapter 2, Fig. 6.13 shows the maximum TON recorded for **UrFe** with the associated error bars over 3 repeats.

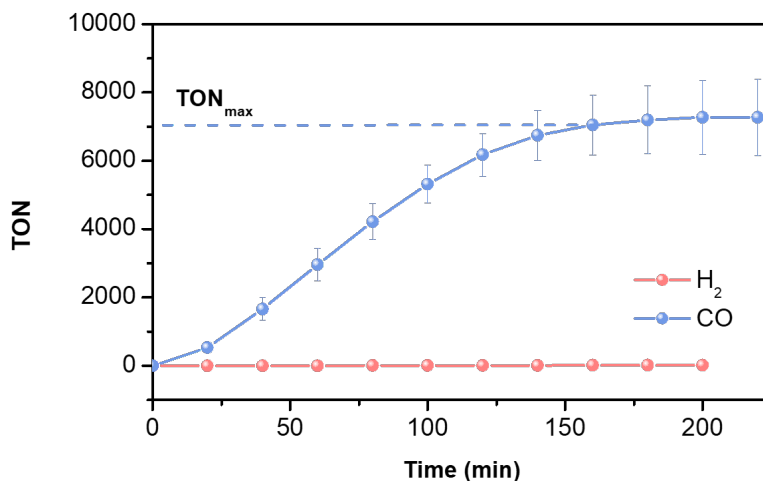


Figure 6.13: Time evolution of CO (blue) and H₂ (red) produced under light irradiation with a blue LED ($\lambda_{em}=460$ nm 100 W m⁻²) of **UrFe** as catalyst with 20 μ M concentration; [Ru(bpy)₃]²⁺ photosensitizer 1 mM, BIH sacrificial electron donor 250 mM in CO₂-saturated DMF/H₂O 9:1. The data is the average of 3 runs, error bars represent the standard error.

6.1.4 . UV-Vis spectroelectrochemistry

UV-vis spectroelectrochemical measurements were done in a quartz cuvette with Pt honeycomb electrode (PINE research) and a Pt wire pseudo-reference electrode. To probe the sample the spectrophotometer Agilent Technologies

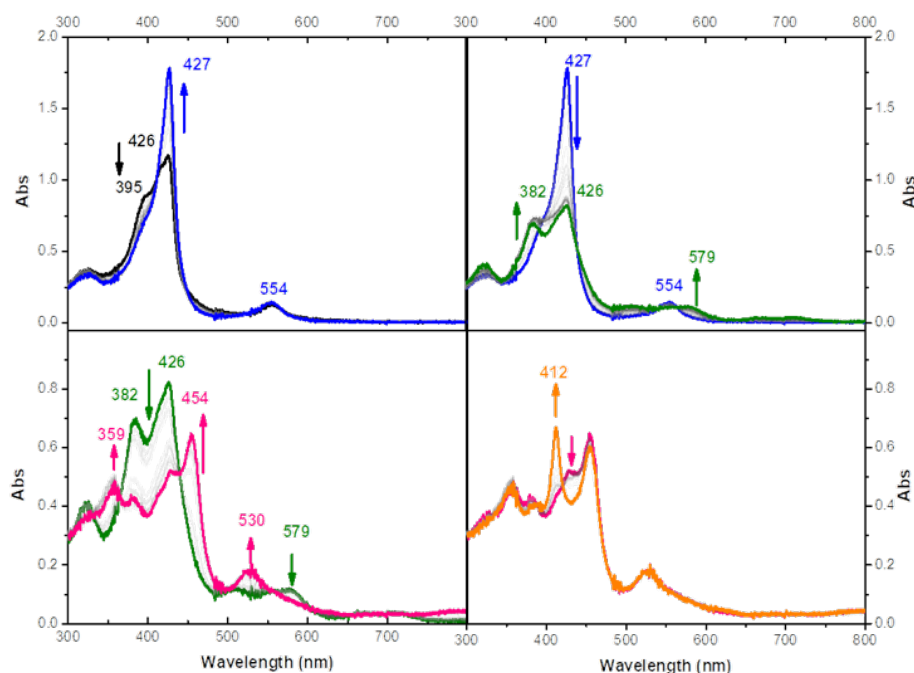


Figure 6.14: UV-Vis spectral evolution in spectroelectrochemistry experiment with **F₂₀TPPFe** 40 μ M in CO₂-saturated DMF_{dry}, 0.2 M TBAPF₆, Pt working electrode, Pt counter electrode and Pt pseudoreference electrode; room temperature. Top left: Fe(III) to Fe(II) reduction. Top right: Fe(II) to Fe(I) reduction. Bottom left: Fe(I) to Fe(0) reduction. Bottom right: Further changes before porphyrin degradation.

Cary 50 UV-Vis was used. The potentials were applied through the potentiostat Metrohm Autolab 204 in the chronoamperometry method.

6.1.5 . Photoaccumulation

Photoaccumulation experiments were conducted in a 1 cm optical path quartz cuvette hermetically closed with a septum. To probe the sample a Agilent Technologies Cary 60 UV-Vis spectrophotometer was used, adapted with a liquid nitrogen dewar and thermostated around the cuvette to perform measurements down to -196 °C. This apparatus is connected to the temperature controller (CoolSpek UV USP-203 by Unisoku), able to regulate the flux of liquid nitrogen and to heat the cuvette. During the measurement, the sample is irradiated with a blue LED light source (SugarCube). The solution is stirred during the measurement. Spectra acquisition is operated through the CaryWin software, in the Scanning Kinetics mode.

6.1.6 . Infrared spectroscopy

Infrared spectroelectrochemical measurements were recorded with an FT-IR Thermo Scientific Nicolet 6700 spectrometer, with ATR diamond accessory. A

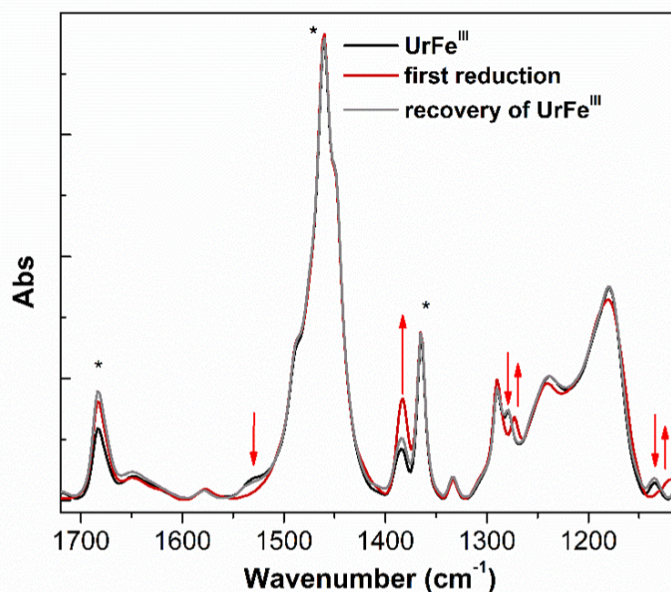


Figure 6.15: IR reversible conversion of Fe(III) to Fe(II) in spectroelectrochemistry experiment with UrFe 1 mM in Ar-saturated THF, 0.1 M TBAPF₆, GC Working Electrode, Pt Counter Electrode and AgNO₃/Ag Reference Electrode; Room Temperature. Peaks with asterisk are due to the solvent.

home-made PTFE electrochemical cell fitted ATR crystal was filled with 1 mL of THF solution containing 1 mM catalyst and 0.1 M TBAPF₆ in a three-electrode system including a GC working electrode, Pt counter electrode and Ag/AgNO₃ (10 mM) reference electrode (+0.54 V vs. NHE) under a continuous flow of Argon or CO₂. Applied potential was varied by 200 mV steps and three infrared spectra were recorded for each potential applied.

Additionally to what was shown in Chapter 2, we also studied the reversibility of the first reduction of **UrFe** catalyst in IR-spectroelectrochemistry (Fig. 6.15).

6.1.7 . Computational study

DFT calculations were performed using the Gaussian 16 program package [5]. PBE0functional was used to predict geometries and relative energies [6] [7], B3LYP was used for the calculation of vibrational spectra. In both cases, dispersion correction with Becke-Johnson damping (D3BJ) [8] was introduced to better reproduce the weak interactions occurring at the 2nd sphere coordination and solvent effects (DMF) were included using the CPCM approach [9]. Lanld2z with ECP [10] and 6-31G(d) [11] basis sets were chosen for Fe and main group atoms respectively. To speed up the calculations, the two arms at the opposite of the coordination face of the porphyrin were replaced with protons. The corresponding model porphyrin is denoted **mαUr**. The F₂₀TPPF_e

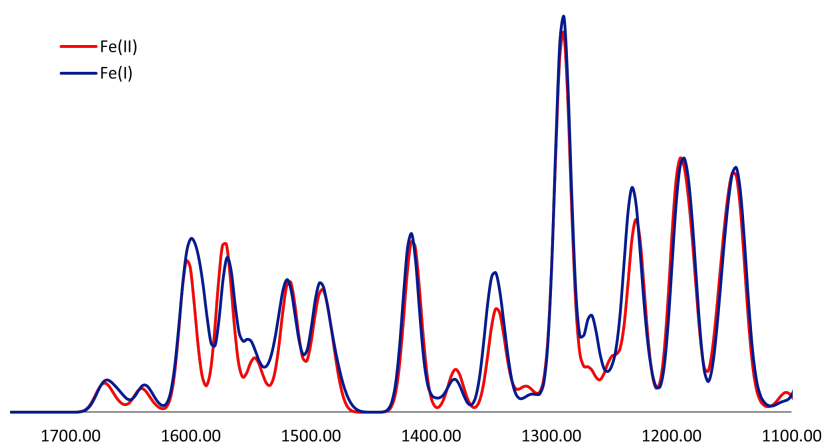


Figure 6.16: Theoretical IR band spectra (gaussian fit $w_{1/2}=15\text{ cm}^{-1}$) obtained for Red: $\alpha\alpha\text{UrFe}^{\text{II}}$, Blue: $\alpha\alpha\text{UrFe}^{\text{I}}$

was optimized as is. The geometry of intermediates were optimized as singlet, open singlet ($S=1$) and triplet ($S=3$) for formally Fe(II) species, and as doublet ($S=2$) for Fe(I) species. Only the most stable configurations are detailed herein. IR spectra were generated by convoluting the theoretical stick spectra with a Gaussian fit (half-width $W_{1/2}=15\text{ cm}^{-1}$). Figures, charges and spin analysis were performed using ChemCraft program.

In addition to what was described in the Chapter, we display here the simulated IR spectra for the Fe(II) and Fe(I) states of UrFe (Fig. 6.16).

6.2 . Chapter 3: Heterogeneous photocatalysis for CO₂ reduction

6.2.1 . Catalyst synthesis and characterizations

The synthetic procedure for **OMeUrFe** complex was described in Chapter 3. Here, additional characterizations are provided.

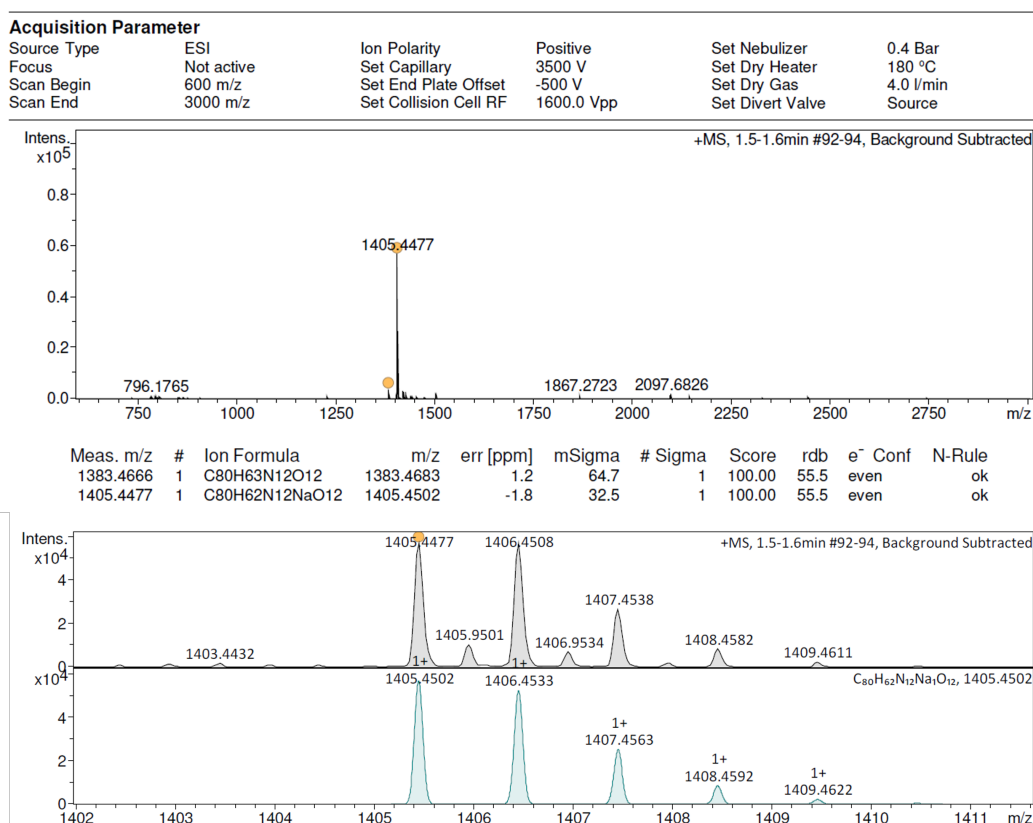


Figure 6.17: ESI-HR mass spectrum of **TPPOMe** (top), showing the experimental (center) and simulated (bottom) isotope pattern.

TPPOMe

¹H-NMR((CD₃)₂CO, 298 K, 300 MHz): δ_H 8.876 (8H, s, β_{pyrrole}), 8.496 (4H, d, J = 7.5 Hz), 7.90 (10H, m), 7.599 (4H, s), 7.49 (10H, m), 7.203 (4H, s), 6.940 (8H, d, J = 8.7 Hz), 3.726 (12H, s), -2.764 (2H, s, NH_{pyrrole}).

ESI-HRMS calculated m/z = 1405.4502 [M+Na⁺]⁺ for C₈₀H₆₂N₁₂NaO₁₂, found 1405.4477; calculated m/z = 1383.4683 [M+H⁺]⁺ for C₈₀H₆₃N₁₂O₁₂, found 1383.4666.

UV-vis absorption peaks, λ in nm: 422, 514, 548, 589, 650.

OMeUrFe

ESI-HRMS calculated m/z = 1436.3800 [M-Cl⁻]⁺ for C₈₀H₆₀FeN₁₂O₁₂, found 1436.3724; calculated m/z = 1490.3882 [M-Cl⁻+Na⁺+OMe⁻]⁺ for C₈₁H₆₃FeN₁₂

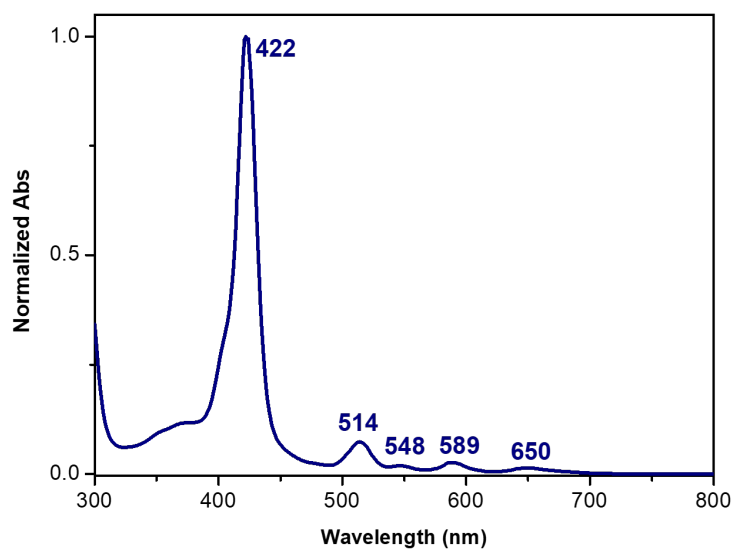


Figure 6.18: Normalized UV-vis spectral absorption of the free-base porphyrin obtained after the first reaction step (OMeUrTPP).

NaO₁₃, found 1490.3810.

UV-vis absorption peaks, λ in nm: 415, 514, 687.

6.2.2 . Electrode assembly

For the electrode assembly, we used FTO TEC 7 on glass support plates of Sigma Aldrich. Each glass slide was cut to form 1.5 cm × 2.5 cm electrodes. After cutting, each electrode was washed with soapy water, acetone, EtOH and distilled water for 15 min of sonication each.

For Cr and Au CVD deposition we used the FTM7 Film thickness monitor coupled to the Auto 306 Vacuum coater by Edwards.

Electrodeposition of Cu₂O was done in an air-saturated three-electrode cell, where the FTO substrate was used as working electrode, with an exposed area of 1.5 cm × 1.5 cm. Pt grid was used as counter electrode and Ag/AgCl as reference. The electrolyte was prepared from a 0.2 M CuSO₄, 0.5 M K₂HPO₄ and 3 M lactic acid solution brought to pH 12 with addition of KOH 2 M. CuSO₄, K₂HPO₄, lactic acid and KOH were purchased from Sigma Aldrich. A current of 0.225 mA (0.1 mA cm⁻²) was applied for 105 min with a potentiostat Metrohm Autolab PGSTAT128N.

For the ALD layers, Al₂O₃, AZO (ZnO:Al) and TiO₂ were prepared in a BENEQ TFS-200 ALD reactor, according to reported procedures [12] [13]. Trimethyl aluminium (TMA, Al(CH₃)₃, Optograde, Rohm Haas), diethyl zinc (Zn(C₂H₅)₂, DEZ, EpiPure, SAFC), titanium (IV) i-propoxide (Ti(OiPr)₄, TTIP, min. 98%, STREM), and deionized water were used as Al, Zn, Ti, and O sources, respectively. All chemicals were used without further purification. Nitrogen (N₂, 99.9999%, Air Liquide) was used as both carrier and purging gas. TTIP was heated in a hot solid source system Beneq HS300 at TTTIP = 85 °C, while other precursors were kept at room temperature. Experiments were performed at Tdep = 200 °C, and the pressure in the reaction chamber was kept in the range of 12 mbar.

Typical growth cycles are Al₂O₃ = TMA/N₂/H₂O/N₂ = 0.15/0.5/0.1/ 0.7 s; AZO = 20 × ZnO + Al₂O₃ with ZnO = H₂O/N₂/DEZ/N₂ = 0.1/1/0.1/0.7 s, and TiO₂ = [TTIP]/N₂/H₂O/N₂ = [0.5/0.05/0.5/0.5]/5/2/5 s. "Combination" mode was chosen to ensure proper mass transport of TTIP and is composed of four steps ([t1/t2/t3/t4]). First, N₂ is injected in the TTIP source (t1), then all valves are kept closed (t2), and the TTIP precursor is pulsed (t3). Finally, N₂ is injected with a simultaneous precursor pulse (t4). The number of cycles was set to yield 20 nm AZO and 10 nm TiO₂ on Si wafer references.

Mesoporous TiO₂ was prepared by drop-casting a suspension of TiO₂ nanoparticles in water. The suspension was prepared with 25 mg/mL of TiO₂ 21 nm nanoparticles powder (Sigma Adrich) in distilled water, sonicated and further



Figure 6.19: Photograph of the setup used for photoelectrochemical measurements.

diluted 16 times in distilled water. After a second sonication step, 20 μL of the suspension were drop-casted on a surface with 0.55 cm of diameter, templated thanks to Kapton tape.

6.2.3 . Electrode characterizations

The photoelectrodes described in Chapter 3 were characterized for their photoelectrochemical response in an H-cell electrochemical setup. On one side, the working and reference electrodes were placed, with the WE having an exposed area of 0.55 cm diameter, the rest being masked by Kapton tape and a black plastic mask to prevent illumination of the rest of the electrode surface. The WE was front-irradiated with a SugarCube white LED with a power of approximately 600 W m^{-2} , and the light was chopped with 1 s on/off intervals thanks to T132 Shutter Driver/Timer by UniBlitz. On the other side, the Pt grid CE is separated by a frit, but the two headspaces are connected by a bridge (see Fig. 6.19).

The ATR-FTIR measurements were recorded with an FT-IR Thermo Scientific Nicolet 6700 spectrometer, with ATR diamond accessory.

In addition to the data provided in the Chapter, XPS measurements in dedicated regions for different samples are reported here.

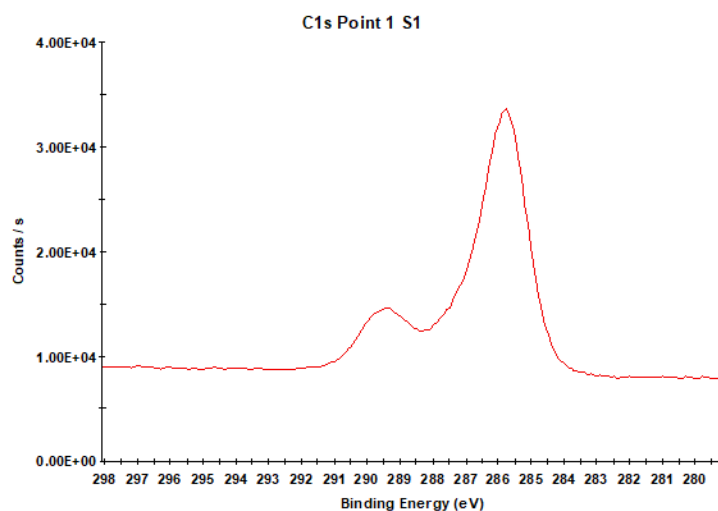


Figure 6.20: XPS spectrum for the C 1s region of FTO/DC-TiO₂/UrFe.

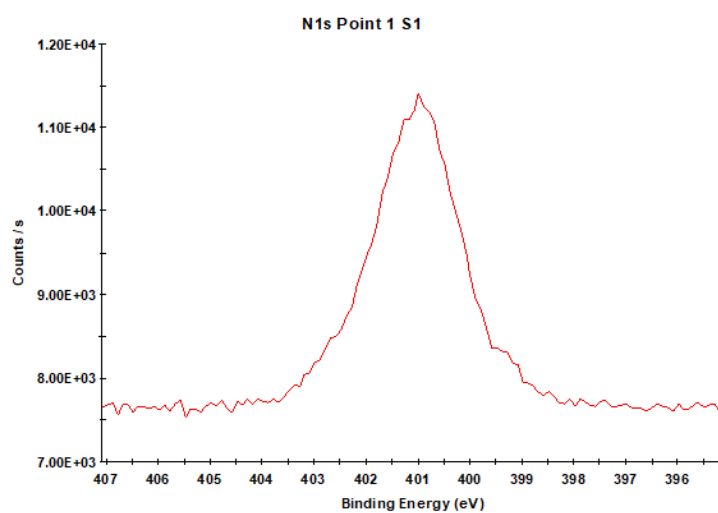


Figure 6.21: XPS spectrum for the N 1s region of FTO/DC-TiO₂/UrFe.

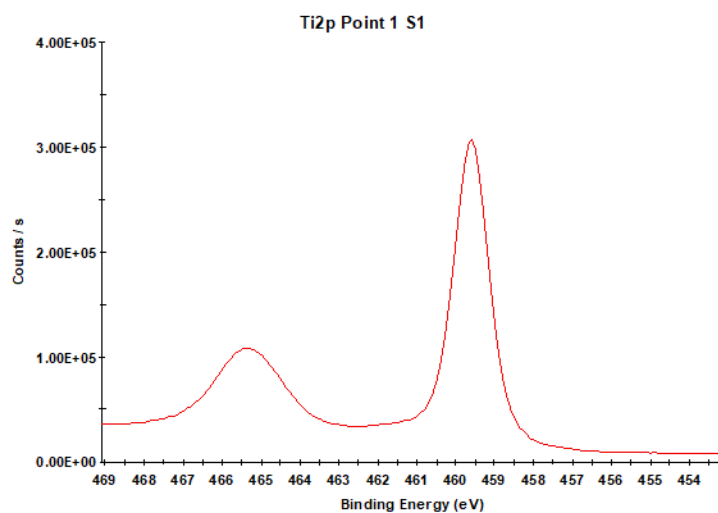


Figure 6.22: XPS spectrum for the Ti 2p region of FTO/DC-TiO₂/UrFe.

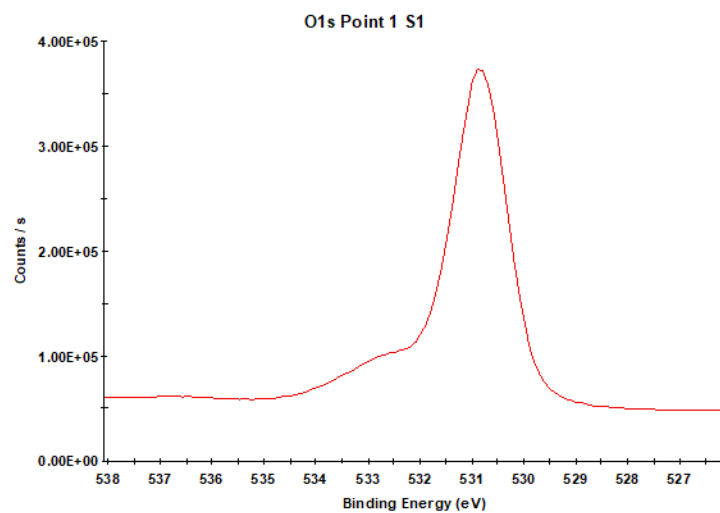


Figure 6.23: XPS spectrum for the O 1s region of FTO/DC-TiO₂/UrFe.

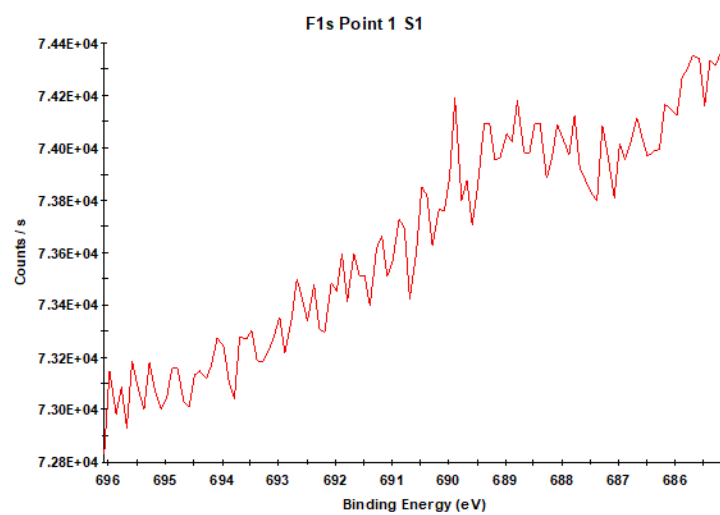


Figure 6.24: XPS spectrum for the F 1s region of FTO/DC-TiO₂/UrFe.

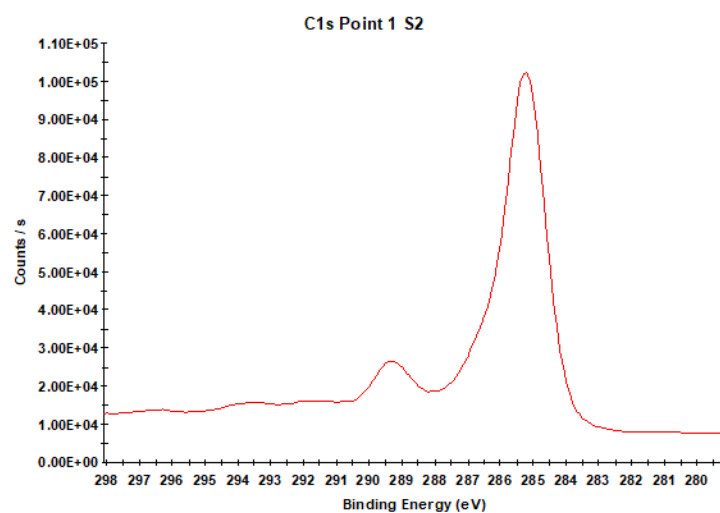


Figure 6.25: XPS spectrum for the C 1s region of FTO/DC-TiO₂/Link-UrFe.

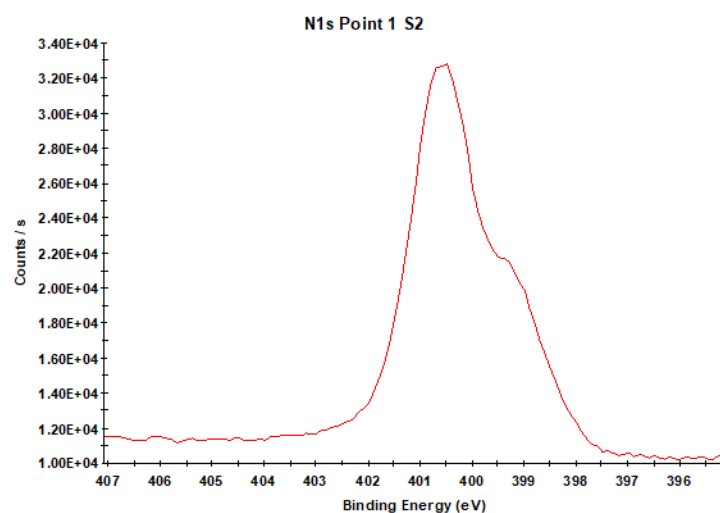


Figure 6.26: XPS spectrum for the N 1s region of FTO/DC-TiO₂/Link-UrFe.

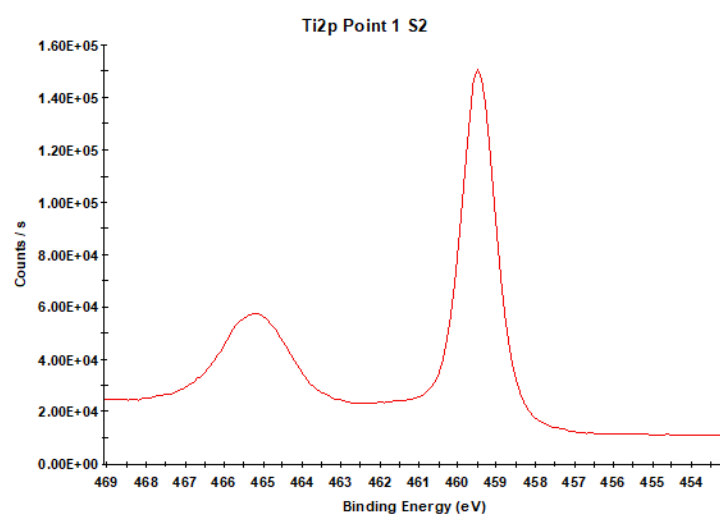


Figure 6.27: XPS spectrum for the Ti 2p region of FTO/DC-TiO₂/Link-UrFe.

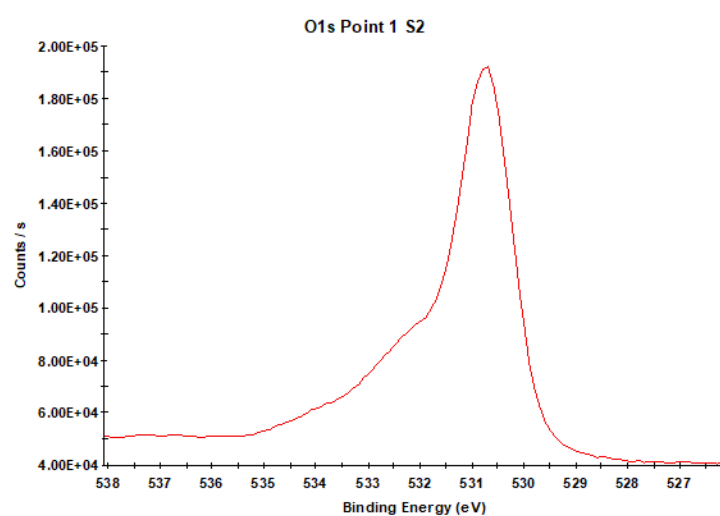


Figure 6.28: XPS spectrum for the O 1s region of FTO/DC-TiO₂/Link-UrFe.

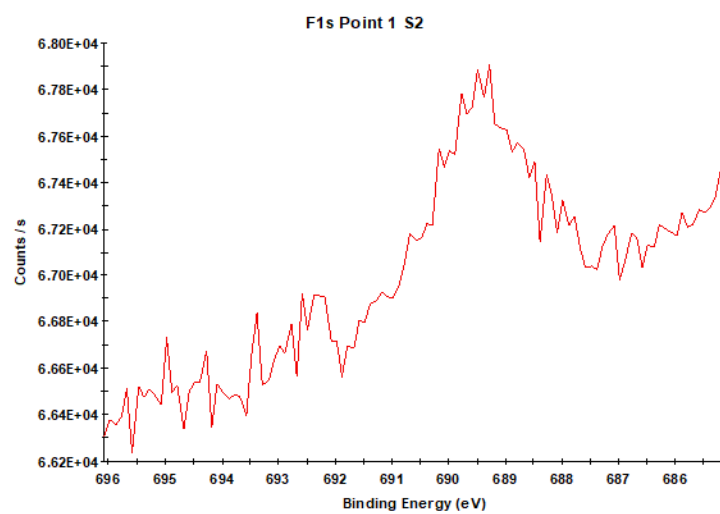


Figure 6.29: XPS spectrum for the F 1s region of FTO/DC-TiO₂/Link-UrFe.

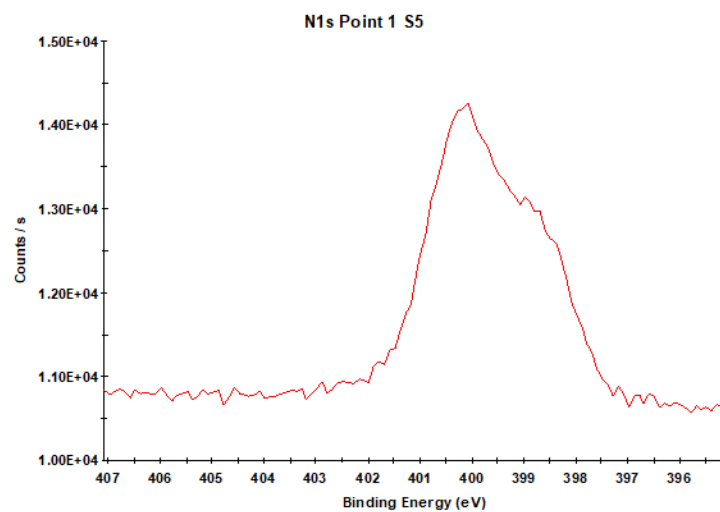


Figure 6.30: XPS spectrum for the N 1s region of the Cu₂O/ALD-Al₂O₃/ALD-TiO₂/DC-TiO₂/Link-UrFe electrode after photocurrent measurements.

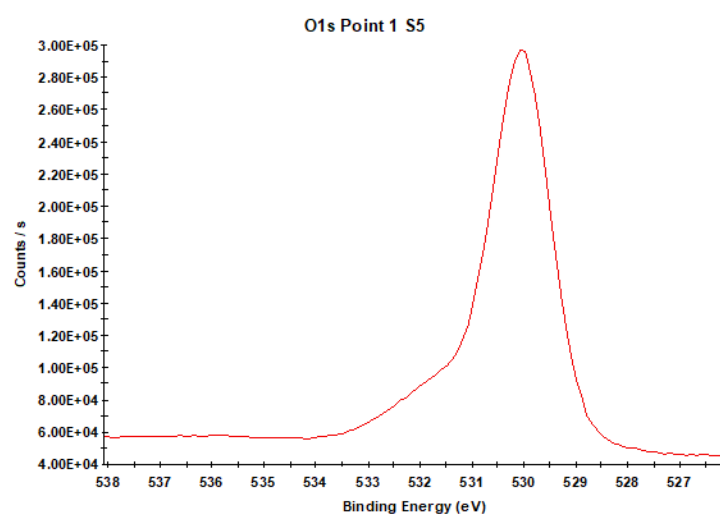


Figure 6.31: XPS spectrum for the O 1s region of the Cu₂O/ALD-Al₂O₃/ALD-TiO₂/DC-TiO₂/Link-UrFe electrode after photocurrent measurements.

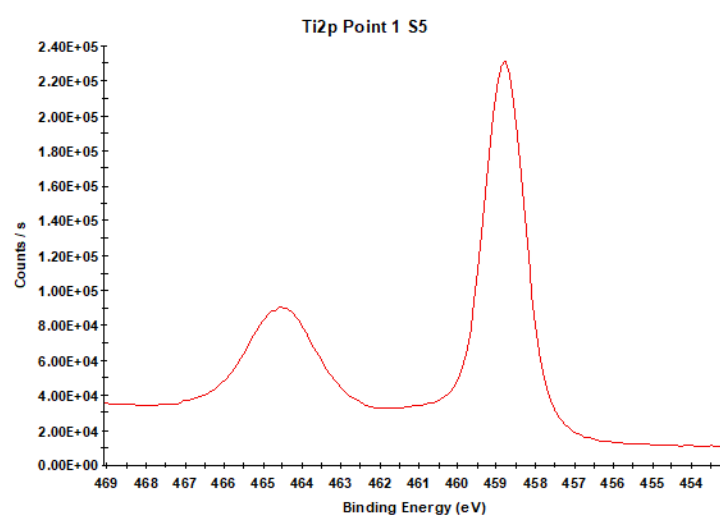


Figure 6.32: XPS spectrum for the Ti 2p region of the Cu₂O/ALD-Al₂O₃/ALD-TiO₂/DC-TiO₂/Link-UrFe electrode after photocurrent measurements.

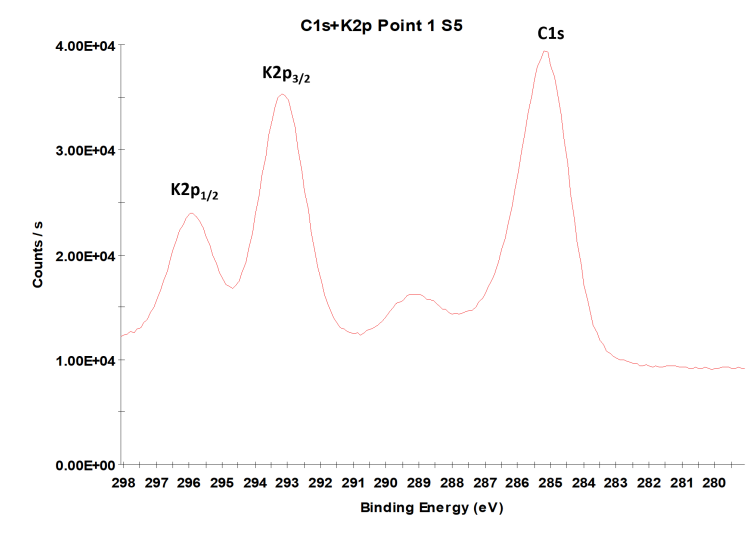


Figure 6.33: XPS spectrum for the C 1s and K 2p regions of the Cu₂O/ALD-Al₂O₃/ALD-TiO₂/DC-TiO₂/Link-UrFe electrode after photocurrent measurements.

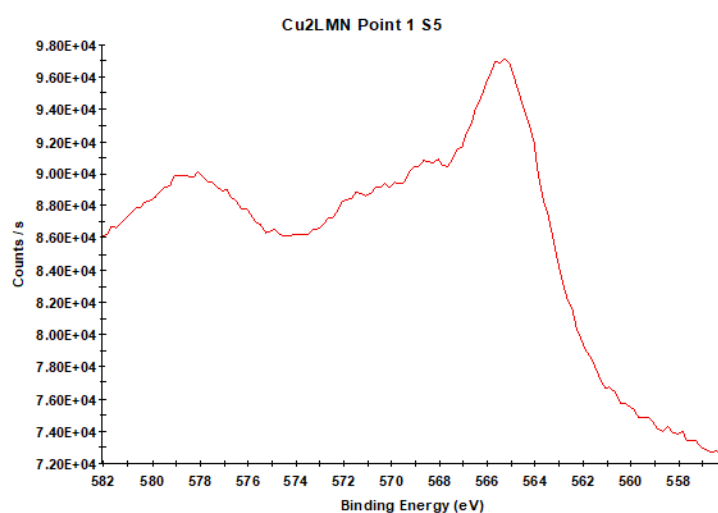


Figure 6.34: XPS spectrum for the Cu 2LMN region of the Cu₂O/ALD-Al₂O₃/ALD-TiO₂/DC-TiO₂/Link-UrFe electrode after photocurrent measurements.

6.3 . Chapter 4: Photocatalysis for oxygen atom transfer reactions

6.3.1 . Materials and instrumentation

Iron (II) triflate, methyl viologen dichloride hydrate (98 %) and sodium 4-styrene sulfonate were purchased from Sigma-Aldrich. Deuterium oxide and dioxygen-18O (97 %) were purchased from EURISO-TOP. The $[L_5Fe^{II}]^{2+}$ complex has been previously synthesized in the group by following reported works [14] [15] [16] [17].

UV-visible absorption spectra were recorded in solution using 1 cm quartz cuvettes on a Varian Cary 60 UV-vis spectrophotometer. NMR spectroscopic measurements were performed using a Bruker Avance III 400 MHz.

For Laser Flash Photolysis (LFP) experiments, samples were prepared in 1 cm quartz cuvettes. Transient absorption and emission measurements were recorded on an Edinburgh Instruments LP920 laser flash photolysis spectrometer. Laser excitation pulses were generated from a Continuum Surelite OPO laser (5 ns pulses duration, typical energy 10 mJ per flash) for excitation at 460 nm. The probe source is a pulsed 450 W Xenon lamp and the detectors are either a Hamamatsu photomultiplier tube (PMT) or a water-cooled Andor intensified charge coupled device (ICCD) camera.

6.3.2 . Photocatalysis

Photocatalysis experiments were carried out in Britton Robinson (BR) buffer pH 4.0 at 25 °C with a white LED from Metaphase Technology equipped with a Wratten 2B filter $\lambda > 450$ nm. The high performance liquid chromatography experiments (HPLC) were performed on 1260 infinity II LC system (Zorbax Eclipse Plus C18 column) from Agilent Technologies. The Thermo Scientific DSQ 2004 model from Thermo Fischer Scientific Company was employed for recording the electrospray ionization mass spectrometry experiments with an ESI method.

Photocatalysis experiments under $^{18}O_2$ atmosphere were prepared in a Schlenk tube. The reaction mixture was subjected to 3 times vacuum/argon cycles then one time vacuum/ $^{18}O_2$. After reaction, samples were treated with 1M HCl then extracted with ethyl acetate. The products formed were separated by preparative HPLC then analyzed by HRMS-ESI. Their identification and quantification was achieved by 1H -NMR with addition of 10% deuterium oxide to be used as reference. The substrate and products were identified and quantified from the following peaks: styrene sulfonate by doublet at 6.75 ppm, benzaldehyde by

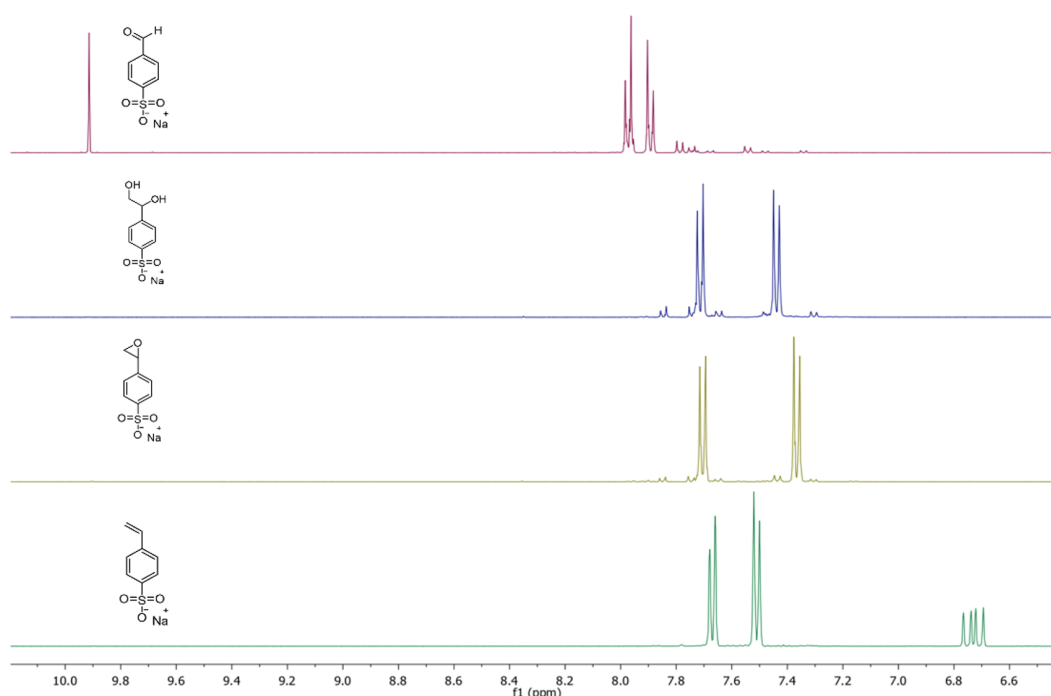


Figure 6.35: Extracts of the $^1\text{H-NMR}$ spectra of 4-styrenesulfonate, 4-(1,2-dihydroxyethyl)benzenesulfonate, 4-(oxiranyl)benzenesulfonate, 4-formylbenzenesulfonate. Solvent: D_2O

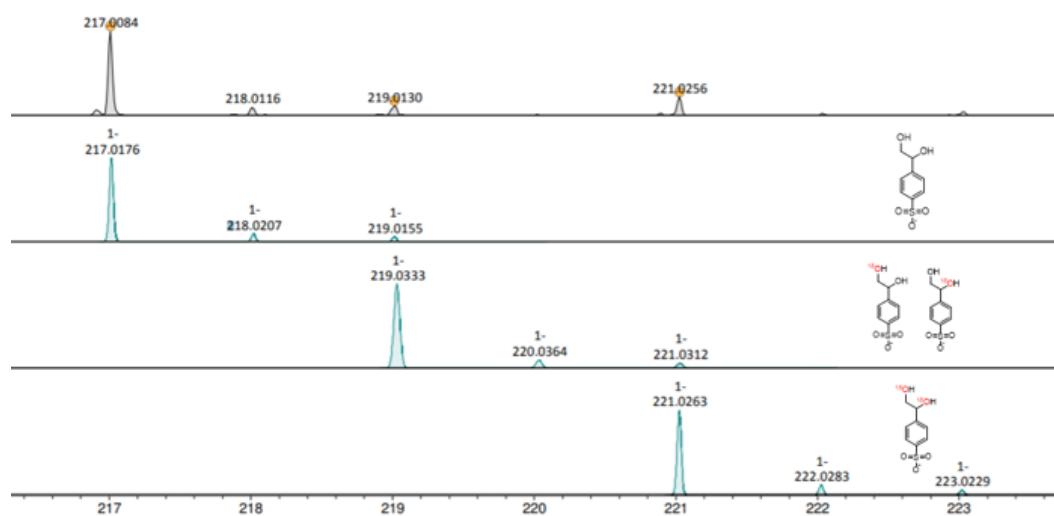


Figure 6.36: (Black) HRMS-ESI $^-$ of diol formed in sodium 4-styrenesulfonate oxygenation under irradiation for 22 hours (area backlight white LED = 1 mW cm^{-2} equipped with a Wratten filter 2E, $\lambda > 450 \text{ nm}$) in BR pH 4 buffer in presence of $[\text{Ru}^{\text{II}}(\text{bpy})_3]^{2+}$ ($30 \mu\text{M}$), MV^{2+} (4 mM), $[\text{L}_5\text{Fe}^{\text{II}}]^{2+}$ ($30 \mu\text{M}$) and sodium 4-styrenesulfonate (10 mM) with $^{18}\text{O}_2$ and (Cyan) HRMS-ESI $^-$ simulations of diol with ^{16}O and ^{18}O content.

singlet at 9.91 ppm, diol by doublet at 7.42 ppm, epoxide by doublet at 7.37 ppm.

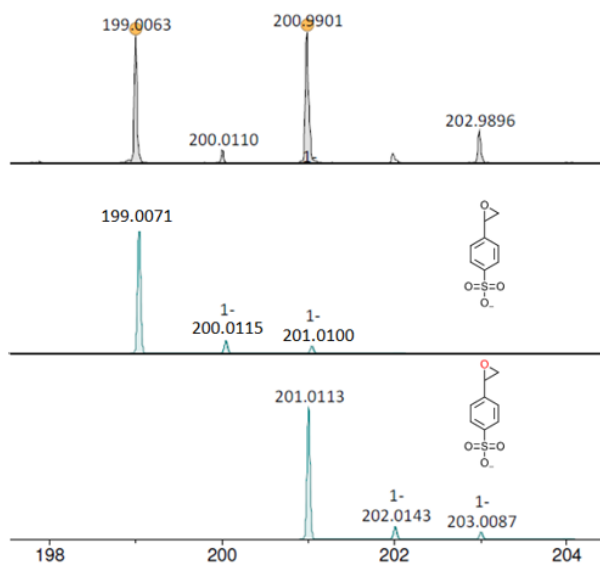


Figure 6.37: (Black) HRMS-ESI⁻ of epoxide formed in sodium 4-styrenesulfonate oxygenation under irradiation for 22 hours (area backlight white LED = 1 mW cm⁻² equipped with a Wratten filter 2E, λ > 450 nm) in BR pH 6 buffer in presence of [Ru^{II}(bpy)₃]²⁺ (30 μM), MV²⁺ (4 mM), [L₅Fe^{II}]²⁺ (30 μM) and sodium 4-styrenesulfonate (10 mM) with ¹⁸O₂ and (Cyan) HRMS-ESI⁻ simulations of diol with ¹⁶O and ¹⁸O content.

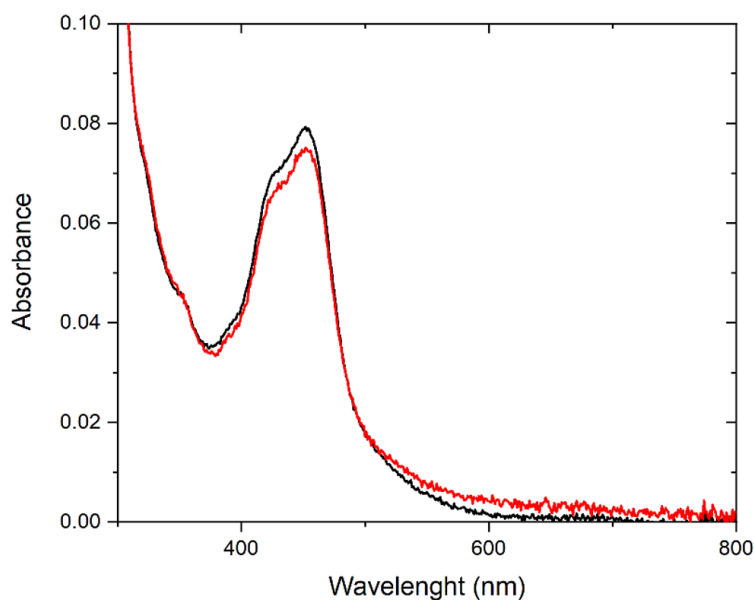


Figure 6.38: UV-visible spectra of [Ru^{II}(bpy)₃]²⁺ (30 μM) in BR buffer at pH 4 before (black) and after (red) irradiation for 22 h.

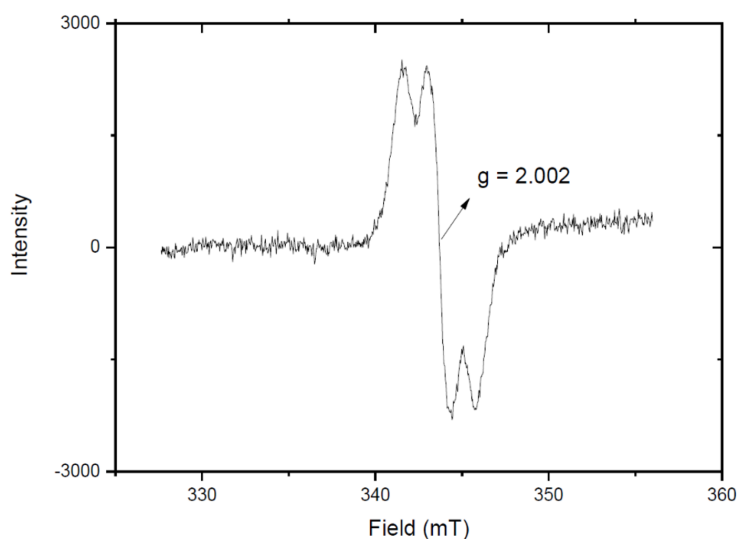


Figure 6.39: EPR spectrum of sodium 4-styrenesulfonate radical observed by mixing $[\text{Ru}^{\text{III}}(\text{bpy})_3]^{3+}$ (1 mM) with sodium 4-styrenesulfonate (10 mM) in BR pH4 buffer under argon. The spectrum was recorded on a X-band spectrometer at 80 K. The splitting of the signal is due to the hyperfine coupling with the α protons.

6.3.3 . Electronic paramagnetic resonance spectra

For Electron Paramagnetic Resonance (EPR) measurement, X-band cw-EPR spectra were recorded with a Bruker Elexsys 500 X-band spectrometer equipped with a standard ER 4102 (Bruker) X-band resonator, a Bruker teslameter, an Oxford Instruments cryostat (ESR 900) and an Oxford ITC504 temperature controller.

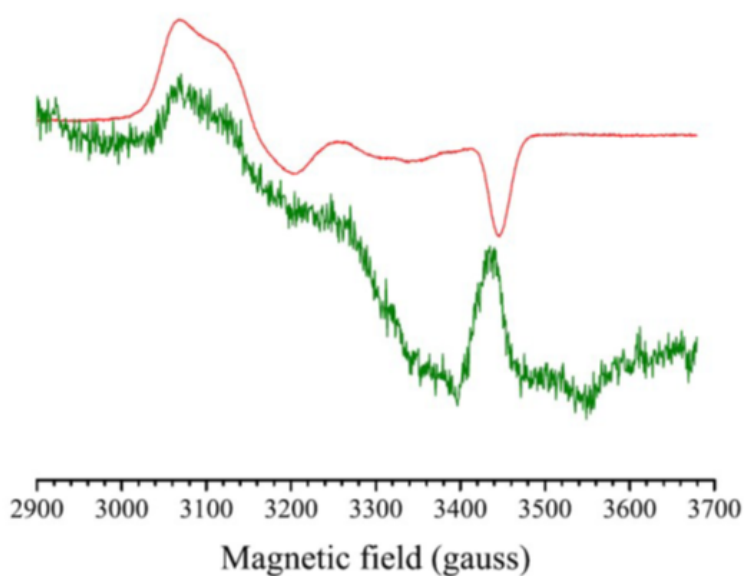


Figure 6.40: Amplified region of Fig. 4.20. EPR spectra of a B&R buffer pH 4 solution containing $[\text{Ru}^{\text{II}}(\text{bpy})_3]^{2+}$ ($30 \mu\text{M}$), MV^{2+} (20 mM), $[\text{L}_5\text{Fe}^{\text{II}}]^{2+}$ ($100 \mu\text{M}$) and 20 mM EDTA (red) or 200 mM TEOA (green) irradiated for 1 s with 100 W m^{-2} blue LED. In red, EPR spectrum of the photo-generated low spin $[\text{L}_5\text{Fe}^{\text{III}}\text{-OOH}]^{2+}$ species, in green EPR spectrum of the photo-generated high spin $[\text{L}_5\text{Fe}^{\text{III}}\text{-}\eta^2\text{O}_2]^+$ species.

Bibliography

- (1) Hasegawa, E.; Seida, T.; Chiba, N.; Takahashi, T.; Ikeda, H. Contrastive Photoreduction Pathways of Benzophenones Governed by Regiospecific Deprotonation of Imidazoline Radical Cations and Additive Effects. *The Journal of Organic Chemistry* **2005**, *70*, 9632–9635.
- (2) Gotico, P.; Boitrel, B.; Guillot, R.; Sircoglou, M.; Quaranta, A.; Halime, Z.; Leibl, W.; Aukauloo, A. Second-Sphere Biomimetic Multipoint Hydrogen-Bonding Patterns to Boost CO₂ Reduction of Iron Porphyrins. *Angewandte Chemie International Edition* **2019**, *58*, 4504–4509.
- (3) Prier, C. K.; Rankic, D. A.; MacMillan, D. W. C. Visible Light Photoredox Catalysis with Transition Metal Complexes: Applications in Organic Synthesis. *Chemical Reviews* **2013**, *113*, 5322–5363.
- (4) Jödecke, M.; Pérez-Salado Kamps, Á.; Maurer, G. An Experimental Investigation of the Solubility of CO₂ in (N, N-Dimethylmethanamide + Water). *Journal of Chemical & Engineering Data* **2012**, *57*, 1249–1266.
- (5) Frisch, M. J.; Trucks, G. W.; Schlegel, H. B.; Scuseria, G. E.; Robb, M. A.; Cheeseman, J. R.; Scalmani, G.; Barone, V.; Mennucci, B.; Petersson, G. A. Gaussian Inc. Wallingford CT, 2009.
- (6) Gotico, P.; Roupnel, L.; Guillot, R.; Sircoglou, M.; Leibl, W.; Halime, Z.; Aukauloo, A. Atropisomeric Hydrogen Bonding Control for CO₂ Binding and Enhancement of Electrocatalytic Reduction at Iron Porphyrins. *Angewandte Chemie International Edition* **2020**, *59*, 22451–22455.
- (7) Davethu, P. A.; de Visser, S. P. CO₂ Reduction on an Iron-Porphyrin Center: A Computational Study. *The Journal of Physical Chemistry A* **2019**, *123*, 6527–6535.
- (8) Grimme, S.; Ehrlich, S.; Goerigk, L. Effect of the damping function in dispersion corrected density functional theory. *Journal of Computational Chemistry* **2011**, *32*, 1456–1465.
- (9) Tomasi, J.; Mennucci, B.; Cammi, R. Quantum Mechanical Continuum Solvation Models. *Chemical Reviews* **2005**, *105*, 2999–3094.
- (10) Hay, P. J.; Wadt, W. R. *Ab initio* effective core potentials for molecular calculations. Potentials for K to Au including the outermost core orbitals. *The Journal of Chemical Physics* **1985**, *82*, 299–310.
- (11) Francl, M. M.; Pietro, W. J.; Hehre, W. J.; Binkley, J. S.; Gordon, M. S.; DeFrees, D. J.; Pople, J. A. Self-consistent molecular orbital methods. XXIII. A polarization-type basis set for second-row elements. *The Journal of Chemical Physics* **1982**, *77*, 3654–3665.
- (12) Coutancier, D.; Zhang, S.-T.; Bernardini, S.; Fournier, O.; Mathieu-Pennober, T.; Donsanti, F.; Tcherynycheva, M.; Foldyna, M.; Schneider, N. ALD of ZnO:Ti: Growth Mechanism and Application as an Efficient Transparent Conductive Oxide in Silicon Nanowire Solar Cells. *ACS Applied Materials & Interfaces* **2020**, *12*, 21036–21044.
- (13) Le Tulzo, H.; Schneider, N.; Lincot, D.; Patriarche, G.; Donsanti, F. Impact of the sequence of precursor introduction on the growth and properties of atomic layer deposited Al-doped ZnO films. *Journal of Vacuum Science & Technology A* **2018**, *36*, 041502.
- (14) Bohn, A.; Chinaux-Chaix, C.; Cheaib, K.; Guillot, R.; Herrero, C.; Sénéchal-David, K.; Rebilly, J.-N.; Banse, F. Base-controlled mechanistic divergence between iron(IV)-oxo and iron(III)-hydroperoxo in the H₂O₂ activation by a nonheme iron(II) complex. *Dalton Transactions* **2019**, *48*, 17045–17051.
- (15) Bohn, A. Approche électrochimique de l'activation réductrice du dioxygène à l'aide d'un complexe de fer(II) non hémique, PhD Thesis, 2018.
- (16) Bohn, A.; Sénéchal-David, K.; Rebilly, J.-N.; Herrero, C.; Leibl, W.; Anxolabéhère-Mallart, E.; Banse, F. Heterolytic OO Bond Cleavage Upon Single Electron Transfer to a Nonheme Fe(III)OOH Complex. *Chemistry – A European Journal* **2022**, *28*, DOI: [10.1002/chem.202201600](https://doi.org/10.1002/chem.202201600).

-
- (17) Buron, C.; Groni, S.; Ségaud, N.; Mazerat, S.; Dragoë, D.; Fave, C.; Sénéchal-David, K.; Schöllhorn, B.; Banse, F. Self-assembled monolayer formation of a (N₅)Fe(II) complex on gold electrodes: electrochemical properties and coordination chemistry on a surface. *Dalton Transactions* **2016**, 45, 19053–19061.

List of Publications

1) Pugliese, E.; Gotico, P.; Wehrung, I.; Boitrel, B.; Quaranta, A.; Ha-Thi, M-H.; Pino, T.; Sircoglou, M.; Leibl, W.; Halime, Z.; Aukauloo, A. Dissection of Light-Induced Charge Accumulation at a Highly Active Iron Porphyrin: Insights in the Photocatalytic CO₂ Reduction. *Angewandte Chemie International Edition* **2022**, *61*, 14, e202117530.

2) Pugliese, E.; Vo, N.T.; Boussac, A.; Banse, F.; Mekmouche, Y.; Simaan, J.; Tron, T.; Gotico, P.; Sircoglou, M.; Halime, Z.; Leibl, W.; Aukauloo, A. Photocatalytic generation of a non-heme Fe(III)-hydroperoxo species with O₂ in water for the oxygen atom transfer reaction. *Chemical Science* **2022**, *13*, 12332-12339.

3) Oliveira Udry, G. A.; Tiessler-Sala, L.; Pugliese, E.; Urvoas, A.; Halime, Z.; Maréchal, J.D.; Mahy, J.-P.; Ricoux, R. Photocatalytic Hydrogen Production and Carbon Dioxide Reduction Catalyzed by an Artificial Cobalt Hemoprotein. *International Journal of Molecular Sciences* **2022**, *23*, 14640.

Résumé en langue française

La photosynthèse naturelle nous enseigne comment transformer l'énergie solaire en une forme d'énergie facilement utilisable par les organismes. Dans une époque marquée par la crise énergétique et la nécessité d'abandonner les combustibles fossiles, les chimistes se tournent vers cette machine hautement fonctionnelle pour traduire ses enseignements en systèmes artificiels, capables d'utiliser la lumière du soleil pour faire des réactions chimiques. On appelle cette approche « photosynthèse artificielle ».

Dans la première partie de cette thèse, nous nous sommes intéressés à étudier la réduction du CO₂ par voie photocatalytique. Convertir le CO₂ en produits chimiques à plus grandes valeurs est de grand intérêt pour la communauté scientifique, étant donné les émissions croissantes de gaz à effet serre dans l'atmosphère.

La réduction du CO₂ induite par la lumière peut être assez complexe à suivre et à comprendre, car de nombreux éléments différents sont présents dans la réaction et peuvent l'affecter. Dans cette étude, nous avons pu comprendre le rôle que jouent des nombreux facteurs sur l'activité photocatalytique. En choisissant le chromophore approprié, nous avons pu étudier la réactivité d'une famille de porphyrines de fer, notamment en mettant en évidence le rôle crucial que la deuxième sphère de coordination peut jouer dans la catalyse. Le catalyseur **UrFe** modifié avec des groupements urée montre une excellente activité pour la production de CO pour un système homogène, en termes de stabilité (TON), de vitesse (TOF) et de sélectivité (près de 100% de CO). Ce système a été étudié aussi avec différentes techniques spectroscopiques, afin d'identifier les intermédiaires réactifs et l'étape cinétiquement déterminante dans le mécanisme. Travailler dans un milieu homogène nous a permis l'application de ces techniques pour obtenir d'importantes informations. Les formes réduites de la porphyrine ont pu être identifiées, et une interaction inattendue du CO₂ avec l'état Fe(I) a été observée. Tout au long de l'étude, nous avons cherché à comparer ce catalyseur au **F₂₀TPPFe**, qui a le même potentiel de réduction, mais sans la deuxième sphère de coordination de **UrFe**. Pour le dernier, nous n'avons pas pu détecter d'interaction du CO₂ sur l'état Fe(I), ce qui nous a permis de déduire que la liaison précoce du substrat sur **UrFe** est cruciale pour augmenter la force motrice de la réaction, débloquant une nouvelle espèce qui

est plus facilement réduite. De nos résultats, nous avons également déduit que la liaison au substrat peut être l'étape cinétiquement déterminante dans le cycle catalytique.

Dans l'ensemble, il reste encore beaucoup à apprendre pour suivre le processus de transfert d'électrons multiples, mais nous avons pu mettre en place des méthodes simples pour extraire des informations importantes sur le mécanisme de la réaction.

Dans le chapitre 3, nous avons choisi d'intégrer le même catalyseur à base de porphyrine de fer sur une photocathode pour rendre la photocatalyse hétérogène, en essayant de nous rapprocher à des dispositifs plus intéressants du point de vue des applications. Assembler un dispositif hétérogène de réduction de CO_2 assistée par la lumière peut apporter plusieurs avantages par rapport à une système photocatalytique homogène (milieu aqueux, recyclage du catalyseur, plus petite quantité de catalyseur, stabilité du dispositif, *etc.*). Cependant, la construction d'un tel dispositif peut être assez difficile étant donné que chaque couche doit être optimisée pour maximiser le photocourant tout en minimisant la photocorrosion et la recombinaison de charge. Dans cette étude, nous avons construit un système hybride qui consiste d'un semi-conducteur Cu_2O de type p modifié avec le catalyseur **Link-UrFe** pour la réduction du CO_2 . Nous avons pu démontrer l'importance d'optimiser la méthode de dépôt de Cu_2O et ses conséquences sur la cellule photoélectrocatalytique. Nous avons aussi mis en évidence le rôle crucial que joue l'ancrage covalent dans la fixation du catalyseur sur la surface.

Pour ancrer le catalyseur moléculaire, nous avons mis en place une couche mésoporeuse de TiO_2 , où la porosité est fondamentale pour assurer une quantité maximale du catalyseur. Le TiO_2 a été choisi car il s'agit d'un matériau bien connu à la fois pour former des films transparents et pour permettre l'ancrage covalent de molécules. Nous avons rencontré quelques difficultés dans cette étape, car la pâte de TiO_2 peut dégrader la couche de Cu_2O . Nous avons finalement utilisé une technique de drop-casting qui nécessitera d'autres améliorations en particulier pour la transparence.

Différentes couches ALD ont également été ajoutées à l'électrode pour améliorer la stabilité et minimiser la photocorrosion. Nous avons remarqué un courant plus stable par rapport à une électrode où Cu_2O est directement en contact avec la couche mésoporeuse de TiO_2 . Bien que la densité de photocourant puisse être diminuée en raison des interfaces ajoutées, nous pensons qu'un gain de stabilité est plus important pour constituer un appareil applicable à l'industrie.

Des études électrochimiques sur des électrodes sans photoabsorbeur ont confirmé que même immobilisé en surface, le catalyseur **Link-UrFe** peut effectuer la réduction du CO₂, bien que la présence de TiO₂ pourrait affecter la sélectivité du produit.

Dans l'ensemble, cette étude préliminaire offre un panorama sur les défis auxquels nous sommes confrontés lors de l'assemblage d'une photocathode pour la réduction de CO₂. Utiliser un semi-conducteur très réducteur est avantageux en terme de potentiel de réduction auquel nous pouvons accéder, mais nécessite une stabilisation soignée pour éviter l'auto-réduction. D'autres travaux sont envisagés afin d'optimiser l'assemblage des différentes couches et de tirer parti de la deuxième sphère de coordination que le catalyseur moléculaire offre.

Dans le chapitre 4, nous nous sommes tournés vers un autre type de réactivité induite par la lumière, impliquant l'activation réductrice du O₂ pour faire des réactions de transfert d'atome d'oxygène. L'activation du dioxygène pour les réactions de transfert d'atome d'oxygène par photocatalyse peut être avantageuse grâce à la génération *in situ* d'espèces réductrices qui peuvent transférer des électrons à l'O₂. Cependant, contrôler les transferts d'électrons multiples induits par la lumière et leur directionnalité peut être une tâche difficile.

Dans cette étude nous avons choisi de combiner un module photoredox basé sur [Ru(bpy)₃]²⁺ et MV²⁺ comme relais d'électrons, avec le catalyseur [L₅Fe^{II}]²⁺ pour oxyder le sulfonate de styrène (S) comme substrat modèle, en utilisant du dioxygène. Une étude individuelle des événements photophysiques nous a aidés à suivre la chaîne des réactions qui se déroulaient dans ce système. Nous sommes ensuite passés à l'étude de l'activité photocatalytique, pour trouver trois produits possibles : aldéhyde, époxyde et diol. Les TON trouvés ici sont en ligne avec d'autres articles présentant des catalyseurs similaires utilisant H₂O₂ comme source d'atomes d'oxygène. La sélectivité du diol par rapport à l'époxyde semble être sensible au pH, car l'époxyde est moins stable dans des conditions acides.

Après avoir vérifié d'être dans un régime catalytique, nous avons cherché à caractériser des intermédiaires réactifs dans les mêmes conditions catalytiques. Nous avons réussi à capturer à la fois les intermédiaires [L₅Fe^{III}OOH]²⁺ et [L₅Fe^{III}OO]⁺ par photoaccumulation, en milieu aqueux et à température ambiante. Ces espèces ont été caractérisées par spectroscopies UV-vis et RPE. Il est particulièrement intéressant de générer des intermédiaires réactifs dans les mêmes conditions que la catalyse car elle apporte une preuve directe de leur implication dans le cycle catalytique. Dans ce chapitre, nous avons pu

rassembler les différentes données pour proposer un mécanisme, dont deux des principaux intermédiaires ont été identifiés expérimentalement. Plus d'études seront nécessaires pour mieux comprendre le cycle catalytique, où des espèces du type fer-oxo sont très probablement impliquées, mais aucune preuve directe n'a pu être trouvée pour le moment. Ces résultats donnent une démonstration de l'application de réactions photo-induites pour effectuer l'oxydation de substrats organiques à l'aide de l'O₂, source abondante dans l'atmosphère. Cela peut nous permettre d'opérer dans des conditions douces, même s'il reste encore beaucoup à comprendre pour maîtriser la chimie complexe de l'O₂.